Laser Desorption Time-of-Flight Mass Spectrometry

by

Kevin Francis Costello

A thesis presented for the degree of
Doctor of Philosophy in the
Faculty of Science at the
University of Edinburgh
1991

Declaration

This thesis was composed by myself and is based on work carried out whilst a member of the molecular beam laser spectroscopy group in the Chemistry Department at the University of Edinburgh.

Signed

_____ _____

Date 29/1/91

To mum and dad; hope this completes the set.

"Someone wants to know
If I know all the answers,
Or am I just guessing?
Guess we'll never really know."

B. Mould, 1985.

Abstract

The techniques of supersonic molecular beam cooling and laser multiphoton ionisation (MPI) spectroscopy have been combined to give a potentially powerful analytical technique. Two methods of sample introduction into the molecular beam have been employed, namely resistive heating and laser desorption. The resistive heating method allowed 2-colour MPI spectra of naphthalene, anthracene and perylene to be recorded in a simple free jet apparatus. A sensitivity for anthracene of 600 ppb is estimated.

A time-of-flight (TOF) mass spectrometer has been developed, incorporating both linear and reflecting-geometry (reflectron) flight tubes, to allow laser desorption MPI (LD-MPI) mass spectra to be recorded for a number of involatile and thermally unstable compounds. Mass resolutions of 300 (linear) and 850 (reflectron) have been obtained for aniline.The constraints affecting the mass resolving power of both spectrometer designs are discussed.

Finally, the potential of LD-MPI mass spectrometry as a sensitive, selective analytical technique is evaluated. The mass spectra of a number of polynuclear aromatic hydrocarbons, porphyrins and amino acids are presented, along with those of a simple mixture of the three aromatic amino acids tryptophan, tyrosine and phenylalanine. A sub-nanomole detection limit is estimated for tryptophan. Means to improve the sensitivity of the technique are discussed. The wider analytical applications of LD-MPI mass spectrometry are considered.

Acknowledgements

This thesis would not have been possible without contributions from several people and organisations. Firstly, thanks must go to the Carnegie Trust for the Universities of Scotland, who funded me during the period of this work. BP Research provided much of the money required to construct the time-of-flight mass spectrometer, and also funded the acquisition of the pulsed CO_2 laser employed during part of this work. Without this provision, none of these experiments would have been possible.

My thanks must go to my two supervisors, Pat Langridge-Smith and Robert Donovan, for not only stimulating my interest in laser spectroscopy and mass spectrometry in the first place, but for their guidance and encouragement throughout the course of this work.

Particular thanks must be given to my coworkers in the laboratory. Trevor Ridley taught me all I know about the use of excimer pumped dye lasers, whilst Paul Greenhill designed the heated nozzle system employed as part of this work. Paul also helped to finalise the design of the vacuum system of the time-of-flight mass spectrometer. The inmates of Lab 73 deserve a special mention. George Keenan not only constructed all the ion optics used in this work, but also was a very able assistant and partner in the search for ion signals into the wee small hours. Andrew Butler wrote the suite of software employed to control and extract data from the time-of-flight experiments. Peter Cartwright provided many words of wisdom on the subject of time-of-flight mass spectrometry, whilst the enthusiasm and experience of Andy James was a vital factor in the initial mass spectrometric

studies.

The skill of the technical staff of both the mechanical and electronic workshops at the department of Chemistry is acknowledged. Without the expertise of Stuart Mains, John Ashfield, Gordon Waugh and Duncan MacLean, the many delays and interruptions which hampered this work would have been considerably longer.

This thesis was produced by employing the SCRIBE word processor. I am grateful to Roger Hare for allowing access to his database, and to Pat Langridge-Smith and Murray Brown for proof-reading this thesis.

I would like to thank all members, both past and present, of the laser chemistry group for creating such an amicable working and social atmosphere during my time in Edinburgh. Finally, I would like to thank Scott, Bob, Murray, Andy, Trevor and Jim for their rapid (and often scathing) wit, which helped to see me through the dark days of no equipment.

Table of Contents

Chapter 1
Introduction.

A large percentage of the information that is presently available about the structure and properties of molecules has come from experiments in the gas-phase. Only in the gas-phase are molecules free from solvent and environmental effects. Optical spectroscopy has made significant contributions to the understanding of the energy levels, structure, reactivity and photochemistry of molecules. Thus, gas-phase spectroscopic techniques are extremely important tools, not only in basic research but also for chemical analysis. The advent of high power, tunable lasers has led to the development of many new spectroscopic techniques [1]. One of these methods, multiphoton ionisation (MPI), has found a wide range of applications in pure spectroscopy and in chemical analysis.

For many gas-phase molecules, the minimum energy required to remove an electron, the ionisation potential (I.P.), is typically of the order of 7 to 10 eV [2], [3]. Thus, single-photon ionisation, as illustrated in figure 1.1(a), can only be accomplished by absorption of an energetic vacuum ultraviolet (VUV) photon, with $\lambda < 180$ nm. Radiation of this wavelength is relatively difficult to work with experimentally, requiring evacuated light paths. However, in MPI, a molecule absorbs two or more, less energetic, visible or ultraviolet (UV) photons to excite it from the ground state to above the ionisation potential (see figures 1(b)-1(d)). Such visible and UV photons, which are routinely available from a wide variety of lasers, are considerably more convenient to work with than VUV radiation.

Figure 1.1. Ionisation Schemes.

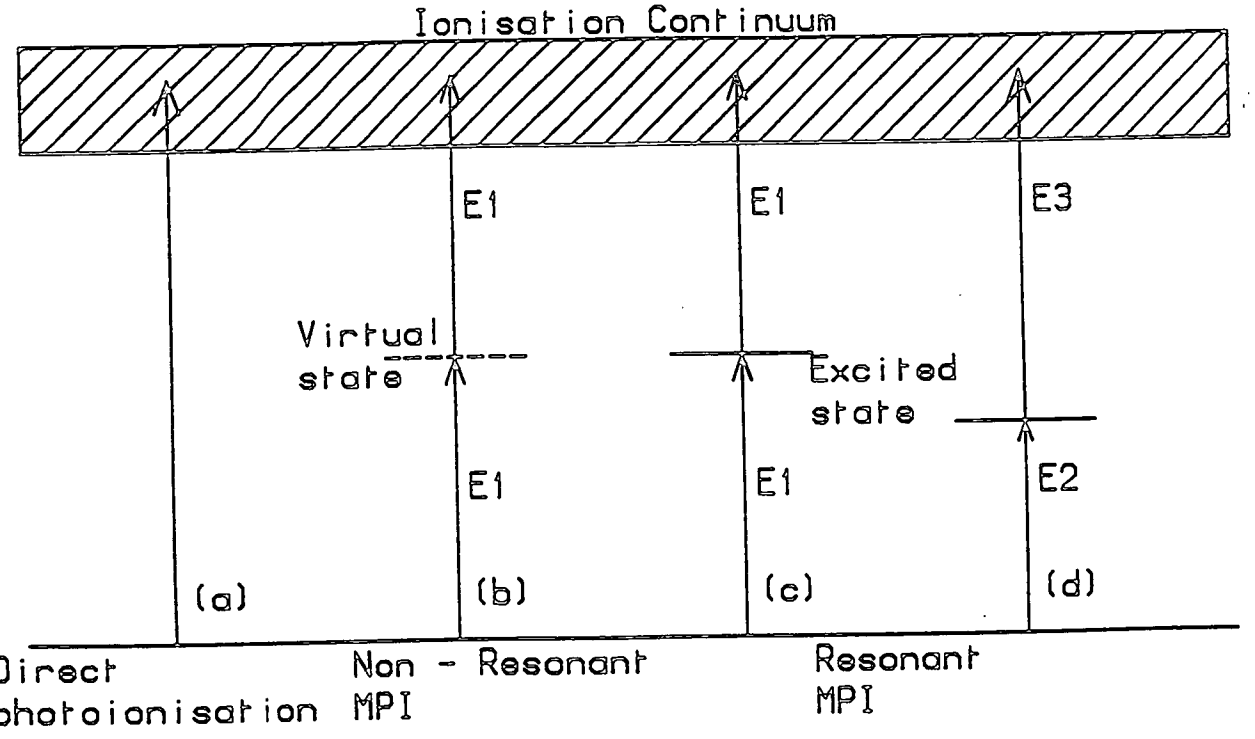

The simplest multiphoton process, namely non-resonant, simultaneous absorption of two photons by a molecule was predicted by Göppert-Mayer as early as 1931 [4]. This process, which can result in photoionisation, is illustrated in figure 1.1(b). In order to account for the 30 year gap before the first observation [5] of laser multiphoton absorption, it is instructive to consider the kinetics of such processes. The rate of an n-photon absorption process, W_n, is given by

$$W_n = \sigma_n I^n,$$

where σ_n is the cross section for n-photon absorption (units $cm^{2n}s^{n-1}$) and I is the instantaneous photon flux (photons $cm^{-2}s^{-1}$). Cross sections for strongly-allowed one-photon transitions are of the order of 10^{-17} to 10^{-18} cm^2. However, those for allowed two-photon absorptions are typically only ~ 10^{-50} cm^4s. Thus, typical UV arc-lamps, which can provide 10^{15} photons $cm^{-2}s^{-1}$ within a useful bandwidth, are not sufficiently powerful to drive such a process. A typical narrow bandwidth pulsed laser, on the other hand, can provide fluxes in excess of 10^{28} photons $cm^{-2}s^{-1}$ especially when tightly focused. Such a laser can easily drive two-photon absorption processes.

In general, the absorption of photons by a molecule is a low efficiency process. In a simultaneous two-photon absorption, a "virtual" state is populated at the one-photon level. This "virtual" state is not a real eigenstate of the molecule, but is described quantum mechanically by an energy-weighted summation of real states with the appropriate symmetry. The effective lifetime of such a state is very short, approximately 1 femtosecond, which corresponds to the photon fly-by time. The molecule can only absorb a second photon during this lifetime if the

photon flux is sufficiently high.

The situation is radically different if the laser photon energy corresponds to the difference in energy between the electronic ground state and a real excited rovibronic state of the molecule (as illustrated in figures 1.1(c) and 1.1(d)). If the transition is allowed, conventional one-photon absorption can occur. Since the real excited state has a lifetime of 1 nanosecond or greater, the efficiency of this step-wise absorption process is increased by several orders of magnitude over that of the non-resonant process [6], [7], particularly if the wavelength of the photon corresponds to a maximum in the absorption spectrum of the molecule. This process is known as resonantly-enhanced MPI (REMPI). Figures 1.1(c) and 1.1(d) illustrate the REMPI method which has been most extensively applied, and the one which was employed in the work described in this thesis. This is resonant 2-photon ionisation (R2PI), in which one photon absorption promotes a molecule to an excited electronic state and a second photon then ionises the molecule. Clearly, the sum of the two photon energies must be greater than the molecular ionisation potential for R2PI to occur. The two photons can have either the same (figure 1.1(c)) or different (figure 1.1(d)) wavelengths. All the molecules studied in this work have ionisation potentials between 7 and 10 eV, so R2PI can be accomplished using near UV pulsed laser sources. Other molecules may require two or more photons to reach the first resonant state. Since at least one photon is non-resonant, and therefore interacts with a "virtual" state, the efficiency for ionisation in these processes is far less than that achieved in R2PI.

The application of MPI to molecular spectroscopy was first reported by Johnson and coworkers [8] and Petty et al. [7] in 1975. The enormous potential of MPI

and, in particular, R2PI as both a spectroscopic and an analytical tool has been widely exploited since that time [9], [10]. If a narrow bandwidth dye laser, which can provide tunable visible and UV radiation, is employed, an absorption-like spectrum can be obtained by monitoring the photoion signal as a function of wavelength. The simplest R2PI experiment involves irradiating a low pressure gas, at room temperature, in a cell using the tunable output from a single laser system, and collecting the ions irrespective of their mass. Such a spectrum is presented in figure 1.2, which shows the origin band region for the S_1-S_0 ($^1B_2$ - $^1A_1$) transition in aniline at a pressure of 10^{-6} torr.

Of course, the R2PI/MPI spectra are not necessarily identical to the conventional absorption spectra. If the resonant state decays on a timescale comparable to that of the absorption of the second photon, the efficiency of the ionisation process is affected. Thus, Rydberg states are often detected by MPI whilst isoenergetic high-lying valence states remain unseen [11]. These valence states commonly undergo fast radiationless transitions to states with low ionisation cross sections. Similarly, if the ionisation cross section varies with wavelength, the R2PI spectrum will differ from the absorption spectrum. In general, for excitation out of the low-lying first excited singlet (S_1) state of aromatic molecules, this variation in ionisation cross section is small, especially if the absorption of the second photon excites the molecule to well above its ionisation potential [12].

Some of the advantages afforded by R2PI are best illustrated by comparison with another laser-based spectroscopic method, namely laser-induced fluorescence (LIF). R2PI offers potentially higher sensitivity than LIF, since ions can be collected with much higher efficiency than photons ($\sim$100% compared to $\sim$5%)

Figure 1.2. R2PI Spectrum of Aniline. The electronic transition pumped is the $^1B_2$-$^1A_1$ (S_1-S_0) transition.

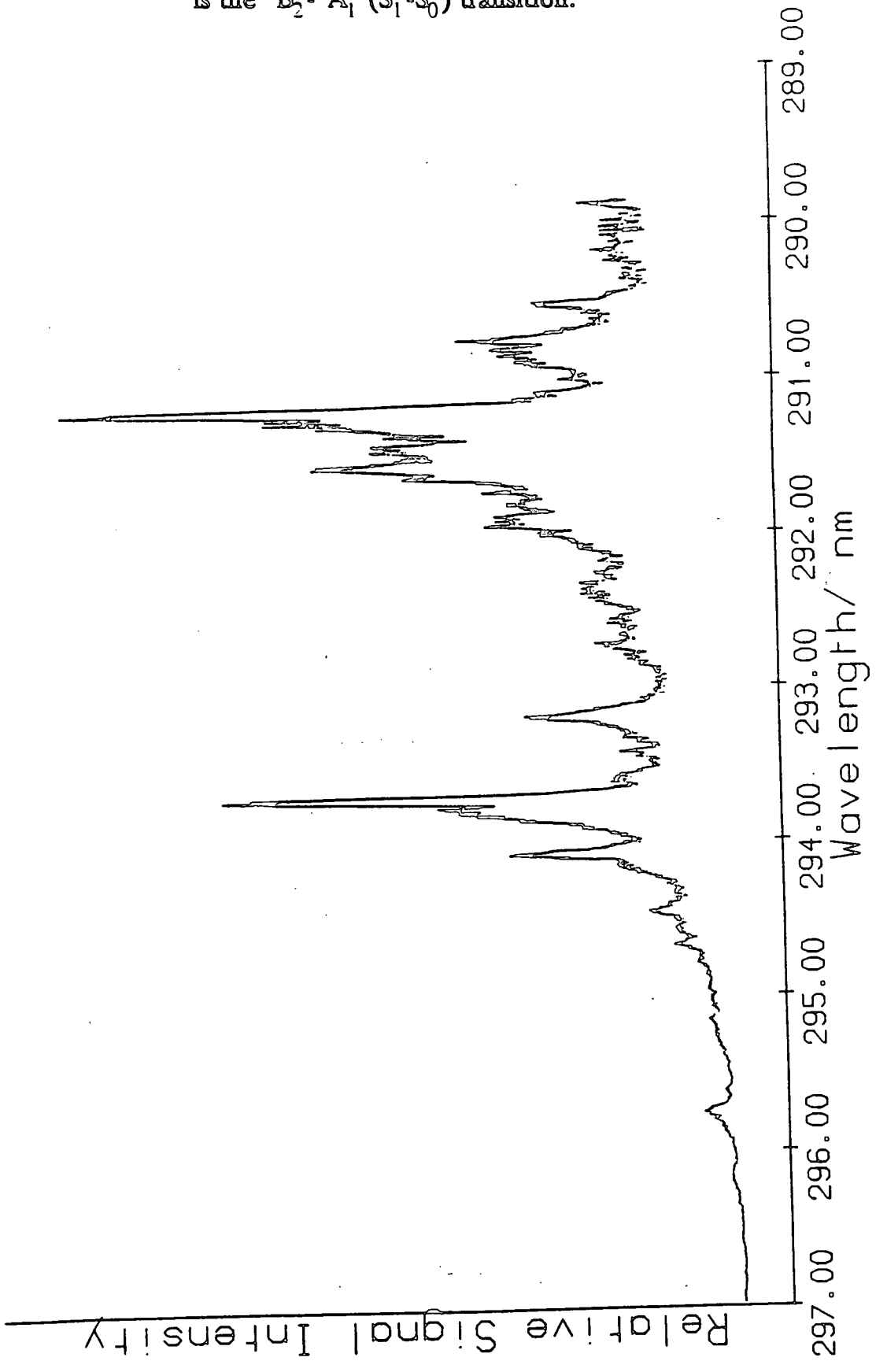

and can be directly converted into a meaningful signal. Also, problems arising from scattered laser light, which are prevalent in LIF, are minimal in R2PI experiments. In many cases, for molecules which are at best weakly fluorescent, multiphoton techniques are the only spectroscopic methods that can be feasibly employed. Of course, the reciprocal argument is also true. Often, it is not possible to obtain an R2PI (or any other multiphoton ionisation) signal, due to excessively high ionisation potentials, resonant intermediate electronic absorption bands that are in inaccessible parts of the spectrum, or to rapid inter-system crossing. In these cases, fluorescence detection techniques are clearly superior.

A variety of techniques that are based upon MPI have been developed since the middle of the 1970's. For example, the symmetries of the states involved in MPI processes can be investigated by using polarised light [13]. By employing two lasers, measurements have been made on the adiabatic ionisation potentials of some polyatomic molecules [14], and by varying the time delay between the excitation and ionisation lasers, excited state lifetimes have been measured [15]. However, it has been the combination of MPI with mass spectrometry which has attracted most attention. MPI mass spectrometry (MPIMS) has proved to be a powerful analytical tool, since it has the potential of being a molecule-specific detector, with both high sensitivity and high selectivity.

In MPIMS, molecules are not only identified by their mass spectra, but also by their MPI spectra. Thus, a second wavelength dimension can be added to the mass axis in conventional mass spectrometry. The observed maxima in a MPI spectrum, and thus the energy of the resonant intermediate state, are intrinsic properties of the molecule. This is of great importance in the discrimination of

molecules with similar mass spectra, since no two molecules have identical absorption spectra. This wavelength tunability is also important in the study of mixtures of molecules, since the component that has an excited state in resonance with the laser wavelength used is preferentially ionised. It is therefore possible for trace amounts of material in a mixture to be detected with increased sensitivity [16]; this wavelength selectivity is a feature that no other mass spectrometric technique can offer.

As shown in figure 1.2, the gas-phase R2PI spectra of polyatomic molecules at room temperature show broad features, since a large number of rotational and vibrational states are populated. In order to maximise selectivity in ionisation, it is desirable that spectral congestion is minimised. The standard means of achieving this is to make use of the adiabatic cooling available in supersonic molecular beams [17]- [20]. The principle of cooling in supersonic molecular beams is relatively simple, and is outlined in some detail in Appendix A. Briefly, molecules in a high pressure reservoir are allowed to expand into a vacuum through a very small orifice. The orifice dimensions are chosen such that the expanding gas undergoes many two-body collisions, with the result that the random energy associated with the source gas is converted into directed mass flow velocity. As shown in figure 1.3, this has the net effect of collapsing the room temperature Maxwell-Boltzmann velocity distribution to a narrow range centred around the directed mass flow velocity. The translational temperature, which describes the width of the new " jet-cooled" distribution, can be as low as 0.1 K. The rotational and vibrational degrees of freedom come into equilibrium with those of translation, leading to rotational temperatures of around 10 K and

Figure 1.3. Velocity distributions for He at room temperature and in a supersonic molecular beam at a translational temperature of 10 K.

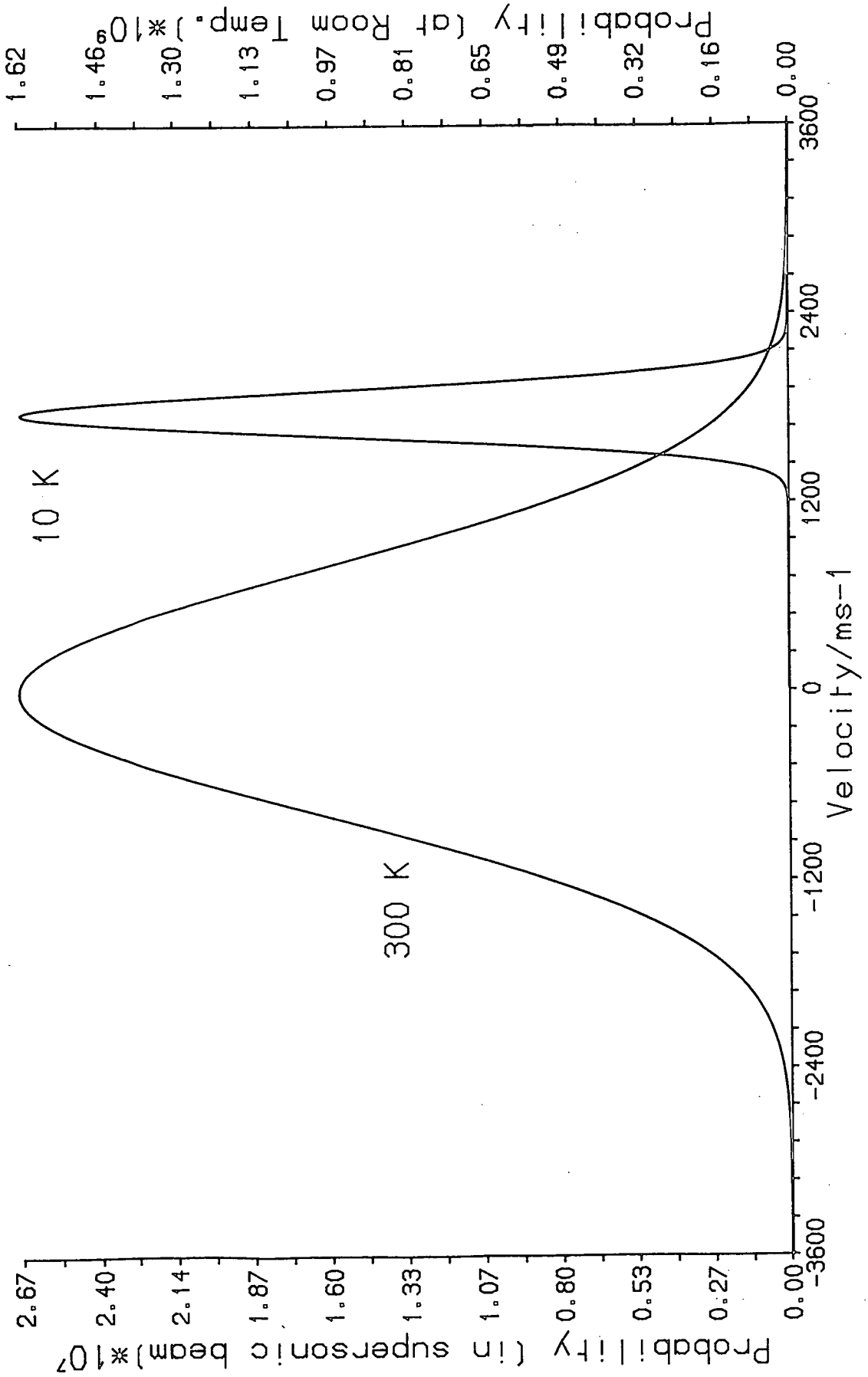

vibrational temperatures of about 100 K. Molecules of interest can be seeded at low concentrations into expansions of either monatomic (e.g. He or Ar), diatomic (e.g. N_2) or polyatomic (e.g. CO_2) gases.

At such low temperatures, the number of rotational and vibrational states of a molecule that are populated are reduced relative to those populated at room temperature, and so consequently are the number of observed transitions in a R2PI spectrum. This allows enhanced discrimination of structurally-similar molecules, such as geometric isomers. For example, figure 1.4 shows the R2PI spectra of the three isomers of xylene. These spectra correspond to the origin band regions of the S_1-S_0 electronic transitions of the three molecules [21]- [23]. The spectra exhibit narrow (3.3 cm^{-1} FWHM) peaks, well separated from each other. The wavelengths at which the S_1-S_0 electronic origin bands occur for these three isomers are 272.21 nm (p-xylene), 270.53 nm (m-xylene) and 267.97 nm (o-xylene). Under the expansion conditions employed, there is no interference between the p-xylene origin band and sequence bands from either of the other two isomers. Therefore, by tuning the ionisation laser wavelength to λ = 272.21 nm, p-xylene would be preferentially ionised from an equimolar mixture of the three isomers under these supersonic expansion conditions.

The primary limitation of MPIMS, in common with conventional mass spectrometric techniques, is that spectra can only be obtained for gases or for molecules with sufficiently high vapour pressures at room temperature. Of the 7 million or so chemical compounds known, these criteria only apply to a very small number, thus limiting the analytical power of the technique. Conventional resistive heating has been used to increase the range of compounds which can be

Figure 1.4. Jet-cooled R2PI Spectra of the Isomers of Xylene.

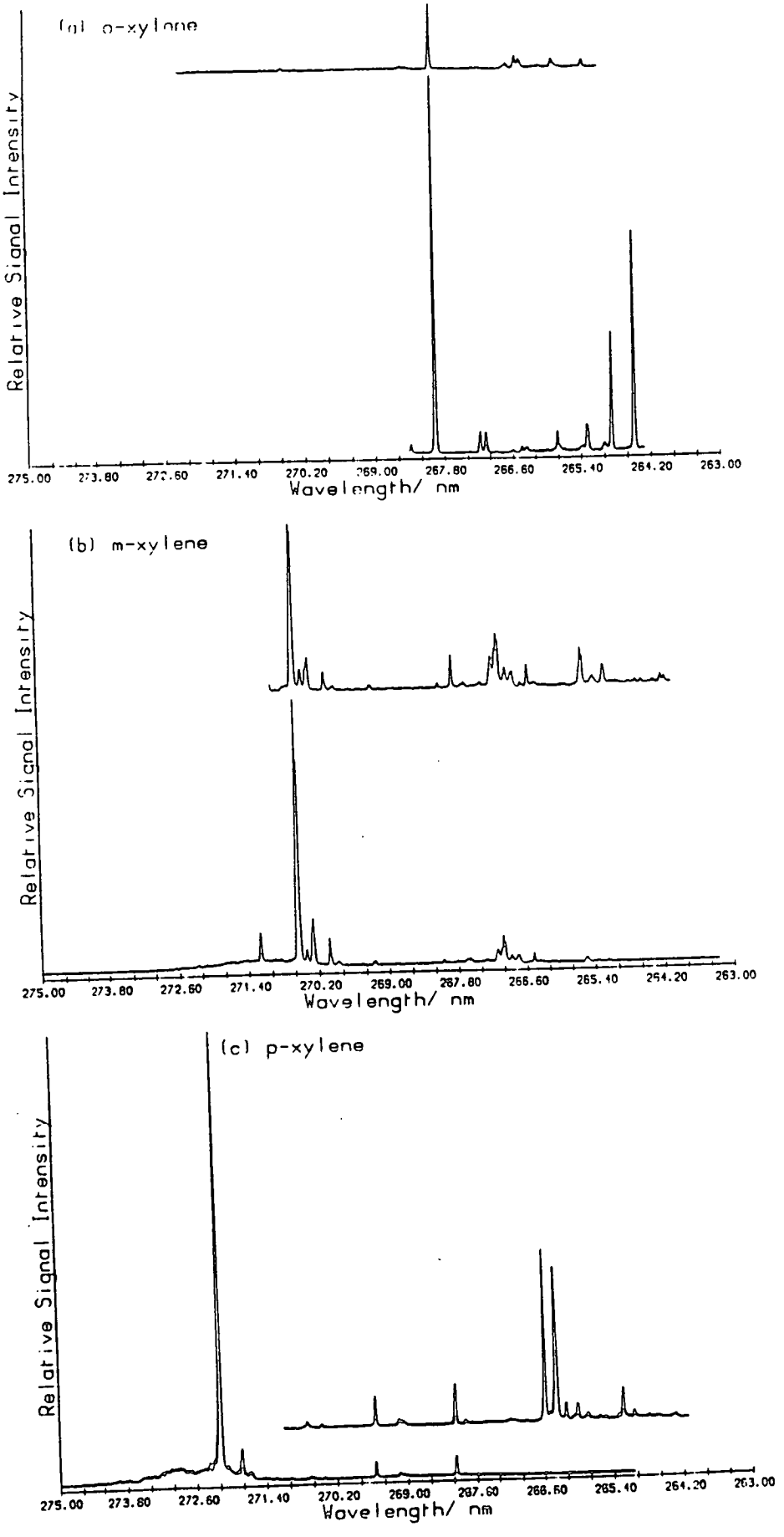

studied, but this method obviously precludes the study of a large range of thermally labile molecules and molecules of specific biological interest. In methods, such as fast atom bombardment (FAB) mass spectrometry and secondary ionisation mass spectrometry (SIMS), which have been devised to study such molecules, sample vaporisation and ionisation occurs in one step. These methods, however, produce more neutral molecules than ions [24], [25]. It is therefore sensible to neglect the ions created in this step and to post-ionise the gas-phase neutral molecules. This allows separate optimisation of the desorption and ionisation steps.

Laser desorption with a pulsed infrared laser, in common with FAB and SIMS, produces many more neutral molecules than ions: typically, the ratio is about 10^4:1 [26], [27]. Although many details of the desorption process are not well understood, it is known that the rate of heating by the infrared pulse is about seven orders of magnitude faster than by conventional methods ($\sim 10^7$ Ks^{-1}). This favours desorption of intact molecules over decomposition [28]. Combination of pulsed laser desorption with MPI of the desorbed neutrals extends the benefits afforded by the latter technique to a much wider range of molecules, especially if the desorbed species are cooled in a supersonic molecular beam. This combination of techniques is known as laser desorption multiphoton ionisation mass spectrometry (LD-MPIMS).

This thesis comprises two separate, but related parts. The principal objective of the work was to investigate the analytical applications of MPI. In chapter 2 some two-colour R2PI experiments that were carried out on a simple free jet apparatus are described. This work was primarily undertaken to establish the range of

systems that could be studied using simple resistive heating to increase sample vapour pressure. The potential sensitivity of this method is assessed, and the need for alternative means of sample introduction is discussed. However, the remainder of the thesis is concerned with the development of LD-MPIMS as an analytical method. In chapter 3 the role of lasers in mass spectrometry is examined. A survey of the two important areas of application of MPI as an ionisation method in mass spectrometry, as well as the use of laser desorption as a means of introducing low volatility samples into the ion source of a mass spectrometer is presented. The combination of techniques employed in the remainder of the thesis are also briefly introduced in this chapter. Chapter 4 contains a description of the experimental methods and equipment employed to carry out LD-MPIMS studies, whilst chapter 5 contains an outline of the time-of-flight mass spectrometer designed and developed in order to allow these experiments to be undertaken. In chapter 6 some of the preliminary results obtained in LD-MPIMS studies on polynuclear aromatic hydrocarbons, amino acids and porphyrins are presented. Some comments are made on the possible directions of future work. Finally, in chapter 7, a survey is given of the work carried out elsewhere using this technique and an assessment made of the place of LD-MPIMS in the analytical laboratory.

References

[1] K. Kleinermanns, J. Wolfrum, Angew. Chem. Int. Ed. Engl., **26**, 38, (1988)

[2] R. Boschi, E. Clar, W. Schmidt, J. Chem. Phys., **60**, 4406, (1974)

[3] J. L. Franklin, *Ionisation potentials, appearance potentials and heats of formation of gaseous positive ions*, National Bureau of Standards (Washington), 1969.

[4] M. Göppert-Mayer, Ann. Phys., **9**, 273, (1931)

[5] W. Kaiser, C. G. B. Garrett, Phys. Rev. Lett., **7**, 229, (1961)

[6] P. M. Johnson, C. E. Otis, Ann. Rev. Phys. Chem., **32**, 139, (1981)

[7] G. Petty, C. Tai, F. W. Dalby, Phys. Rev. Letters, **34**, 1207, (1975)

[8] P. M. Johnson, M. R. Berman, D. Zakheim, J. Chem. Phys., **62**, 2500, (1975)

[9] E. W. Schlag, H. J. Neusser, Acc. Chem. Res., **16**, 335, (1983)

[10] D. A. Gobeli, J. J. Yang, M. A. El-Sayed, Chem. Rev., **85**, 529, (1985)

[11] T. G. Blease, *Ph.D. Thesis*, University of Edinburgh, 1985.

[12] V. S. Antonov, V. S. Letokhov, *Ch. 7 in 'Laser Analytical Spectrochemistry'*, Adam Hilger (Bristol), 1985.

[13] D. M. Friedrich, J. Chem. Ed., **59**, 472, (1982)

[14] J. Lemaire, I. Dimicoli, F. Piuzzi, R. Botter, Chem. Phys., **115**, 119, (1987)

[15] T. G. Dietz, M. A. Duncan, R. E. Smalley, J. Chem. Phys., **76**, 1227, (1982)

[16] S. Leutwyler, U. Even, Chem. Phys. Letters, **81**, 578, (1981)

[17] A. Kantrowitz, J. Grey, Rev. Sci. Instrum., **22**, 328, (1951)

[18] J. B. Anderson, J. B. Fenn, Phys. Fluids, **8**, 780, (1965)

[19] J. B. Anderson, R. P. Andres, J. B. Fenn, Adv. Chem. Phys., **10**, 265, (1965)

[20] J. M. Hayes, Chem. Rev., **87**, 745, (1987)

[21] P. J. Breen, J. A. Warren, E. R. Bernstein, J. I. Seeman, J. Chem. Phys., **87**, 1917, (1987)

[22] C. D. Cooper, M. L. N. Sastri, J. Chem. Phys., **20**, 607, (1952)

[23] C. D. Cooper, H. Sponer, J. Chem. Phys., **20**, 1248, (1952)

[24] E. Schroder, H. Munster, H. Budzikiewicz, Org. Mass Spectrom., **21**, 707, (1986)

[25] R. B. Frees, A. M. Ross, J. E. Campana, J. Am. Chem. Soc., **107**, 6195, (1985)

[26] R. J. Cotter, Anal. Chim. Acta, **195**, 45, (1987)

[27] R. B. Van Breemen, M. Snow, R. J. Cotter, Int. J. Mass Spectrom. Ion Phys., **49**, 35, (1983)

[28] R. N. Zare, R. D. Levine, Chem. Phys. Letters, **136**, 593, (1987)

Chapter 2
Jet-cooled R2PI spectroscopy.

2.1 Introduction.

As mentioned in chapter 1, MPI techniques have been used to great effect in the fields of spectroscopy and chemical analysis, especially when combined with supersonic jet cooling. In the main, however, the advantages of this technique have been limited to studies of molecules with non-vanishing vapour pressures at room temperature. This obviously precludes a large number of important molecules. One such class of molecules is the polynuclear aromatic hydrocarbons (PNAHs), which generally have low vapour pressures at room temperature.

PNAHs are formed at elevated temperatures by the incomplete combustion of organic matter. They are an environmentally important class of molecules because they are potential carcinogens [1]. In view of the structural dependence of the biological activities exhibited by PNAHs, it is very important to be able to positively identify individual components, and in particular, isomeric species.

PNAHs also compose a large fraction of complex coal and oil samples. Oils generally contain hundreds of low and high molecular weight organic compounds, so it is difficult to carry out direct analysis on them for the presence of PNAHs. Presently, the most common analytical method is to isolate the PNAHs as a compound class, followed by the isolation and characterisation of the individual molecules by various chromatographic and spectroscopic

techniques. These include the use of capillary column GC-MS [2], [3], HPLC with fluorescence detection [4]- [6] and laser Shpol'ski spectroscopy [7]- [9]. The combination of laser-induced fluorescence (LIF) and traditional resistive heating methods, the latter being used to increase the sample vapour pressure, has allowed the gas-phase spectroscopy of the lower molecular weight members of this series to be studied. Jet-cooled R2PI spectroscopy is a potentially powerful tool in the study of PNAHs, since it is relatively easy to distinguish isomers, for example, by exploiting differences in their cold vibronic spectra.

The ultimate aim of this work was to develop a mass spectrometer which would allow analysis of involatile and thermally unstable samples. The preferred method of sample introduction into the ion source of this spectrometer was infrared laser desorption [10] into a supersonic molecular beam. The jet-cooled desorbed molecules could then be probed by R2PI. Differences in their cold vibronic spectra could then be used to differentiate between isomers and to allow selective ionisation of single components in complex mixtures.

Whilst this spectrometer was being designed and built, however, an alternative method of sample introduction into a molecular beam was evaluated, namely simple resistive heating. Experiments were carried out using a free jet apparatus, with non-selective detection of ions. Three low molecular weight PNAHs were selected as test cases. These experiments were extremely useful, since not only did they allow assessment of the limitations of resistive heating as a means of sample introduction but they also provided an important insight on the ease of applicability of R2PI to the study of relatively involatile materials.

The three molecules that were chosen for these studies, namely naphthalene, anthracene and perylene, have had their lowest energy excited singlet (S_1) states well-characterised by, amongst other methods, LIF in supersonic jets. For R2PI, however, they present a problem in that the energy required to access the vibrationless level of the S_1 state is less than half the molecular ionisation potential (IP). Thus R2PI through the origin band of the S_1 - S_0 transition is not possible using a one colour 1 + 1 ionisation scheme. It is, however, practicable to carry out two-colour R2PI experiments. The spectroscopy of the S_1-S_0 transition can be studied by keeping the second (ionising) wavelength fixed and scanning the first.

The experimental set-up employed in this work is shown schematically in figure 2.1. It principally consisted of two tunable lasers and a single vacuum chamber, which housed a supersonic pulsed nozzle and simple collection plates for monitoring total ion current as a function of wavelength. The various components of this experiment will be discussed in detail in the following sections.

2.2 Experimental Techniques.

2.2.1 Excimer pumped dye lasers

The pulsed output from a single excimer laser (Lambda Physik EMG 201 MSC) was used to pump two dye lasers (Lambda Physik FL3002E and FL2002) by using a 50 % beamsplitter. The excimer laser, operating on the XeCl (B-X) lasing transition, emitted broadband radiation centred at 308 nm. The laser cavity was

Figure 2.1. Schematic of the free jet apparatus.

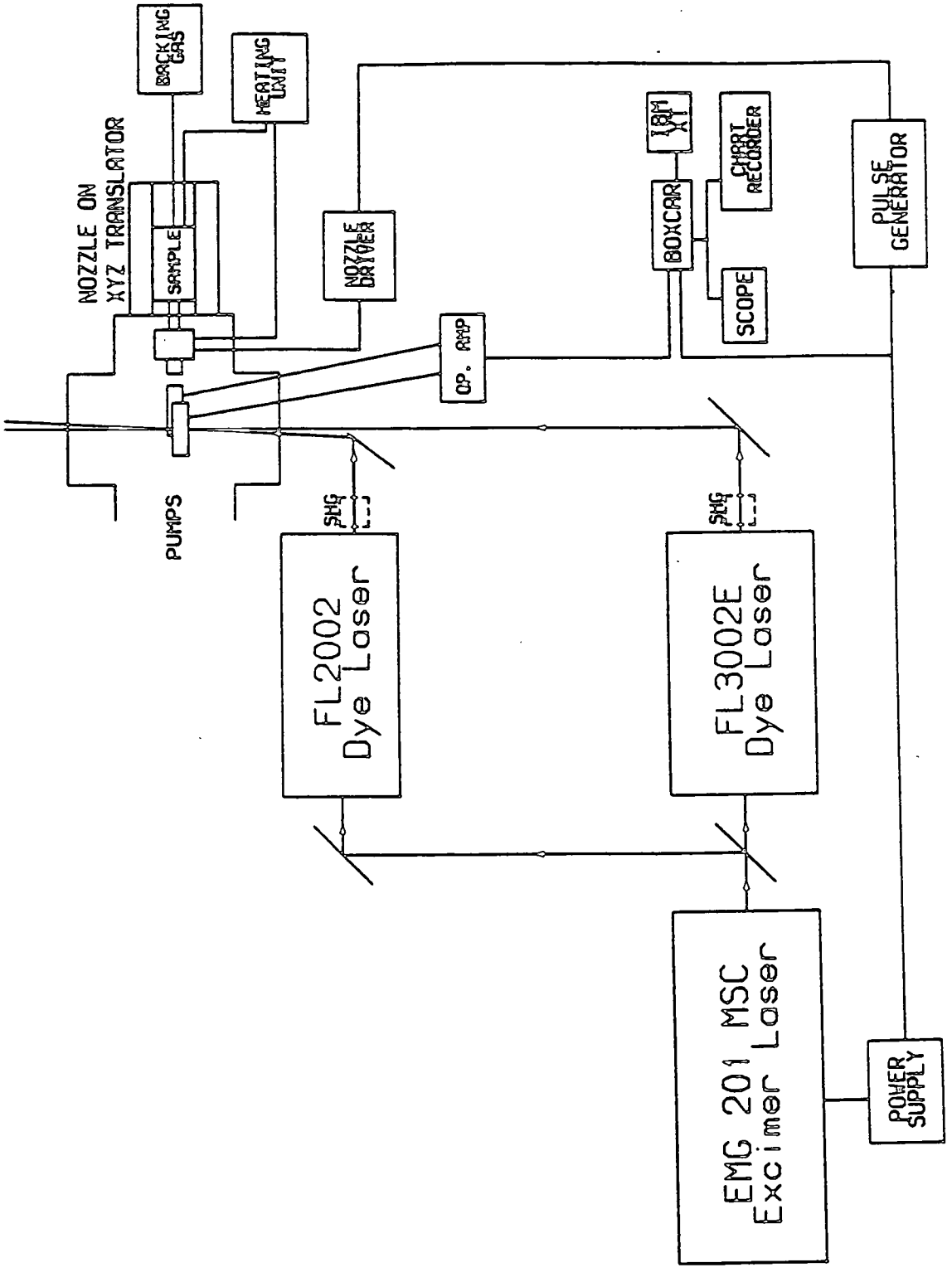

filled with a neon-based gas mixture [11]; a high voltage (18 kV) discharge, switched by a thyratron, initiated formation of the exciplex. The laser typically delivered a peak pulse energy of 385 mJ in a 30 ns FWHM pulse at a repetition rate of 2-6 Hz. After passing through the beamsplitter, the effective energy available to pump the FL3002E dye laser was about 155 mJ per pulse. Further losses following reflection at a coated mirror, displaced approximately 1.5 metres from the beamsplitter, meant that the UV radiation employed to pump the FL2002 dye laser typically had a pulse energy of 115 mJ. All pulse energies were measured by a Gentec ED200 joulemeter.

In both dye lasers, 10 % of the effective excimer output transversely pumped a cuvette, containing a continuously circulating dye solution, which was situated between the cavity end mirror and a prismatic beam expander (PBE) in a Hänsch-type laser cavity [12]. The broadband fluorescence from the dye passed through the PBE and was incident on a grating (600 lines/mm) mounted in the Littrow configuration.

Expansion of the beam ensured that it illuminated a large enough area of the grating to provide good resolution, and helped to reduce the power density of the beam, thereby preventing damage to the grating. Wavelength selection was accomplished by tilting the grating. This varied the angle of incidence of the beam on to the grating, and in turn, the wavelength of the light that was reflected back into the cavity; all other wavelengths were dispersed. A small portion of the beam then passed back through the dye cuvette, which acted as a pre-amplifier, and out of the cavity. The multimode oscillator output, with a bandwidth of ~ 0.2 cm^{-1}, was collimated by a telescope, and further amplified in a second dye

cuvette, which was transversely pumped by the remaining 90 % of the excimer beam. The pulse widths of the output from both dye laser was measured to be 17 ns FWHM.

The wavelength ranges and efficiencies of the dye solutions used to generate the data presented later in this chapter is given in table 2.1.

Table 2.1

Dye	solvent	range/nm	peak/nm	efficiency/% [53]
Rhodamine 6G	methanol	569-608	581	16.3
Rhodamine B	methanol	588-644	600	12.4
DMQ	dioxan	346-377	360	8.5
PBBO	dioxan	386-420	396	7.3
Coumarin 307	methanol	479-553	500	16.3

Fortunately, the low energy S_1-S_0 transitions in both anthracene and perylene coincide with the lasing ranges of two commercially-available UV dyes. An alternative method, however, of producing UV light had to be employed for all other required wavelengths, namely second harmonic generation (SHG).

SHG, using either a potassium dihydrogen phosphate (KDP) or a potassium pentaborate (KPB) crystal (Lambda Physik FL30 or FL32), allowed UV radiation to be produced from the visible dyes. Such "frequency doubling" requires that the phase velocities of the fundamental and second harmonic beams are equal, so that all the individual SHG point sources within the crystal constructively interfere [13]. In order to achieve this, it is necessary to maintain the correct angle between the propagation vector of the beam and the principal axis of the crystal. In the FL3002E, therefore, the doubling crystal was mounted on a

motorised tilting mechanism (Lambda Physik FL535B) along with a quartz compensating crystal, which corrected for any beam walk-off as a function of wavelength. The latter was particularly important in view of the large displacement of the nozzle chamber from this laser (about 2 metres) but was unnecessary for the FL2002, since the wavelength and crystal tilt angle were not varied. The frequency doubled light was separated from the fundamental using a UG5 filter (Corning) placed in the beam after the FL535B. Table 2.2 lists the combinations of dyes and doubling crystals employed in obtaining the R2PI spectra presented later in this chapter.

Table 2.2

Molecule	Dye(FL3002E)	SHG(FL3002E)	Dye(FL2002)	SHG(FL2002)
Naphthalene	Rhodamine B	FL30	Rhodamine 6G	FL30
Anthracene	DMQ	none	Rhodamine 6G	FL30
Perylene	PBBO	none	Coumarin 307	FL32

Wavelength scanning and tracking of the SHG crystal in the FL3002E was controlled by a dedicated microprocessor (Lambda Physik FL538), which synchronously adjusted the grating and the tilt angle of the crystal. To ensure "phase matching" at every wavelength in a scan, the conversion efficiency of the FL30 was maximised at a number of wavelengths, and the microprocessor interpolated between them to determine the correct angle.

As shown in table 2.1, energy conversion efficiencies of between 7-16 % could be achieved at the peaks of the dye gain profiles, e.g. for DMQ in the FL3002E, at 360 nm, the dye laser output was ~ 12 mJ per pulse. The SHG conversion efficiencies of the FL30 and FL32 were ~ 5 % and < 1 % respectively. Thus,

for Coumarin 307 in the FL2002, using the KPB crystal to produce 250 nm radiation, the pulse energy was typically ~ 100μJ.

The dye laser beams were spatially and temporally overlapped in the ionisation region within the nozzle chamber (see below). In order to avoid saturation effects and to ensure that any contribution from non-resonant or higher-order ionisation processes was minimised, the ionisation laser was set at a wavelength where no known resonance occurred, and the flux of the scanning laser was adjusted so that no ion signal was observed in the absence of the second colour photons. Both beams were unfocussed, giving power densities of ~0.1-0.2 $MWcm^{-2}$ in the ionisation region.

2.2.2 Wavelength calibration.

Since the S_1-S_0 transitions of the three molecules studied have been well characterised by gas-phase LIF measurements, the object of these experiments was not to make novel spectroscopic measurements, but rather to obtain reproducible spectra characteristic of the three molecules studied. Due to non-availability of the required equipment, it was not possible to record optogalvanic calibration lines concurrently with the ion signal; rather, the values on the FL3002E laser dial were used implicitly, since these were known to be accurate to within 5 cm^{-1}. The laser grating position at the start and end of each scan were input as parameters in the control program (see later) and it was assumed that the grating was stepped in a linear fashion. This allowed the laser wavelength at each point in the spectrum to be easily calculated.

2.2.3 Supersonic nozzle chamber

The pulsed valve used to generate the supersonic free jet was based on the modified automobile fuel injector design of Behlen and Rice [14]. A Toyota fuel injector (461674-4) was used in this work. The only modifications that were made were to remove a plastic sheath around the electrical connectors and to reduce the orifice diameter from 1mm by glueing a 500 μm pinhole (Ealing Optics) over it. The solenoid coil of the valve was driven by a 30 volt square wave pulse of about 500 μs duration from a home-built control unit. This pulse lifted the nozzle plunger from its seating, thereby releasing a plug of seeded gas into the chamber.

The valve was mounted on a home-built XYZ translator on the top flange of a small aluminium chamber. Manipulation of the XYZ positions allowed easy optimisation of the nozzle-to-laser beam distance. The chamber, which had an internal volume of 2.4 litres, was evacuated by a 4" rotary-backed oil diffusion pump (Edwards E04 backed by Edwards ED200; pumping speed for air 600 ls^{-1}). The chamber pressure was monitored by an Edwards PRL10K pirani gauge head, attached to a digital readout (Edwards 1005), which was mounted on one of the side flanges of the chamber. The pumping system provided a background chamber pressure of less than 10^{-4} mbar. During experiments, the chamber pressure was less than 10^{-3} mbar.

The solid samples were purchased from Aldrich (99+ % purity) and were used without further purification. Samples were placed in a sintered steel filter (Hoke) with nominal 1 μm elements, which was then placed inside an in-line filter

(Hoke 6315G45), through which the inert carrier gas (He) was passed. The filter was mounted directly above the nozzle, within the body of the XYZ translator. In order to increase the sample vapour pressures to about 0.1 to 1 torr, the filter was heated using a 22 ohm coaxial heater element (ARI Industries Ltd.) connected to a variable output ac power supply. To prevent any sample condensation in the nozzle itself, it was heated by a second coaxial heater element, to a temperature 2-5 degrees in excess of that of the sample reservoir. The temperatures of both nozzle and sample were measured by two type K thermocouples (Ancom), attached to a digital thermometer (RS 258-186) via a twelve-way selector switch (RS 332-969). All electrical connections were passed into the chamber via a home-built vacuum feedthrough, mounted on the side flange opposite the pressure gauge. Typically, 3 atmospheres of helium were used as carrier gas. This gave rise to a measured nozzle throughput of 0.53 torr litre s^{-1} at 6 Hz. This suggests the nozzle pulse duration was approximately 450 μs.

The laser beams entered and exited the chamber via Spectrosil B windows mounted on the remaining two flanges of the vacuum chamber. The unfocussed laser beams crossed the supersonic free jet approximately 1-2 cm downstream from the nozzle. This was found to provide the best compromise between sensitivity and cooling in the experiment.

Photoions and photoelectrons created by the R2PI process were collected by a pair of nickel electrodes mounted 7 mm either side of the beam axis, supported on ceramic rods. A bias voltage of ± 90 V was applied to either plate, which were then connected, via the vacuum feedthrough, to the input of a home-built differential input operational amplifier [15]. The gain of this amplifier could be

varied, in the range 10^3 to 10^7 V/A, by varying the resistance of the output load.

2.2.4 Data Handling and Storage

The relatively low repetition rate of these experiments, which was determined by the capacity of the vacuum pumps, meant that there was a long period of time between laser shots where no signal was produced. Continuous monitoring of the signal would therefore have resulted in poor signal-to-noise ratios. To avoid this, the amplified signal was fed into a Stanford Research Systems SR250 gated integrator and boxcar averager. This device consisted of a gate generator, a fast gated integrator and an exponential averaging facility. The SR250 was triggered by a pulse synchronous with the firing of the excimer laser (see section 2.2.5) and sampled the output from the operational amplifier after a fixed time delay. This delay and the width of the gate were optimised by monitoring both the gate and the signal on a four channel oscilloscope (Tektronix 2445, 150 MHz). During the gate opening time, the signal was integrated and normalised by the gate width. A moving exponential average of the normalised signal was carried out over a pre-selected number of shots; the latter was determined by the scan rate of the laser.

The boxcar output was then displayed on a chart recorder (Kipp and Zonen BD9 2-channel) and, after digitisation, stored on an IBM PC-XT 286 microcomputer. Digitisation was achieved, at a maximum rate of 2 kHz, using a Stanford Research Systems SR245 Computer Interface Module, controlled by custom software, which had an input range of ± 10.24 volts DC with 12 bit resolution.

2.2.5 Timing

The timing sequence required for these experiments was initiated by a pulse from a dual-channel pulse generator (Farnell PG102), which triggered the nozzle control unit. After about 1.2 ms, a pulse from the second channel of the PG102 was employed to trigger the excimer laser. This delay was to allow for the nozzle solenoid response time, and the transit time of the pulse of seeded gas to the ionisation region. By manually scanning this delay time whilst monitoring the ion signal, it was possible to maximise the latter. An approximately constant signal was observed for a period of about 400 μs, after which time the signal decreased dramatically. Although no measurement of relative rotational temperatures was made in this "plateau" region, it was thought likely that cooling would be optimum at an early delay time, due to an increase in chamber pressure with increasing duration of the time the nozzle was open [14]. The time delay used in obtaining all the spectra presented later in this chapter was about 50 μs delayed from the onset of the strong plateau signal. The boxcar and oscilloscope were also triggered from the second, delayed pulse. The computer interface was triggered from the boxcar. Further trigger pulses were ignored by this unit until the laser grating (and SHG crystal) position had been incremented by the FL538.

2.3 Jet-cooled R2PI spectroscopy of PNAHs

2.3.1 Nomenclature of transitions and coordinate axes.

The three molecules studied are planar in their ground states. The coordinate nomenclature system employed in this work is that of Pariser [16], since it

appears to be the most prevalent in the literature. In naphthalene and anthracene, the z-axis is perpendicular to the plane of the molecule, whilst the x- and y-axes correspond to the long and short in-plane axes, respectively. In perylene, the out-of-plane axis is the z-axis, but the long in-plane is now the y-axis, with the short in-plane axis being the x-axis.

For a given molecule, the normal modes of a particular symmetry are numbered, with "1" being the vibration of highest frequency. In naphthalene and anthracene, the b_{1g} symmetry vibrations are distinguished from the a_g vibrations by a bar over the mode number; for example, $\bar{8}$ is the lowest frequency b_{1g} mode in naphthalene [17], [18]. Normal modes of other symmetry species are denoted by the mode number followed by the symmetry species in parentheses.

The convention of subscripts and superscripts, indicating the number of quanta of active vibrational modes in the lower and upper electronic states, is used here for description of vibronic transitions [19]. If one quantum of mode X is excited in the upper electronic state after a transition from the vibrationless level in the lower electronic state, this transition is designated as X_0^1. The electronic origin band, between the vibrationless levels of the lower and upper electronic states, is denoted 0_0^0.

2.3.2 Symmetry rules and Herzberg-Teller intensity stealing.

The intensity of a one-photon transition between vibronic states m and n is proportional to the square of the magnitude of the electric dipole transition moment, R_{nm}.

$$R_{nm} = \int \psi_v^n \psi_v^m d\tau_v \int \psi_e^n \hat{\mu}_e \psi_e^m d\tau_e, \qquad (2.1)$$

where the first integral is the vibrational overlap integral and the second is the electronic transition moment R_e. Herzberg and Teller [20] found that if the vibrational overlap integral is totally symmetric, then R_e is independent of vibrational motion, and the relative vibronic intensities are given by the square of the vibrational overlap integral, the so-called Franck-Condon factor. If, however, the vibrational overlap integral is non-totally symmetric, R_e becomes dependent on vibrational motion. An important consequence of this is that electronic and vibronic states of the same symmetry can mix, or "vibronically couple". This allows otherwise weak allowed vibronic transitions to gain considerable intensity through interaction with a strong allowed electronic transition. The above equation for R_{nm} can be expanded to the form

$$R_{nm} = (R_e)_{eq} \int \psi_v^n \psi_v^m d\tau_v \qquad (2.2a)$$

$$+ \sum [\partial R_e / \partial Q_t]_{eq} \int \psi_v^n Q_t \psi_v^m d\tau_v \qquad (2.2b)$$

$$+ \sum [\partial R_e / \partial Q_a]_{eq} \int \psi_v^n Q_a \psi_v^m d\tau_v \qquad (2.2c)$$

where Q_t and Q_a are the normal coordinates associated with totally symmetric and non-totally symmetric vibrations. Vibronic transitions which gain intensity through mixing with electronic states of the same symmetry do so through the second and third terms in the above equation. This is known as Herzberg-Teller

intensity stealing.

For a transition to be electronically allowed, the product of the symmetry species of ψ_e^n, ψ_e^m and μ must contain the totally symmetric species. Thus, if ψ_e^n is totally symmetric, ψ_e^m must have the same symmetry as one of the components, μ_x, μ_y or μ_z, of μ. These vector components have the same symmetry species as their respective translation operators (T_x, T_y and T_z). If the transition is electronically allowed, the first term in the above equation is non-zero, and the latter two terms may also be non-zero. In an electronically forbidden system, only the final term of the above equation is non-zero.

2.3.3 Naphthalene.

Naphthalene is a planar molecule belonging to the D_{2h} point group. In Pariser's notation, the S_1 state is of B_{3u} symmetry, whilst the S_2 state is of B_{2u} symmetry [21], [22]. Both the S_1-S_0 and S_2-S_0 transitions are dipole allowed, and are polarised along the long axis and short axis of the molecule respectively [23].

Both the S_1-S_0 and S_2-S_0 transitions in naphthalene have been studied using LIF [14], [24]- [26] and MPI techniques [27]- [29]. A distinguishing feature of the S_1-S_0 spectrum is the weakness of the 0_0^0 transition. This is because, even though this transition is symmetry allowed, the electronic transition moment is small, with an oscillator strength of only ~ 0.001 [30]. This is much smaller than would be expected for a strong symmetry allowed transition. The strongest bands in the naphthalene S_1-S_0 spectrum are those corresponding to transitions in b_{1g} vibrational modes, which gain intensity by vibronically coupling with the S_2 state. The S_2-S_0 transition is quite strong (oscillator strength f ~ 1.0), so it is not

surprising that the 8_0^1 band is much stronger than the origin band in the S_1-S_0 spectrum of naphthalene. Since these bands gain most of their intensity from the mixing of the $^1B_{2u}$ state with the S_1 state, these bands are short-axis polarised, giving rise to B-type rotational contours, with prominent P- and R-branches, but no Q-branch [23], [31]. The 9_0^1, 8_0^1, 7_0^1 and 3_0^1 transitions are stronger in intensity than the S_1-S_0 origin band. These bands gain their intensity through vibronic coupling of the S_1 state with some higher singlet state of the same symmetry [23]. If the S_n-S_0 transition is stronger than the S_1-S_0 transition, then the intrinsic S_1-S_0 transition moment is enhanced by the vibronic coupling to the more energetic state, but without modifying the B_{3u} character of the transition. Thus, these bands are long-axis polarised and give rise to A-type rotational band contours [23], [31]. These differ from the B-type rotational contours by having a pronounced Q-branch in addition to P- and R-branches.

The molecular I.P. of naphthalene is 8.13 eV [28]. Since the origin band of the S_1-S_0 transition occurs at ~312.3 nm, the fixed laser wavelength chosen for these experiments had to be less than 300 nm for efficient R2PI to occur. The laser wavelength used was 286 nm, since no ion signal was observed at this setting in the absence of the tunable laser photon. A nozzle temperature of 48 ^oC was used, which corresponds to a vapour pressure of ~0.8 torr. The R2PI spectrum obtained is shown in figure 2.2, whilst the band position, intensities and assignments are given in table 2.3. No account has been taken of the variation in the laser power as a function of wavelength in this spectrum, nor indeed in any of the spectra presented in this chapter. The laser power density, in fact, varies by about a factor of two across the wavelength region in figure 2.2, with the

Figure 2.2. 2-colour R2PI spectrum of jet-cooled naphthalene.

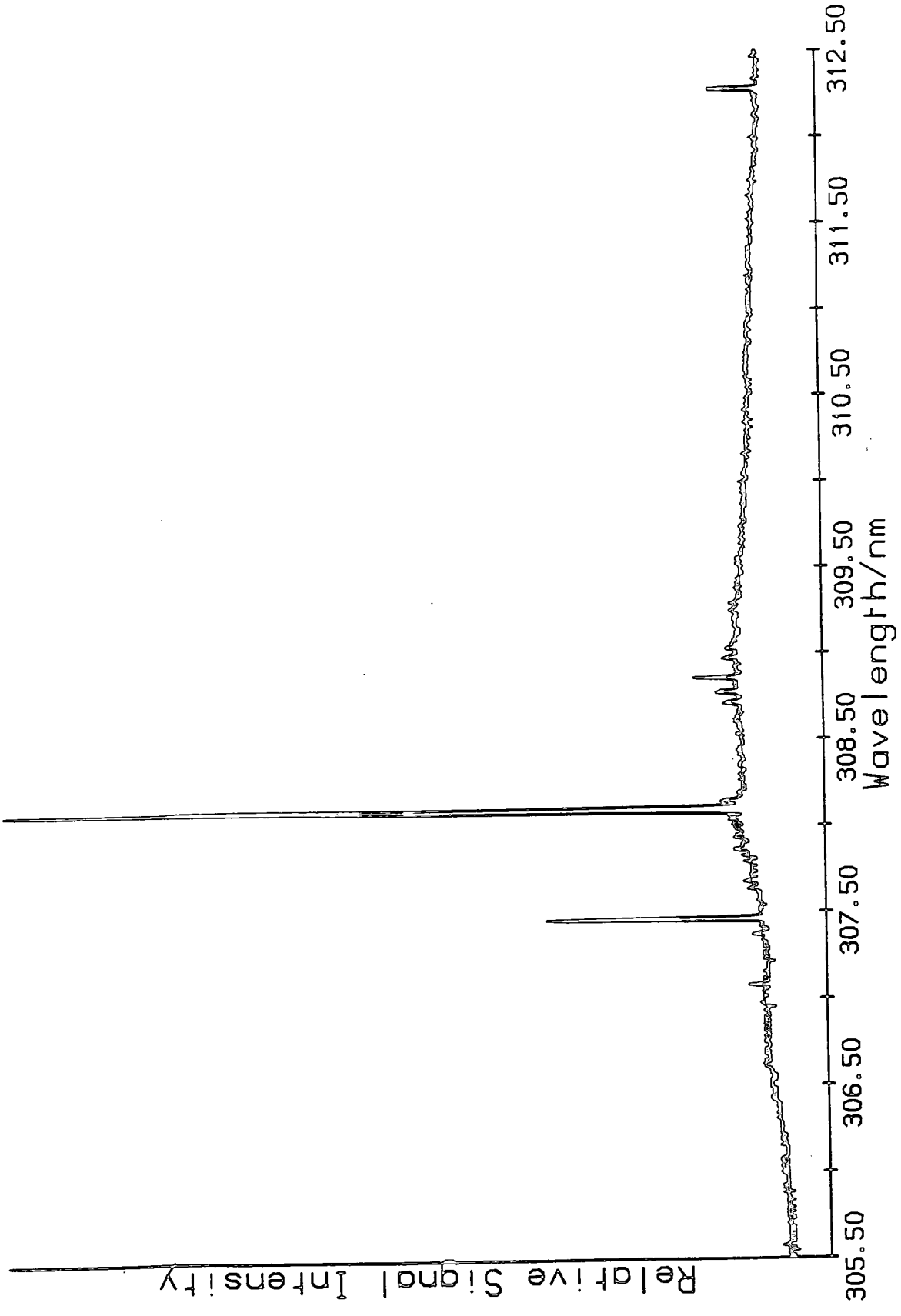

Table 2.3. Line positions in the R2PI spectrum of naphthalene.

λ(air) /nm	$\tilde{\nu}$(vac) /cm^{-1}	$\Delta\tilde{\nu}$ /cm^{-1}	Rel. Int.	Assignment	Behlen [26]
312.270	32014	0	6.5	0_0^0	32018 cm^{-1}
309.025	32350	336	1.6	$\bar{8}_0^1 4(b_{3g})_1^1$	337
308.969	32356	342	2.5	$\bar{8}_0^1 3(b_{3g})_1^1$	343
308.858	32368	354	6.5		
308.777	32377	363	3.3	$\bar{8}_1^2$	365
308.709	32384	370	2.4	$\bar{8}_0^1 3(b_{2g})_1^1$	372
308.129	32444	430	2.9	$\bar{8}_0^1 8(b_{2u})_1^1$	430
308.087	32449	435	100	$\bar{8}_0^1$	435
307.460	32515	501	29.3	9_0^1	501
307.081	32555	541	2.4	$3(b_{1u})_0^1 4(b_{1u})_0^1$	543

maximum in power density being at ~308 nm and the minimum being at ~305.5 nm. This helps to explain the rather non-flat baseline, with there obviously being some non-resonant contribution to the ion signal. The non-resonant contribution tends to follow the output profile of the tunable dye laser. This means that the relative signal intensities of those features between ~307.5 and 309.5 nm are enhanced relative, for example, to the origin band. No power normalisation was carried out, however, since no measurements were made of the second (fixed) laser power output as a function of time; of course, any variation of this power during the wavelength scan would affect the appearance of the spectrum obtained.

The origin band for the S_1-S_0 transition in naphthalene was observed at 32014±5 cm^{-1}. This agrees well with reported values for this transition. The band positions reported in this chapter were taken from the band peaks, since no rotational simulation program was available to estimate the correct band origins. However, due to the narrowness of the bands due to the jet cooling, this introduce an error of only ~1 cm^{-1} in the band positions, which is negligible compared to the error associated with the accuracy of the dye laser grating read-out. The spectrum in figure 2.2 shows two other prominent features, displaced by 435 cm^{-1} and 501 cm^{-1} from the origin band. These correspond to transitions from the vibrationless level of the S_0 state to the first excited level of the lowest frequency b_{1g} and a_g normal modes in the S_1 state. The $\bar{8}_0^1$ band at 308.087 nm has a FWHM of 2.1 cm^{-1}, whilst the 9_0^1 band at 307.460 nm has a FWHM of 2.6 cm^{-1}. These correspond to rotational temperatures in the range 10 K > T_{ROT} > 2K [31], [32]. The remaining features in the spectrum are assigned

following the work of Rice and coworkers [26], and are in most cases combination bands comprising the $\bar{8}_0^1$ transition with sequence bands in non-totally symmetric vibrations. An estimation of the vibrational temperature for one of these modes, namely $8(b_{2u})$ can be made from the relative intensities of the $\bar{8}_0^1$ and the $\bar{8}_0^1 8(b_{2u})_1^1$ bands. Assuming that the Franck-Condon factors and degeneracies are the same for both transitions, this intensity ratio depends on the relative populations in the v"=0 and v"=1 levels. This is given by a simple Boltzmann factor. The $8(b_{2u})$ mode has a vibrational frequency of 359 cm^{-1} in S_0 [31], so given an intensity ratio of 34:1, the vibrational temperature for this mode is ~ 150 K. Although this seems somewhat higher than might be expected, it is in general agreement with the work of Hollas and coworkers [31]. It is clear that this in-plane b_{2u} vibration is not efficiently cooled in a jet expansion.

2.3.4 Anthracene.

Anthracene has D_{2h} symmetry. The ground electronic state is therefore A_g in symmetry. Using Pariser's notation, the S_1 state is B_{2u} in symmetry, and there is a low-lying B_{3u} state, approximately 13600 cm^{-1} above the B_{2u} state, which has a large oscillator strength to the ground electronic state [33]. There are no low-lying electronic states of B_{1u} symmetry. The S_1-S_0 electronic transition in anthracene is short-axis polarised, and corresponds to a $^1B_{2u}^+$-$^1A_g^-$ (π^*-π) transition. Therefore, only a_g, b_{1g} and b_{3g} vibrational levels should be observed in absorption from the vibrationless level of the S_0 state. The strongest transitions in the S_1 excitation spectra correspond to the totally symmetric a_g vibrations, whilst the non-totally symmetric b_g vibrations have vanishingly small

Franck-Condon factors. Transitions involving these vibrations can, however, gain intensity by vibronic coupling of S_1 to other electronic states. Due to the proximity of the B_{3u} state to S_1, b_{1g} levels should gain significant intensity by Herzberg-Teller intensity stealing, but the b_{3g} modes, which couple S_1 with B_{1u} electronic states, remain weak in intensity.

A comprehensive study of the jet-cooled gas-phase spectroscopy of anthracene has been carried out by Zewail and coworkers [34]- [40]. They employed a heated nozzle set-up to obtain fluorescence excitation and single vibronic level (SVL) fluorescence spectra of anthracene. The features in the R2PI spectra obtained in this work will be assigned by comparison with the work of Lambert et al. [34] and of Keelan and Zewail [40].

The molecular ionisation potential of anthracene is 7.47 eV [41]. Since the origin band of the S_1-S_0 transition occurs at ~ 361 nm, the second (fixed) laser wavelength chosen had to be less than 308 nm for efficient R2PI to occur. The laser wavelength used was 290 nm, since this corresponds to the maximum in the Rhodamine 6G dye gain profile. A nozzle temperature of 158 ^{o}C was employed, which corresponds to a sample vapour pressure of ~2.2 torr. The R2PI obtained is displayed in figure 2.3, whilst table 2.4 summarises the band positions, intensities and assignments.

The jet-cooled R2PI spectrum of anthracene exhibits a strong S_1-S_0 origin band at 27685±5 cm^{-1}, with a FWHM of 1.4 cm^{-1}. There are relatively few strong

Figure 2.3. 2-colour R2PI spectrum of jet-cooled anthracene.

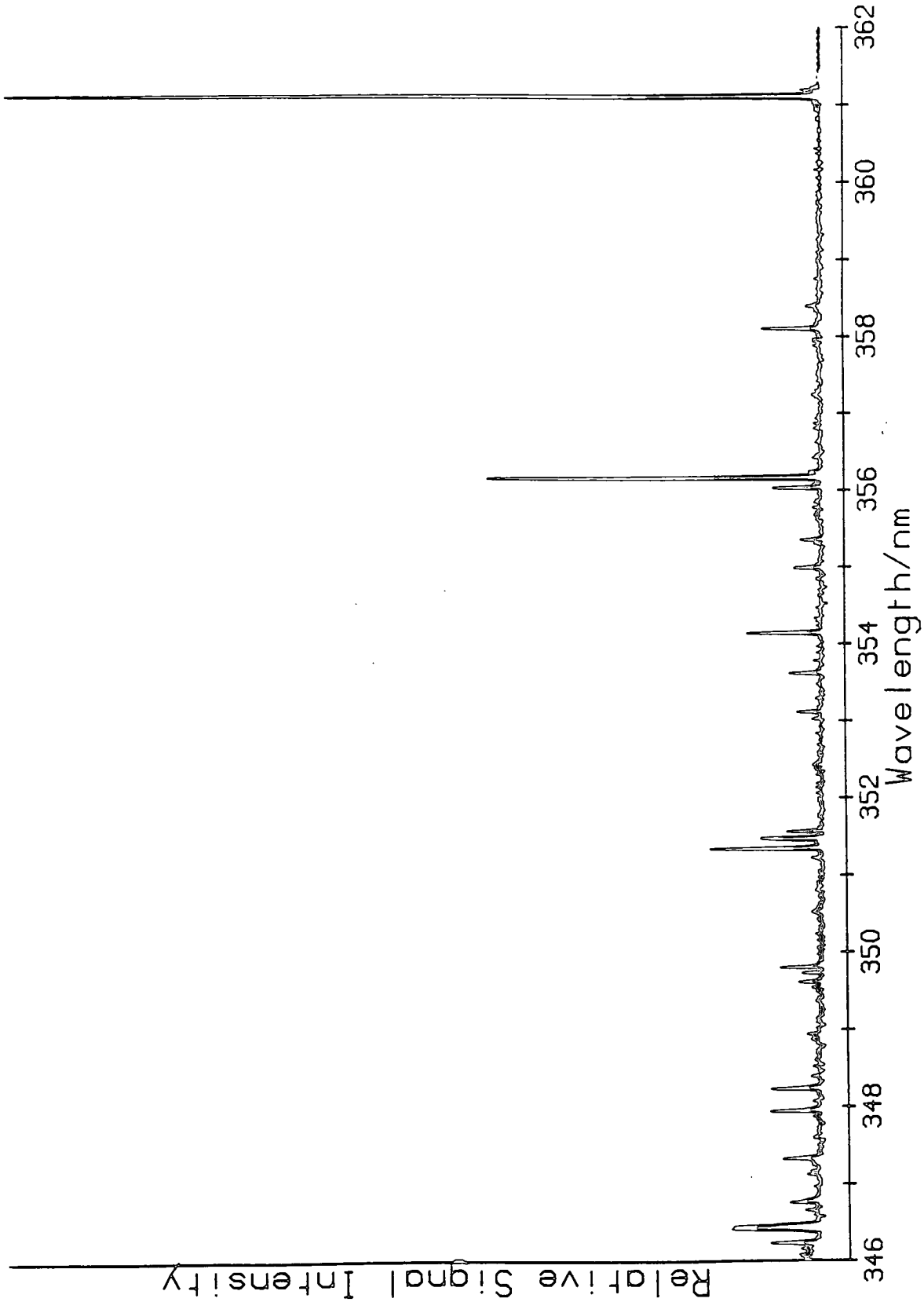

Table 2.4. Line positions in the R2PI spectrum of anthracene.

λ(air) /nm	$\tilde{\nu}$(vac) /cm^{-1}	$\Delta\tilde{\nu}$ /cm^{-1}	Rel. Int.	Assignment	Zewail [34], [40]
361.107	27685	0	100	0_0^0	27687 cm^{-1}
358.398	27894	209	1.5		209
358.102	27917	232	7.0	$\bar{1}1_0^1$	232
356.239	28063	378	1.3	12_1^2	
356.160	28069	384	40.9	12_0^1	385
356.025	28080	395	5.9		395
355.355	28133	448	2.4	$\bar{1}0_1^2$	
354.985	28162	477	3.3	$\bar{1}0_0^1$	473
354.140	28229	545	9.1	$\bar{1}1_0^2$	541
353.618	28271	586	3.9	11_0^1	583
353.113	28311	627	3.0		
353.020	28319	634	1.3		
351.563	28436	752	4.3		748
351.481	28443	758	7.6		
351.472	28444	759	7.6		755
351.459	28445	760	6.5	10_0^1	
351.341	28454	770	13.9	12_0^2	766
351.219	28464	779	1.3		
350.520	28521	836	1.3		
349.805	28579	894	5.2	$\bar{9}_0^1$	889
349.731	28585	900	2.6		895
349.613	28595	910	2.8		905

Table 2.4.(cont.) Line positions in the R2PI spectrum of anthracene.

λ(air) /nm	$\tilde{\nu}$(vac) /cm^{-1}	$\Delta\tilde{\nu}$ /cm^{-1}	Rel. Int.	Assignment	Zewail [34], [40]
348.233	28708	1023	6.5	9_0^1	1019
347.941	28732	1048	6.7		1042
347.323	28783	1099	5.2		1094
347.167	28796	1112	2.2		
346.757	28830	1146	4.3		1146
346.657	28859	1154	2.4		1158
346.448	28856	1171	11.3	8_0^1	1168
346.418	28839	1174	11.5	7_0^1	1168
346.396	28861	1176	5.2		
346.235	28874	1189	6.7	$\bar{7}_0^1$	1184
346.213	28876	1191	3.9		
346.196	28877	1192	2.4		
346.157	28880	1196	3.0		
346.083	28887	1202	3.2		
346.057	28889	1204	3.0		
346.035	28891	1206	2.6		

features in the energy range 750 cm^{-1} above this band, but, as expected, the spectrum becomes more complicated at higher energies. This is not wholly unexpected, since the density of states increases approximately exponentially with energy. For example, in the S_1 state of anthracene, the density of vibrational states is ~ 1 per cm^{-1} at 750 cm^{-1}, 25 per cm^{-1} at 1400 cm^{-1} and 120 per cm^{-1} at 1800cm^{-1} [37]. The line positions agree well with those obtained by fluorescence methods, although the intensities are somewhat different. The laser power output varies by a factor of ~2 over the wavelength range 346-362 nm, with the maximum occurring at ~360 nm and the output decreasing almost monotonically to the blue of this wavelength. This has the effect of enhancing the origin band strength relative to the higher energy transitions. However, even if this spectrum is power normalised, the relative intensities of the various bands differ from those in the LIF spectra. This reflects the different nature of the two techniques.

There are 12 a_g vibrational modes in anthracene, but three of these (C-H stretching vibrations) are not active in π^*-π transitions. Thus, nine a_g fundamentals are expected in the R2PI spectrum. Lambert et al. [34] assigned many of the low energy a_g excited state modes by measuring dispersed fluorescence spectra from these features. If a SVL of the form X^1 is excited, then the X_1^1 band generally acts as a false origin for an 0^0-like fluorescence spectrum. The ground state vibrational frequencies of anthracene are well-known [34], [42], [43], so it is relatively easy to make these assignments.

SVL spectra also allowed the assignment of the $\bar{9}_0^1$, $\bar{10}_0^1$ and $\bar{11}_0^1$ bands. The latter assignment is somewhat tentative, since it implies a very large (158 cm^{-1}) shift

between the vibrational frequencies in the S_0 and S_1 states. The emission spectrum of the SVL populated by excitation of the band 541 cm^{-1} in excess of the origin band was very similar to that obtained from the 11_0^1 band, so it was assigned to 11_0^2.

Rotational band contour analysis was also employed to allow assignment of the vibrational symmetries of the various features [34], [40]. At energies below 1100 cm^{-1} above the S_1-S_0 origin, all but one of the transitions observed by Keelan and Zewail [40] were found to belong to one of two well-defined contour groups. The 0_0^0 and 12_0^1 bands exhibited B-type rotational contours, as would be expected from the short-axis polarisation of the S_1-S_0 transition moment. Transitions to b_{1g} levels in S_1 gave A-type contours. Although b_{3g} contours were simulated, no such contours were observed experimentally, thus negating a previous assignment of the 209 and 395 cm^{-1} features as the fundamental and overtone of the lowest energy b_{3g} vibrational mode, respectively [34].

The band at 755 cm^{-1} appeared to be a superposition of two a_g contours separated by 2 cm^{-1}. By obtaining dispersed fluorescence spectra from either side of this contour, it was possible to associate the band at 754 cm^{-1} with a ground state vibrational energy of 835 cm^{-1}, whilst that at 756 cm^{-1} is associated with a level at 755 cm^{-1} in S_0 [40]. Although these levels are clearly separated in S_0, they are quasi-degenerate in S_1. The feature at 756 cm^{-1} is clearly the 10_0^1 band, whilst the feature 2 cm^{-1} to the red must be some combination or overtone band whose intensity has been enhanced by Fermi resonance. A similar pattern was obtained at 1168 cm^{-1}, where the features were assigned to 8_0^1 and 7_0^1.

2.3.5 Perylene.

Perylene has D_{2h} symmetry. X-ray diffraction measurements suggest that perylene is not a "true" aromatic molecule, but is composed of two naphthalene moieties connected by almost single C-C bonds [44]. This structure is not very rigid, and several low frequency vibrational modes, and even a deviation from planarity, may be expected. In contrast to both naphthalene and anthracene, perylene has a large separation between S_1 and S_2 [45], and consequently, no Herzberg-Teller effects are observed in the S_1-S_0 transition [46]- [50].

The S_1-S_0 transition in perylene has been extensively studied, both in crystals [45] and in the gas phase [46]- [50] by laser induced fluorescence. Whilst the symmetry of several of the observed vibronic bands can be deduced from the Raman work of Hochstrasser and Nyi [45], the actual normal modes involved in a particular transition are not well established. The mode numbering system employed by Leutwyler [47] and Fourmann et al. [49] will therefore be employed here.

The molecular I.P. of perylene is 7.00 eV [41]. Since the origin band for the S_1-S_0 transition occurs near 415.6 nm, the fixed laser wavelength chosen had to be less than 310 nm for efficient R2PI to occur. A wavelength of 290 nm was initially used, but little or no ion signal near the origin band was obtained, so a shorter wavelength of 250 nm was employed to obtain the R2PI spectrum shown in figure 2.4. A nozzle temperature of 240 ^{o}C was used. Band positions, intensities and assignments are given in table 2.5.

The origin band of the S_1-S_0 ($^1B_{2u}$-$^1A_{1g}$) transition in the R2PI spectrum of

Figure 2.4. 2-colour R2PI spectrum of jet-cooled perylene.

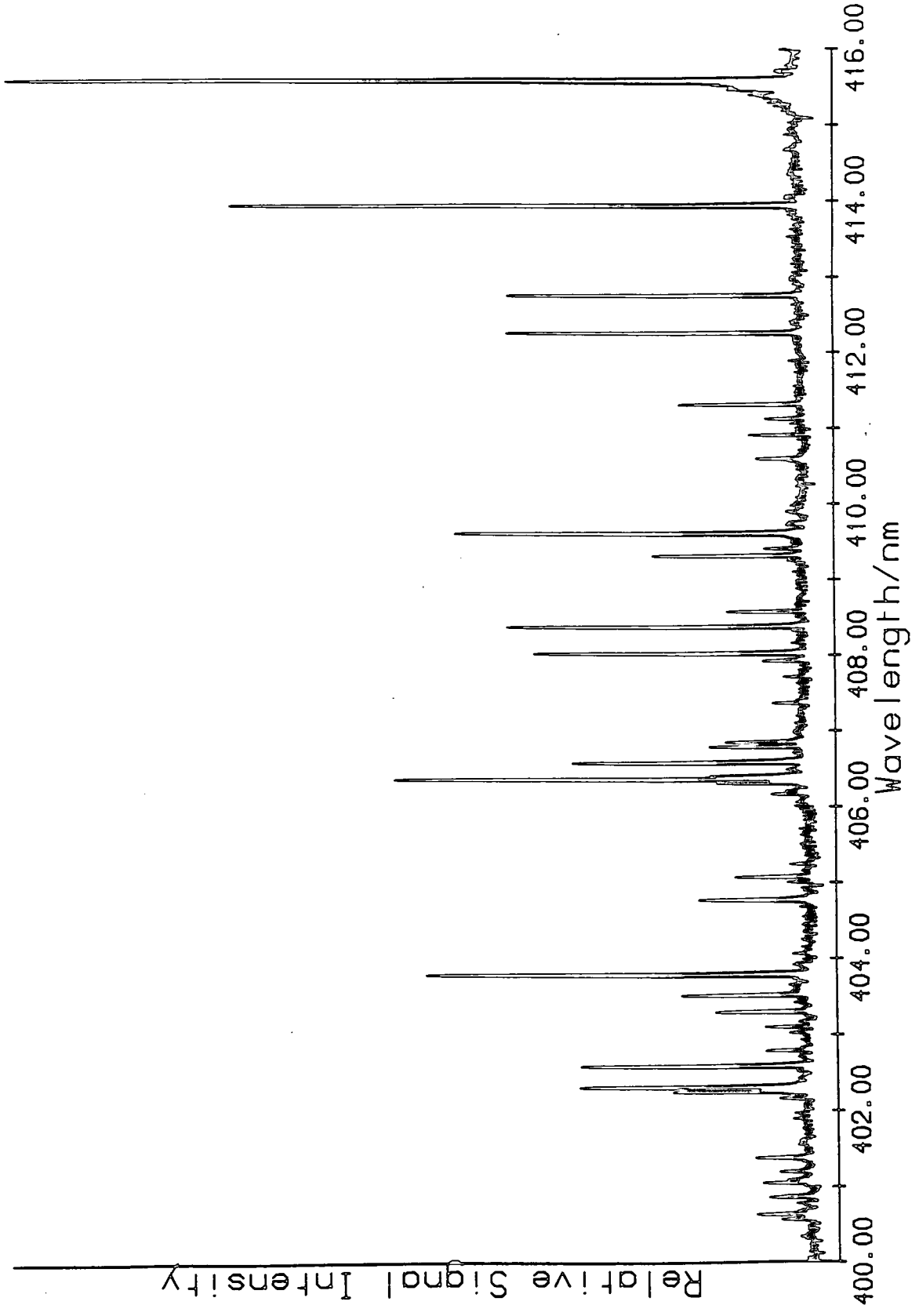

Table 2.5. Line positions in the R2PI spectrum of perylene.

λ(air) /nm	$\tilde{\nu}$(vac) /cm^{-1}	$\Delta\tilde{\nu}$ /cm^{-1}	Rel. Int.	Assignment	Topp [50]
415.574	24056	0	100	0_0^0	24065 cm^{-1}
413.941	24151	95	72.4	G_0^2	96
412.754	24221	164	37.9	Y_0^1	164
412.255	24250	194	38.0	G_0^4	195
411.310	24306	249	16.5	K_0^2	
411.125	24317	260	5.7	$G_0^2 Y_0^1$	
410.911	24329	273	7.8	$J_0^1 K_0^1$	
410.597	24348	292	6.9	G_0^6 or J_0^2	
409.610	24407	350	44.4	A_0^1	353
409.408	24419	362	5.9	Z_0^1	
409.315	24424	368	19.9	L_0^1	371
408.577	24468	412	10.7	M_0^1	
408.375	24480	424	38.2	B_0^1	427
408.025	24501	445	34.8	$A_0^1 G_0^2$	447
407.924	24508	451	6.2		
407.366	24541	485	5.0	G_0^{10}(?)	
406.855	24572	516	11.0		
406.793	24576	519	13.0	$B_0^1 G_0^2$	
406.583	24588	532	29.9	N_0^1	536
406.395	24560	543	12.9	$A_0^1 G_0^4$	
406.364	24602	545	51.8	C_0^1	549
406.312	24605	548	12.1		

Table 2.5.(cont.) Line positions in the R2PI spectrum of perylene.

λ(air) /nm	$\tilde{\nu}$(vac) /cm^{-1}	$\Delta\tilde{\nu}$ /cm^{-1}	Rel. Int.	Assignment	Topp [50]
406.1682	24613	557	5.2	$Z_0^1 G_0^1$	
405.243	24670	613	2.8	$B_0^1 G_0^1$	
405.074	24680	624	9.8	O_0^1	
405.006	24684	628	3.2		
404.775	24698	642	14.4	$C_0^1 G_0^2$	643
403.791	24758	702	48.5	A_0^2	703
403.519	24775	719	16.6	$A_0^1 L_0^1$	721
403.299	24789	732	12.4	P_0^1	735
403.103	24801	744	6.2		
403.027	24805	749	3.1		
402.786	24820	764	6.0		
402.586	24832	776	29.3	$A_0^1 B_0^1$	779
402.311	24849	793	29.4	R_0^1	794
402.247	24853	797	17.8	$A_0^2 G_0^2$	799
402.163	24858	802	4.4		
401.380	24907	851	7.6	X_0^1	
401.198	24918	862	4.5		
401.090	24925	869	3.5		
401.048	24928	871	6.7		
400.859	24939	883	5.9		
400.635	24953	897	7.5	$A_0^1 C_0^1$	899
400.566	24958	901	4.3		

perylene was observed strongly at 24056±5 cm^{-1}, which agrees well with values reported previously in the literature. This feature was 2.5 cm^{-1} wide FWHM, which is somewhat broader than was reported by Schwartz and Topp [49], who recorded an origin band of 1.3 cm^{-1} width, which corresponded to a rotational temperature of 4 K.

There are a number of strong transitions in the range $0 < \Delta\tilde{\nu} < 350$ cm^{-1}. These features are completely absent in crystal spectra [45], indicating that they are due to excitation of out-of-plane (non-totally symmetric) vibrations which are clamped in the solid matrix [47]. If the two lowest vibrational excitations at 96 and 164 cm^{-1} are in G and Y respectively, then most of the low frequency features in the R2PI spectrum can be assigned to progressions and a combination band in these modes.

The excitation of at least two out-of-plane modes implies that perylene may be non-planar in S_1. On the basis of dispersed fluorescence spectra, the feature at 96 cm^{-1} has been assigned to G_0^2 [48]- [50], the so-called "butterfly mode", with the corresponding transition at 194 cm^{-1} being assigned to G_0^4 [50]. The features at 292 and 485 cm^{-1} have been tentatively assigned to further members of this progression. The 292 cm^{-1} feature has been alternatively assigned as J_0^2, where J is an out-of-plane mode [50]. By assigning the feature at 249 cm^{-1} to K_0^2, Fourmann et al. were able to further assign the 273 cm^{-1} transition as $J_0^1 K_0^1$ [50].

The strong band at 350 cm^{-1}, assigned as A_0^1, is likely to be due to excitation of the $14a_g$ mode in S_1 [48]. The remaining strong features are assigned to a number of fundamentals and combination bands. On the basis of crystal work

[45], the bands at 368, 545 and 793 cm^{-1} involve the excitation of totally symmetric vibrations, whilst that transition at 793 cm^{-1} involves a b_{3g} mode.

2.3.6 Sensitivity Measurements.

The detection limit of the free jet apparatus was determined by recording the S_1-S_0 origin band in anthracene as a function of nozzle temperature. The nozzle temperature was reduced from 158 ^{o}C to 85 ^{o}C, allowing 30 minutes equilibration time between recording of spectra. The spectrum recorded at 85 ^{o}C is shown in figure 2.5. The vapour pressure of anthracene at 85 ^{o}C is approximately 20 millitorr.

The signal to noise in figure 2.5 is approximately 30:1. Assuming that vapour equilibrium is achieved in the sample reservoir, then the sample concentration in the molecular beam is 20 x 10^{-3} / (3 x 760) i. e. 1 part anthracene in 1.14 x 10^{5} helium. If the assumption that the signal varies linearly with sample vapour pressure is made, the minimum detectable concentration (at a signal-to-noise ratio of two) is 600 parts per billion. This is a dangerous assumption to make because conditions in the beam are not necessarily at equilibrium. Certainly, measurements of the same origin band at higher temperatures do not give a linear increase in signal with sample pressure. However, no recognisable resonant feature was observed at a nozzle temperature of 50 ^{o}C, at which temperature, the anthracene vapour pressure is approximately 1 millitorr. Of course, by increasing the laser power densities, non-resonant ion signal can be produced. Without mass spectrometric detection, there is no way of assigning this signal to anthracene rather than hot background gas.

Figure 2.5. 2-colour R2PI spectrum of jet-cooled anthracene.
Nozzle temperature = 85 °C.

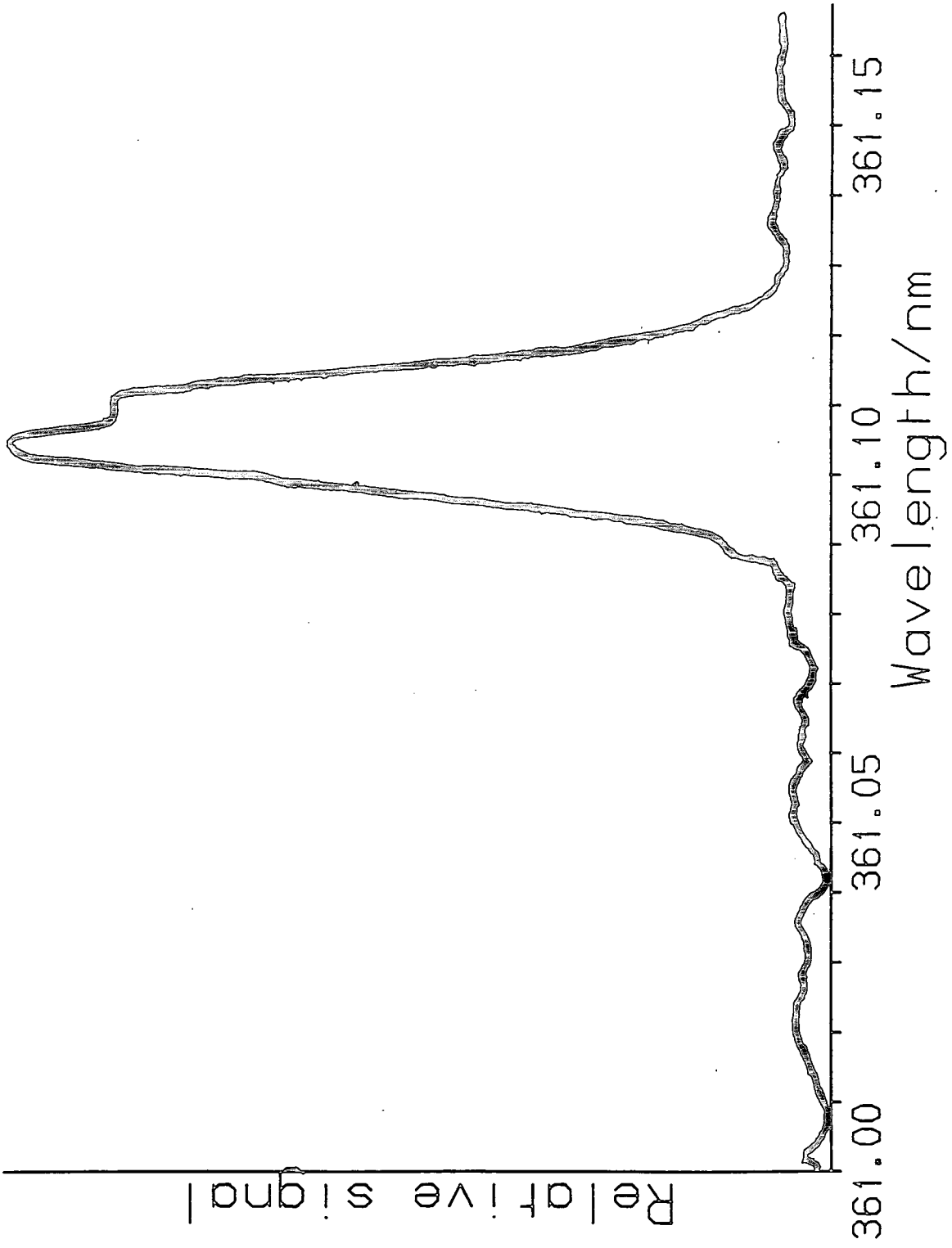

The spectrum shown in figure 2.5 was recorded using a nozzle-ionisation distance of 2 cm. Using equations (20) and (21) in appendix A, the sample concentration at this position is 6.4 x 10^{10} molecules anthracene cm^{-3}. Assuming a linear variation of signal with sample concentration, the minimum detectable concentration, under conditions at which a recognisable R2PI spectrum can be recorded, is 4.2 x 10^{9} molecules anthracene cm^{-3}.

2.4 Concluding Remarks.

Two-colour R2PI has proved to be a relatively simple technique for obtaining reproducible vibronic spectra from molecular species cooled in supersonic jet expansions. Selectivity in ionisation from a mixture of compounds is possible, but only if the spectroscopy of the molecules thought to be present in the mixture is known. This, of course, requires some prior knowledge of the composition of the mixture. No measurements were made on a mixture of the three PNAHs studied here, since the lack of mass spectrometric detection does not allow discrimination of ion signals from each of the components. It is obvious, however, that it would be reasonably easy to selectively ionise perylene from a mixture of the other two, assuming a nozzle temperature of > 430 K was employed. If jet cooling is used, there is highly unlikely to be any hot band features from either naphthalene or anthracene at λ = 415.5 nm (the S_1-S_0 origin band for perylene), since the S_1-S_0 origins for anthracene and naphthalene are shifted by 3622 and 7944 cm^{-1} to the blue of this feature, respectively. Selective ionisation of the other two components is likely to be more difficult due to background absorption from the other components at energies higher than those of their S_1-S_0 origin bands. As mentioned above, the origin band for

naphthalene is ~8000 cm^{-1} to the blue of the same feature in perylene. At this higher energy, the spectrum of perylene is likely to be complex due to the large density of states present. This congestion, even in a jet-cooled spectrum, obviously reduces the potential selectivity in ionisation.

One-colour R2PI may be of some use in the study of mixtures of PNAHs, but since the S_1-S_0 origin band shifts to lower energy as the degree of conjugation increases, it will only be possible to access the higher energy vibronic transitions, thereby reducing the possible degree of selectivity available. For example, the I.P. of tetracene is 7.04 eV [41], whilst the S_1-S_0 origin band corresponds to 2.78 eV [51]. Thus one-colour MPI would be possible only if a photon energy of ~ 6000 cm^{-1} above the origin band energy were employed. The lower energy vibronic levels accessed by two-colour MPI are much less congested, and therefore confer a potentially very high degree of selectivity in ionisation.

The high temperature nozzle set-up proved to be useful for only a limited range of small PNAHs. Attempts to record the R2PI spectrum of pentacene, which required nozzle temperatures in excess of 250 ^{o}C, were unsuccessful. At these temperatures, the non-metallic parts of the fuel injector started to melt, with the result that the nozzle remained open at all times, thereby flooding the vacuum chamber and choking the diffusion pump. No information is available on the thermal degradation of the compounds tested. Although in the case of the PNAHs, thermal damage is likely to be small, the heated nozzle approach is unlikely to be of much use when studying thermally labile species, such as peptides and proteins. A much more widely-applicable technique is laser desorption [10]. In this case, the sample and any substrate used is heated

extremely rapidly (10^6 Ks^{-1} [52]) so that sample desorption occurs before any thermal degradation can happen (see chapter 3).

In conclusion, a combination of jet-cooling and 2-colour R2PI spectroscopy has allowed vibronic spectra to be recorded for several PNAHs. A minimum detectable limit of 4.2×10^9 molecules cm^{-3} has been obtained for anthracene, so the technique, even with rather primitive ion collection optics, has been shown to have good sensitivity. However, the heated nozzle approach is clearly limited to molecules which have reasonably high vapour pressures ($\sim$ 0.1 torr) at temperatures below 250 ^{o}C. Moreover, it is clearly essential that mass spectrometric analysis of the ions created by R2PI is carried out, since this greatly increases the versatility of the technique. Laser desorption has proved to be a more generally-applicable method of sample introduction, and the remaining chapters of this thesis are concerned with the technique of laser desorption MPI mass spectrometry of involatile and thermally unstable molecules.

References

[1] K. Bridbord, J. G. French, *in 'Carcinogenesis, Vol. 3: Polynuclear Aromatic Hydrocarbons'*, Raven Press, New York, 1978.

[2] K. S. Chin, K. Biemann, K. Krishnan, S. L. Hill, Anal. Chem., **56**, 1610, (1984)

[3] C. W. Wilkerson Jr., S. M. Colby, J. P. Reilly, Anal. Chem., **61**, 2669, (1989)

[4] T. Imasaka, K. Ishibashi, N. Ishibashi, Anal. Chim. Acta, **142**, 1, (1982)

[5] L. E. Milton, D. L. Vassilaros, C. M. White, N. Milos, Anal. Chem., **51**, 768, (1979)

[6] S. A. Wise, S. N. Chester, H. S. Hertz, L. R. Hilpert, W. E. May, Anal. Chem., **49**, 2406, (1977)

[7] G. F. Kirkbright, C. G. DeLima, Analyst, **99**, 338, (1974)

[8] Y. Yang, A. P. D'Silva, V. A. Fassel, Anal. Chem., **53**, 894, (1981)

[9] C. S. Woo, A. P. D'Silva, V. A. Fassel, Anal. Chem., **52**, 159, (1980)

[10] J. Grotemeyer, U. Boesl, K. Walter, E. W. Schlag, J. Am. Chem. Soc., **108**, 4233, (1986)

[11] Lambda Physik, *Excimer Laser EMG 201 MSC Instruction Manual*, Göttingen, 1985.

[12] T.W. Hänsch, Appl. Opt., **11**, 895, (1972)

[13] W. Demtröder, *Laser Spectroscopy Basic Concepts and Instrumentation*, Springer-Verlag (Berlin), 1981.

[14] F. M. Behlen, S. A. Rice, J. Chem. Phys., **75**, 5672, (1981)

[15] T. E. Adams, R. J. S. Morrison, E. R. Grant, Rev. Sci. Instrum., **51**, 141, (1980)

[16] R. Pariser, J. Chem. Phys., **24**, 250, (1956)

[17] M. Stockburger, H. Gattermann, W. Klusmann, J. Chem. Phys., **63**, 4519, (1975)

[18] M. Stockburger, H. Gattermann, W. Klusmann, J. Chem. Phys., **63**, 4529, (1975)

[19] J. H. Calloman, T. M. Dunn, I. M. Mills, Proc. Roy. Soc. London, **A259**, 499, (1966)

[20] G. Herzberg, E. Teller, Z. Phys. Chem., **B21**, 410, (1933)

[21] D. S. McClure, J. Chem. Phys., **22**, 1668, (1954)

[22] D. S. McClure, J. Chem. Phys., **24**, 1, (1956)

[23] J. M. Hollas, S. N. Thakur, Mol. Phys., **22**, 203, (1971)

[24] S. M. Beck, D. E. Powers, J. B. Hopkins, R. E. Smalley, J. Chem. Phys., **73**, 2019, (1980)

[25] S. M. Beck, J. B. Hopkins, D. E. Powers, R. E. Smalley, J. Chem. Phys., **74**, 43, (1981)

[26] F. M. Behlen, D. B. McDonald, V. Seturaman, S. A. Rice, J. Chem. Phys., **75**, 5685, (1981)

[27] R. Frueholz, J. Wessel, E. Wheatley, Anal. Chem., **52**, 281, (1980)

[28] M. A. Duncan, T. G. Dietz, R. E. Smalley, J. Chem. Phys., **75**, 2118, (1981)

[29] D. E. Cooper, R. P. Freuholz, C. M. Klimcak, J. E. Wessel, J. Phys. Chem., **86**, 4892, (1982)

[30] M. J. Robey, I. G. Ross, R. V. Southwood-Jones, S. J. Strickler, Chem.

Phys., **23**, 207, (1977)
[31] J. M. Hollas, T. Ridley, P. A. Freedman, Chem. Phys. Letters, **92**, 317, (1982)
[32] A. C. Jones, *private communication*,
[33] S. Fischer, E. Lim, Chem. Phys. Letters, **26**, 312, (1974)
[34] W. R. Lambert, P. M. Felker, J. A. Syage, A. H. Zewail, J. Chem. Phys., **81**, 2195, (1984)
[35] W. R. Lambert, P. M. Felker, A. H. Zewail, J. Chem. Phys., **81**, 2209, (1984)
[36] W. R. Lambert, P. M. Felker, A. H. Zewail, J. Chem. Phys., **81**, 2217, (1984)
[37] P. M. Felker, A. H. Zewail, Chem. Phys. Letters, **108**, 303, (1984)
[38] J. A. Syage, P. M. Felker, A. H. Zewail, J. Chem. Phys., **81**, 2233, (1984)
[39] J. A. Syage, P. M. Felker, D. H. Semmes, F. Al Adel, A. H. Zewail, J. Chem. Phys., **82**, 2396, (1985)
[40] B. W. Keelan, A. H. Zewail, J. Chem. Phys., **82**, 3011, (1985)
[41] R. Boschi, E. Clar, W. Schmidt, J. Chem. Phys., **60**, 4406, (1974)
[42] G. J. Small, J. Chem. Phys., **52**, 656, (1970)
[43] J. Räsänen, F. Stenman, E. Penttinen, Spectrochim. Acta A, **29**, 395, (1973)
[44] A. Camerman, Y. Trotter, Proc. Roy. Soc., **A279**, 129, (1964)
[45] R. M. Hochstrasser, C. A. Nyi, J. Chem. Phys., **72**, 2591, (1980)
[46] C. Bouzou, C. Jouvet, J. B. Leblond, P. Millie, A. Tramer, M. Sulkes, Chem. Phys. Letters, **97**, 161, (1983)
[47] S. Leutwyler, J. Chem. Phys., **81**, 5480, (1984)
[48] S. A. Schwartz, M. R. Topp, Chem. Phys., **86**, 245, (1984)
[49] B. Fourmann, C. Jouvet, A. Tramer, J. M. Le Bars, P. Millie, Chem. Phys., **92**, 25, (1985)
[50] M. M. Doxtander, E. A. Mangle, A. K. Bhattacharya, S. M. Cohen, M. R. Topp, Chem. Phys., **101**, 413, (1986)
[51] A. Amirav, U. Even, J. Jortner, J. Chem. Phys., **75**, 3770, (1981)
[52] R. Zenobi, J. H. Hahn, R. N. Zare, Chem. Phys. Letters, **150**, 361, (1988)
[53] Lambda Physik, Dye Laser Data Sheet, Göttingen, 1985

Chapter 3
Lasers in mass spectrometry.

3.1 Introduction.

The use of light as an ionisation source in mass spectrometry dates back some sixty years. In 1929, Ditchburn and Arnot [1] recorded the photoionisation mass spectrum of potassium vapour by using the output from an iron arc lamp coupled with a magnetic-sector mass spectrometer. As discussed in chapter 1, however, single photon ionisation of gas-phase molecules generally requires a photon energy of ~ 10 eV, which lies in the vacuum ultraviolet (VUV) region of the electromagnetic spectrum. The development of photoionisation using the output from incoherent arc lamps as a routine method in mass spectrometry was hampered by the low power of the available VUV and UV light sources. This fact, coupled with the requirement of evacuated light paths for VUV photoionisation, resulted in very little progress in this area for the following 25 years. The next reported use of photoionisation came in 1956, when Lossing and Tanaka [2] obtained the photoionisation mass spectrum of butadiene using resonance lines from a krypton arc lamp as light source. Hurzeler and coworkers developed the VUV monochromator for photoionisation mass spectrometric studies in the following year [3], [4]. Nevertheless, because of the experimental complexities and low signal levels involved with the use of VUV radiation, the photoionisation mass spectrometer never became a common laboratory tool for routine analysis.

However, the development of high power pulsed lasers made a new means of photon-induced ionisation possible, namely multiphoton ionisation (MPI). MPI mass spectrometry (MPI-MS) was quickly recognised as a powerful new technique. As early as 1970, Bereshetskaya et al. reported multiphoton ionisation and fragmentation of H_2 using the output of a Nd^{3+}:glass laser in a time-of-flight (TOF) mass spectrometer [5]. At about the same time, Chin [6] reported MPI of I_2, CCl_4 and D_2O using the pulsed output from a ruby laser, again with TOF mass spectrometric detection. With the appearance of commercial dye lasers, the combination of tunable MPI with mass spectrometric detection was developed both as a tool for spectroscopy and for chemical analysis [7]- [11].

In the following section the physical processes which can affect the appearance of an MPI mass spectrum are considered. The model that has been proposed to explain the observed fragmentation patterns in MPI-mass spectrometry will be discussed, and comparisons made with conventional mass spectrometry. Finally, the advantages of MPI as an ionisation method will be discussed, including a number of illustrative examples.

3.2 Laser MPI Mass Spectrometry.

A multiphoton ionisation mass spectrum is the result of a fast, complex, multi-step photophysical process. The process can be divided into three distinct parts, namely

1. Excitation i.e. the mechanism below the ionisation potential.
2. Ionisation.

3. Fragmentation.

The unifying element throughout this process is the kinetic competition between further excitation of a molecule ("up-pumping") and other decay processes (notably dissociation) for the various excited state populations. Each of the three parts of the process will be discussed separately in the following sections.

3.2.1 Excitation.

REMPI mass spectrometry relies on the ability to tune the laser wavelength to a real excited state of the molecule as a step on the way towards ionisation. This feature, which is unique to MPI as an ionisation method in mass spectrometry, not only allows the possibility of selective ionisation but also greatly reduces the laser power density required to achieve efficient ionisation. Non-resonant ionisation is possible at much higher power densities than those involved in REMPI schemes; however, at sufficiently high intensities, even the background gas in the ion source will be ionised. At the high intensities required for non-resonant ionisation, extreme fragmentation usually occurs, which is of limited use for analytical purposes.

One of the prerequisites for a successful means of ionisation in mass spectrometry is the ability to generate useful information from limited amounts of sample. In order to achieve the highest sensitivity possible, therefore, R2PI schemes are usually employed in MPI-MS experiments. Generally, the excitation proceeds via the first excited singlet state (S_1) of the molecule, which usually has the best-characterised and simplest spectroscopic features. The following discussion will be limited to two photon ionisation via excited eigenstates.

As shown in figure 3.1, there are several possibilities which can occur at the resonant excited state of the neutral molecules, namely

1. The excited molecule absorbs a second photon and is excited to above its ionisation potential (figure 3.1(a)).
2. Decomposition of the neutral molecules occurs, forming fragment species. Observation of the parent molecular ion is thereby prevented (figure 3.1(b)).
3. The molecules undergo intersystem crossing to a triplet electronic state, which cannot be ionised by a photon of the same energy as was used for excitation (figure 3.1(c)).
4. The excited state decays via fluorescence on a timescale which competes with process 1, thereby reducing the ionisation yield.

Gedanken et al. [12] have classified molecules according to their behaviour at the real resonant excited state. They have proposed two extremes of behaviour, depending on the relative rates W of up-pumping, $W=\sigma I$ (for single-photon absorption), and dissociation, $W=\gamma$, where σ is the one photon absorption cross section (cm^2), I is the photon flux (photons $cm^{-2}s^{-1}$) and γ is the dissociation rate. "Class A" systems, which are multiply-bound organic molecules, exhibit ionisation followed by fragmentation, since $\sigma I >> \gamma$. In "Class B" systems, on the other hand, $\gamma >> \sigma I$ and fragmentation precedes ionisation. Typical "Class B" molecules are inorganic and organometallic compounds having one or more heavy metal atoms, such as $Fe(CO)_5$ [13].

In benzene and its derivatives, ionisation via the S_1 state yields spectra typical of class A behaviour. Benzene itself has been the subject of a great deal of

Figure 3.1. Possible events at the excited molecular state in an R2PI scheme.

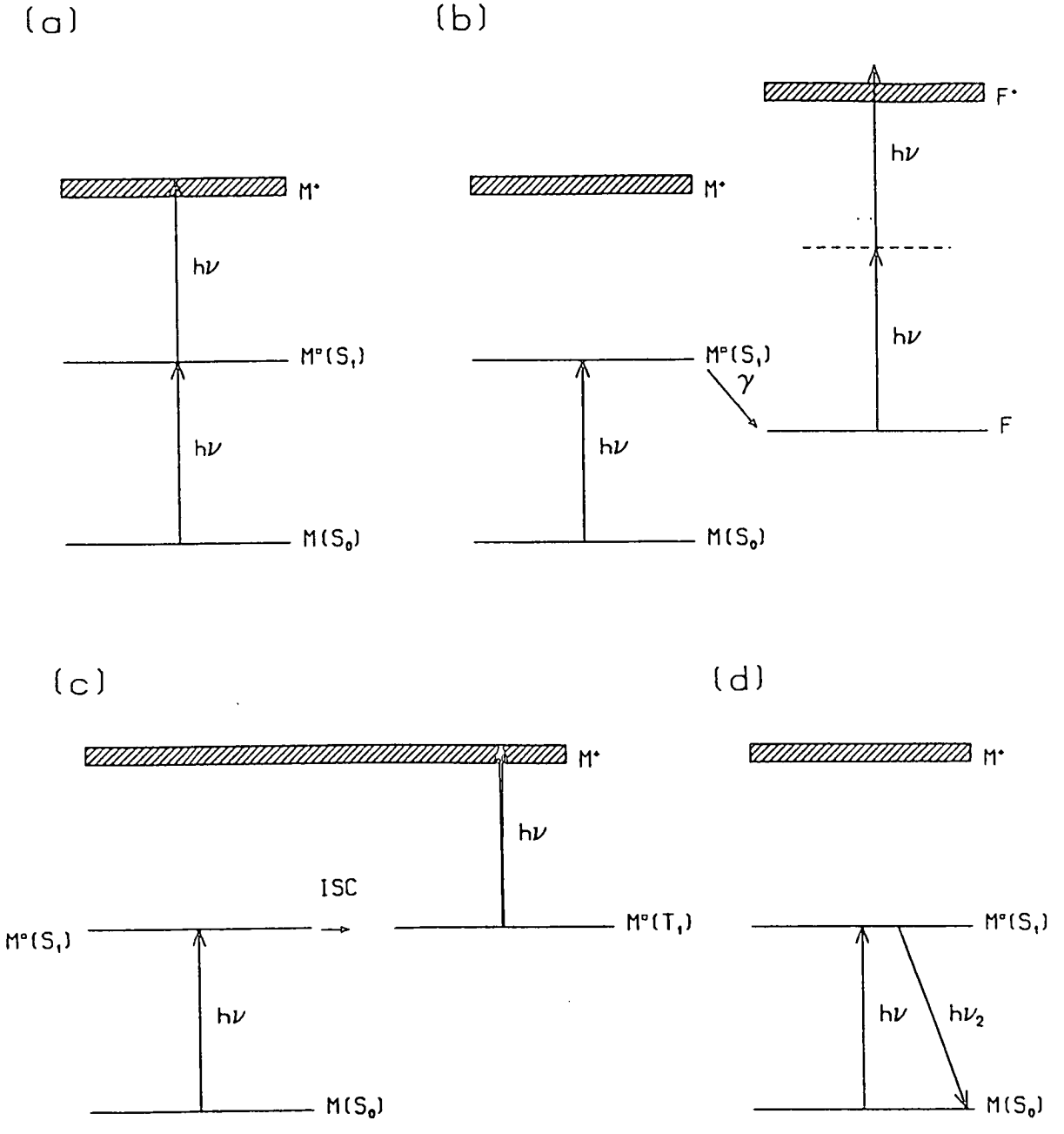

photoionisation work, and has proved to be the archetypal molecule for mechanistic studies in organic MPI mass spectrometry. In non-laser work, no evidence has been found for dissociation in benzene up to 9500 cm^{-1} above the S_1 origin [14]. In independent experiments, Boesl et al. [15] and Pandolfi et al. [16] showed that even if laser irradiation of benzene does cause dissociation from the S_1 state, the effect is not observed in the MPI mass spectrum. In the experiment of Boesl et al., a (UV) laser was used to produce benzene molecular ions by R2PI via the S_1 state. These ions were then irradiated 17 ns later by a second laser (λ = 483.22 nm), yielding fragment ions. Since the total ion current was the same in the absence of the second laser pulse as in its presence, Boesl et al. concluded that the molecular ion must have been the precursor for all the observed fragment ions. This is typical class A behaviour. Pandolfi et al. utilised a similar laser excitation scheme, but after their ionisation laser had fired, the molecular ions were accelerated out of the focal region of the second laser before it fired. No fragment ions were observed, confirming the involvement of the molecular ion in their production.

A notable exception to the general picture of class A behaviour for aromatic molecules is found for benzaldehyde, for which the lowest π^*-π transition is S_2-S_0. At low laser intensities, formation of the stable dissociation products CO and C_6H_6 has been reported to compete with S_2 photon absorption [17], [18]. At the higher laser power densities typically employed in MPI-MS work, however, even this system reverts to class A behaviour.

Molecules with groups that induce radiationless transitions, such as chlorinated and brominated groups on aromatic rings, generally exhibit less efficient

ionisation than their unsubstituted counterparts. This situation is illustrated in figure 3.1(c), where efficient intersystem crossing occurs (the rate constant for intersystem crossing in bromobenzene is $\sim 2 \times 10^{11}$ s^{-1} [19]). In general, ISC results in the population of a vibrationally excited level in the first excited triplet state. The Franck-Condon factor for the subsequent ionisation step from this state is small, so efficient R2PI will not occur.

3.2.2 Ionisation.

There are two processes which must be considered for the ionisation step, namely direct ionisation and autoionisation. In the former process the molecule is excited directly to the ionisation continuum, with the result that an electron is ejected leaving the molecular ion either in its ground state or an electronically excited state. In the case of autoionisation, although the total electronic energy is greater than the ionisation potential, no single electron has sufficient energy to be ejected. A super-excited neutral state, known as an autoionising state, is populated above the molecular ionisation potential. The electronic configuration of this state can change spontaneously so that one electron acquires sufficient energy to enable ionisation to occur, a process known as electronic autoionisation.

It is possible to determine whether photon absorption above the ionisation potential is by neutral species or by ions, i.e. whether or not autoionisation precedes up-pumping. A simple calculation, assuming an autoionisation rate of 10^{13} s^{-1} [20] and a super-excited cross section of 10^{-16} cm^2, suggests that autoionisation should dominate under typical laser ionisation conditions ($I < 10^{29}$ photons $cm^{-2}s^{-1}$). At least two pieces of experimental evidence back up

this conclusion.

Firstly, MPI-PES studies of benzene and its derivatives at a number of laser wavelengths show no peaks corresponding to ionisation involving absorption of more photons than the minimum number required to exceed the ionisation potential. Secondly, in the experiments of Boesl et al. [15], the MPI mass spectrum of benzene was found to be independent of the delay (0-17 ns) between the ionisation and fragmentation lasers. In 17 ns, any super-excited state would have had sufficient time to autoionise, so that absorption of the delayed laser pulse, which results in the appearance of fragment ions, must be by ionic species. Since the same mass spectrum was observed in the absence of any delay between the two laser pulses, the same mechanism was assumed to be operating.

3.2.3 Fragmentation.

Multiphoton ionisation results in the formation of molecular ions in a well-defined vibronic level, usually the vibrationless level of the ground electronic state of the ion [21]. The excess energy supplied in the ionisation step is removed as kinetic energy by the ejected electron, leaving the molecular ions with a narrow energy spread. With increasing laser intensity, absorption of further photons by these molecular ions induces fragmentation. Several mechanisms have been proposed to explain this fragmentation [22]- [26], with the generally-accepted model being the so-called "ladder switching" model of Dietz et al. [26] which is shown schematically in figure 3.2(b).

Figure 3.2. Comparison of the ionisation mechanisms for EI and MPI.

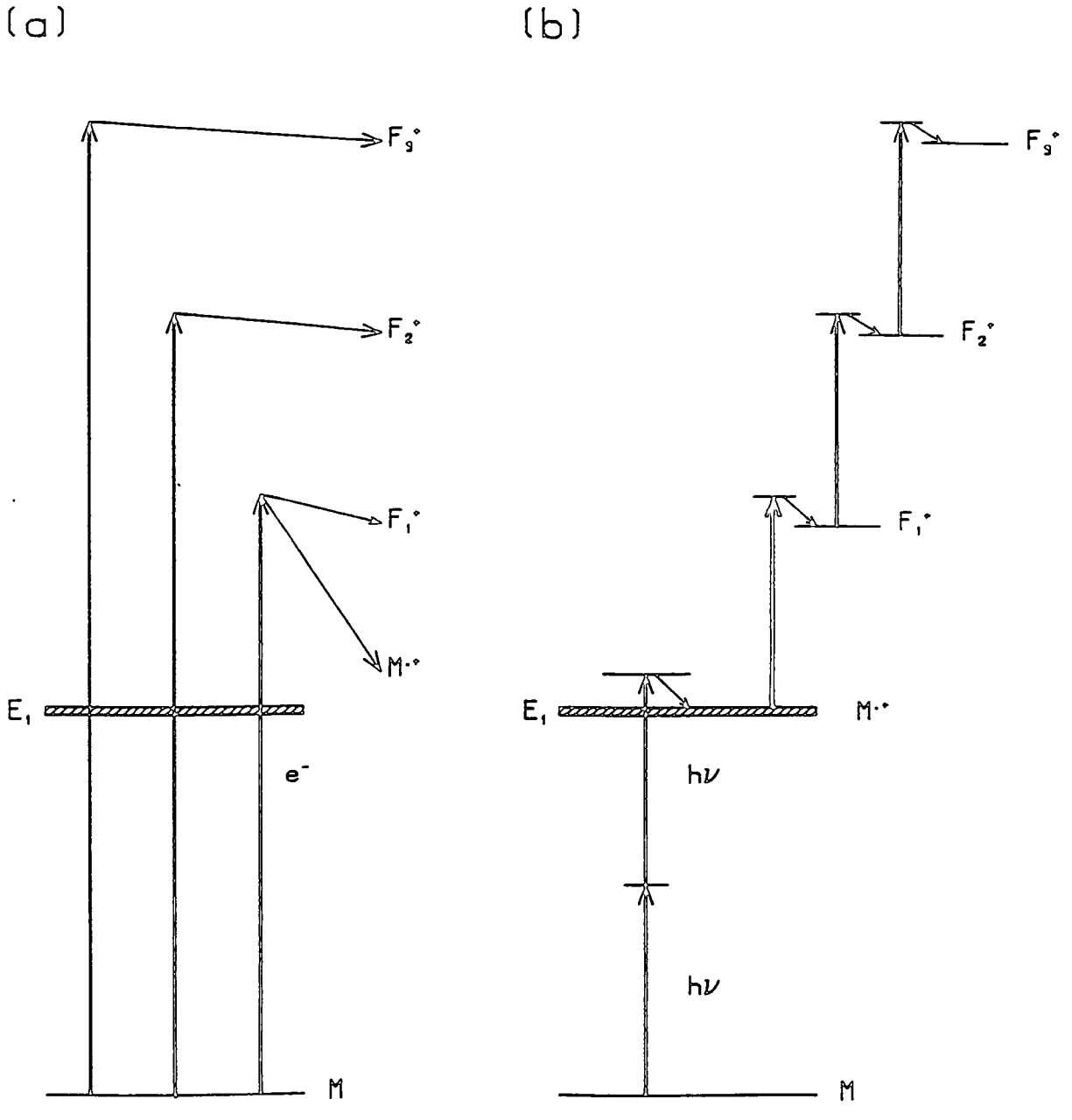

In this model, the neutral molecule absorbs two or more photons on its "absorption ladder" resulting in photoionisation. If the photon density is high enough, the molecular ion then absorbs one or more photons. In common with the quasi- equilibrium theory of conventional mass spectrometry [30], MPI is accompanied by fragmentation of the molecular ion once certain energy thresholds are exceeded. At sufficiently high excitation energies, the dissociation rates of the molecular ions become fast enough to compete with further optical excitation, and eventually, the rate of dissociation will become dominant. This places an effective maximum energy on the molecular ion absorption ladder, and causes the system to switch to a new ladder of product ions. These product ions can then in turn absorb light during the laser pulse and undergo further excitation until their maximum energy is reached, and then they in turn undergo ladder switching.

There is experimental evidence to support this model. Hering et al. [31] observed that the fragmentation of benzene molecular ions was reduced if a single picosecond laser pulse was employed rather than a much less intense nanosecond pulse. This was explained in terms of the ladder switching model, since it was proposed that molecular ion fragmentation occurred too slowly for the primary ion fragments to be generated before the end of the picosecond pulse. Boesl and coworkers [32], in a later study, selectively irradiated primary fragment ions from benzene with a second laser, and observed a mass spectrum similar to that generated in a single laser photoionisation experiment. They concluded from this that the fragmentation pathway involved absorption by these fragment ions, which directly supported their ladder switching model. Both

Dietz et al. [26] and Rebentrost and Ben-Shaul [25] have shown that absorption of one UV photon by the molecular ion of benzene, up to an excitation energy of ~ 5 eV, results in up-pumping rather than dissociation. However, at the two photon level dissociation becomes dominant, and a ladder switch takes place. This energy level is much lower than the appearance potential of small ionic fragments such as C^+, so the ladder switching model must be invoked to explain their appearance in MPI mass spectra of benzene in intense laser fields.

3.2.4 Comparison of MPI-MS with EI-MS.

MPI of gas-phase molecules results in the formation of radical cations. Conventional mass spectroscopic methods such as electron impact ionisation (EI) and ionisation via charge exchange (CE) also give rise to radical cations. A comparison of MPI with EI shows some of the potential advantages of the former as an ionisation method in mass spectrometry.

One of the most important advantages that is offered by MPI-MS is high sensitivity, which is the direct result of being able to select the correct laser wavelength and power density for the problem being tackled. The ionisation efficiency depends on the magnitudes of the absorption and ionisation cross sections. For a typical R2PI scheme, with cross sections of 10^{-18}-10^{-17} cm^2 for the two steps, roughly 5 % of the neutral molecules irradiated can be ionised by a 1 kW, 5 ns laser pulse [27]. For example, Boesl et al. [28] measured the absorption and ionisation cross-sections for a number of organic molecules in an effusive beam. For broad-band excitation (1 cm^{-1}) at 10^7 Wcm^{-2}, approximately 25 % of the ground-state population resonant with the laser bandwidth could be

ionised. In the case of aniline, Boesl et al. estimated that about 30 % of all ground state molecules were able to absorb, yielding an overall ionisation efficiency of about 7.5 %. By saturating either the absorption or ionisation step, through the use of higher laser powers, higher ion yields can be obtained, but at the cost of loss of both selectivity and softness of ionisation. In contrast, ionisation efficiencies in EI mass spectrometry are generally much lower, typically on the order of 10^{-4} [29]. Increasing the electron beam density can, in some cases, increase the ion yield but disturbs the ion optical properties of the ion source. In terms of duty cycle, however, it should be noted that whilst most pulsed lasers can operate up to ~ 10 Hz, most EI sources typically operate at 10 kHz upwards. This means that in terms of overall efficiency, laser ionisation is at best comparable with EI as an ionisation method. However, the feature which most distinguishes MPI from other ionisation methods in mass spectrometry is the degree of control which can be exerted over the extent of fragmentation of the molecular ion.

The analysis of EI mass spectra requires consideration of a series of competing, consecutive unimolecular decomposition reactions between energetically excited ions [30]. With MPI-MS, however, additional competition exists between these processes and any subsequent photon absorption. The most important distinction between the two ionisation methods is illustrated in figure 3.2. In EI-MS (figure 3.2(a)) and other conventional forms of mass spectrometry, all the excitation energy is given to the molecular species. In the ladder-switching model of MPI-MS (figure 3.2(b)), a large proportion of the total excitation energy can be absorbed by fragment ions. The transitions occurring in a multiphoton

ionisation/fragmentation scheme are Franck-Condon controlled. These photon-induced transitions occur vertically, and only certain states are accessible. Also, because of spin conservation selection rules, fewer states are accessible than by EI-MS. Ionisation by 70 eV electrons corresponds to light of de Broglie wavelength equal to 0.15 nm, so that strong perturbation of the molecule occurs. Therefore transitions need no longer be vertical. Many more states are therefore accessible than with MPI-MS, with the potential for much more interesting fragmentation processes. There is therefore no reason for the fragmentation patterns to be similar in each case, although similarities may exist, especially in the formation of high mass ions, where fragment ion excitation is generally not important. The contrast between these techniques is best illustrated by an example: R2PI of aniline via the origin band of the S_1-S_0 electronic transition, at a laser wavelength of 293.75 nm(air).

MPI mass spectra of aniline have been reported previously, exhibiting predominantly the molecular ion peak and facile ionisation at relatively low laser intensities. Upon increasing the laser intensity, extensive fragmentation occurs, with fragment ions corresponding to C_1 species being observed [33]- [35]. Figure 3.3 shows the mass spectral fragmentation patterns of jet-cooled aniline at 293.75 nm as a function of laser power density. These mass spectra were obtained in the reflecting-geometry time-of-flight mass spectrometer described in the following two chapters. Figure 3.3(a) was obtained with a laser power density of $\sim$ 0.1 $MWcm^{-2}$, and shows "soft" ionisation of aniline, with no fragmentation of the molecular ion (m/e = 93). Two photons at 293.75 nm corresponds to an energy of 8.46 eV, which is 0.79 eV greater than the molecular ionisation potential [36].

Figure 3.3. MPI Mass Spectra of Aniline at 293. 76 nm.

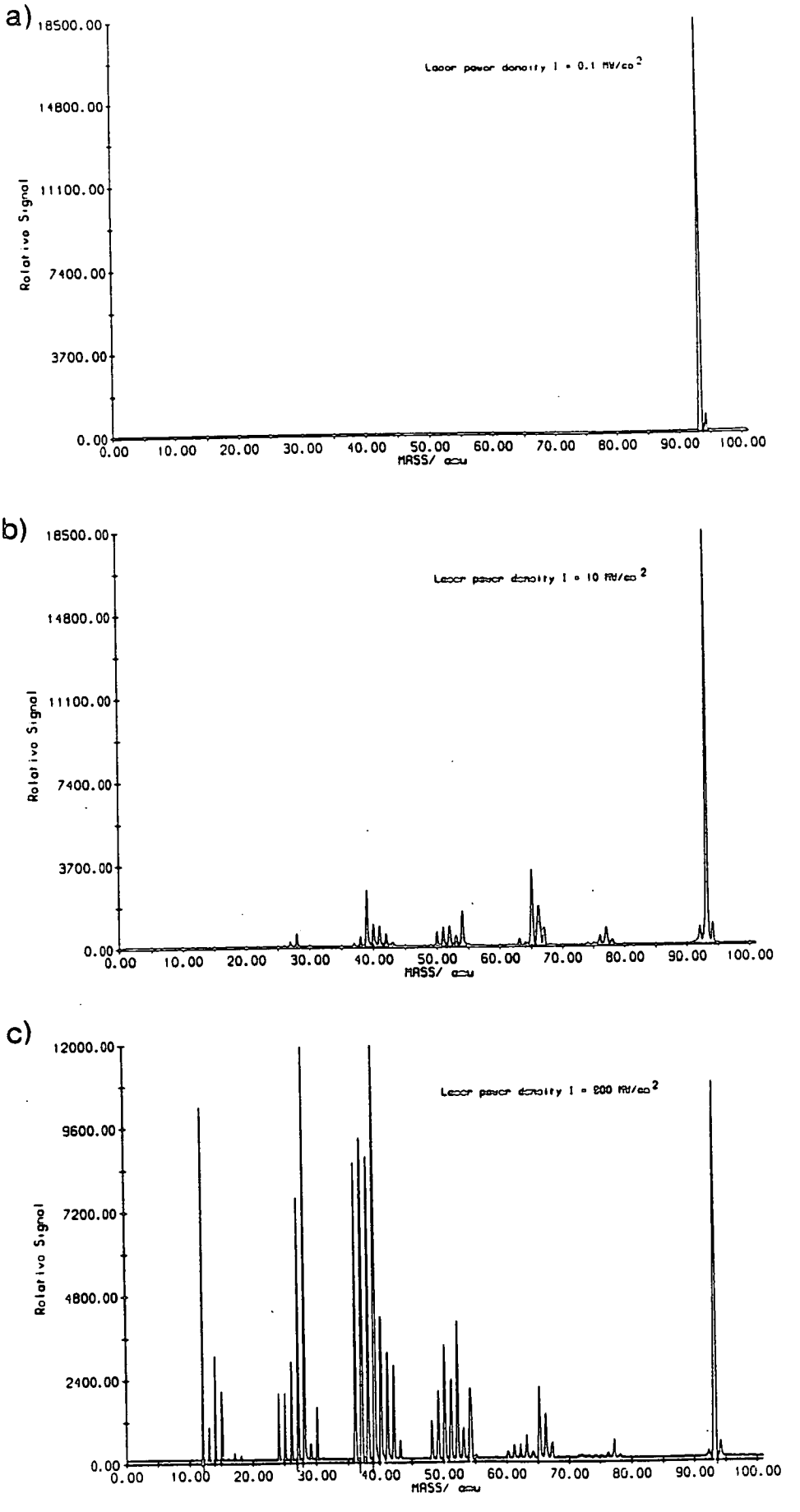

This excess energy is insufficient to fragment the molecular ion. With increasing laser power density, the rate of up-pumping from the S_1 state is increased, so the total ion signal increases. Figure 3.3(c) was recorded using a laser power density of ~900 $MWcm^{-2}$. The relative shift of ion signal to the lower mass fragments, so-called "hard ionisation", is expected since the rate of up-pumping of the molecular ion to dissociative states also increases with laser power density. The low mass fragments have higher heats of formation than the molecular ion and therefore require higher-order photon processes for their formation. Kühlewind et al [37] have deduced that the ion at m/e = 15, namely CH_3^+, is formed after absorption of five 266 nm photons: this corresponds to 6 photon absorption at 293.75 nm. Figure 3.3(b) was recorded with a laser power density of 10 $MWcm^{-2}$, and shows "medium-hard" ionisation.

Figure 3.4 shows the 70 eV EI mass spectrum of 6 x 10^{-6} torr of aniline, recorded using a simple quadrupole mass spectrometer (VG Quadrupoles, SX200). Comparison of this mass spectrum with those in figure 3.3 reveals that although the mass peaks appear at the same positions, there are two major differences. Firstly, the appearance of C_1^+ fragments in the high intensity R2PI mass spectrum emphasizes that the absorption of excitation energy by ions can lead to far more extensive fragmentation than is possible with EI excitation of the neutral precursor by a similar, or even greater amount of energy. It is also clear that a larger proportion of the fragment ions are at low masses in the R2PI spectrum with respect to the EI mass spectrum, where the m/e = 66 ion is the dominant fragment. Conversely, soft ionisation, as illustrated in figure 3.3(a), can only be achieved using EI with a significant loss in sensitivity. The second

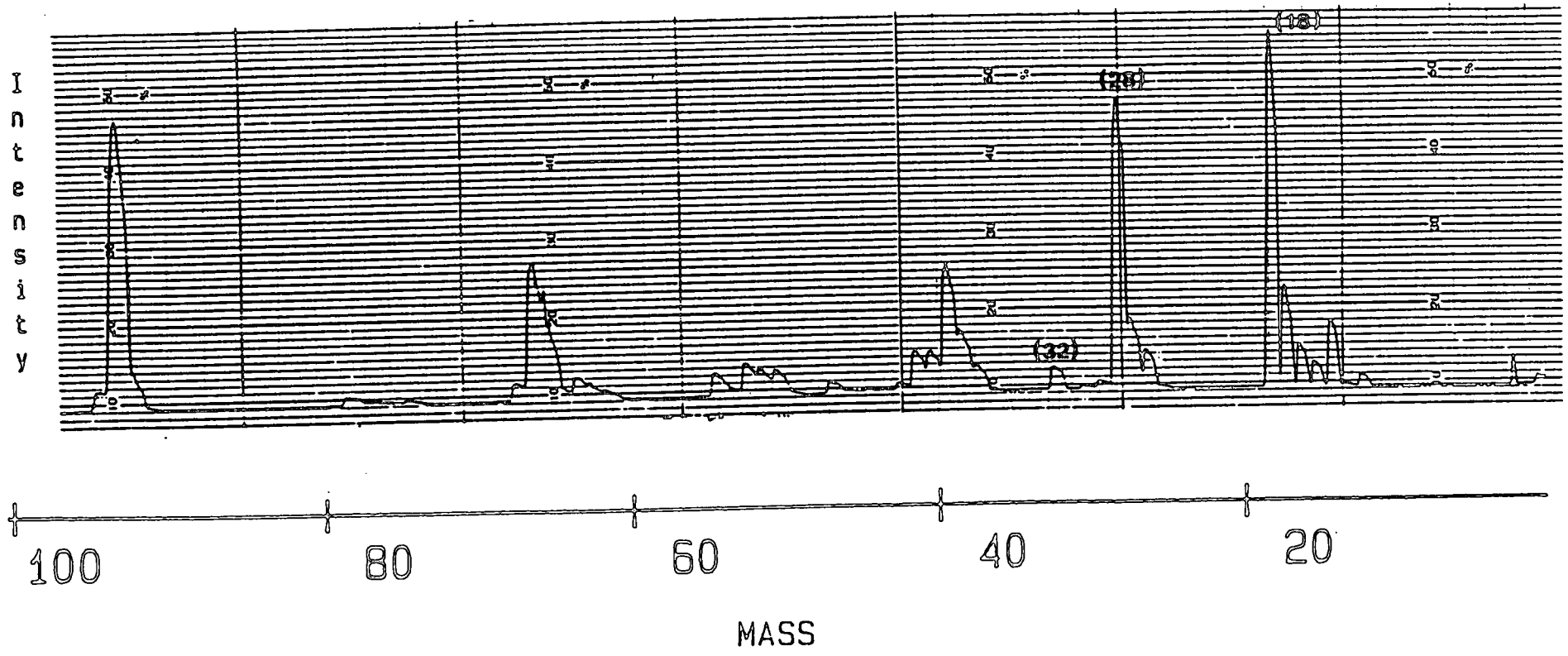

Figure 3.4. 70 eV EI Mass Spectrum of Aniline.
Peaks due to background are indicated.

important difference is that no air or water background is apparent in the R2PI mass spectra until extremely strong laser fields are used. Even then, the contribution of these peaks to the mass spectrum is insignificant when compared to that in the EI mass spectrum. Although the experimental conditions in these experiments were not identical, the background pressures in both ion sources were similar. R2PI mass spectra obtained with a static gas sample in the SX200 were comparable to those shown in figure 3.3. This demonstrates the selectivity of MPI-MS. The aniline signal is readily ionised at $\lambda = 293.75$ nm, whereas at the same wavelength, there is no resonance-enhancement for MPI of the air/water vapour background. The ionisation cross section for these molecules are many orders of magnitude smaller than that for aniline, and, consequently, the aniline is selectively ionised. This possibility of selective ionisation has been of major importance in the development of MPI-MS as an analytical tool, and will be discussed in the following section.

3.2.5 Applications of MPI-MS.

The ability to achieve selective ionisation can help in solving problems which may be difficult to address using conventional mass spectroscopy. Such problems include isomer discrimination, isotope-selective analysis and analysis of trace components in complex mixtures.

In order to distinguish between isomers by conventional mass spectroscopic techniques, different mass spectral fragmentation patterns must be produced, which is difficult to achieve in many cases. Therefore tandem techniques such as gas or liquid chromatography-MS (GC-MS or LC-MS) [38] are employed to

select one component from a mixture prior to final mass spectroscopic analysis. For substitutional isomers and compounds with similar structure, however, the degree of discrimination may be limited.

In MPI-MS, not only is it possible to obtain mass spectra with varying degrees of fragmentation by changing the laser power density, but also the wavelength of the laser can be varied. Thus by monitoring a given (molecular) ion peak as a function of laser wavelength, the MPI spectrum of that species can be generated. The absorption maximum of a molecule and thus the resonant intermediate state energy are intrinsic properties of the molecule and are therefore substance specific. At each peak in such a spectrum, a mass spectral fragmentation pattern may be recorded. Such a two-dimensional mass spectrum is highly species-specific: at a given laser intensity, no two molecules will have the same 2D MPI-mass spectrum.

By the addition of this second (wavelength) dimension to the mass axis of conventional mass spectrometry, it is possible to discriminate between, and selectively ionise, molecules by exploiting disparities in their MPI spectra. In the analysis of complex mixtures, for instance, the component that has an intermediate state in resonance with the laser wavelength will be preferentially ionised. It is therefore possible to detect trace amounts of a material in a mixture with increased sensitivity. For MPI-MS of large polyatomic molecules, the use of supersonic jet-cooling is usually necessary. In the bulk gas, spectral selectivity is lost due to overlapping transitions from the large number of rovibronic levels populated at room temperature. In the analysis of mixtures, the degree of selective ionisation that can be achieved is determined by the overlap of the

resonances of the individual components.

Several groups have been active in this field. The work of Lubman and coworkers, employing an integrated supersonic nozzle/ time-of-flight mass spectrometer, has been particularly impressive. In 1980, they showed that, by correct tuning of the laser wavelength, they could discriminate between the isomers naphthalene and azulene [11]. In later work, the analytical power of the MPI-MS technique was demonstrated in a study of the isomers of cresol [39], [40]. A discrimination limit corresponding to a single part of one isomer in 300-500 parts of another and a sensitivity limit of 20 parts per billion of cresol in nitrogen was obtained. In a similar experiment [41], Lubman and colleagues obtained jet-cooled R2PI spectra of four isomers of dichlorotoluene in a TOF mass spectrometer, thereby allowing discrimination of the isomers.

In some cases, optical selectivity can be obtained without jet-cooling, based either on widely different absorption properties of molecules [42], or on different ionisation potentials. Reilly and coworkers [43] demonstrated selective ionisation of chrysene (IP = 7.8 eV) over triphenylene (IP = 8.1 eV) by judicious choice of laser wavelength, such that the two photon energy was above the chrysene molecular ionisation potential but below that of triphenylene. In a multi-component system, however, only the species with lowest ionisation potential can ever be selectively ionised by this method.

In most reported MPI-MS studies, the fragmentation patterns of isomers have been found to show no more significant differences than in their EI mass spectra. Any isotopic discrimination must therefore be accomplished by

wavelength-selective ionisation alone. However, Parker and Bernstein [44] have demonstrated that, in the case of some alkyl iodide isomeric pairs (isopropyl iodide versus n-propyl iodide, and tert.-butyl iodide versus n-butyl iodide), whereas the EI mass spectra of the isomers are virtually identical, those resulting from MPI are significantly different. In this case, it was concluded that rearrangement of these isomers to a common structure was taking place during the EI process, but that this did not occur during the MPI process.

Several examples have appeared in the literature of enhanced sensitivity of components in a mixture through selective ionisation. For example, in blood serum, several metals and organometallic compounds can be measured quantitatively in concentrations of about 1 ng per 1 ml serum [45]. The use of 2D MPI-MS has been demonstrated for detection of p-cresol (m.wt. = 108) in p-fluoroaniline (m.wt. = 111) with a discrimination of 1:5000 in a TOF mass spectrometer. This limit was due to the presence of thermalised p-fluoroaniline molecules in the ionisation chamber, but discrimination of better than $1:10^5$ has been predicted [39].

Figure 3.5 shows the R2PI spectrum of a sample of aniline with natural isotopic composition (mass 93/ mass 94 = 100/ 13.87 %). The mass 94 contribution is made up of mono-^{13}C-substituted aniline, and mono-^{15}N-substituted aniline, with the former isobar dominating. The band shown corresponds to the jet-cooled origin band of the $^1B_2$-$^1A_1$ (S_1-S_0) transition. It can be seen that the positions for the absorption maxima for the two isotopomers differ slightly, with the mass 94 isotopomer band shifted 4.6 cm^{-1} to the blue of the mass 93 isotopomer band.

Figure 3.5. R2PI Spectra of Aniline (Mass 93) and Isotopically-Substituted Aniline (Mass 94). This is the 0_0^0 band of the $^1B_2$-$^1A_1$ transition.

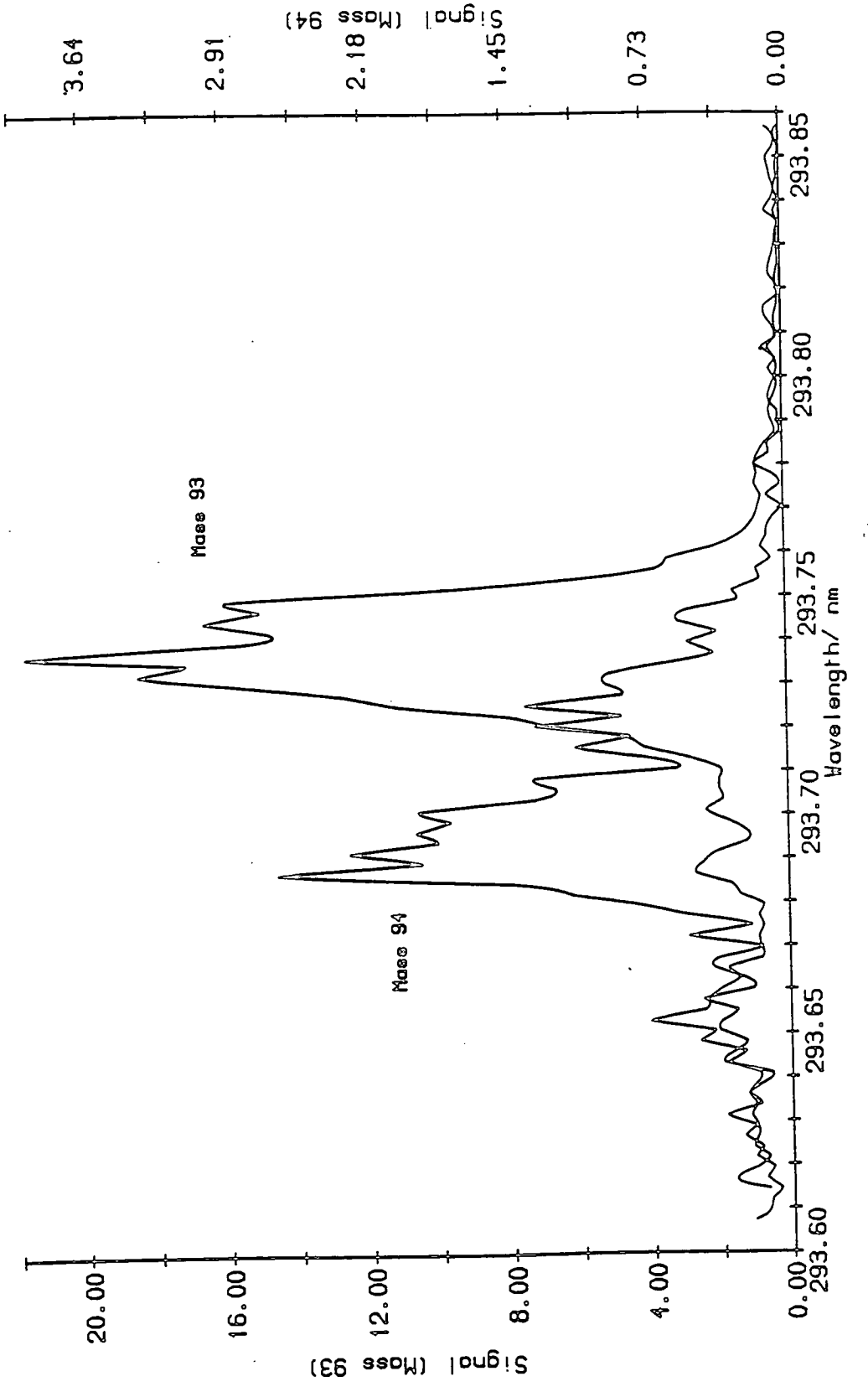

By choosing the appropriate wavelength, the signal of the mass 94 aniline molecular ion can be either amplified or suppressed. Figure 3.6 shows the ratio of the mass 93 to mass 94 signal intensity as a function of wavelength across the origin band region. The horizontal line across this spectrum corresponds to the natural isotopic ratio. At spectral positions where the experimentally-determined signal ratio is below this line, the mass 94 peak is enhanced relative to the mass 93 peak. Conversely, at wavelengths where the ratio lies above this line, the mass 93 peak is enhanced. Thus irradiation in the centre of the rotational envelope of the mass 93 origin band results in a dominant contribution from mass 93 aniline, while at higher energies, dramatic isotope enrichment occurs.

Leutwyler and Even [46] have defined an isotopic separation factor γ for binary mixtures, where

$$\gamma = C_f/(100-C_f) * (100-C_i)/C_i.$$

In this case C_f and C_i refer to the observed abundance and the natural isotopic abundance of the mass 94 isotopomer. Clearly, there are in fact three species present in a natural mixture of aniline isotopomers, but since the ^{13}C species dominates over the ^{15}N species in their contributions to the mass 94 peak, the above equation is valid. Maximum enhancement of the mass 94 isotopomer occurs at 293.696 nm, where the ratio of mass 94: mass 93 is 5 times greater than the natural isotopic ratio. Conversely, the mass 93: mass 94 ratio is maximised at a wavelength of 293.737 nm (air), where it is 6 times the naturally abundant ratio.

Figure 3.7 shows mass spectra of aniline recorded under similar conditions to

Figure 3.6. Variation of Mass 93: Mass 94 Ion Signal Ratio across the origin band region of the $^1B_2$-$^1A_1$ transition in Aniline.

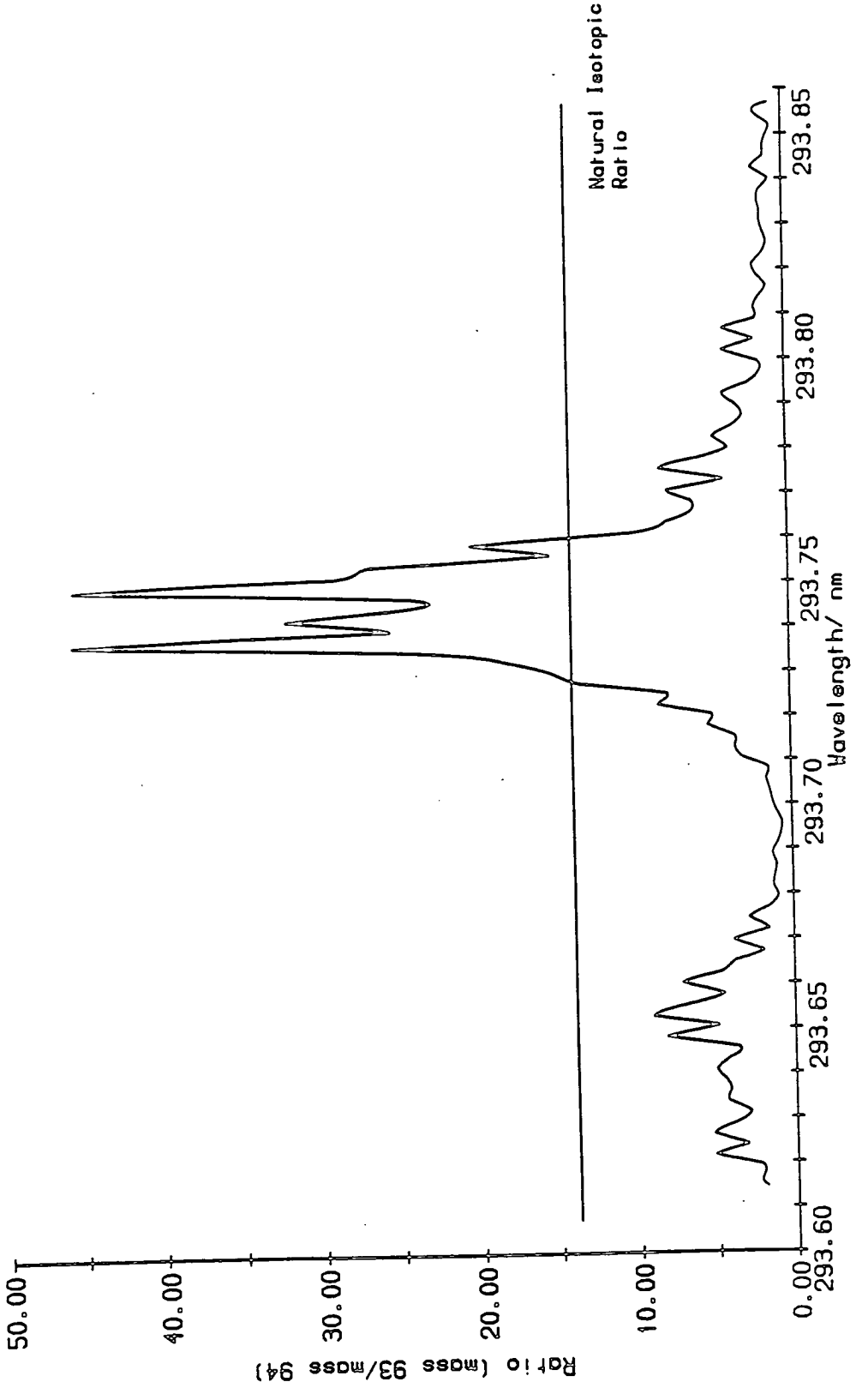

those used to obtain figure 3.5. No fragmentation of the molecular ions was observed under these conditions. Figure 3.7(a) was obtained at λ = 293.757 nm (air) and demonstrates the enhancement of mass 93 relative to mass 94: here the intensity ratio is 27.0. Figure 3.7(b) was obtained at λ = 293.677 nm and shows depletion of the mass 93 signal relative to mass 94 (intensity ratio = 1.97).

Isotopic shifts in R2PI may involve isotope effects in either the absorption step or ionisation step, or indeed both. In the case of single-colour R2PI of aniline via the origin band of the S_1-S_0 transition, absorption of two photons excites the molecule to 0.79 eV above its ionisation potential. It is unlikely that at this energy above threshold the molecule exhibits autoionisation structure distinct enough to produce strong isotope effects, so the observed isotopic shift must be entirely determined by the absorption step. Since the isotopic shift of the origin band of the mass 94 species is to the blue of the mass 93 origin, the difference in zero-point vibrational energy of the two isotopic molecules must be larger in the $^1A_1$ state than in the $^1B_2$ state. Leutwyler and Even attribute this shift to a non-mode-specific overall reduction in the force constants in the $^1B_2$ state relative to the ground electronic state[46].

Boesl and coworkers [47] obtained similar results for mono-^{13}C p-xylene. In naturally occurring p-xylene, the ratio of m/e 106: m/e 107 is 100: 8.8. By varying the R2PI laser wavelength over the S_1-S_0 electronic origin band, this ratio was drastically influenced, giving limiting ratios of 100: 0.5 and 50: 100. Isotopic detection of NO using VUV laser excitation has been demonstrated by Zacharias et al. [48] and more recently by Miller [49] in supersonic jets in the near UV using a 2-photon excitation, overall 3-photon ionisation MPI scheme. Lubman

Figure 3.7. R2PI Mass Spectra of Aniline, illustrating the effect of selective ionisation as a function of wavelength.

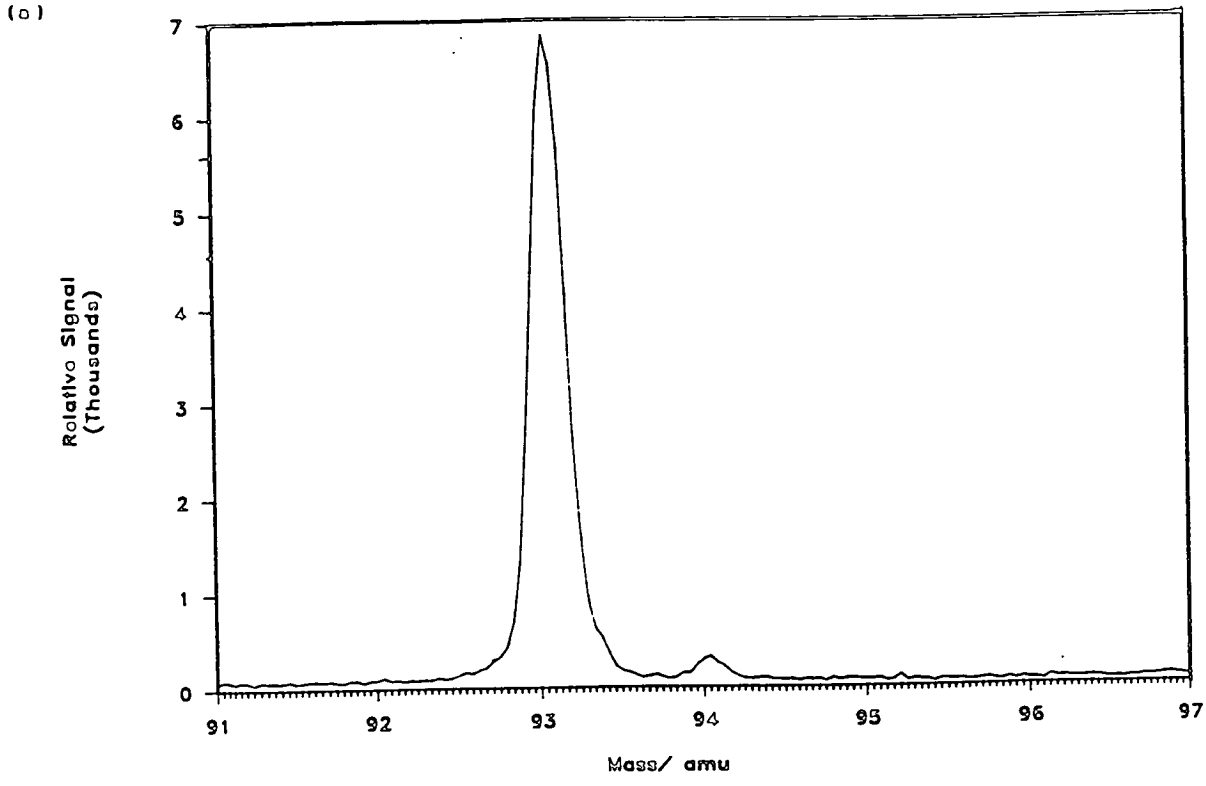

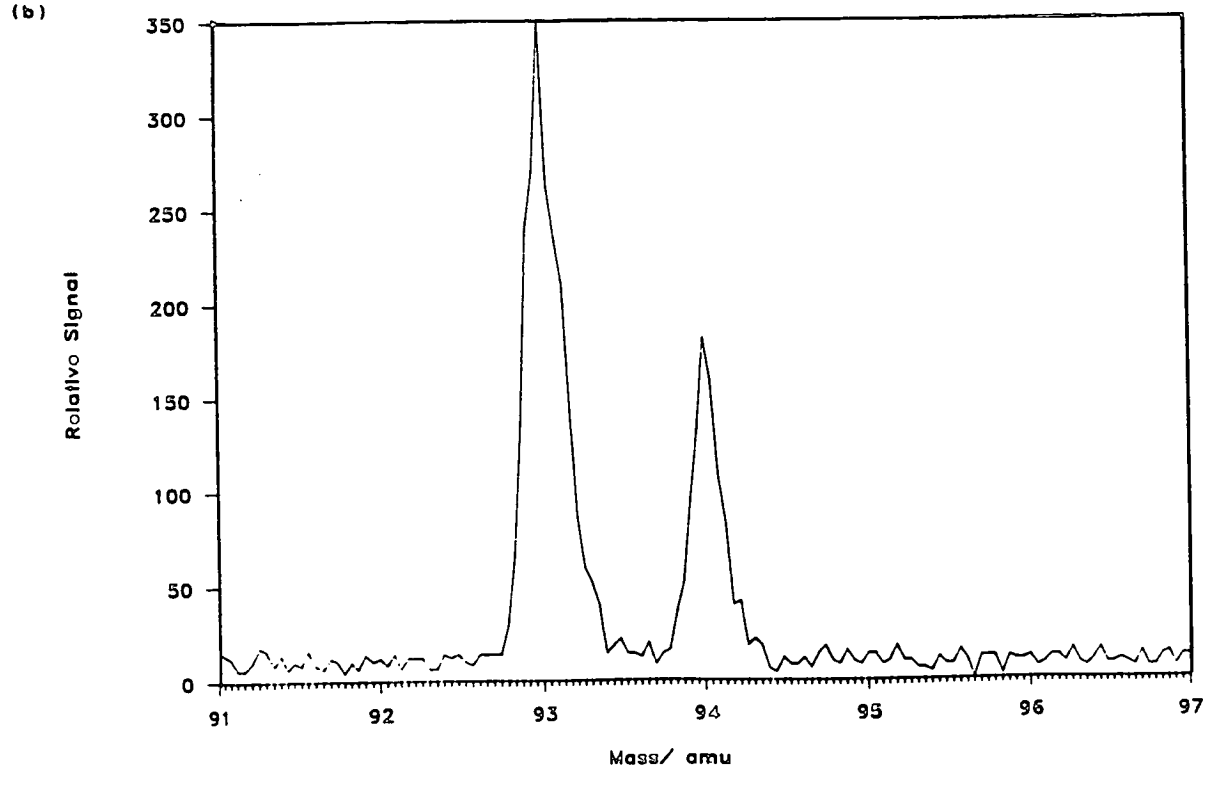

and coworkers have studied the laser induced ionisation of the isotopomers of dichlorotoluene [39], in which the natural abundances of the Cl isotopes $^{35}Cl_2$: $^{35}Cl^{37}Cl$: $^{37}Cl_2$ is 9:6:1. By choosing the correct wavelength, an enhancement of each isotopomer was possible, in the range 16-64, over the naturally abundant ratio.

The ultimate limitations on the general applicability of MPI as a sensitive and selective method of ionisation depends on suppressing the background non-resonant ionisation and the resonant continuum background absorption that becomes increasingly stronger as the laser wavelength decreases [50]. In addition, other problems may arise if the fragmentation thresholds or the relative absorption cross sections of the compounds in a mixture are very different, so that extensive fragmentation occurs in one compound while another just begins to ionise. However, the additional wavelength selectivity provided by MPI may aid in solving otherwise intractable trace analysis problems.

3.3 Laser desorption mass spectrometry.

3.3.1 Introduction.

Mass spectrometry has long been recognised as one of the most powerful analytical tools available to the scientist, being characterised by both high sensitivity and high information content. In general, however, the conventional methods of ionisation (EI and CI) used in mass spectrometry (and indeed also MPI-MS) require that the sample under investigation be present in the ion source in the gas-phase. For gases and volatile materials, obviously, this does not

present a problem. In the case of substances having low vapour pressures under normal conditions, however, special techniques must be used. The direct inlet system [51] allows the mass spectra of molecules with vapour pressures below 10^{-6} torr to be obtained. This methodology entails placing the sample into an open-ended capillary, situated in the ion source, which can be heated to several hundred degrees, thereby generating sufficient vapour pressure for analysis. This procedure is, however, inappropriate for a large number of organic and bio-organic compounds due to their low vapour pressures and thermal instabilities.

The first efforts made to obtain mass spectra from this large class of "difficult" molecules involved the development of chemical derivatisation techniques in order to increase their volatility [52]. However, these methods could only be applied to a limited number of molecules and often led to more complicated spectral analysis. As a result, a number of different methods have been developed to allow mass spectra of non-volatile and labile species to be recorded, without prior chemical modification. These are the so-called desorption methods.

The common feature of all these methods is that the sample, either in solid form or dissolved in a suitable solvent, is placed directly into the ion source of the mass spectrometer. The characteristic features of the techniques that have been employed depend largely on the method of ion production. These can be classified broadly as follows:

1. Ions created due to bombardment of the sample by a beam of energetic atoms-

   Fast Atom Bombardment mass spectrometry (FABMS) [53], [54].

2. Ions created due to bombardment of the sample by a beam of energetic ions- Secondary Ion Mass Spectrometry (SIMS) [55].
3. Ions created due to bombardment of the sample by the decay products of ^{252}Cf nuclei- Plasma Desorption Mass Spectrometry(PDMS) [56].
4. Field desorption mass spectrometry (FDMS) [57]- [59].
5. Laser desorption mass spectrometry (LDMS) [60], [61].

The combination of the technique of laser desorption with the unique properties afforded by MPI as a means for ionisation in mass spectrometry, i.e. laser desorption multiphoton ionisation mass spectrometry (LD-MPIMS), has emerged as a powerful new analytical method [62]- [64]. The remainder of this thesis will deal with the design and development of an apparatus constructed at the University of Edinburgh to exploit this new approach.

In the following sections of this chapter the history of laser desorption mass spectrometry will be briefly reviewed, followed by a discussion of the various desorption/ ionisation mechanisms involved. Finally, the advantages of using post-ionisation of laser desorbed neutral molecules will be considered, including a brief introduction to the techniques that will be introduced in later chapters. Chapters 4 and 5 contain further details of the experimental procedures and equipment employed during this work. In chapter 6 some of the preliminary results that have been obtained at Edinburgh are presented, along with some discussion concerning possible future developments in the technique. Finally, chapter 7 gives a survey of the work carried out elsewhere using the technique of LD-MPIMS, and concludes with some discussion concerning its suggested role in

analytical chemistry.

3.3.2 Pioneering work in LDMS.

Early uses of high-power lasers combined with mass spectrometry were confined to the vaporisation of graphite [65] and coal [66], as well as pyrolysis of non-volatile compounds to produce volatile fragments to provide structural information [67]. Another area of some activity was elemental analysis of solids by ionisation of surfaces [68], [69]. In 1968, however, Vastola and Pirone [70] used the pulsed output from a ruby laser to obtain mass spectra from conjugated aromatic compounds, alkyl-substituted aromatics and the amino acid leucine. Laser irradiation of the sample gave rise to both ions and neutral molecules, the latter being detected through subsequent ionisation by an electron beam. A common feature in all the laser-produced mass spectra obtained was the presence of a rather intense molecular ion ($M^{+\cdot}$) signal. The mass spectra of the conjugated aromatics consisted almost entirely of the $M^{+\cdot}$ ion, whilst those of the alkyl-substituted aromatics also showed heavier ions and light fragment ions. The mass spectrum of leucine consisted of a molecular ion and a large number of fragment ions.

In subsequent papers [71], [72], Vastola and coworkers obtained LD mass spectra of sodium and potassium salts of sulphanates, sulphates and thiosulphates. In contrast to their earlier work, the only organic ions that were formed were due to alkali cation attachment to the parent molecule $(M+c)^+$. No molecular or fragment ions were observed.

In 1978, Posthumus et al. [60] published a paper that was of special significance

in the development of LDMS as applied to non-volatile and thermally unstable bio-molecules. They obtained mass spectra of several oligosaccharides, glycosides, nucleotides, amino acids, peptides and some other biological molecules by using laser irradiation with the output from either a pulsed CO_2 laser ($\lambda = 10.6\ \mu m$) or a Nd^{3+}:glass laser ($\lambda = 1.06\ \mu m$). All the mass spectra showed peaks at $(M+Na)^+$ and $(M+K)^+$, along with characteristic fragment ion peaks.

During the following three years, several laboratories conducted laser desorption experiments using a variety of instruments. Heresh et al. [73] used repetitive laser desorption on a magnetic sector instrument, whilst Hardin and Vestal [74] and Stoll and Röllgen [75] used quadrupole analysers, the latter group using a cw CO_2 laser. Cotter [76] used a sector instrument, with which CI of desorbed neutral compounds was studied. Meanwhile, Hercules and coworkers [77] and Seydel and Lindner [78], amongst others, were developing laser microprobe mass spectrometers for the analysis of large organic molecules. This early work in LDMS was reviewed by Conzemius and Capellan in 1980 [79].

More recently, many experiments have been performed using a variety of laser and mass spectrometric hardware. These experiments can be classified into three distinct groups, namely those in which IR laser radiation, UV laser radiation or laser microanalytical mass spectrometers have been employed. The degree of understanding of the mechanisms of ion formation and the level of technical development of these methods differ greatly. For example, the elementary processes involved in UV laser desorption/ photoionisation are well understood at present, but the mass spectrometric data obtained by this technique have, until recently, been relatively sparse. On the other hand, a large amount of mass

spectroscopic data has been obtained for organic and inorganic molecules using the laser microanalytical method. Indeed, commercial instruments have been developed by both Leybold Heraeus (LAMMA-500 and -1000) [80] and Cambridge Mass Spectrometry Ltd. (LIMA) [81]. However, there are still many unsolved mechanistic problems associated with this technique.

In the following sections, the three distinct LDMS methods will be discussed. Significant experiments which shed light on the ion formation mechanisms will be outlined, and examples will be given of mass spectra of several different classes of organic and bio-organic molecules.

3.3.3 LDMS using IR radiation.

A wide variety of equipment has been used in IR-LDMS. As mentioned above, Kistemaker and coworkers [60] have used both pulsed CO_2 and Nd^{3+}:glass lasers with a home-built magnetic sector mass spectrometer. In a later study [82] they also employed a cw CO_2 laser. Cotter initially employed a pulsed CO_2 laser with a double-focusing mass spectrometer before switching to a time-of-flight (TOF) mass analyser, whilst Stoll and Röllgen [75] used a quadrupole mass spectrometer to study ion formation using cw laser desorption. Although there are obvious experimental differences between the techniques employed by these research groups, a number of common features emerge.

All of the aforementioned IR-LDMS experiments employed "bulk analysis" instruments, in which the sample was dissolved in a suitable solvent, applied to a probe and dried. This method allowed the production of a relatively uniform film, thousands of angstroms thick. Electrospraying from methanol solutions [60]

has also been used to produce more uniform films. The laser beam is weakly focused on to the sample ("reflection mode"), with a typical power density for a pulsed laser source being 10^6-10^7 Wcm^{-2}. If a cw source is employed, a typical power density is 10^2 -10^4 Wcm^{-2}. The total energy per pulse can be as high as 500 mJ.

A number of different biologically important compounds have been studied by IR- LDMS, and, in some cases, their mass spectra were obtained for the first time. In order to give some impression of the most important features of typical IR-LDMS spectra, a class of non-volatile compounds which have been extensively studied using this technique, namely the oligosaccharides, will be considered.

Sucrose is one of the simplest saccharides. Unlike glucose, which can be evaporated without extensive thermal fragmentation [57], sucrose is practically involatile. In mass spectra of sucrose produced by means of thermal evaporation and EI light fragment ions prevail. The signal at the molecular ion mass is very weak or absent [83]. Posthumus et al. [60] obtained relatively soft mass spectra of sucrose using pulsed CO_2 ($\lambda = 10.6$ μm) or Nd^{3+}:glass ($\lambda = 1.06$ μm) laser radiation. These mass spectra showed intense quasi-molecular ions at m/e 365 and 381, due to the attachment of alkali metal cations to the parent molecule, $(M+Na)^+$ and $(M+K)^+$. A few peaks around m/e 200 were observed corresponding to cationised fragments of the sucrose molecule. The fragments were due to cleavage at the glycosidic oxygen, followed by hydrogen transfer. At lower mass, peaks due to Na^+, K^+, H_2ONa^+ and H_2OK^+ were also observed.

Posthumus et al. obtained similar mass spectra at both laser wavelengths, despite the fact that the absorption of sucrose is much greater at 10.6 μm than at 1.06 μm. This fact suggests that heating of the substrate rather than the sample itself is important. In a later experiment [82], Kistemaker's group emphasised this point even further. No ions were observed when a thin layer (0.1 μm) of sucrose was applied to a stainless steel rod and exposed to cw CO_2 laser radiation (10^3 Wcm^{-2}). However, upon switching to a quartz substrate, which absorbs IR radiation more strongly than stainless steel, both alkali metal ions and quasi-molecular ions of sucrose were obtained.

Stoll and Röllgen [75] managed to observe the formation of quasi-molecular ions of sucrose using only 20 $MWcm^{-2}$ of cw CO_2 laser radiation. In this case, however, they used a thick sample (0.5 mm) mixed with NaI. This spectrum also contained peaks due to the loss of water from sucrose, $(M\text{-}H_2O+c)^+$, which are characteristic of oligosaccharide pyrolysis. Similar results were obtained by Heresch et al. [73], who recorded mass spectra using pulsed laser radiation. It was found that prolonged heating of the sample by either cw or repetitive pulsed laser radiation leads to stronger thermal fragmentation of sucrose compared to the case with single-shot irradiation.

Besides sucrose, a number of other unsubstituted oligosaccharides were studied by Kistemaker and coworkers [60]. In nearly all cases, the quasi-molecular ion was the base peak in the spectrum, with lower mass peaks corresponding to cationised molecular fragments.

In general, the mass spectra produced by IR-LDMS have similar characteristics

to those of the oligosaccharides. These features are summarised below.

1. In nearly all mass spectra, the ions are formed as a result of alkali cation attachment to the molecule or its fragments.
2. For some classes of compound, ions of protonated molecules are also observed. In a few cases, radical molecular ions are observed at high laser powers [84].
3. In general, the spectra exhibit soft ionisation, with quasi-molecular ions very abundant. Pyrolysis products are observed, but usually only under conditions of prolonged heating.
4. The amount of structural information that can be inferred from the mass spectra is limited, due to the moderate or low degree of molecular fragmentation.

The principle conclusion that can be drawn from these studies is that a pulsed CO_2 laser appears to give optimum results [61].

3.3.4 Mechanism of ion formation in IR-LDMS.

The absorption of infrared laser radiation by a solid leads directly to its heating. It is therefore logical that the formation of organic pseudo-molecular ions using IR irradiation should be linked in some way to the heating of the sample. Indeed, the spectra obtained in IR-LDMS, which usually exhibit a high degree of alkali cation attachment, have the same general appearance as those obtained by rapid thermal desorption/ ionisation [84]. Cotter and Fenselau [85]have also shown that rapid heating of the sample plays an important role in promoting pseudo-molecular ions rather than pyrolysis products in CI-MS.

There is a large body of experimental evidence which suggests that a thermal model is appropriate for ion formation in IR-LDMS. Ions can be observed using both pulsed radiation with $I = 10^6$ Wcm^{-2} and cw radiation with $I = 10$ Wcm^{-2}. An important condition of ion formation is the absorption of radiation by either a thick layer of the sample molecule itself or by the substrate. If an optically thin layer of the sample molecule is used, the efficiency of ion formation appears to be almost independent of the infrared laser wavelength used.

Alkali metal cations are always found in LDMS mass spectra as very intense peaks. The emission of alkali atoms from a heated surface was described as early as 1918 [86], and is related to ordinary thermal ionisation resulting from sufficiently strong heating of the sample surface [87]. In LDMS, alkali metal salts are generally not added to the sample under study, since the resulting metal ion peaks tend to dwarf the rest of the spectrum. The frequently-observed Na^+ and K^+ ion peaks usually result from the heating of the sample surface to a temperature in excess of 700^0 C, at which point impurities in the probe surface are ionised, or ions in the sample are mobilised [88]. Measurement of the kinetic energy of laser desorbed Na^+ ions [89] show that the velocity of these ions is near the thermal value.

Since the formation of quasi-molecular ions in IR-LDMS is always accompanied by intense emission of alkali ions, it has been proposed that $(M+c)^+$ ions most likely are formed as a result of attachment of an alkali ion to the intact neutral molecule [60], [75], [89]. This attachment may occur on the surface, in a thin semi-fluid layer near the surface [90] or in the gas-phase above the surface.

Evidence to support this theory comes primarily from the research carried out in the early 1980's by Kistemaker and coworkers, and Cotter and associates. van der Peyl et al. [91] have monitored the temperature dependence of the ion signals K^+ and $(M+K)^+$ from a sucrose sample which was heated by a cw laser. The desorption of neutral molecules, monitored by EI ionisation, was found to occur strongly at temperatures of about 400-500 K. As the surface temperature rose to above 800 K, first the K^+ ion and then the $(M+K)^+$ and fragment ions started to appear. A similar correlation was found for the case of pulsed CO_2 laser heating [92]. It is unlikely that $(M+K)^+$ ions are emitted from the hot surface, since they would have to survive at a temperature of above 800 K. Also, at temperatures insufficient for formation of K^+ ions, no quasi-molecular ions were observed. This suggests that the high surface temperature is required to form K^+ and not $(M+K)^+$. van der Peyl et al. [91] suggested that the quasi-molecular ions were formed in the gas-phase, or on colder sections of the surface when K^+ ions collided with it. They also proposed that the alkali metal ions were desorbed from the central hot part of the laser focal region, whilst the neutrals were emitted from cooler regions of the surface surrounding this central spot.

van der Peyl et al [91] also demonstrated that for sucrose similar mass spectra to those obtained by IR-LDMS alone could be obtained at significantly lower surface temperatures if K^+ ions were thermionically emitted from a separate sample probe. They observed that there was only a small temperature region, from about 460-475 K (melting point of sucrose ~ 460 K), where sucrose molecules desorbed with little or no fragmentation, but in sufficient quantities to

be detected. This again provides evidence in support of the proposed gas-phase complexation model of ion formation.

In separate experiments, Tabet and Cotter [93]- [97] employed a 40 ns pulsed CO_2 laser and a TOF mass analyser to study time-resolved ion formation. They showed that prompt ion emission (over a period of ~60 ns) was possible at the threshold for ion emission, but that these ions had excess kinetic energy. It is likely that these ions are produced by non-equilibrium excitation [98]. Increasing the laser power density resulted in emission of ions lasting for several microseconds. These "later" ions had lower energies than the "prompt" ions, and were characteristic of thermal emission. They also had reduced internal energies compared to their earlier counterparts, since mass spectra obtained several μs after the laser pulse exhibited reduced fragmentation and narrower peaks.

The generally-accepted model for IR laser desorption of organic species coated on a surface is that proposed by Kistemaker [88]. In this model, it is assumed that for a substrate having high thermal absorptivity, the presence of the thin organic layer does not influence the substrate temperature distribution. The laser energy is mainly absorbed by the substrate and then transferred to the organic layer. Although the heat flux in the organic layer is small relative to that in the substrate, it is sufficient to heat the sample to the peak substrate temperature. Although the laser power densities typically used in this type of experiment are similar to those employed in the LAMMA method (see later), the total energy per pulse is considerably higher. The time taken for the substrate to dissipate this energy is reflected in the observed timescales of ion and neutral desorption. The rate of desorption of ions (or neutrals) depends only on the provision of

sufficient energy to remove them from the surface:

$$dn^{(+)}/dt \propto C \exp(-E_d/kT),$$

where $n^{(+)}$ is the number of ions or neutrals in the gas phase, C is the surface concentration of species, E_d is the activation energy for desorption of an ion or neutral molecule, and T is the surface temperature. The activation energy for desorption of neutral molecules will generally be lower than that for ions, so neutrals will be emitted at lower surface temperatures and for longer times than ions [96]. This topic will be discussed further in chapter 6.

3.3.5 LDMS using UV radiation.

When the surface of an organic crystal is exposed to UV laser radiation, the range of physical processes that can occur is much wider than in the case of IR laser irradiation. The absorption of UV radiation primarily results in electronic excitation of the molecule, which in turn can lead to a number of processes, such as the formation of excitons, electrons and holes in the conduction band of crystals, and emission of electrons from the surface. As a result of non-radiative relaxation processes, the electron excitation energy is transferred to vibrational molecular energy, and molecular desorption occurs. The neutral molecules which leave the surface can also interact further with the UV radiation resulting in their excitation, fragmentation or ionisation. At a sufficiently high intensity of laser radiation, the situation becomes more complicated due to the possibility of non-linear processes in both the crystal and the gas-phase (see section 3.3.6).

At laser intensities of less than 10^6 Wcm^{-2}, organic crystals can absorb UV

radiation, leading to single-photon transitions in the molecules. The resultant heating is not large enough to produce phase transitions, but produces significant numbers of desorbed neutral molecules and ions.

In 1981, Schode et al. [99] obtained mass spectra from crystals of some nucleic acid bases and of anthracene using 20 ns pulses of KrF excimer radiation (λ = 248 nm) with intensities in the range 10^4-10^6 Wcm^{-2}. In all cases, the molecular ion was present as a major peak in the mass spectrum. Metal cation peaks, Na^+ and K^+, and cationised quasi-molecular ions were also observed for some of the nucleic acid bases.

In this early work, it was assumed that the role of sample heating, which is so important in IR-LDMS, was not important in the ion formation mechanism following UV laser irradiation. In the case of adenine [100], [101] irradiated by a UV laser, it was found that the increase in surface temperature did not exceed 100 K (T_{melt} ~ 360 ^{o} C) at the threshold of ion formation. The kinetic energy of the molecular ions was relatively high, which seemed to confirm that thermal processes were not significant. If, however, the adenine crystals were cooled [61], the ion signal dropped. This suggested that the efficiency of ion formation depended on the initial temperature of the crystals. In subsequent experiments, desorption of neutral molecules was observed along with the formation of molecular ions, with the neutrals heavily outnumbering the ions.

These facts suggested that the formation of ions from UV laser irradiation of aromatic crystals was a direct result of laser photoionisation of thermally desorbed molecules. The only fact which appeared to be inconsistent with this

model was the high kinetic energies of the ions formed. It was, however, shown that ions formed near the surface of the crystal could attain energies of several eV as a result of acceleration in the electric field due to the surface charge[61].

3.3.6 LDMS using microanalytical techniques (LAMMA/LIMA).

The technique of laser microanalytical mass spectrometry grew out of the need to study biological materials, such as tissue sections and cells, with high spatial resolution. As mentioned previously, the LAMMA (LAser Microprobe Mass Analyser) and LIMA (Laser Ionisation Mass Analyser) machines have been developed and successfully marketed.

In contrast to the other LDMS techniques, these laser microprobe mass spectrometers generally work in the so-called "transmission mode". In this configuration the sample, in the form of crystals or thin sections, is mounted on a thin foil. A UV laser beam is tightly focused($\sim$ 0.5 μm in diameter) on to the opposite side of the foil from the sample. The analysis of organic molecules generally requires that laser power densities of 10^6-10^{10} Wcm^{-2} be used, with a total pulse energy of only a few mJ. This is sufficient to create a hole in the foil, but apart from the region directly around this hole, there is little excess energy to be absorbed and subsequently dissipated by the substrate. The desorption of ions is therefore prompt, usually within the laser pulse, which provides a suitable start event for time-of-flight analysis. Both positive and negative ions are created in this process.

Initially, the "LAMMA method" was applied to elemental analysis of biological samples with high spatial resolution ($<$ 1 μm). These early mass spectra also

showed ions of organic origin; for example, in the LAMMA spectra of nicotinic acid, the quasi-molecular ions $(M+H)^+$ and $(M-H)^-$ dominated the spectra [102].

Due to the availability of commercial laser microprobes, the volume of mass spectrometric information generated with the LAMMA method exceeds that from any other LDMS method. Useful spectra have been generated with molecules containing polar groups and aromatic moieties. On the other hand, it has been found impossible to produce quasi-molecular ions from non-polar, non-aromatic molecules, such as unsaturated hydrocarbons, using this method.

For some classes of compounds, the LAMMA method generates odd-electron ions, similar to those observed in EI-MS. For example, polycyclic aromatics such as anthracene, phenanthrene, dibenzothiophene and dibenzofuran [103] yield abundant $M^{+\cdot}$ ions in the positive ion spectra. Radical ions are also generated for a number of compounds containing heteroatoms in addition to aromatic functions. As an example, the LAMMA mass spectrum of bis(dimethylamino) benzophenone gives $M^{+\cdot}$ ions, with some contribution from $(M+H)^+$. Aromatic amino acids also yield abundant odd-electron molecular cations [61]. In some cases, for example triphenylphosphine, molecular ions are only detected at low power densities, whilst protonated quasi-molecular ions $(M+H)^+$ dominate at higher power densities.

In general, two types of quasi-molecular ions are observed in LAMMA-type mass spectra, namely protonated ions $(M+H)^+$ and cationised ions $(M+c)^+$, where c is usually Na or K. In some cases, both types of ions are observed. The LAMMA spectrum of glycocholic acid shows peaks corresponding to $(M+H)^+$ and

$(M+Na)^+$ in approximately equal abundance [104]. In other cases, $(M+c)^+$ ions are the only quasi-molecular ions detected. For example, the mass spectrum of stachyose (a carbohydrate) shows no protonated molecular ions. However, cationised molecular ions are observed, along with cationised fragments, corresponding to detachment of one or more glycosidic units from the parent molecule.

A number of other classes of molecule have been studied by the LAMMA method, including organic acids [105], peptides [106], glycosides [78] and polymers [107]. The mass spectra of these compounds show a variety of different features, both in terms of the degree of fragmentation, and the relative abundances of molecular ions, protonated ions and cationised ions. These differences are probably due to the fact that several ion formation mechanisms are likely to be operative in the high intensity light field.

3.3.7 Ion formation mechanisms in LAMMA-type experiments.

At the high UV laser power densities employed in LAMMA type experiments, multiphoton absorption in organic crystals and in molecules present in the gas phase can occur. For organic molecules containing heteroatoms such as O and N, multiphoton absorption is very effective because all these molecules have a weak, but resonant, absorption at 266 nm (which is the most commonly used wavelength in this type of experiment). This absorption is likely to be very strong in aromatic molecules. Strong heating of the sample surface occurs, leading to phase transitions and evaporation of the sample. Photoionisation processes in the vapour phase above the sample give rise to a plasma. The plasma forms very

rapidly, and ion-molecule reactions can occur before the system has time to reach equilibrium. This means that simple thermodynamic relationships cannot be applied to the gas-phase processes.

Unlike the other two methods of LDMS, very few experiments have been carried out to investigate the mechanism of ion formation. Hercules and coworkers [104] suggest that four spatial regions exist where different mechanisms of ion formation are operative,

In the region of the sample directly irradiated by the laser beam, the temperature may reach 3000-6000 K. This is sufficient for direct ionisation of atoms and for emission of light molecular fragments. A region of high temperature gradient is set up adjacent to the hottest part of the sample. This is subjected to both the action of the shock wave generated by the laser, and of the collapsing plasma. Hercules et al. [104] suggest that heavier neutral fragments of molecules and their ions are emitted from this cooler part of the sample. The formation of heavy ions, including molecular and quasi-molecular ions, is thought to occur at the surface of the sample immediately adjacent to the laser beam, as well as in the gas phase over the impacted region. This gas-phase ion formation can be the result of ion-molecule reactions or by absorption of UV photons by desorbed neutral species. Evidence seems to suggest that both solid-state and gas-phase ionisation processes occur, although the relative importance of the two processes is still the topic of some debate.

The mechanism of ion formation in the laser microprobes is best studied by comparing the LAMMA mass spectra of model compounds with those obtained

by IR- and UV-LDMS.

Briefly, the mass spectra of carbohydrates obtained by the LAMMA and IR-LDMS methods are similar. This suggests that the same ionisation mechanism applies in both cases, namely cation attachment to the intact molecule in the gas-phase. In the case of sucrose [108], the actual appearance of the mass spectrum was found to depend on the size of the crystal under investigation. The quasi-molecular ion yield decreased dramatically as the crystal size was reduced, suggesting that the formation of these ions occurs in the peripheral regions rather than the region of direct UV laser irradiation. The importance of gas-phase reactions was confirmed by the observation of $(\text{sucrose} + \text{Li})^+$ ions in spite of using spatially separated sources of sucrose and Li^+.

The molecular ions of aromatic compounds are also observed, as is the case with UV-LDMS. These ions are therefore probably formed by the gas-phase two-photon ionisation of neutral molecules evaporating from the heated surface.

In the case of triphenylphosphine [61], the molecular ion dominates the spectrum at low laser intensities, but is replaced by the protonated quasi-molecular ion at higher intensity. This suggests that at sufficiently high radiation levels, strong evaporation of the sample occurs, leading to a dense plasma being formed in which ion-molecule reactions proceed efficiently.

Until recently, the wavelength of the incident radiation was thought to be of minor significance in the desorption process. However, Hillenkamp and coworkers have shown that resonant absorption of UV laser radiation by amino acids results in soft ionisation [109]. This concept of resonant absorption by the

sample has been extended to that of a matrix-assisted desorption, where quasi-molecular ions of non-absorbing materials have been obtained by dissolving them in absorbing solutes [110]. The application of this technique to biological molecules will be discussed in chapter 7.

3.3.8 Desorption of neutrals in LDMS experiments.

Several investigators have noticed that neutral species are also desorbed from a surface by laser irradiation, and may be detected by conventional mass spectroscopic means [70], [93], [94], [111], [112]. In the original LDMS experiment carried out by Vastola and Pirone [70], they observed that neutral molecules were the major product of the desorption process, and that neutral emission occurred over a longer period than desorption of ions, as predicted by the model discussed in section 3.3.5 above.

The ratio of ions to neutrals in a laser-induced desorption experiment is determined by the rapid jump in surface temperature, and is given to a first approximation by the Langmuir-Saha equation [113],

$$n^+/n^0 = \exp\{(W-I)/kT\},$$

where W is the work function of the substrate, I is the ionisation potential of the various sample molecules and T is the temperature. This equation, which describes a gas phase thermal equilibrium process between ions and neutrals, has been applied with some success, even in cases where non-equilibrium processes dominate. The surface temperature depends on the laser power density; consequently, the ratio of ions to neutrals varies with laser power density [79].

At power densities below 10^8 Wcm^{-2}, the ratio of ions to neutrals is approximately 10^{-5}, whilst with power densities of 10^9-10^{10} Wcm^{-2}, this ratio has been reported to be as high as 0.01-0.1. Cotter [93], [94] reported that with a 40 ns, 700 mJ CO_2 laser pulse and power densities in the former range, ions were emitted from the surface for about 1 µs, whilst neutrals desorbed over a period of 100 µs. The ratio of ions to neutrals was heavily biased in favour of the neutrals. Using EI to detect the neutrals, Van Breemen et al [94] showed that the ion signal generated from desorbed neutral tetraalkylammonium salts was 6 to 20 times greater than that from the laser desorbed ions alone. In this case, since only a small fraction of the neutral species was actually ionised by the electron beam, it is likely that the neutral molecules formed the vast majority of the desorption product.

3.3.9 Mechanism of molecular desorption in LDMS.

There is much experimental evidence that rapid heating of a surface results in desorption of molecules adsorbed to that surface, and that if the heating rate is sufficiently rapid, the molecules will desorb internally "lukewarm" [114]- [116]. The mechanisms of intact neutral desorption are not fully understood at this time. However, Zare and Levine [117] have proposed a mechanism which attempts to explain this phenomenon.

A molecule physisorbed to a surface is bound by a weak, van der Waals type bond. This bond therefore has a low vibrational frequency, similar to those of the surface phonons of the substrate. On the other hand, the chemical bonds in the physisorbed species will have much higher frequencies. If the substrate acts as

a chromophore which absorbs the incident laser radiation, it is therefore to be expected that the physisorption bond will be readily pumped. However, a "bottleneck" may occur in the flow of energy from the van der Waals bond to chemical bonds in the adsorbed species due to the frequency mismatch between these bonds. This restricts the flow of energy into the adsorbate, so that relatively cold molecules can desorb from the surface. Thus it is possible to break the surface-adsorbate bond preferentially, even if it is stronger than some bonds in the free molecule.

The criterion derived by Zare and Levine for lukewarm desorption of molecules from a surface is

$$\tau\nu\exp(-\xi) < 1,$$

where τ is the time taken for the hot surface to transfer energy to the physisorption bond in excess of its desorption energy, ν is the frequency of the physisorption bond, and ξ is the adiabaticity parameter, which represents the ability of the adsorbate molecule to resist changes in vibrational excitation. ξ is related to the ratio of the vibrational frequency of a chemical bond to that of the van der Waals bond. Experimental evidence from the unimolecular decomposition of van der Waals adducts [118]- [119] has shown that values of $\xi > 10$ are not uncommon. With values of $\xi > 10$, heating rates as high as 10^{12} Ks^{-1} can be used to desorb even strongly bound molecules (bond dissociation energy ~ 1000 cm^{-1}) with reasonably small internal energies.

Seydel and Lindner [120] have proposed an alternative mechanism whereby the

initial desorption of material from the surface sends a shock wave through the solid. This causes more material to desorb into the gas phase. This mechanism is likely to be strongly enhanced in cases where the surface-to-adsorbate bond is weak and especially in thick, absorbing samples where the majority of bonding is intermolecular.

3.3.10 Post-ionisation of desorbed neutral molecules.

One of the primary aims of mass spectrometry is to generate data which is of some analytical use, with high sensitivity. It would therefore appear to be more efficient to ionise and detect the desorbed neutrals by some means, rather than to observe the nascent ions directly. Multiphoton ionisation, especially if coupled with supersonic molecular beam techniques, can be employed to achieve ionisation with a high degree of selectivity, as discussed in Section 3.2.

Since 1985, four groups have developed the technique of laser photoionisation of laser desorbed neutrals combined with TOF mass spectrometry [62]- [64], [121]. Although some experimental details differ, the same basic principles are common to the work of all four groups. Pulsed laser desorption is carried out using either a CO_2 laser or the second harmonic output from a Nd^{3+}:YAG laser. The desorbed material is carried into the ion source of a time-of-flight mass spectrometer, where UV radiation, either from a tunable dye laser or the fourth harmonic of a Nd^{3+}:YAG laser, is used for photoionisation. All but one of the four groups employ supersonic molecular beam entrainment and cooling of the desorbed neutrals. A commercial instrument has been developed by Bruker in conjunction with Schlag and coworkers [47], [122], [123].

Tembreull and Lubman [62] have employed three different laser systems for desorption purposes, namely a pulsed CO_2 laser (λ = 10.6 μm), the second harmonic from a Nd^{3+}:YAG laser (λ = 532 nm) and a pulsed KrF excimer laser (λ = 248 nm). The latter was used for single-colour desorption/ionisation experiments as discussed above, whilst the fourth harmonic from a Nd^{3+}:YAG laser (λ = 266 nm) was employed for ionisation with either of the other two desorption lasers. Lubman's group have obtained mass spectra for a number of polynuclear aromatic molecules, and found similar results using either the infrared or the Nd^{3+}:YAG second harmonic laser, with the exception that the signals obtained using the CO_2 laser were at least an order of magnitude stronger than those obtained using the Nd^{3+}:YAG laser. This was attributed to the fact that less fragmentation is generally caused by the infrared rather than the green light. Aromatic molecules have strong 2-photon absorptions at 532 nm, and in strong laser light fields, ionisation or fragmentation of these molecules can occur. Although multiphoton ionisation and desorption is possible at 10.6 μm, it is much less efficient, at similar power densities, than with the more energetic green photons. The KrF laser proved unsuitable for high melting point molecules such as tetracene and chrysene, since the power needed to achieve efficient desorption was sufficient to strongly fragment the molecular ions generated by MPI. It is therefore better to use an infrared source for desorption, since this reduces the possibility of unwanted photochemical processes occurring.

A variety of sample forms have been employed in previous studies. Initially, Lubman and coworkers [62] and Grotemeyer et al. [64] employed rather thick films of material dissolved in a suitable solvent. Later, Lubman's group

discovered that the use of a glycerol matrix helped to form thin, even sample layers from which the shot-to-shot stability was better than ± 5% [124]. Meanwhile, Zare's group [125] have employed very thin films of sample material, along with substrate materials which absorb the desorption wavelength, as suggested by Zare and Levine's proposed desorption model. Levy's group [121], [126], [127] have tried a variety of sample preparations including pellets doped with laser dye (the latter added to strongly absorb the 532 nm laser radiation used for desorption), before settling on thin films deposited from methanol. These films were about 10 μm thick, corresponding to several thousand monolayers. The applicability of Zare and Levine's model to this type of system is questionable, especially if the sample itself absorbs the incoming radiation to any great extent. However, the observed behaviour, namely that these films desorb equally well with or without addition of a strongly-absorbing chromophore (the dye) suggests that an effect which transfers energy from the hot substrate to the bulk sample is operative.

The importance of substrate absorption in the case of thin films has been demonstrated [125]. The molecular ion signal from protoporphyrin IX dimethyl ester desorbed by a CO_2 laser from a glass surface was found to be five orders of magnitude larger than that from a NaCl surface. The latter is transparent at λ = 10.6 μm. No equivalent experiment has been reported for thick films.

The use of supersonic jet-cooling in tandem with laser mass spectrometry has three advantages. The entrainment of the lukewarm desorbed molecules into an expanding supersonic molecular beam helps to internally and translationally cool them. This not only reduces the possibility of fragmentation of the desorbed

molecules between the desorption probe and the ion source of the mass spectrometer, but allows for the possibility of both selective desorption and, indeed, jet-cooled gas-phase spectroscopy [121], [124], [126]- [130]. Translational cooling of the molecules also reduces the spread in their kinetic energies, and in turn leads to a reduction in the kinetic energy distribution of the ions produced by MPI. This leads to improved resolution in time-of-flight mass spectrometry [62], [131].

3.4 Concluding Remarks.

Resonant laser molecular multiphoton ionisation has several unique properties for analytical applications. These include

1. Selectivity in ionisation, especially when coupled with jet-cooling techniques.
2. High efficiency, and therefore high sensitivity, in ionisation.
3. Controllable fragmentation, without extreme loss in sensitivity.

The use of IR laser radiation at power densities less than $\sim 10^8$ Wcm^{-2} has proved to be an efficient means of desorbing and vaporising involatile and labile molecules from a sample probe. Immediate entrainment of these molecules into a molecular beam minimises fragmentation in this desorption process, resulting in a relatively cold beam of intact neutral molecules which can then be interrogated by MPI techniques.

This tandem approach, in which both the desorption and ionisation steps can be independently optimised, promises to be an extremely useful analytical method,

especially when combined with mass spectrometry. Although perhaps not as widely-applicable as IR-LDMS or LAMMA methods, LD-MPI MS looks likely to be able to solve many problems, both analytical and fundamental, which have so far proved intractable with these other methods.

References

[1] R. W. Ditchburn, F. L. Arnot, Proc. Roy. Soc. London Series A, **A123**, 516, (1929)

[2] F. P. Lossing, I. Tanaka, J. Chem. Phys., **25**, 1031, (1956)

[3] H. Hurzeler, M. G. Inghram, J. D. Morrison, J. Chem. Phys., **27**, 313, (1957)

[4] H. Hurzeler, M. G. Inghram, J. D. Morrison, J. Chem. Phys., **28**, 76, (1958)

[5] N. K. Bereshetskaya, G. S. Voronov, G. A. Delone, N. B. Delone, G. K. Piskova, Sov. Phys. JETP (Engl. Transl.), **31**, 403, (1970)

[6] S. L. Chin, Phys. Rev. A, **4**, 992, (1971)

[7] R. V. Ambartsumayn, V. S. Letokhov, Appl. Opt., **11**, 354, (1972)

[8] U. Boesl, H. J. Neusser, E. W. Schlag, Z. Naturforsch. A, **33A**, 1546, (1978)

[9] L. Zandee, R. B. Bernstein, D. A. Lichtin, J. Chem. Phys., **69**, 3427, (1978)

[10] G. J. Fisanick, T. S. Eichelberger IV, B. A. Heath, M. B. Robin, J. Chem. Phys., **72**, 5571, (1980)

[11] D. M. Lubman, R. Naaman, R. N. Zare, J. Chem. Phys., **72**, 3034, (1980)

[12] A. Gedanken, M. B. Robin, N. A. Kuebler, J. Phys. Chem., **86**, 4096, (1982)

[13] M. A. Duncan, T. G. Dietz, R. E. Smalley, Chem. Phys., **44**, 415, (1979)

[14] J. H. Callomon, J. E. Perkin, R. Lopez-Delgardo, Chem. Phys. Letters, **13**, 125, (1972)

[15] U. Boesl, H. J. Neusser, E. W. Schlag, J. Chem. Phys., **72**, 4327, (1980)

[16] R. S. Pandolfi, D. A. Gobeli, M. A. El-Sayed, J. Phys. Chem., **85**, 1779, (1981)

[17] J. J. Yang, D. A. Gobeli, R. S. Pandolfi, M. A. El-Sayed, J. Phys. Chem., **87**, 2255, (1983)

[18] S. R. Long, J. T. Meek, P. J. Harrington, J. P. Reilly, J. Chem. Phys., **78**, 3341, (1983)

[19] B. D. Koplitz, J. K. McVey, J. Chem. Phys., **81**, 4963, (1984)

[20] T. G. Blease, *Ph. D. Thesis*, University of Edinburgh, 1985.

[21] J. Grotemeyer, E. W. Schlag, Angew. Chem. Int. Ed. Engl., **27**, 447, (1988)

[22] J. Silberstein, R. D. Levine, Chem. Phys. Letters, **74**, 6, (1981)

[23] J. Silberstein, R. D. Levine, J. Chem. Phys., **75**, 5735, (1981)

[24] F. Rebentrost, K. L. Kompa, A. Ben-Shaul, Chem. Phys. Letters, **77**, 394, (1981)

[25] F. Rebentrost, A. Ben-Shaul, J. Chem. Phys., **74**, 3255, (1981)

[26] W. Dietz, H. J. Neusser, U. Boesl, E. W. Schlag, S. H. Lin, Chem. Phys., **66**, 105, (1982)

[27] J. Grotemeyer, U. Boesl, K. Walter, E. W. Schlag, Org. Mass Spectrom., **21**, 645, (1986)

[28] U. Boesl, H. J. Neusser, E. W. Schlag, Chem. Phys., **55**, 193, (1981)

[29] D. H. Parker, *Ch. 4 in 'Ultrasensitive Laser Spectroscopy'*, Academic Press (New York), 1983.

[30] H. M. Rosenstock, Adv. Mass Spectrom., 4, 523, (1968)
[31] P. Hering, A. G. M. Maaswinkel, K. L. Kompa, Chem. Phys. Letters, **83**, 222, (1981)
[32] U. Boesl, H. J. Neusser, E. W. Schlag, Chem. Phys. Letters, **87**, 1, (1982)
[33] C. T. Rettner, J. H. Brophy, Opt. Letters, 4, 337, (1979)
[34] U. Boesl, H. J. Neusser, E. W. Schlag, Chem. Phys., **55**, 193, (1981)
[35] C. T. Rettner, J. H. Brophy, Chem. Phys., **56**, 53, (1981)
[36] J. L. Franklin, *Ionisation potentials, appearance potentials, and heats of formation of gaseous positive ions*, National Bureau of Standards (Washington), 1969.
[37] H. Kühlewind, H. J. Neusser, E. W. Schlag, J. Chem. Phys., **82**, 5452, (1985)
[38] T. R. Covey, E. D. Lee, A. P. Bruins, J. D. Henion, Anal. Chem., **58**, 1451A, (1986)
[39] R. Tembreull, D. M. Lubman, Anal. Chem., **56**, 1962, (1984)
[40] C. H. Sin, R. Tembreull, D. M. Lubman, Anal. Chem., **56**, 2776, (1984)
[41] D. M. Lubman, R. Tembreull, C. H. Sin, Anal. Chem., **57**, 1084, (1985)
[42] C. Klimcak, J. E. Wessel, Anal. Chem., **52**, 1233, (1980)
[43] G. Rhodes, R. B. Opsal, J. T. Meek, J. P. Reilly, Anal. Chem., **55**, 280, (1982)
[44] D. H. Parker, R. B. Bernstein, J. Phys. Chem., **86**, 60, (1982)
[45] L. J. Moore, J. E. Hurst, E. H. Taylor, D. W. Beekman, M. T. Spaar, Int. Phys. Conf. Ser., **84**, 239, (1986)
[46] S. Leutwyler, U. Even, Chem. Phys. Letters, **81**, 578, (1981)
[47] U. Boesl, J. Grotemeyer, K. Walter, E. W. Schlag, Anal. Instrum., **16**, 151, (1987)
[48] H. Zacharias, H. Rottke, K. H. Welge, Appl. Phys., **24**, 23, (1981)
[49] J. C. Miller, Anal. Chem., **58**, 1702, (1986)
[50] D. M. Lubman, Anal. Chem., **59**, 31A, (1987)
[51] J. H. Beynon, *Mass Spectrometry and Its Application to Organic Chemistry*, Elsevier (Amsterdam), 1960.
[52] A. M. Lawson, R. N. Stillwell, M. M. Tacker, K. Tsybogama, J. A. McCloskey, J. Am. Chem. Soc., **93**, 1014, (1971)
[53] D. J. Surman, J. C. Vickerman, J. Chem. Soc. Chem. Comm., 324, (1981)
[54] M. Barber, R. S. Bordoli, R. D. Sedgwick, A. N. Tyler, J. Chem. Soc. Chem. Comm., 325, (1981)
[55] A. Benninghoven, W. K. Sichtermann, Anal. Chem., **50**, 1180, (1978)
[56] R. D. Macfarlane, D. F. Torgerson, Science, **191**, 920, (1976)
[57] H. D. Beckey, *Principles of Field Ionisation and Field Desorption Mass Spectrometry*, Pergamon(Oxford), 1977.
[58] R. P. Lattimer, H.-R. Schulten, Anal. Chem., **61**, 1201A, (1989)
[59] D. E. C. Rogers, P. J. Derrick, Org. Mass Spectrom., **19**, 490, (1984)
[60] M. A. Posthumus, P. G. Kistemaker, H. L. C. Meuzelaar, M. C. Ten Noever de Brauw, Anal. Chem., **50**, 986, (1978)
[61] A. N. Shibanov, *Ch. 8 in 'Laser Analytical Spectrochemistry'*, Adam Hilger (Bristol), 1985.
[62] R. Tembreull, D. M. Lubman, Anal. Chem., **58**, 1299, (1986)
[63] F. Engelke, J. H. Hahn, W. Henke, R. N. Zare, Anal. Chem., **59**, 909, (1987)

[64] J. Grotemeyer, U. Boesl, K. Walter, E. W. Schlag, J. Am. Chem. Soc., **108**, 4233, (1986)
[65] J. Berkowitz. W. A. Chupka. J. Chem. Phys., **40**, 2735, (1964)
[66] N. E. Vanderborgh, C. E. R. Jones. Anal. Chem., **55**, 527, (1983)
[67] K. A. Lincoln, Anal. Chem., **37**, 541, (1965)
[68] N. C. Fenner, N. R. Daly, J. Mater. Sci., **3**, 259, (1968)
[69] N. C. Fenner, N. R. Daly, Rev. Sci. Instrum., **37**, 1068, (1966)
[70] F. J. Vastola, A. J. Pirone, Adv. Mass Spectrom., **4**, 107, (1968)
[71] F. J. Vastola, R. O. Mumma, A. J. Pirone, Org. Mass Spectrom., **3**, 101, (1970)
[72] R. O. Mumma, F. J. Vastola, Org. Mass Spectrom., **6**, 1373, (1972)
[73] F. Heresch, E. R. Schmid, J. F. K. Huber, Anal. Chem., **52**, 1803, (1980)
[74] E. D. Hardin, M. L. Vestal, Anal. Chem., **53**, 1492, (1981)
[75] R. Stoll, F. W. Röllgen, Org. Mass Spectrom., **14**, 642, (1979)
[76] R. J. Cotter, Anal. Chem., **52**, 1767, (1980)
[77] S. W. Graham, P. Dowd, D. M. Hercules, Anal. Chem., **54**, 649, (1982)
[78] U. Seydel, B. Lindner, *in 'Ion Formation from Organic Solids II'*, SpringerVerlag (Berlin), 1983.
[79] R. J. Conzemius, J. M. Capellen, Int. J. Mass Spectrom. Ion Phys., **34**, 197, (1980)
[80] E. Denoyer, R. Van Gieken, F. Adams, D. F. S. Nautsch, Anal. Chem., **54**, 26A, (1982)
[81] T. Dingle, B. W. Griffiths, J. C. Ruckman, Vacuum, **31**, 571, (1981)
[82] P. G. Kistemaker, M. M. Lens, G. J. Q. van der Peyl, A. J. H. Boerboom, Adv. Mass Spectrom., **8A**, 928, (1980)
[83] U. Giessmann, F. W. Röllgen, Org. Mass Spectrom., **11**, 1094, (1976)
[84] R. J. Cotter, A. L. Yergey, Anal. Chem., **53**, 1306, (1981)
[85] R. J. Cotter, C. Fenselau, Biomed. Mass Spectrom., **6**, 287, (1979)
[86] A. J. Dempster, J. Phys. Rev., **11**, 316, (1918)
[87] J. F. Ready, *Effects of High Power Laser Radiation*, Academic Press (New York), 1981.
[88] G. J. Q. van der Peyl, J. Haverkamp, P. G. Kistemaker, Int. J. Mass spectrom. Ion Phys., **42**, 125, (1982)
[89] G. J. Q. van der Peyl, W. J. Van der Zande, K. Bederski, A. J. H. Boerboom, P. J. Kistemaker, Int. J. Mass Spectrom. Ion Phys., **47**, 7, (1983)
[90] J. F. Holland, B. Soltmann, C. C. Sweeleey, Biomed. Mass Spectrom., **3**, 340, (1976)
[91] G. J. Q. van der Peyl, K. Isa, J. Haverkamp, P. G. Kistemaker, Int. J. Mass Spectrom. Ion Phys., **47**, 11, (1983)
[92] R. Stoll, F. W. Röllgen, Z. Naturforsch., **37A**, 9, (1982)
[93] R. J. Cotter, Anal. Chem., **52**, 1767, (1980)
[94] R. B. Van Breeman, M. Snow, R. J. Cotter, Int. J. Mass Spectrom. Ion Phys., **49**, 35, (1983)
[95] R. J. Cotter, J.-C. Tabet, Int. J. Mass Spectrom. Ion Phys., **53**, 151, (1983)
[96] J.-C. Tabet, R. J. Cotter, Int. J. Mass Spectrom. Ion Proc., **54**, 151, (1983)
[97] J.-C. Tabet, R. J. Cotter, Anal. Chem., **56**, 1662, (1984)
[98] F. Hillenkamp, Int. J. Mass Spectrom. Ion Phys., **45**, 305, (1983)
[99] U. Schode, R. Stoll, F. W. Röllgen, Org. Mass Spectrom., **16**, 441, (1981)

[100] V. S. Antonov, V. S. Letokhov, A. N. Shibanov, Appl. Phys., **25**, 71, (1981)
[101] V. S. Antonov, V. S. Letokhov, A. N. Shibanov, Appl. Phys., **28B**, 245, (1982)
[102] R. Kaufmann, F. Hillenkamp, R. Wechsung, H. J. Heinen, M. Schurmann , Proc. Scanning Electron Microsc. Symp., **29**, 279, (1979)
[103] H. J. Heinen, Int. J. Mass Spectrom. Ion Phys., **38**, 309, (1981)
[104] D. M. Hercules, R. J. Day, K. Balasanmugam, T. A. Dang, C. P. Li, Anal. Chem., **54**, 280A, (1982)
[105] H. J. Heinen, S. Meier, H. Vogt, R. Wechsung, Adv. Mass Spectrom., **8A**, 942, (1980)
[106] K. Kupka, F. Hillenkamp, C. Schiller, Adv. Mass Spectrom., **8A**, 935, (1980)
[107] J. A. Gardella, D. M. Hercules, H. J. Heinen, J. Spectrosc. Lett., **13**, 347, (1980)
[108] P. Wieser, R. Wurster, *in 'Ion Formation from Organic Solids II'*, Springer-Verlag (Berlin), 1983.
[109] M. Karas, D. Bachmann, F. Hillenkamp, Anal. Chem, **57**, 2935, (1985)
[110] M. Karas, D. Bachmann, F. Hillenkamp, *Proceedings of the Tenth International Mass Spectrometry Conference*, Wiley, 1986.
[111] D. Bombick, J. D. Pinkston, J. Allison, Anal. Chem., **56**, 396, (1984)
[112] G. Schmelzeisen-Redeker, U. Giessmann, F. W. Röllgen, Org. Mass Spectrom., **20**, 305, (1985)
[113] I. Langmuir, K. H. Kingdon, Proc. Roy. Soc. London (Series A), **61**, 107, (1925)
[114] D. Burgess Jr., R. Viswanathan, I. Hussla, P. C. Stair, E. Weitz, J. Chem. Phys., **79**, 5200, (1983)
[115] C. J. S. M. Simpson, J. P. Hardy, Chem. Phys. Letters, **130**, 175, (1986)
[116] G. Wedler, H. Ruhmann, Surf. Sci., **121**, 464, (1982)
[117] R. N. Zare, R. D. Levine, Chem. Phys. Letters, **136**, 593, (1987)
[118] R. E. Smalley, D. H. Levy, L. Wharton, J. Chem. Phys., **64**, 3266, (1976)
[119] R. E. Smalley, L. Wharton, D. H. Levy, J. Chem. Phys., **66**, 2750, (1977)
[120] B. Lindner, U. Seydel, Anal. Chem., **57**, 895, (1985)
[121] J. R. Cable, M. J. Tubergen, D. H. Levy, J. Am. Chem. Soc., **109**, 6198, (1987)
[122] R. Frey, G. Weiss, H. Kaminski, E. W. Schlag, Z. Naturforsch., **40A**, 1349, (1985)
[123] K. Walter, U. Boesl, E. W. Schlag, Int. J. Mass Spectrom. Ion Proc., **71**, 309, (1986)
[124] L. Li, D. M. Lubman, Appl. Spectrosc., **42**, 418, (1988)
[125] R. N. Zare, J. H. Hahn, R. Zenobi, Bull. Chem. Soc. Jpn., **61**, 87, (1988)
[126] J. R. Cable, M. J. Tubergen, D. H. Levy, Faraday Disc. Chem. Soc., **86**, 143, (1988)
[127] J. R. Cable, M. J. Tubergen, D. H. Levy, J. Am. Chem. Soc., **110**, 7349, (1988)
[128] R. Tembreull, D. M. Lubman, Appl. Spectrosc., **41**, 431, (1987)
[129] L. Li, D. M. Lubman, Appl. Spectrosc., **43**, 543, (1989)
[130] L. Li, D. M. Lubman, Anal. Chem., **60**, 2591, (1988)
[131] R. B. Opsal, K. G. Owens, J. P. Reilly, Anal. Chem., **57**, 1884, (1985)

Chapter 4
Laser desorption MPI mass spectrometry.

4.1 Introduction

In order to carry out the type of desorption-ionisation experiment described in the previous chapter, suitable equipment had to be developed. It was not feasible to incorporate the vacuum system described in chapter 2 into a mass spectrometer, so a new machine was designed. The new vacuum system was based on a modular, differentially-pumped time-of-flight mass spectrometer (TOFMS) already operational at the University of Edinburgh [1]. Experimental control and data acquisition was provided using an integrated system of computer-driven instruments, which had already been developed for this earlier TOFMS.

The mass spectrometer, shown schematically in figures 4.1 and 4.2, was designed to have interchangeable linear and reflecting-geometry (reflectron) TOF [2] configurations. In either case, the experimental details are similar. Neutral molecules were desorbed from a probe in the source chamber (SC) and were transported by a molecular beam into the ionisation chamber (IC), where ions were created by either resonant or non-resonant laser photoionisation. Depending on the geometry used, these ions then traversed a linear flight tube mounted on the top flange of the IC, or passed into the reflectron chamber (RC) before detection by a microchannel plate (MCP) detector.

Figure 4.1. Plan View of the Mass Spectrometer.

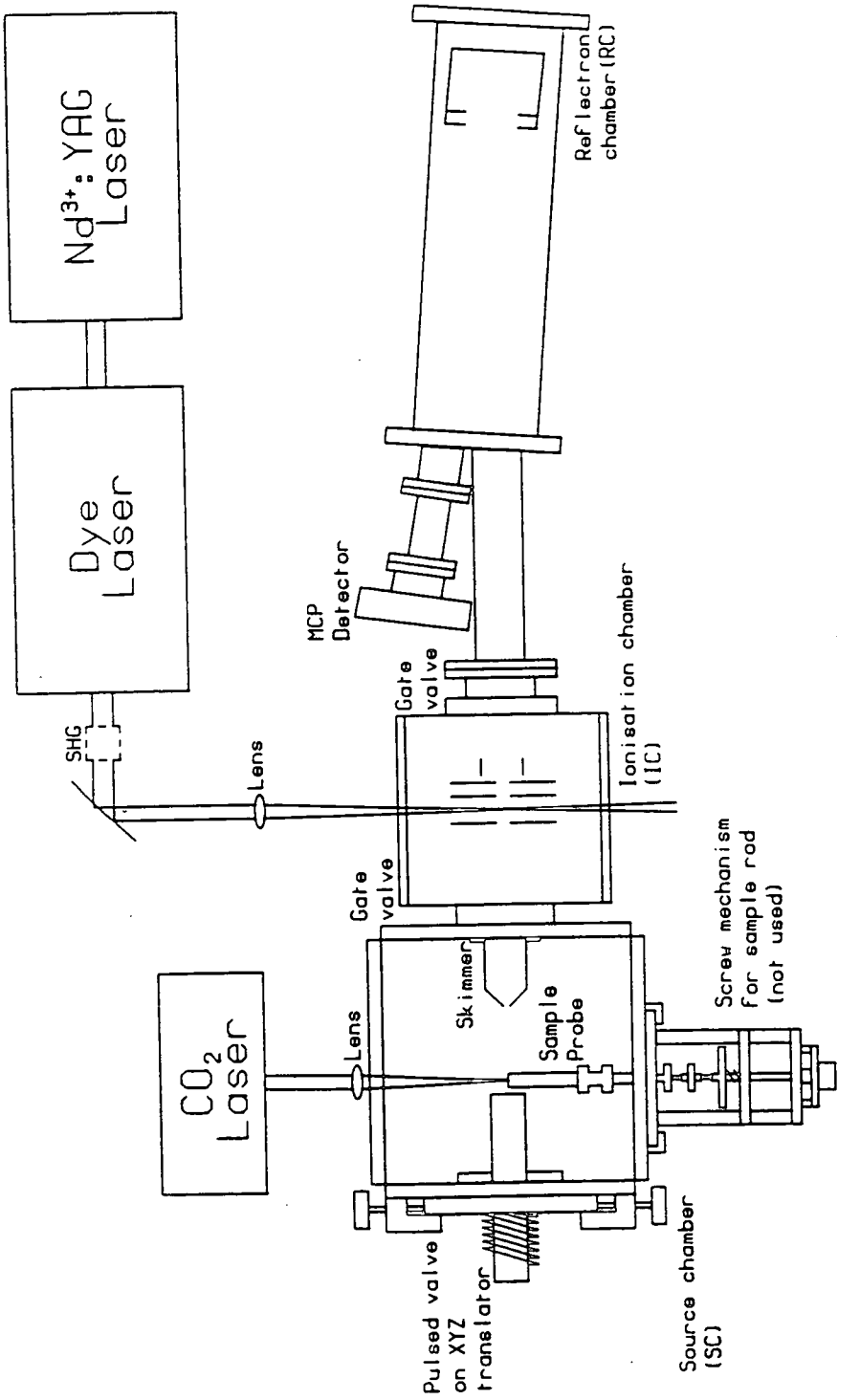

Figure 4.2. Elevation View of the Mass Spectrometer.

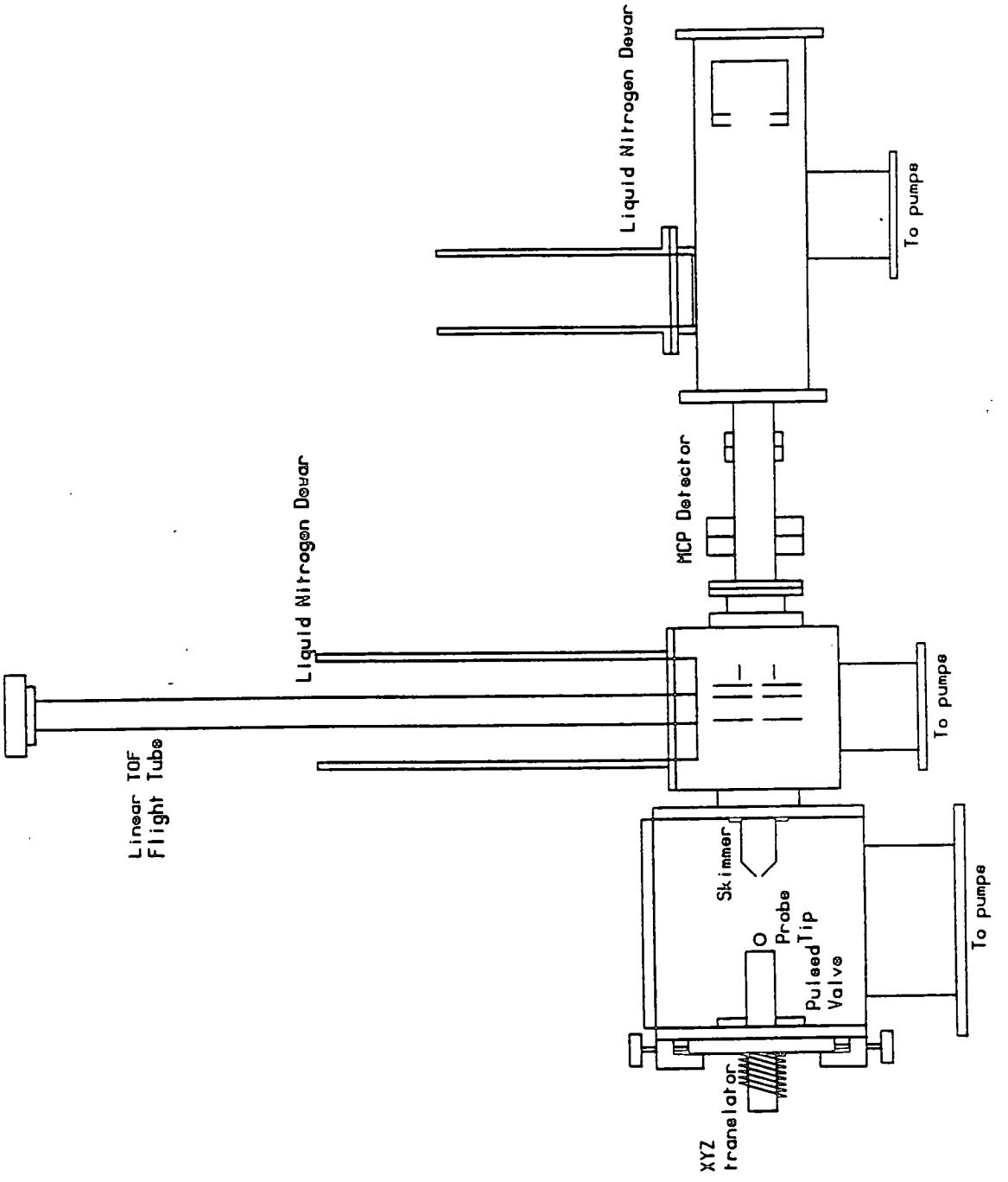

The following sections describe in detail the vacuum system, the lasers used and the data acquisition and experimental control modules. Finally, a brief description of the three experimental modes of operation is given.

4.2 Mass Spectrometer Vacuum System.

The mass spectrometer vacuum system, with the exception of the removable aluminium side flanges on the SC, was constructed from 304 stainless steel. Since UHV conditions were deemed unnecessary, all vacuum seals on the instrument were achieved using Viton O-rings. As shown in figure 4.1, the spectrometer basically consisted of three vacuum chambers separated from each other by manually-operated gate valves (VAT Series 8 and 11). Each chamber was evacuated by an independent rotary backed oil diffusion pump. In addition, both the SC and the RC could be isolated from these pumps by means of gate valves.

4.2.1 Molecular Beam Source Chamber (SC).

The molecular beam source chamber (SC) took the form of a stainless steel cube with external dimension 14.5 in., which had a 6.3 in. long stand-off to which the pump was attached. The internal volume of the chamber was therefore 44.9 litres. This chamber, which housed the pulsed molecular beam valve, sample probe and molecular beam skimmer, was pumped by a 10 in. oil diffusion pump (CVC PMC-10, Convoil 20 pump fluid) equipped with a half-chevron water-cooled baffle. The unbaffled pumping speed of 5250 ls^{-1} (for air up to 10^{-3} mbar) was reduced to approximately 2600 ls^{-1} by the baffle. In order to keep the background pressure in this chamber as low as possible, thereby preventing

disruption of the molecular beam, the diffusion pump had to be capable of handling large gas throughputs. To this end, it was backed by a mechanical booster/ rotary pump combination (Edwards EH250/ E2M40) capable of pumping 8.5 $mbarls^{-1}$ at a typical foreline pressure of 0.1 mbar. The chamber pressure was monitored by an Edwards CP25EK Penning gauge head attached to an Edwards 505 gauge readout. The base pressure in the chamber with the molecular beam valve off was typically 2×10^{-6} mbar. This rose to 2×10^{-4} mbar under normal operating conditions of 3 atmospheres of helium at a repetition rate of 6 Hz.

As mentioned previously, the SC could be isolated from the diffusion pump by a manually-operated gate valve (Vacuum Research Company LP series), which was mounted directly above the baffle. In addition, the diffusion pump could be isolated from the backing pump by means of a pneumatically-operated gate valve (Airco Temescal 5230). This was of particular significance for rapid sample turnaround. Once the chamber had been isolated and vented to atmospheric pressure via an air admittance valve (Edwards AV10K), the diffusion pump could be valved off completely. This allowed the chamber to be evacuated by the rotary pump via an independent roughing line, without having to wait for the diffusion pump fluid to cool down.

In order to allow the infrared desorption laser beam into the SC, a 50 mm diameter NaCl window was mounted on the side flange of the chamber. A second window, of Spectrosil B, was located on the top flange of the chamber, to aid in alignment of the desorption laser beam with the sample rod. Both windows were held in place by PTFE clamps and sealed to the flanges using Viton O-rings.

4.2.2 Molecular beam valve.

The molecular beam valve was mounted on an XYZ translator. This was essential for alignment of the molecular beam with respect to the skimmer aperture, which defined the axis of the machine. Two types of commercial pulsed molecular beam valve were employed for the work presented in chapters 5 and 6: a Newport Research Corporation BV100 and a General Valve Corporation Series 9 valve. Both were capable of delivering higher gas loads than the fuel injector used previously, and were considerably more reliable. A further advantage was the ability to control both the pulse length and intensity with relative ease.

The BV100 valve was of the double solenoid type with a soft iron actuator [3], [4]. When the valve was shut, current flowed continuously through the "close" coil of the solenoid, holding the viton tip seal of the actuator against the 500 μm diameter orifice. Upon receipt of a trigger pulse, however, this current was dropped to zero and current was supplied to the "open" coil instead, which pulled the actuator away from the seal. This allowed gas to flow through the orifice. Altering the duration of the open current pulse allowed the stroke length of the actuator, and hence the intensity of the gas pulse produced, to be varied. In order to seal the valve, a large current pulse was supplied to the close coil. By delaying this close pulse relative to the open pulse, a variety of pulse lengths could be achieved. Figure 4.3 shows a typical pulse of He from this valve. The "time scan" method was employed to obtain this data (see section 4.6.2 later). This pulse profile was obtained with a nominal 900 μs pulse duration setting. Although the valve should have been capable of producing 100 μs pulses, in practice, the valve sealing became unreliable at such low pulse durations.

The General Valve Corporation Series 9 valve consisted of an iron actuator, with a Teflon plunger attached, which was seated against a 1 mm diameter orifice. Sealing was achieved through the action of a spring. The valve was opened by application of a current pulse to a single solenoid, which had the effect of pulling back the actuator. The pulse duration was determined by the length of time the current was applied to the actuator; no control was possible over the beam intensity. In principle, the valve could deliver pulses as short as 10 μs; in practice, however, it was found to work reliably with a lower limit of about 200 μs. Figure 4.4 shows the analogous pulse profile to that in figure 4.3, obtained with a 900 μs pulse duration setting.

4.2.3 Sample probe.

Introduction of liquid samples into the molecular beam was achieved in a manner similar to that outlined in chapter 2. A few ml of the sample were dispersed on to glass wool contained in a stainless steel reservoir. This was mounted directly in the gas feed line to the nozzle. For solid samples, with low vapour pressures at room temperature, the method of infrared laser desorption into the expanding molecular beam was employed. In general, about 1-10 mg of sample was dissolved in a similar amount of glycerol. A few mg of a dispersion of colloidal graphite in methanol were then added, and about 2 mg of the mixture added to the flat end of a 6 mm diameter stainless steel rod. The glycerol matrix caused the sample to form quite a thick (hundreds of monolayers) layer on the probe. The graphite was initially added to aid optical alignment of the desorption laser, but since it acted as a very strong infrared absorber it also aided in the desorption process. A similar technique has recently been used by Grotemeyer

Figure 4.3. Typical He pulse from Newport BV100 nozzle.

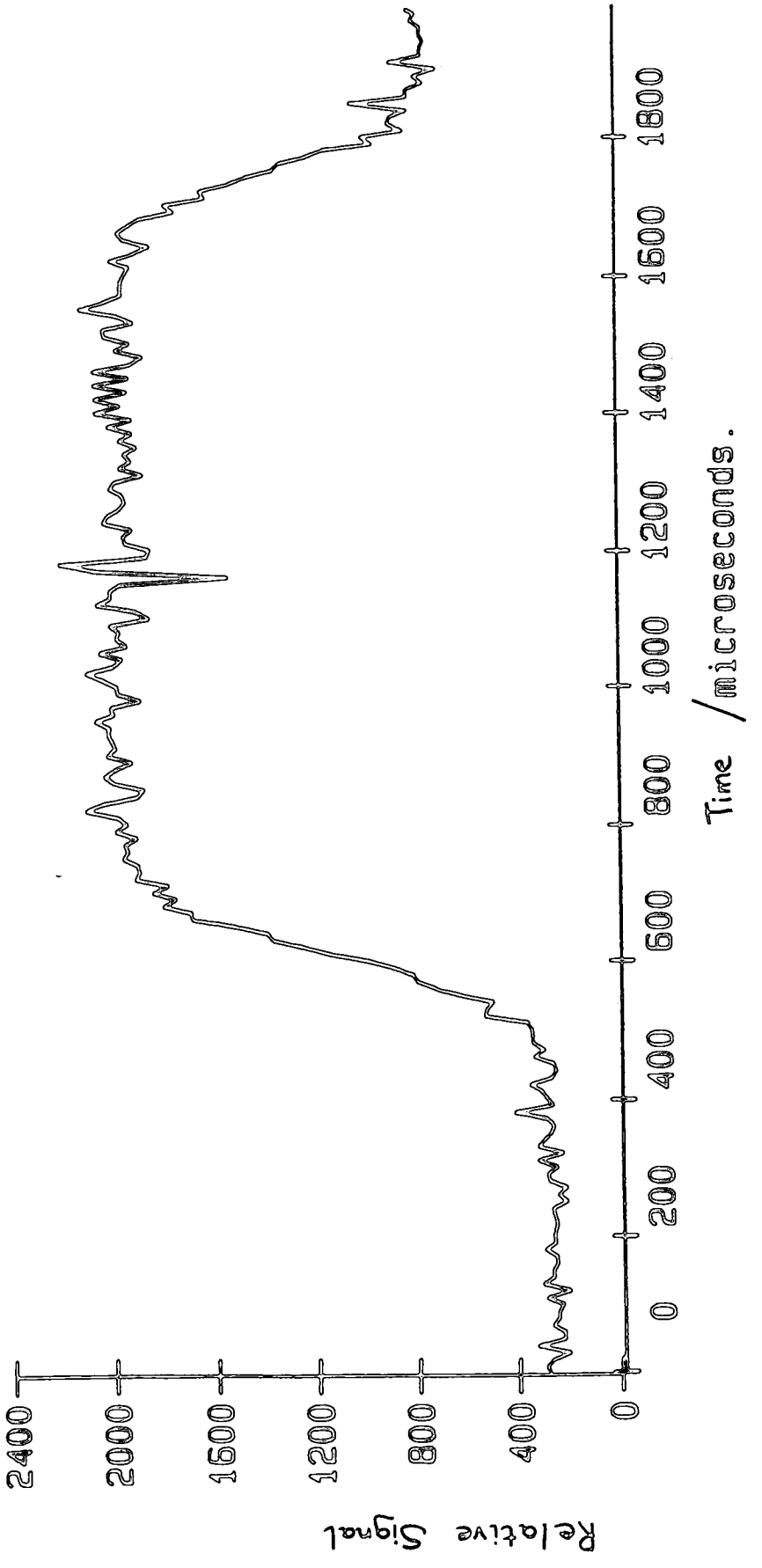

Figure 4.4. Typical He pulse profile from General Valve nozzle.

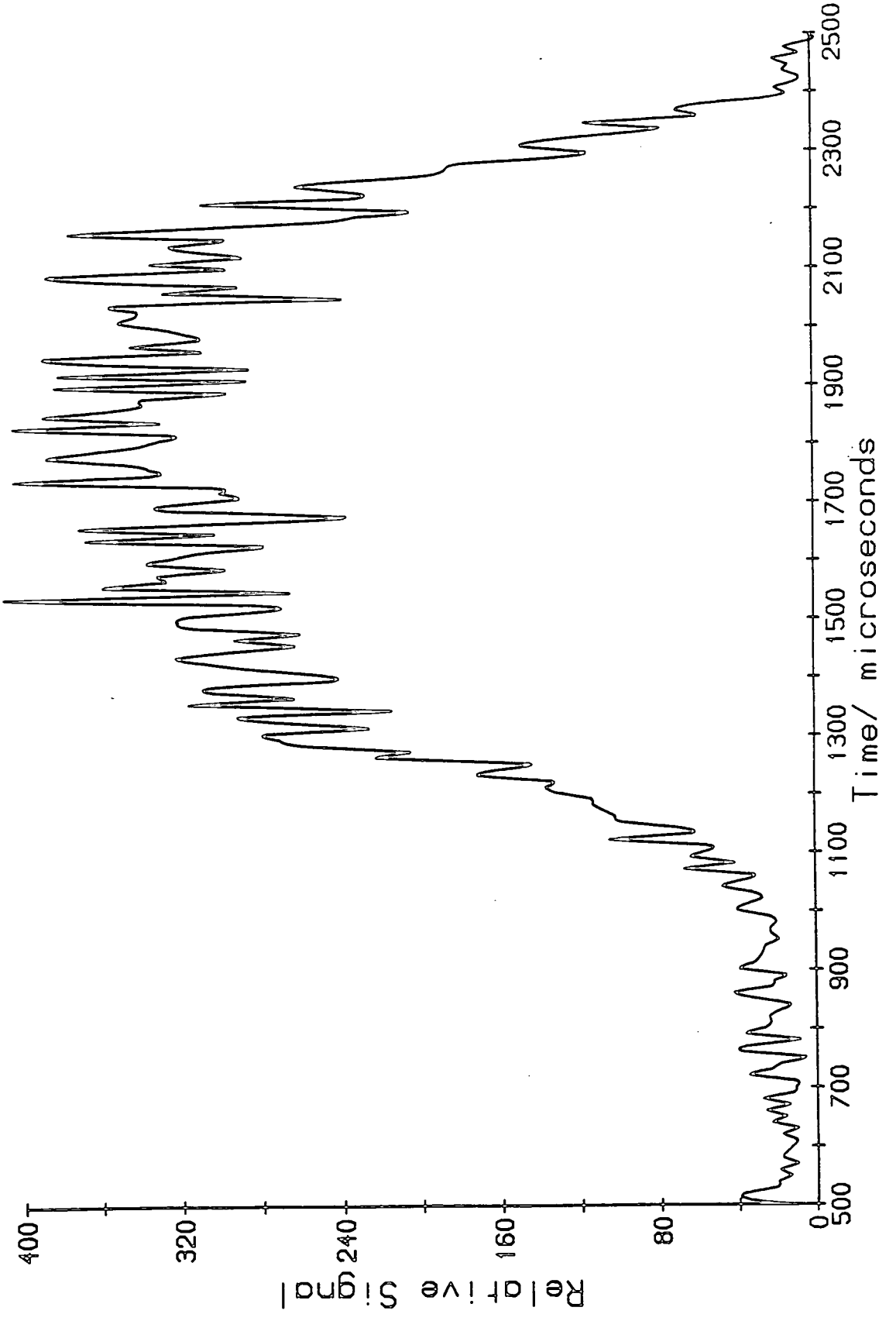

et al. [5] in order to study molecules with low desorption efficiencies. In our experiments, however, due to the relatively low power densities available from the CO_2 laser employed (see section 4.4.1), it was an essential part of the sample mixture. No desorption signals were obtained in the absence of the colloidal graphite.

The stainless steel rod was mounted on an XY translation mechanism, so designed to permit continuous translation and rotation of the rod via a stepper motor screw mechanism (McLennan 34 HS-106 motor driving a 8-32 UNF rod). In the experiments detailed here, however, the screw mechanism was not used, the sample probe remaining stationary. It was imperative, however, to be able to vary the position of the rod relative to both the nozzle orifice and the molecular beam axis. This allowed optimum entrainment efficiency of the desorbed species into the beam of helium carrier gas to be achieved, along with some degree of translational cooling.

The distance from the tip of the rod to the molecular beam axis was generally varied during preliminary runs for a given sample in order to optimise entrainment. Typically, a distance of 2 mm was used, which appeared to give good entrainment without disruption of the beam. Also, the distance from the nozzle orifice to the sample rod was varied in preliminary runs; a distance of 3-4 mm was found to be optimum. At shorter distances, there appeared to be a significant decrease in the signal intensity. Li and Lubman [6] observed a similar phenomenon with entrainment of desorbed species into a beam of CO_2 carrier gas. They attributed this phenomenon to shock waves being set up within the beam as the desorbed species attempt to penetrate into it in the high density

region close to the nozzle orifice. Further downstream, the carrier gas density is lower, so more efficient sample penetration is possible. At even longer distances from the orifice, they found little rovibronic cooling of the seed species, due to the reduced carrier gas density.

In general, shot-to-shot signal stability in these experiments was poor and certainly of insufficient quality to allow spectroscopic studies to be carried out. The mass spectral data presented in chapter 6 represent an average over 250-2000 laser shots, depending on the strength of the single-shot spectra obtained. It was found that a typical sample allowed spectra to be obtained over several hundred shots for a given irradiated area. Rotation of the sample probe to expose a fresh area of sample extended the useful lifetime of a given sample by up to about 20 minutes. If the glycerol was omitted from the sample mixture, the sample lifetime was considerably reduced.

Samples were obtained from either the Sigma Chemical Co. Ltd. or from Aldrich Chemical Co. Ltd., except where indicated in the text, and used without further purification.

4.2.4 Molecular beam skimmer.

A molecular beam skimmer (Beam Dynamics, 5 mm orifice diameter, 50 degrees included angle [7]) was mounted off the inner wall of the SC opposite the nozzle, at a distance of about 7.0 cm from the nozzle. The beam was therefore fully expanded before it was skimmed. The skimmer allowed a pressure differential of about 500 between the SC and the IC to be maintained under typical operating conditions. The skimmer apex was situated approximately 9.5 cm upstream of the

chamber wall closest to the IC, in order to reduce any disruption to the molecular beam caused by skimmed gas reflected back from that wall [8].

4.2.5 Ionisation chamber (IC).

The ionisation chamber consisted of a cube of 11.2 in. dimension (total internal volume 26.0 litres), which housed the ion extraction optics of either TOFMS. It was pumped by an Edwards Diffstak 160/700 diffusion pump (pumping speed 700 ls^{-1}, fluid Edwards L9) backed by an Edwards E2M18 rotary pump. This mechanical pump also backed the diffusion pump on the reflectron chamber via a common foreline.

The drift tube of the linear TOFMS was mounted on the top flange of the chamber (see figure 4.2). This drift tube was 113 cm long, with an internal diameter of 49 mm. When the linear TOFMS was in use, an MCP detector was located at the top of this tube; otherwise, this port was blanked off. The lowermost 65 cm of the drift tube was surrounded by a double-skinned liquid nitrogen dewar, the bottom of which penetrated into the chamber to a depth of 38 mm. The cryopumping effect of this liquid nitrogen reservoir effectively reduced the chamber pressure by an order of magnitude. The background pressure in this chamber was typically less than 10^{-7} mbar, the pressure rising to 4×10^{-7} mbar during experimental runs. The chamber pressure was measured by an Edwards CP25K Penning gauge head connected to an Edwards 1005 Pirani Penning gauge readout. This gauge had a lower operating limit of 10^{-7} mbar, so pressures below this were not measurable.

4.2.6 Extraction Optics

The desorbed neutrals carried into the ion source of the mass spectrometer were ionised by resonant or non-resonant laser photoionisation. The ionisation position was approximately at the centre of the IC; the nozzle to ionisation distance was therefore 34.5 cm.

The ion optics for both TOFMS configurations were mounted on bed bars running along the bottom of the chamber. Schematic diagrams of the ion extraction optics employed for the linear and reflecting-geometry TOFMS are shown in figures 4.5 and 4.6 respectively. Both sets of optics follow the design originally described in 1955 by Wiley and McLaren [9] for a double field spatially focusing TOFMS. In both figures, these fields are defined by the grid plates, labelled R (Repeller), DO (Draw-out) and F (Flight). In the linear TOFMS, ions are extracted at right angles to the molecular beam axis. A pair of electrostatic deflection plates was therefore required to counteract the velocity component of the ions, in the direction of the molecular beam axis, that is acquired by their neutral precursors as a result of their entrainment and expansion in the carrier gas beam. Although this effect should be negligible in the reflectron TOFMS, relative to the case of the linear TOF, deflection plates were utilised in the former as a means of adjusting the ion trajectories. A complete description of the extraction ion optical parameters employed during this work will be given in chapter 5.

All the ion optic plates were home-built, and were fabricated from gold-plated aluminium. Considering the linear TOFMS optics set first, the repeller plate

Figure 4.5. Schematic of the Linear TOFMS Ion Extraction Optics. Dimensions in mm.

There is a second set of deflectors perpendicular to those shown.

Repeller : 2310 V
Draw-out : 1930 V
Flight : GND

Deflector(1) : 0-180 V
Deflector(2) : -50- +50 V

Drift Length : 1.25 m

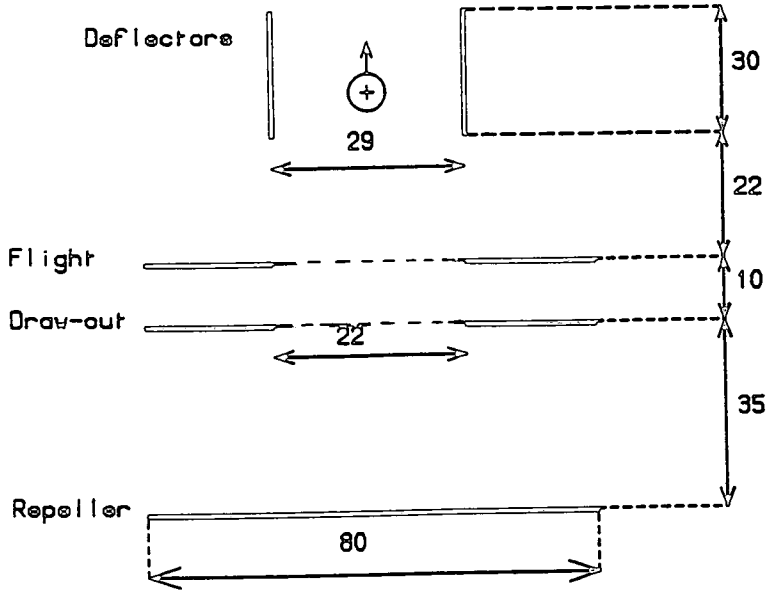

was 80 mm square and 3 mm thick. The draw-out and flight grids were supported on plates of the same area, but which were only 1.5 mm thick. These plates had 22 mm diameter holes cut in their centres to transmit the ions. To reduce the effect of any field homogeneities around these apertures, they were covered by nickel mesh (Buckbee Mears, 90 % transmission) . The mesh was held in place using conducting silver paint. The four deflectors were 30 mm square and 5 mm thick. The three extraction plates had a 5.6 mm hole cut in them at each corner, through which an alumina tube was slip-fitted. Precision machined Delrin spacers were then placed over the alumina rod to achieve the correct separation of the plates. A thin threaded brass rod was slid along the inside of the alumina tube. This allowed the entire assembly to be located atop an aluminium plinth, which fitted over the bed bars, before being clamped in place by a locking plate. The two pairs of deflectors were mounted on PTFE spacers located on an aluminium frame. The latter slotted over the 4-rod support and was separated from the flight grid by Delrin spacers.

The reflectron extraction optic plates were all 1.8 mm thick and consisted of 8 cm gold-coated aluminium squares. The repeller plate had a 7.7 mm diameter hole cut in it to admit the molecular beam to the ion source. This was not covered by mesh, as this reduced transmission of the beam considerably. The draw-out and flight grids had 22.4 mm diameter apertures, covered in 90 % transmitting mesh . The deflection plates were identical to those used in the linear TOFMS.

The linear TOFMS ion optics were surrounded by a bottomless copper box which was in good thermal contact with the bottom of the liquid nitrogen dewar.

Figure 4.6. Schematic of Reflectron TOFMS Ion Extraction Optics. Dimensions in mm.

Repeller	:	1345 V
Draw-out	:	445 V
Flight	:	0 V
Vert. Deflector	:	0 V
Horiz. Deflector	:	-50 - + 50 V

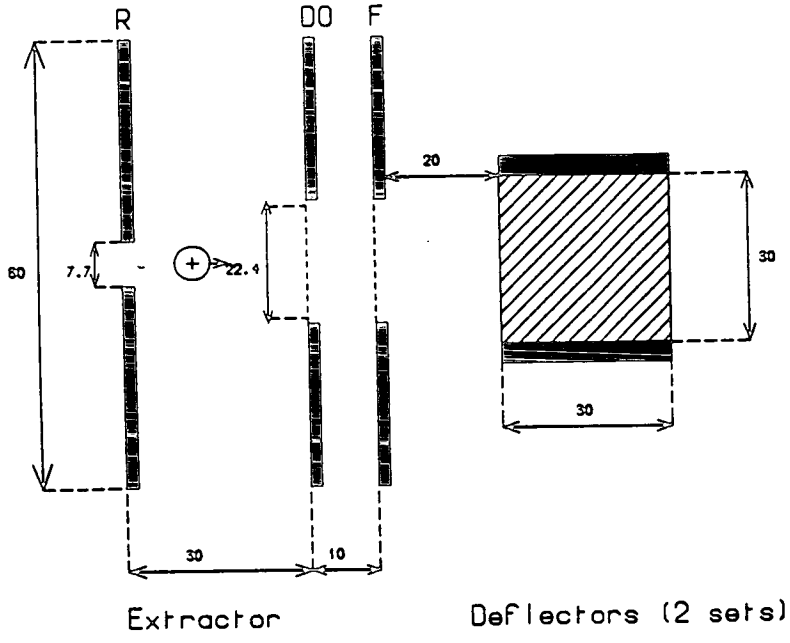

This completely enclosed the optics, apart from five 40 mm diameter apertures, one on each side, which allowed passage of molecular beam, laser beams and extracted ions. When the reflectron optics were fitted, two sides of the box had to be removed. In addition to providing a cryoshield to aid reduction of chamber pressure, this box acted as an electrical earth, thereby reducing the effect of field penetration in the ion source (see chapter 5).

Electrical connections to the ion optics were made via a grub screw situated on the edge of each plate. These were then connected by shielded wire to one of six MHV vacuum feedthroughs mounted on one of the chamber side flanges. These flanges were also equipped with two pairs of Spectrosil B windows to allow entrance and exit of the ionisation laser beams.

4.2.7 Reflectron chamber (RC).

The reflectron chamber was constructed from a cylinder of length 64 cm and internal diameter 19 cm. It was connected to the IC by a stand-off tube (31.2 cm long, 6.3 mm outside diameter), which mated to the gate valve employed to mutually isolate these chambers. A second stand-off section connected the RC to the MCP detector. This stand-off comprised of two smaller tubes, the first of length 5.1 cm and 6.3 cm O. D., the second of length 8.9 cm and 5.1 cm O. D., tilted at an angle of 8 ^{o} to the molecular beam axis. The reflecting field ion optics were mounted off the back flange of the RC and were oriented at 4 ^{o} to the molecular beam axis in order to direct the ions down the second stand-off section to the detector.

The RC was pumped by an Edwards Diffstak CR160/700 diffusion pump (fluid

Edwards L9), which was equipped with both a liquid nitrogen- cooled cryotrap and a quarter-swing butterfly isolation valve. This pump had a pumping speed of 600 ls^{-1} for air, and as mentioned previously, was backed by an Edwards E2M18 rotary pump. The RC was also equipped with a double skinned liquid nitrogen dewar for cryopumping. The base chamber pressure, as measured by an Edwards CP25K/1005 combination, was below 10^{-7} mbar; under typical operating conditions, this rose to 2×10^{-7} mbar.

4.2.8 Reflectron optics.

The ion mirror of the reflecting-geometry TOFMS, shown in figure 4.7, consisted of nine stainless steel plates, each 12 cm in diameter, mounted off the back flange of the chamber. It comprised two distinct sections, denoted in the figure by characteristic lengths d_t and d_k. The mirror backplate was solid, but the remaining plates had a 6 cm diameter hole cut in them. The first two electrodes in the mirror, separated by d_t, each comprised two plates joined together, clamping nickel mesh (Buckbee Mears, 90 % transmission) across the aperture; the apertures on the other four electrodes were not covered with mesh. The entrance ring to the mirror was kept at ground potential, to define the field-free path length, whilst the repelling voltage was supplied to the backplate of the mirror, and dropped across the four "guard rings" and the second electrode by a resistor network as shown. The voltage ratio across the two sections of the mirror was varied by changing the resistance of R_2, which was mounted outside the vacuum chamber. The inter-plate separation was achieved using alumina tube and Delrin spacers in similar manner to that employed for the ion optics in the IC.

Figure 4.7. Schematic of Reflectron TOFMS Ion Mirror.
Dimensions in mm.

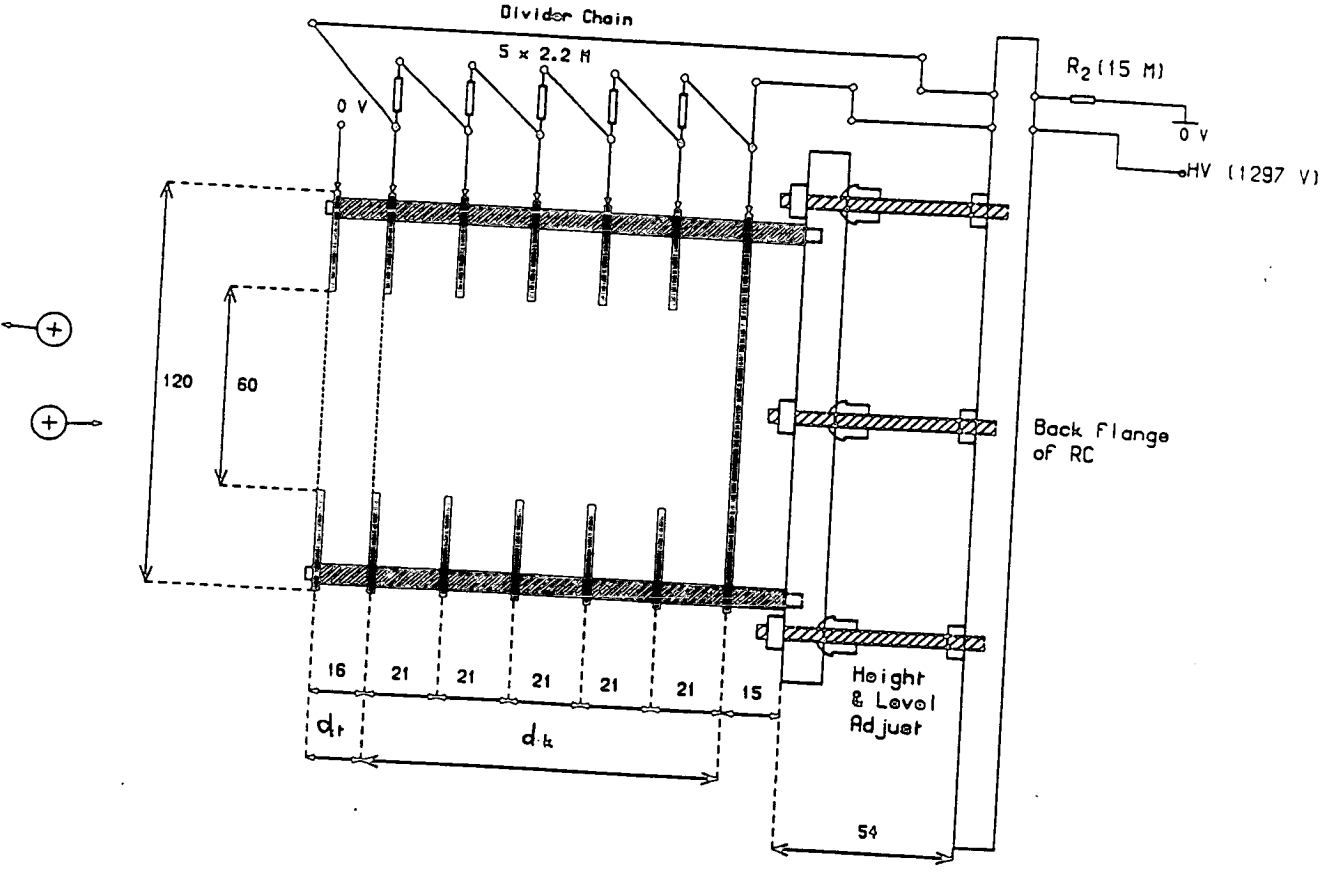

4.2.9 Microchannel plate detector.

The photoion signals were detected by a dual microchannel plate [10]. This MCP (R. M. Jordan) was of a dual chevron design, with two Galileo MCP-18B plates back to back, each having an active area of 2.5 cm^2. A divider chain was built to drop a maximum of 1000 volts across each plate, which had a gain of 10^3 at 1 kV, and a gain of 10^2 at a typical operating voltage of 700 V.

The detector was operated in grounded anode mode [10], thereby allowing easy coupling to the digitisation electronics. This method requires that the front channel plate be held at a large negative voltage, but has the added advantage of increased gain for positive ions, which are accelerated into this plate [10]. The disadvantages of this mode of coupling are that negative ions cannot be detected, and that an earthed grid must be placed in front of the negatively-biased plate in order to define the end of the field-free drift region of the TOFMS. In the design of the Jordan MCP, this grid had a transmission of 82 % which therefore slightly reduced the overall sensitivity of the detector.

The signal from the MCP was taken directly to the input of a transient digitiser, the input impedance of which matched that of the MCP (50 Ω).

4.3 Power supplies.

Voltages were supplied to the various TOFMS lens elements using the following power supplies

- Repeller: Brandenburg 507R

- Draw-out: Brandenburg 475R
- Deflectors: Brandenburg 475R
- Ion mirror: Brandenburg S.0530/10 or EG & G Ortec 556
- MCP detector: Fluke 408B or EG & G Ortec 556

All voltages were delivered through MHV vacuum feedthroughs. The chambers and the table upon which they were mounted were earthed, as were the connectors to the flight grid in the extraction optics, and the entrance grid to the ion reflector.

4.4 Lasers.

The laser desorption-MPI mass spectrometry technique requires the use of two laser systems; one to achieve desorption of the sample and the other to ionise the desorbed species. As mentioned in chapter 3, infrared radiation is particularly suited to the former task, and has been widely used for that purpose. A pulsed CO_2 laser was therefore employed as the desorption laser in this work. Ionisation required the use of powerful UV light; this was provided by either the fourth harmonic of a pulsed Nd^{3+}: YAG laser, or by the tunable output from a YAG pumped dye laser system. These laser sources will be discussed in more detail in the following sections.

4.4.1 PSI LP30 CO_2 laser.

The PSI (Pulse Systems Inc.) LP30 is a transverse-discharge low pressure CO_2 laser, capable of generating approximately 10 µs pulses at repetition rates up to 6 Hz. A gas mixture of 65% He, 15% N_2, 20% CO_2 was flowed continuously through the cavity, which was equipped with NaCl windows, and pumped by an

Edwards ED50 rotary pump. Figure 4.8 shows the laser temporal output pulse profile, as measured by a combination of a room temperature CdHgTe detector, storage oscilloscope and oscilloscope camera [11]. Typical pulse energies were measured to be 100 mJ at the maximum possible repetition of 6 Hz using a joulemeter (Gentec ED200). Excessive arcing occurred within the laser cavity at higher repetition rates, effectively setting this as the maximum duty cycle for these experiments. External control over the operation of this laser required provision of a 10 V trigger pulse, of $>$ 1 μs duration.

The output from this laser was introduced into the SC via two gold plated mirrors, and a 30 cm focal length NaCl lens mounted outside the chamber. As mentioned previously, the use of colloidal graphite in the sample mixture allowed facile alignment of the laser beam with the target rod. The laser cavity was equipped with stable resonator optics. In effect, this limited the minimum focal spot size to about 2.5 mm diameter due to the relatively large divergence (8 mrad) of the beam emerging from this cavity. Taking account of losses at the gold mirrors and subsequent optics, a typical desorption power density was therefore 3 x 10^5 Wcm^{-2}.

4.4.2 Quanta-Ray Nd^{3+}:YAG pumped dye laser system.

The Quanta Ray system consisted of a DCR-2A pulsed Nd^{3+}:YAG laser, a PDL-2 dye laser, and a wavelength extension unit, the WEX-1c, which contained the appropriate doubling and mixing crystals to generate tunable radiation from 217 to 432 nm. The complete suite of Quanta-Ray laser hardware was only used to record the mass spectra of aniline shown in the following chapter, and the

Figure 4.8. Typical output pulse profile from PSI LP30 laser.

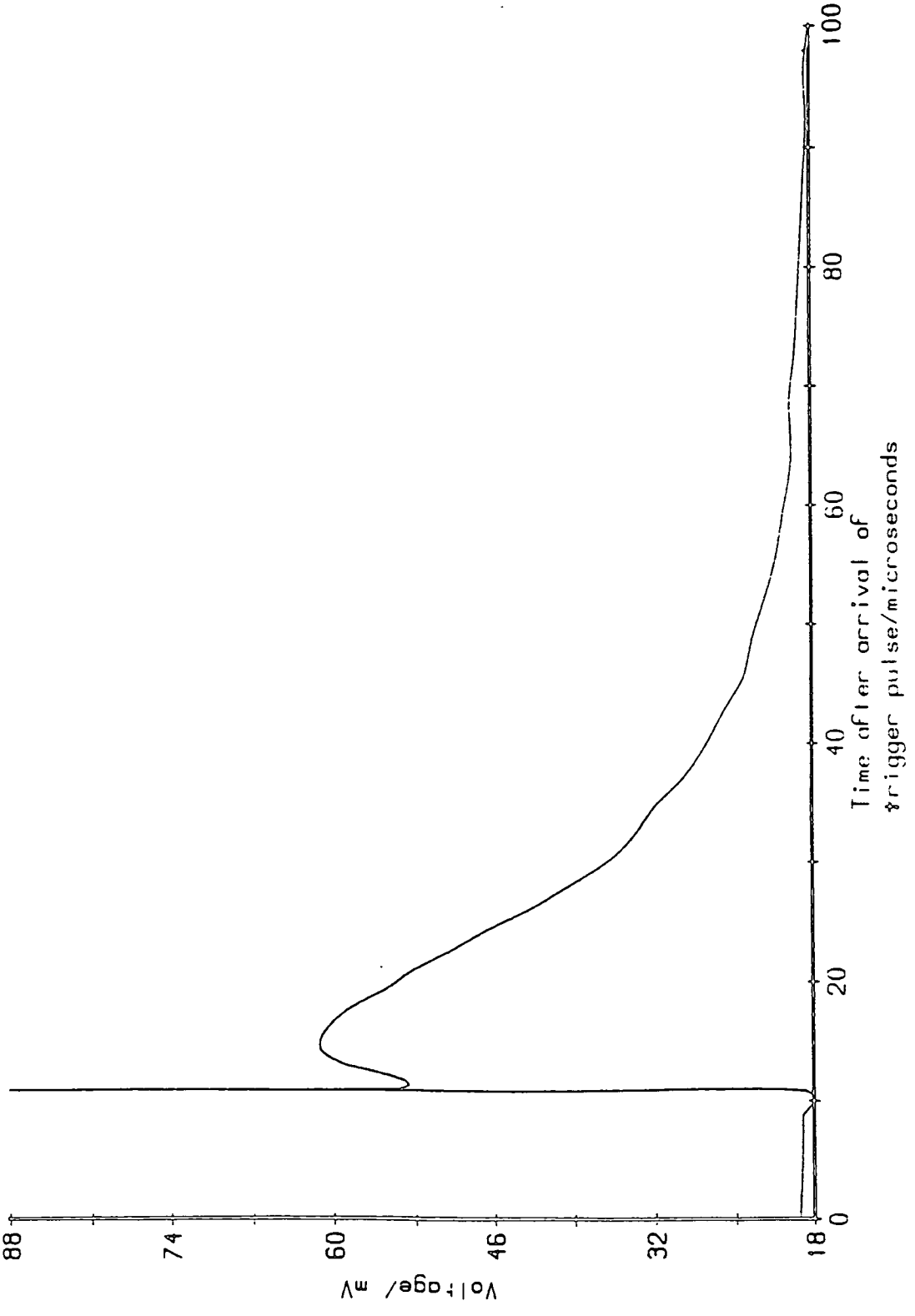

R2PI spectra of that molecule presented in chapter 3. However, the PDL-2 and WEX-1c were employed in conjunction with a JK HY750 Nd^{3+}:YAG laser, to obtain all the desorption mass spectra presented in chapter 6.

The DCR-2A was an oscillator-amplifier Nd^{3+}:YAG laser, capable of delivering 800 mJ pulses of 9 ns FWHM duration at its fundamental wavelength of 1064 nm. The laser also contained KDP crystals for second and third harmonic generation, which were located in a thermostatted oven.

In order to externally control the operation of the DCR-2A, three pulses were supplied to trigger the master oscillator, flashlamps and Q-switch respectively. The first of these TTL level pulses closed the high voltage relay that applied high voltage to the Pockels cell (Q-switch), and initiated charging of the capacitors which created the flashlamp discharge. The second TTL pulse, delayed by 3 ms with respect to the first, fired the flashlamps surrounding the YAG rods, pumping the lasing transition. The third pulse released the high voltage relay supplying the Pockels Cell. It was possible to vary the output energy of the laser pulse by varying the delay between the flashlamps and Q-switch triggers; the output was maximised at a delay of 190 μs.

The 1064 nm fundamental output could be frequency doubled or tripled using the KDP crystals mounted in the oven. In this work, the residual infrared light was spatially separated from the required second harmonic (532 nm) radiation within the Prism Harmonic Separation (PHS) unit, by means of a Pellin-Broca prism, and directed into a beam dump. Optimised pulse energies at 532 nm were 350 mJ, as measured by a calibrated Photon Control volume absorbing

calorimeter (model 25 V/UV).

The PDL-2 dye laser was of the oscillator/amplifier type. It had a transversely pumped oscillator cuvette in a Hänsch-type cavity. Wavelength selection was made by a Littrow grating , and the oscillator output was coupled out of the cavity by a partially transmitting end mirror. The output radiation was then amplified in a transversely-pumped preamplifier, if necessary, and then finally in a longitudinally pumped amplifier. Three dye solutions in methanol were employed in this work; these are detailed in table 4.1. All dyes were obtained from Exciton.

Table 4.1

Dye	range/nm	peak/nm	peak efficiency/%
Kiton Red 620	579-598	584	20.0
Fluorescein 548	541-571	548	24.0
7:3 Rhodamine 590: Rhodamine 610	570-588	575	20.0

The WEX-1c extended the useful wavelength range of the dye laser into the ultraviolet, covering the range 217-432 nm. The unit contained two sets of KDP crystals. The function of the first set was to produce light in the wavelength region 259-432 nm, by either frequency doubling the output of the PDL-2 or by mixing the Nd^{3+}:YAG laser fundamental with the dye laser fundamental. The second set of crystals mixed the doubled dye laser output with the 1064 nm light to cover the wavelength region 217-265 nm. The KDP second harmonic generation (SHG) crystals were used exclusively in this work, the frequency doubled light being separated from the fundamental by a Pellin-Broca prism [12].

In order to maintain the correct phase matching conditions in the chosen SHG crystal as the dye laser wavelength was scanned, a portion of the doubled beam was split off on to a bi-photodiode linked to a servo-motor. Any asymmetry in the UV beam detected by the bi-photodiode was compensated for by adjusting the crystal orientation. When used in a wavelength scanning mode, a trigger pulse, synchronous with the trigger pulse to the DCR-2A Q-switch, had to be sent to the WEX-1c unit. This refreshed the logic circuit of the bi-photodiode/servo system, thereby allowing the comparator/servo circuitry to operate properly at each wavelength.

The WEX-1c was also employed to produce the fourth harmonic of the output from the DCR-2A (or JK HY750). The dye laser was configured in such a way that the 532 nm light produced by the pump laser was introduced into the WEX-1c, without passing through the optics of the PDL-2. In this mode, a trigger pulse to the WEX-1c was not required. In general, however, the DCR-2A laser was engaged in other experiments, proceeding concurrently with those described here. Another pump laser was therefore required to produce the UV light needed for ionisation of the desorbed species. For this purpose a JK HyperYAG HY750 was used.

4.4.3 JK HyperYAG HY750 Nd^{3+}:YAG laser.

The HY750 was a pulsed Nd^{3+}:YAG laser with similar characteristics to the DCR-2A. The Q-switched fundamental output of this oscillator-amplifier type laser was measured to be 800 mJ per pulse at a repetition rate of 10 Hz. Second and third harmonics could be generated by the use of thermally- stabilised CDA

and KDP crystals; typical pulse energies at these wavelengths were 320 and 170 mJ pulse^{-1} respectively. Separation of the desired 532 nm wavelength light from the fundamental wavelength was achieved using two Brewster-angled gull wing prisms placed after the harmonic generation crystals.

External control of this laser required provision of two 15 V trigger pulses, to trigger the flashlamps and Q-switch respectively. In principle, the output energy of the laser could be altered by varying the delay between these pulses, as in the case of the DCR-2A. In practice, however, the Q-switch input circuitry was damaged, so that it could not be externally controlled; the internal circuitry of the laser was used to trigger the Q-switch about 180 μs after the flashlamps had been externally triggered.

The HY750 was used in all the desorption experiments. Although it was occasionally used to pump the PDL-2 operating on one of the dyes listed in table 4.1, in general, the HY750 was normally employed, in conjunction with the WEX-1c, to produce 266 nm radiation for photoionisation . It is likely that since the desorbed species did not undergo true supersonic expansion, their internal temperatures were quite high (> 10 K). In this case, rotational contours in an R2PI spectrum would be quite broad; 266 nm is therefore an "all-purpose" mid-UV wavelength, which will be in resonance with an excited state of most desorbed samples studied in this work.

A typical 266 nm pulse energy generated by the HY750/WEX-1c combination at 6 Hz was 15 mJ per pulse. Since it was not possible to vary the HY750 pulse energy by delaying the Q-switch trigger pulse as outlined above, a series of filters

and apertures were utilised to reduce the pulse energy to less than 1 mJ, suitable for soft ionisation. Pulse energies were measured by a Molectron pyro-electric power meter (model J3). The UV light was focused by a 30 cm focal length plano-convex silica lens into the ion source of the mass spectrometer. Depending on the type of mass spectral information required, the power density of the ionisation laser beam was varied between approximately 10^5 and 10^8 Wcm^{-2} by altering the position of the focusing lens or by reducing or increasing the amount of beam filtering. The focal spot size was measured by employing the "knife-edge" method of Leone [13]. This entailed mounting a flat blade on an XYZ micrometer stage, and translating the blade edge across the focal spot, whilst monitoring pulse energy on a photodiode. The laser spot size with the lens at focus was measured to be 250 μm in diameter.

4.5 Experimental control and data acquisition.

A pulsed laser desorption laser photoionisation experiment requires precise control of several experimental events, and generates a large amount of data which must be processed in a short period of time. It therefore requires a sophisticated computer-based system to facilitate optimisation of the experimental parameters, and to acquire and store data. The use of a computer in this type of experiment has several advantages: data can be displayed on the screen of a VDU as the experiment proceeds, and once optimised, experimental parameters can be easily reset. In addition, digital storage of data facilitates the analysis and presentation of experimental results. The CAMAC (Computer Automated Measurement And Control) system is widely-used for this type of

application [14], [15]; it involves the use of a range of hardware located in a crate, which is controllable by software run on a microcomputer.

Before describing the instrumentation and computer software employed to control the experiment, it is useful to outline the experimental cycle used in this work.

4.5.1 Experimental cycle.

The entire experiment was driven by software, written by a colleague [16], implemented on an IBM PC-AT. This software package controlled experimental timings and acquired data, via a CAMAC interface.

It proved convenient to use a constant repetition rate in these experiments. This had the advantage of circumventing problems associated with thermal lensing in the Nd^{3+}:YAG laser rods. A constant repetition rate was accomplished by employing the interrupt mechanism of the PC-AT, which was easier than trying to synchronise the computer to the experiment using an external clock. The interrupt was generated at 12 Hz, twice the desired experimental repetition rate. On alternate interrupts, the software toggled between two routines for controlling the experimental apparatus and processing the data, known as "TIC" and "TOC" respectively.

On a TIC, the PC-AT sent signals through a CAMAC dataway to trigger a transient digitiser and two pulse generators. The latter delivered trigger pulses to various items of experimental apparatus, in an appropriate sequence. A typical experimental timing set-up is given in figure 4.9. The first item to be triggered

was the pulsed molecular beam valve. After a suitable delay time, the desorption CO_2 laser was fired; a delay was chosen such that the maximum gas density delivered by the pulsed valve was passing the sample probe as the desorption laser impinged on the sample. This was selected to give maximum entrainment efficiency and optimum cooling [17]. After a second, experimentally-determined delay the ionisation laser was fired. This delay was to account for the time taken for the molecular beam containing the desorbed material to traverse the distance from the nozzle to the ion source. The photoion signal generated by the photoionisation process was then detected and amplified by the MCP. The final action taken by the TIC routines was to send a stop pulse to the transient digitiser (TD), which then digitised the ion signal arriving at the MCP until its memory was full.

On a TOC cycle, data stored by the TD was downloaded into a temporary buffer in the PC-AT. This raw data underwent limited processing, namely inversion (to give a positive-going waveform) and summation with previously acquired shots. The experimental cycle was repeated on the next TIC call.

4.5.2 CAMAC crate.

The IEEE CAMAC standard [15] defines a common dataway to which a number of instruments can be interfaced. All the CAMAC instruments were located in a crate (Wes FHD-DV3), whose backplane provided data communication and power lines to each module. A common dataway of 24 read/write lines was used to transmit data to and from the units. Other data lines directed commands

Figure 4.9. Trigger pulse timing set-up for LD-MPI MS experiments (Times in microseconds).

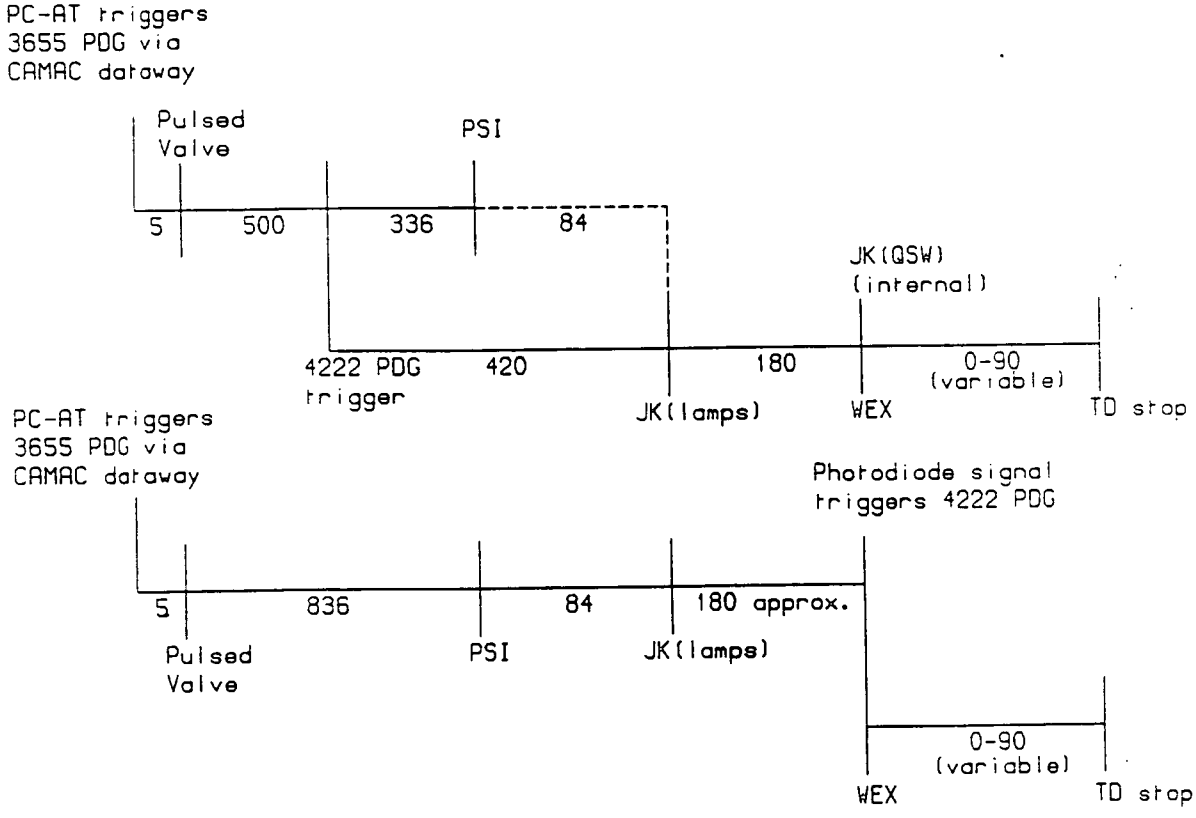

from the software implemented on the IBM PC-AT to the correct module or part of a module, and transmitted acknowledgements of receipt of these commands or requests for attention by each module to the microcomputer.

As shown in figure 4.10, the crate contained several instruments for controlling the experimental timings and acquiring data. These will be discussed individually below.

4.5.3 IBM PC-AT microcomputer.

The IBM PC-AT contained an Intel 80286 (16 bit) processor, clocked at 8 MHz, an 80287 maths co-processor and 640 kb of RAM. Experimental data was displayed on a high resolution (640 x 350 pixels) VDU, driven by an EGA 256 kb graphics card. A 20 Mb hard disk and a 1.2 Mb floppy drive were provided for storage of software and data.

4.5.4 DSP 6002 Crate Controller.

The crate controller (DSP 6002) was located in the rightmost slot of the crate. This dedicated microprocessor, which was programmed through a DSP PC004 interface card located in an 8 bit expansion slot in the PC-AT, accepted commands from the computer to control the experiment, passing these on to the appropriate modules in the crate. It also passed data recorded by the modules back down the dataway to the PC-AT for further processing. Although the transfer rate of data, in blocks of direct memory access (DMA), between the DSP 6002 and the PC-AT was claimed to be 700 kBs^{-1}, the measured rate was only

Figure 4.10. Schematic of CAMAC based experimental control system.

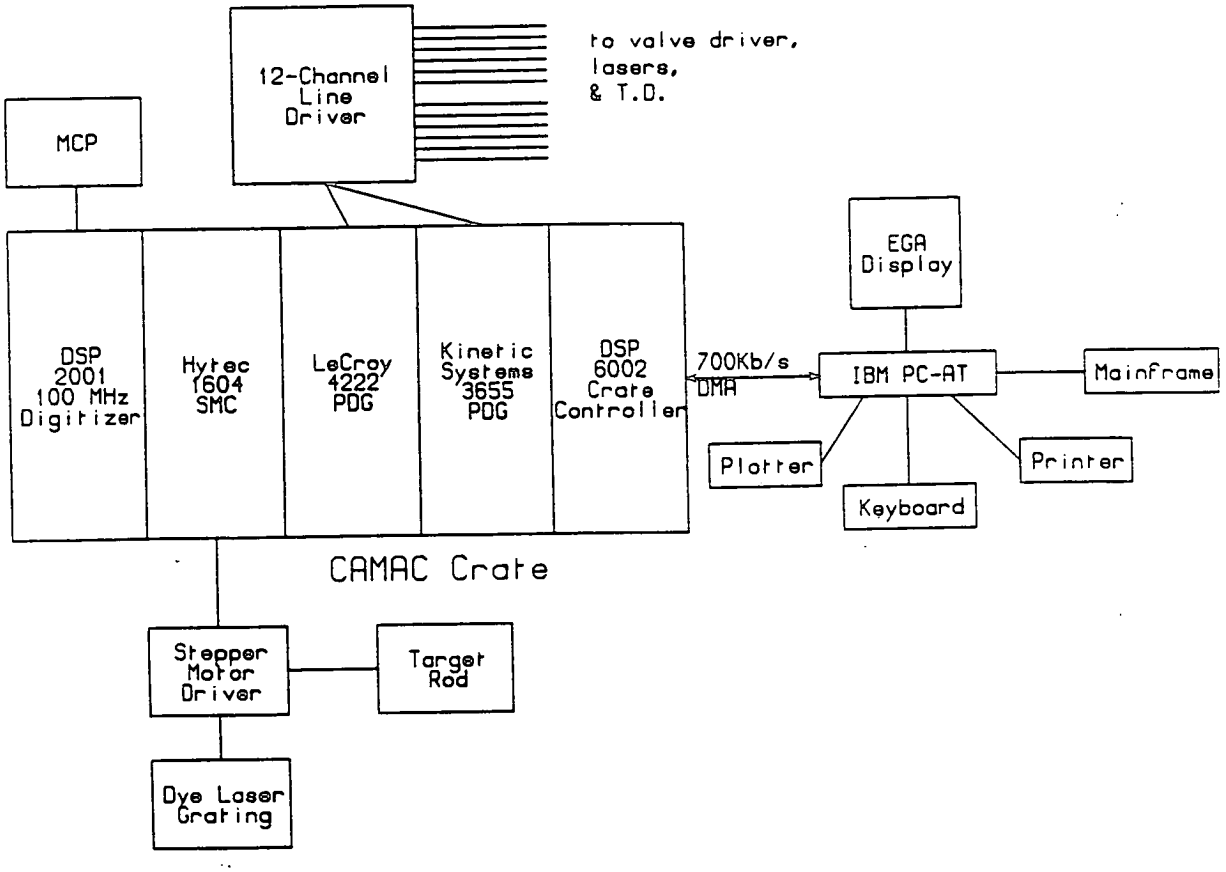

230 kBs^{-1}. This was due to the PC004 interface card occupying an 8-bit expansion slot in the PC-AT; although the data was transferred in parallel 24-bit blocks from the crate, it took three cycles to download this from the interface card into the PC memory.

4.5.5 Pulse Delay Generators.

Two programmable pulse delay generators (PDGs) provided the trigger pulses required to run the experiment. These were a Kinetic Systems 3655 8 channel PDG and a LeCroy 4222 4 channel PDG. The former could produce 200 ns FWHM TTL pulses with microsecond accuracy. It was triggered by an instruction passed through the dataway from the PC-AT. Each channel of this PDG had its own 16 bit register to store a set time delay, typed in at the computer, with respect to the trigger pulse. The minimum possible interval between pulses from successive channels was 1 μs, whilst the jitter between pulses was about 1 ns.

The LeCroy 4222 PDG generated four 100 ns TTL pulses of 1 ns accuracy. Each channel had its own 24 bit register, in which the required delay was stored. The 4222 was "enabled" to receive a trigger pulse on each TIC cycle of the computer, and was triggered via one channel of the KS 3655. Each channel of the 4222 was independent, and could be used in any order or simultaneously. Jitter between pulses was less than 170 ps; consequently, the 4222 was used to trigger devices where very precise control of the timing was required, for example, the transient digitiser.

The pulses from both PDGs did not produce enough current to drive 50 Ω loads over the long coaxial cables required in this experiment. Furthermore, they were

too narrow to trigger some of the external devices, which had trigger thresholds of greater than 10 V or required pulses of greater than 200 ns FWHM. The outputs from the PDGs were boosted by a custom-built 12 channel line driver unit, housed in a NIM bin, which produced either 5 V, 10 μs or 15 V, 50 μs pulses.

4.5.6 Hytec 1604 Stepper Motor Controller.

The Hytec 1604 stepper motor controller (SMC) could control up to four separate stepper motors at once. In this work, however, it was only used to step the PDL-2 grating during frequency scans and to control the motion of the sample probe screw mechanism if this was required. The SMC supplied pulses to two chopped bipolar driver cards (McLennan TM162C) mounted in a 19 in. rack unit, one to drive the PDL-2 stepper motor and one to drive the sample probe stepper motor. A frequency scan involved acquiring data over N shots at a given wavelength, before moving the laser wavelength by a certain mount and repeating the procedure. Thus, every Nth TIC cycle (typically N=30), the SMC delivered a burst of single step commands to the grating motor in order to provide the desired wavelength increment. During this process, the SMC ramped the stepping speed from an initially slow rate to a maximum and back again, to avoid loss of synchronisation due to the inertia of the motor. This was vitally important, since the PDL-2 grating stepper motor had to move exactly by the requested number of steps, otherwise the computer lost track of the grating position.

4.5.7 DSP 2001 Transient Digitiser.

The arrival of ions at the MCP generated a waveform consisting of a series of negative-going current peaks. Digitisation of this signal required the use of a fast sampling device, namely the DSP 2001 transient digitiser (TD). This device had 8 bit resolution, with a range of 512 mV, giving a minimum detectable change of 2 mV. The digitising rate and record length of this device were set using front panel switches. The digitising rate ranged between 1 and 100 MHz. The memory of the TD was divided into different record lengths, selectable in powers of 2 from 256 bytes to 32 kb. The maximum record length that could be processed by the control software at 6 Hz was 2 kb; this was limited by the time it took the maths co-processor to read the accumulated data from memory, and to scale and plot it.

After the TD was armed by a CAMAC dataway command, the input signal was continuously sampled and stored in the chosen fraction of the available memory (2 kb). This data was constantly overwritten, until the receipt of an external stop trigger pulse. The next 2 kb of samples then constituted the required mass spectral data.

The stop trigger was usually synchronised with the ionisation laser Q-switch trigger pulse. In the case of the HY750, however, where this circuitry was damaged, the laser light itself was used to trigger the TD (and WEX-1c where required). In this instance, a reflected laser beam was incident on a Mullard BPY series photodiode (risetime < 1 ns). The output pulse from this was amplified by a factor of 10 in a 50 Ω coupled LeCroy 234 amplifier, and the resulting pulse

then triggered the 4222 PDG. The output from a channel of this PDG then provided the stop pulse for the TD.

Since the maximum record length was 2 kb, only a 20.48 μs portion of the mass spectra could be viewed under highest resolution (100 MHz). The longest flight-times were on the order of 100 μs, so in order to record the entire spectrum in these cases, the TD had to be operated at a lower sampling rate (usually 20 or 50 MHz), with consequent loss in resolution. The TD window was only 3 ns, so the digitiser could miss the peak of a signal and only sample it in the wings, even at 100 MHz. This would have the effect of making an ion signal appear weaker than its true intensity. In order to reliably record a peak shape, at least four samples were required, which placed a lower limit of 40 ns on the width of the ion peaks. In general, however, the FWHM's of the peaks from the reflectron TOFMS were less than this, leading to problems at the lower sampling rates, namely that the TD could totally miss an ion signal if it fell between two sample times. If required, regions of the mass spectrum could be recorded under the highest resolution by inserting a delay between the pulse from the photodiode (or ionising laser Q-switch trigger pulse) and the TD stop trigger. This procedure was employed when obtaining the R2PI spectra of aniline shown in the previous chapter. The relatively large sampling rate at 100 MHz led to better definition of the molecular ion signals than was possible at lower sampling rates.

4.6 Control software.

The use of a CAMAC-based system, in which much of the control and signal processing is carried out external to the computer, greatly reduces the

requirements placed on the software itself. The control software used the language "C" (Microsoft v 5.00), with some assembler (IBM MACRO Assembler v 2.00). The latter was used for the time-critical functions. Further details can be found in reference 15.

There were three basic modes in which the experiment could be run. These are described below.

4.6.1 TOF mode- Acquisition of Mass Spectra.

The TOF mode of operation was the most basic of the experimental modes. The experimental cycle was performed N times. On each TOC cycle, 2 kb of digitiser memory was transferred to the PC-AT to form a cumulative sum of ion signal as a function of TD channel number. Every M cycles (shots), this cumulative mass spectrum was displayed on the screen of the PC-AT. Both values of M and N were programmable, and could be altered during an experimental run, to allow different numbers of single-shot spectra to be added until a satisfactory signal-to-noise ratio was achieved. After N shots had been accumulated, the program either paused, or cycled back to collect another spectrum.

The mass spectra were calibrated to give ion signal versus flight time or mass. The former could be calculated from the known sampling rate of the TD, whilst the latter was achieved by fitting known mass peaks to their time of arrival using a least means squares method (see chapter 5).

4.6.2 Time scan mode - Optimisation of timing delays.

Acquisition of LD-MPI mass spectra required optimisation of several time delays. Some of these, such as the delay between two pulses to fire the DCR-2A, were well established; others could only be estimated crudely *a priori*.

The timing set-up was entered from a software menu, and stored in an array which was used by the TIC function to program the PDGs. Optimisation of the delays was performed by using the function keys on the PC-AT keyboard, which were linked to particular channels of the PDGs, whilst observing the TOF spectrum. This procedure, however, was often tedious and misleading; an easier method to optimise timing delays was to use the time scan method.

In a time scan, the control program scanned one pulse in time relative to the others in a timing set-up, whilst monitoring chosen mass channel(s). The time channels for a given mass peak were determined by running a non-optimised mass spectrum. If, for example, a mass peak was recorded in channels 700-704, it was defined as starting in channel 700 and continuing through the next four channels, in the signal definition routine (SDR). Up to ten different signals could be defined in this way for monitoring at any given time.

Scan start, stop and step sizes were loaded into the timing set-up menu. An experimental cycle was run, the ion signals defined in the SDR integrated and stored, with the average signal for one of the channels being plotted on the screen. The computer then incremented the scanned delay time by the step size, and another cycle was run, with the average signal for this run being plotted on the screen at the correct time increment relative to the first. The procedure was

repeated until the stop time was reached, at which point the whole cycle repeated. With weak or noisy signals, it was often necessary to scan over the defined delay range several times to build up a clear profile. Figures 4.3 and 4.4 were obtained by this method. Here the ionisation laser trigger was scanned relative to the nozzle firing pulse, whilst monitoring the He mass channels. Figure 4.11 shows the analogous time scan obtained in a typical desorption experiment. Here the desorbed material (pentacene) arrives in the ion source region of the mass spectrometer over a period of about 100 μs. The time scan therefore not only allows optimisation of the desorption-ionisation laser time delay, but yields information on the fundamental process of infrared laser induced desorption, as will be discussed further in chapter 6.

4.6.3 Frequency scan mode- Spectroscopic studies.

This method has essentially been described in section 4.5.4 above. Briefly, mass spectra were accumulated as per the TOF mode and ion signals defined as outlined in the preceding section. After a predetermined number of shots had been accumulated at the start wavelength, the ion signals in these channels were integrated, stored and displayed on the screen. The position of the dye laser grating was then incremented by a pre-set amount, giving the new laser wavelength. This process continued until either the preprogrammed stop wavelength was reached, or it was ended by the user.

The frequency scan mode was used rarely in this work. Due to the shot-to-shot instability in the desorption yield, spectroscopic studies were limited to the R2PI spectra of aniline shown in the previous chapter. The PDL-2 laser grating,

Figure 4.11. Desorption profile for pentacene, obtained by time scan.

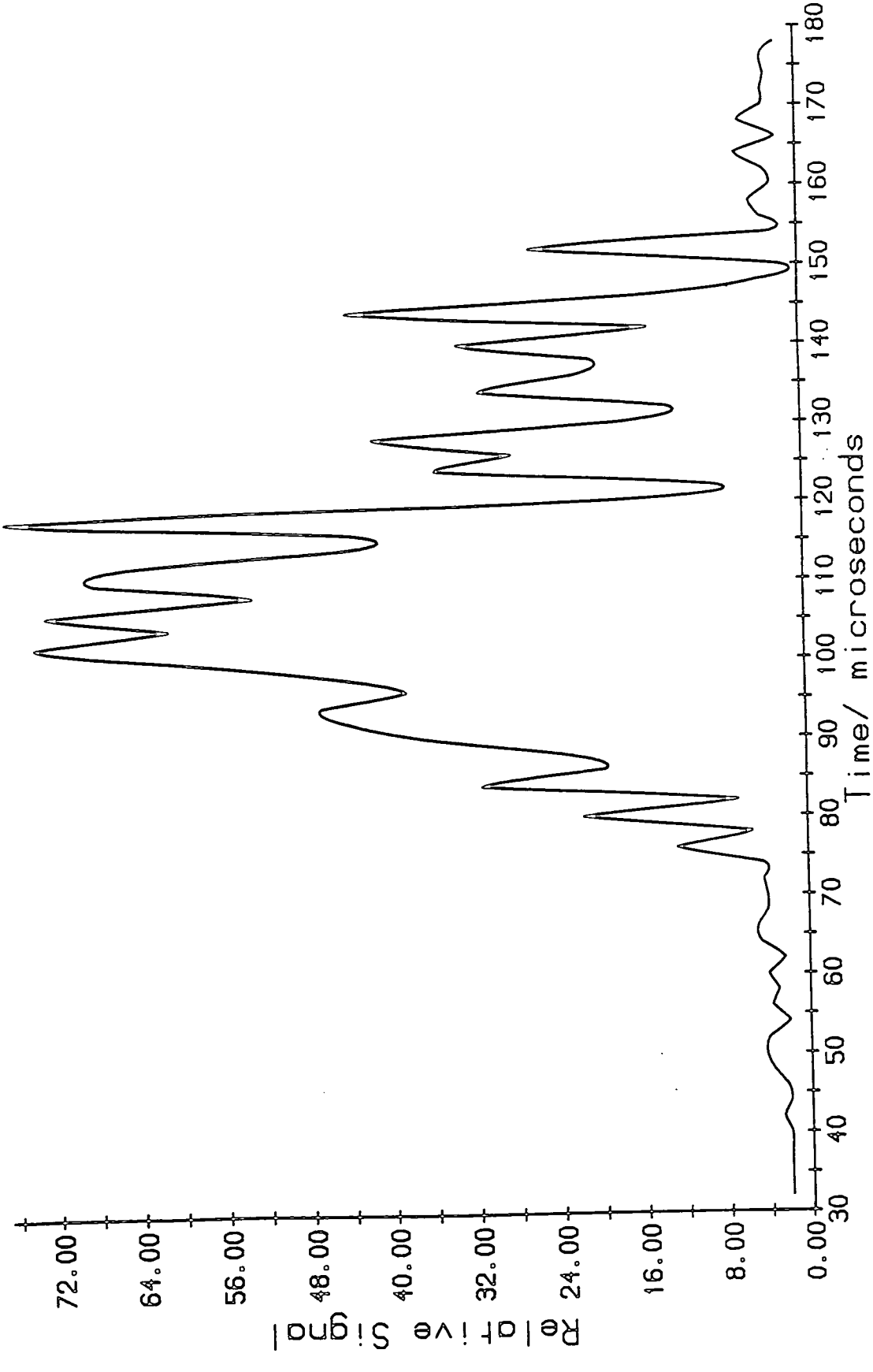

and hence the wavelength scale in those spectra, was calibrated, directly after obtaining the R2PI spectra, by running an optogalvanic spectrum. For accurate spectroscopic work, however, this calibration spectrum should be recorded simultaneously with the R2PI spectrum. The optogalvanic lines could be recorded by a CAMAC-based ADC, and stored to the PC-AT along with the ion signals to provide an absolute wavelength scale.

References.

[1] P. C. Cartwright, *Ph. D. Thesis*, Edinburgh University, 1989.

[2] V. I. Karataev, B. A. Mamyrin, D. V. Shmikk, Sov. Phys. Tech. Phys., **16**, 1177, (1972)

[3] T. E. Adams, B. H. Rockney, R. J. S. Morrison, E. R. Grant, Rev. Sci. Instrum., **52**, 1469, (1981)

[4] J. B. Hopkins, P. R. R. Langridge-Smith, M. D. Morse, R. E. Smalley, J. Chem. Phys., **78**, 1627, (1983)

[5] R. Beavis, J. Lindner, J. Grotemeyer, I. M. Atkinson, F. R. Keene, A. E. W. Knight, J. Am. Chem. Soc., **110**, 7534, (1988)

[6] L. Li, D. M. Lubman, Appl. Spectrosc., **42**, 418, (1988)

[7] W. R. Gentry, C. F. Giese, Rev. Sci. Instrum., **46**, 104, (1975)

[8] P. J. Brucat, L. S. Zherg, C. L. Pettiette, S. Yang, R. E. Smalley, J. Chem. Phys., **84**, 3078, (1986)

[9] W. C. Wiley, I. H. McLaren, Rev. Sci. Instrum., **26**, 1150, (1955)

[10] J. L. Wiza, Nucl. Inst. Methods, **162**, 587, (1979) J. L. Hellsing, L. Karrison, H. O. Andren, H. Norden, J. Phys. E: Sci. Instrum., **18**, 920, (1985)

[11] R. G. Harrison, *Department of Physics, Heriot-Watt University*,

[12] W. M. McClain, Appl. Optics, **11**, 895, (1972)

[13] K. L. Carleton, K. H. Welge, S. R. Leone, Chem. Phys. Letters, **115**, 492, (1985)

[14] L. Costrell, IEEE Trans. Nuc. Sci., **20**, 557, (1973)

[15] D. Horelick, R. S. Larsen, IEEE Spectrum, **13**, 50, (1976)

[16] A. M. Butler, *Ph. D. Thesis*, University of Edinburgh, 1989.

[17] R. Tembreull, D. M. Lubman, Anal. Chem., **58**, 1299, (1986)

Chapter 5
Time-of-Flight Mass Spectrometry.

5.1 Introduction.

One of the major objectives of this work was to design and develop a mass spectrometer to allow laser photoionisation studies to be carried out on laser desorbed molecules. In common with nearly all laser ionisation work, the ionisation laser employed was pulsed. It was therefore logical to utilise a mass spectrometric technique which would most efficiently sample ions created by this pulsed ionisation method. Although scanning mass spectrometers (magnetic and electric sector instruments, and more commonly quadrupoles) have been used in conjunction with MPI, there are a number of drawbacks associated with this methodology. Sector and quadrupole instruments are usually coupled to continuous ion sources, with the separation of ions of different masses being accomplished by scanning electric or magnetic fields so that the different masses impinge on the detector. They are clearly inappropriate for the low duty cycle pulsed laser photoionisation experiments employed here. If MPI is combined with laser desorption, the sample must be subjected to multiple or continuous irradiation in order to record the complete mass spectrum in a scanning field mass spectrometer. As has been discussed in chapter 3, this can lead to sample degradation, with a resultant change in the observed mass spectrum. These problems can be overcome by using time-of-flight mass spectrometry (TOFMS).

TOFMS is one of the simplest, yet most versatile, mass spectrometric techniques.

A schematic of a simplified TOF instrument is shown in figure 5.1(a). Ions are created in the ion source and are accelerated through a fixed potential (extracted), entering a field-free "drift tube". All the ions are extracted, to a first approximation, with the same kinetic energy, so that ions of different masses travel at different velocities through the drift tube, thereby separating in time prior to reaching the ion detector. It is easily shown that for any combination of extraction fields, the flight time (t) depends on the ion mass (m) according to

$$t = Km^{(1/2)}, \tag{5.1}$$

where K is a proportionality constant. The lighter, faster moving ions reach the detector before the slower heavy ions. By recording the ion intensity as a function of time, a time-of-flight mass spectrum is generated.

One advantage that TOFMS possesses over many other mass spectrometric techniques is that a complete mass spectrum can be recorded for each ionisation event. It also offers rapid acquisition of the complete mass range: 100-200 μs for a mass range of 1000 Da being typical of the instruments developed. Furthermore, the ability to generate a complete mass spectrum for each experimental cycle allows facile optimisation of desorption/ionisation conditions without considerable sample depletion.

A further advantage afforded by TOFMS is improved sensitivity compared to sector and quadrupole instruments. Since these latter instruments use spatial, rather than temporal, separation of ions of different masses they reject all ions not focused on to the detector at a particular field setting. When the instrument

Figure 5.1. Schematics of one- and two-field (Wiley-McLaren type) TOF mass spectrometers.

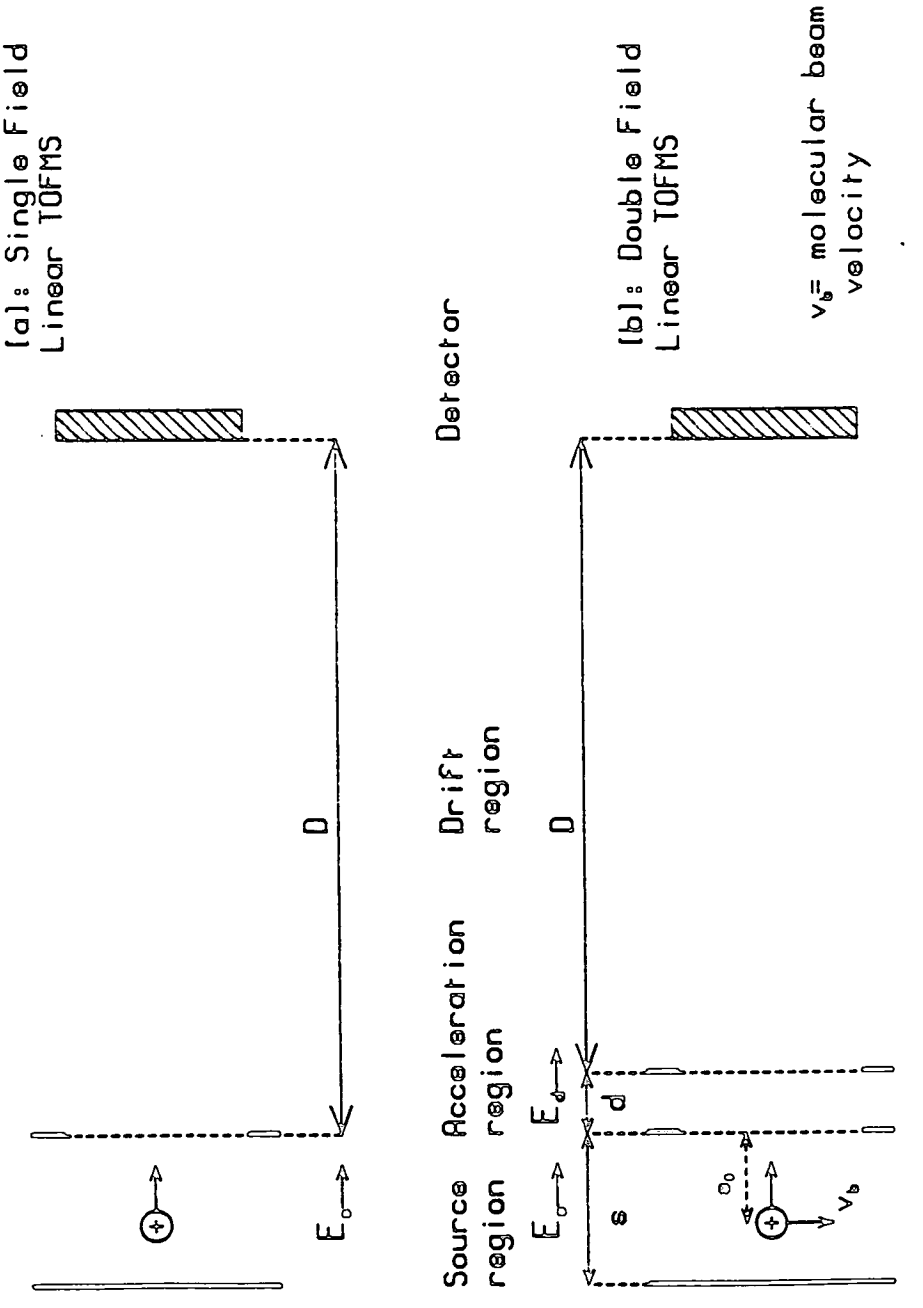

is scanned to record a mass spectrum, only a fraction of the ions created will be focused on to the detector at a particular field setting. In contrast, the transmitted intensity in a TOF mass spectrometer is potentially much higher, since a mass spectrum is recorded with static fields and all ions of a particular mass are extracted along the same trajectory, to a first approximation. Thus the sensitivity of ion collection is enhanced, with the only limitations, in an idealised situation, being the physical transmission of the grids employed in the ion extraction optics.

In the first studies using MPI-MS, quadrupole instruments were used frequently for mass selective detection [1]- [3]. Quadrupoles are relatively simple devices with rapid scanning cycles, and are easy to use. However, due to their limited mass range ($\sim$2000 Da), their generally low mass resolution, low ion transmission and, in many cases, undesirably sharp transmission functions, these devices are not ideal for coupling with MPI. In contrast, an idealised TOFMS has a much less mass-dependent transmission function and theoretically there is no upper limit to the mass detected, although in practice a number of constraints affect mass transmission (see section 5.7.).

The open design of TOF ion sources readily permits access by both laser and molecular beams, which is of prime importance in the experiments undertaken in this work. A further important factor in favour of TOFMS is the ease of both construction and operation of a TOF instrument, since the stringent design constraints of uniform magnetic fields and precise mechanical alignment required for sector instruments are not necessary. This also means that TOF instruments are considerably cheaper than sector instruments.

The major disadvantage of TOFMS, which limited its applicability in the past, is its limited mass resolution compared to other mass spectrometric methods. Sector instruments routinely have mass resolving powers of 10000, whilst early TOF devices were limited to mass resolution of around 100. The factors which determine the resolving power of a TOF mass spectrometer will be considered in the following section. There then follows a description of the two mass spectrometers designed during this work, along with a description of their operational limitations.

5.2 Resolution in a TOF Mass Spectrometer.

The mass resolving power (resolution) of a TOF mass spectrometer is defined as

$$R = m / \Delta m = t / 2\Delta t, \tag{5.2}$$

where m is the ion mass, Δm is the FWHM spread in ion mass, t is the ion flight time and Δt is the temporal width (FWHM) of the ion packet. Schlag and coworkers [4] introduced an alternative definition of mass resolution, namely

$$R = m * (t_2 - t_1) / \Delta t, \tag{5.3}$$

where $(t_2 - t_1)$ is the difference in time-of-flight for two neighbouring mass peaks, of mass m and $(m+1)$, and Δt is the temporal width of the ion packets.

Clearly, the resolving power of a TOF mass spectrometer depends on two factors:

1. the difference in arrival times at the detector of two adjacent mass peaks.

2. the temporal width of each individual mass peak.

As mentioned previously, flight times are given by $Km^{(1/2)}$, so that the difference in flight times between adjacent mass peaks decreases as mass increases. At high masses, therefore, the resolving power of the instrument is degraded, and eventually, when the FWHM of the individual ion packets is equal to the temporal difference between neighbouring peaks, it will not be possible to resolve ions separated by 1 a.m.u. The conditions at which this point is reached depend on the widths of the ion packets and the value of K, a proportionality constant determined by the particular design parameters of the instrument. A narrow ion packet width and a large value of K increase the maximum mass resolvable. The temporal width of an individual ion packet is limited by a number of broadening mechanisms, which are discussed in turn below.

5.2.1 Spatial Resolution.

In an ideal TOF mass spectrometer, all ions formed in a given source plane perpendicular to the electric field extract the same kinetic energy from the field, and, in the absence of any other peak broadening mechanisms, all ions of the same mass-to-charge ratio will arrive at the detector simultaneously. However, since it is impossible to focus a laser beam or any other ionisation source down to a single point, ions are created over a finite spatial volume in the ion source of a TOF mass spectrometer. If two ions of the same mass to charge ratio and initial kinetic energy are created at the same time, but at different positions along the spectrometer axis, they will be extracted from the source with different kinetic energies, and therefore enter the drift region with different velocities. The ion

which started further away from the draw-out grid will acquire greater kinetic energy, and if a sensible drift tube length is used, will arrive at the detector before the other ion. This difference in time-of-flight due to formation of ions over a range of positions, and therefore potentials, within the ion source broadens the ion temporal profiles. This is also true for ions that are created in the same plane, but which have different kinetic energies due to field inhomogeneities. Since the peak broadening is caused by the creation of ions at different positions within the ion source, the resolution which can be achieved, limited by this effect, is known as the spatial resolution of the mass spectrometer.

Clearly, the use of a focused or spatially apertured laser beam to create ions limits the range of potentials at which the ions are created, and therefore reduces the spatial broadening contribution. However, tight focusing can lead to other broadening mechanisms becoming operative, namely space-charge effects, which will be discussed later. A method of improving spatial resolution was described by Wiley and McLaren in 1955 [5], who introduced the "spatially-focusing", double-field ion source. This design will be discussed in some detail in section 5.3.

5.2.2 Energy Resolution.

The resolution of a TOF device is also affected by the initial velocity distribution of the ions parallel to the spectrometer axis. The simplest way to describe this effect is to consider the case of two ions with the same mass-to-charge ratio which are formed at the same position in the source, but which have velocities directly opposed along the axis of the spectrometer ($+v$ towards the detector and

-v away from it). These initial velocities are derived from the velocities of the precursor neutral molecules. Clearly, the two ions will reach the detector at different times, since the ion initially moving away from the detector must be decelerated to zero velocity before returning to its initial position with velocity +v towards the detector. This ion then follows the same trajectory as the other ion, and arrives at the detector delayed by the "turn-around time". The magnitude of this delay depends on the ion energy and the electric field strengths in the ion source. A distribution of initial ion kinetic energies, caused by the distribution of kinetic energies for the initial neutral molecules, therefore results in ion packets of finite width. The limiting resolution due to this effect is known as energy resolution.

In a simple single field TOF device, the effects of the initial energy distribution on resolution can be minimised by using high extraction fields to increase the ratio of the ion energy to the initial kinetic energy spread, although a long drift tube would have to be used to ensure adequate time separation between adjacent ion masses. The narrow velocity distribution afforded by a supersonic molecular beam propagating either parallel or perpendicular to the flight tube axis of a TOF mass spectrometer can help substantially to improve the energy resolution.

In their 1955 paper, Wiley and McLaren described a way of energy focusing in their double-field source. They introduced a time delay between the ionisation pulse and the application of a pulsed extraction field, which allowed the ions to move to new initial positions in the source. By correct selection of the time lag, it was possible to eliminate most of the initial energy spread. However, the gain in energy resolution in this case was offset by a loss in spatial resolution, since the

device had to be operated away from space-focusing conditions.

5.2.3 Timing Resolution.

In a simple TOF mass spectrometer, it is not possible to produce ion packets which have temporal widths less than that characteristic of the ionisation technique employed. Consider two ions of identical mass-to-charge ratio, with identical initial positions and velocities, created by the leading and the trailing edges, respectively, of a laser pulse of width Δt. These ions will arrive at the detector separated in time by an amount Δt if all other broadening mechanisms are ignored. Before the advent of pulsed lasers, poor timing resolution was the principal reason for the low mass resolution of TOF devices, since it was not a trivial problem to design short pulse duration electron impact ionisation sources. Nowadays pulsed lasers which produce pulses in the 10-20 ns range are routinely available, which makes laser ionisation ideal for coupling with TOFMS.

The effect of timing resolution can be minimised by simply increasing the overall ion flight times, as this increases the temporal separation of neighbouring ion peaks. Since the temporal width of the laser is fixed, it becomes less important as the ion flight time increases. A better, but more expensive way of reducing the contribution of this broadening effect is to use shorter ionisation pulses, either from picosecond lasers [6] or by employing pulse-cutting techniques [7], [8]. This approach, rather than increasing the flight path, provides better ion transmission because velocity components perpendicular to the flight tube axis of the spectrometer become more significant as the flight time increases.

5.2.4 Detector Response.

Any ion detector has a finite response time before an electrical signal is generated following the impact of ions on its active area. This response time, and the time taken to process the signal, affect the observable mass resolution of a TOF mass spectrometer without influencing its intrinsic resolution. If the detector significantly broadens the mass peaks in a spectrum, or if the final signal is recovered using a transient digitiser with limited sampling rate, it is possible that resolved peaks will not be observed even though they were produced in the mass spectrometer. It is therefore imperative that the detector and digitiser are chosen to match the capability of the mass spectrometer.

In the case of microchannel plate detectors, which have found wide application in TOFMS, the rise-time is usually in the sub-nanosecond regime [9]. The limitations due to the transient digitiser sampling rate have been discussed in the previous chapter.

5.2.5 Space-charge effects.

The width of an ion packet can be broadened due to electrostatic repulsion between the ions. It has been estimated that these effects become significant at ion number densities of 10^7-10^8 cm^{-3} [10]. In the desorption experiments carried out in this work, the ion number density was calculated to be in the range 10^5-10^6 cm^{-3} (see section 6.5), so space-charge effects should have a negligible influence of mass resolution.

5.3 The Wiley-McLaren Spatial Focusing TOF Mass Spectrometer.

The dependence of ion flight times on the initial position of ionisation and the initial velocity distribution can be, at least partially, eliminated by introducing ion focusing conditions into the TOF mass spectrometer. As mentioned previously, Wiley and McLaren developed a two-field acceleration region, which produced a first-order focusing of the ion packets, so that ions created at different positions in the source arrived at the detector at approximately the same time. The linear TOF instrument constructed in the work is based on this design. In the remainder of this section the spatial focusing properties of this type of TOF device are described.

As an introduction to focusing, consider the simple single-field TOF instrument shown in figure 5.1(a). The ion time-of-flight is given by the sum of the times spent in the acceleration and drift regions:

$$t(U_0, s_0) = [(2m)^{1/2}/qE_s\ (U_{tot}^{1/2} - U_0^{1/2})] + (2m)^{1/2} D/2U_{tot}^{1/2}, \qquad (5.4)$$

where U_0 is the initial kinetic energy of the ion, $U_{tot} = (U_0 + qs_0E_s)$ is the total kinetic energy of the ion after acceleration, s_0 is the initial distance of the ion from the draw-out grid, D is the drift length, m is the ion mass, q is the ion charge and E_s is the electric field strength in the source. With MPI, singly charged ions are invariably formed, so that q can be replaced by e, the electronic charge.

In order to spatially focus the ions at the detector, a value of D must be found so

that the flight times of ions of a given mass-to-charge ratio become independent of the initial ion position, i.e.

$$(\partial t/\partial s_0) = 0. \tag{5.5}$$

As mentioned previously, ions created at different positions (and hence, potentials) within the ion source acquire different velocities. Although an ion of given mass-to-charge ratio created close to the draw-out grid enters the drift region before an ion created further away from this grid, the latter ion will eventually overtake the former due to its creation at a higher potential. The position in the drift region at which the two ions are equidistant from the draw-out grid represents the position of the spatial focus. For this simple spectrometer, the condition for first-order spatial focusing is simply

$$D = 2s_0, \tag{5.6}$$

which is of limited practical use for two reasons. Firstly, if the position of ionisation changes, the only way to achieve spatial focusing is to change the position of the detector. Secondly, since s_0 is usually small, the drift length is too short to allow adequate separation of ions of different mass, and resolution is therefore poor. Wiley and McLaren noted that a much more versatile TOF device could be obtained by addition of a second field to the extraction region, as shown in figure 5.1(b). The flight time in this device is now given by the sum of the times spent in the three regions of the spectrometer, namely the source, acceleration and drift regions. The ion time-of-flight can be easily derived by application of Newton's equations of motion. The total flight time is now:

$$t_{tot} = t_s + t_d + t_D, \tag{5.7}$$

where t_s is the time spent in the source, t_d is the time spent in the acceleration region, and t_D is the time spent in the drift region. These times are given by the following expressions.

$$t_s = (2m)^{1/2}/qE_s[(U_0 + qs_0E_s)^{1/2} \pm U_0^{1/2}] \tag{5.8}$$

$$t_d = (2m)^{1/2}/qE_d[U_{tot}^{1/2} - (U_0 + qs_0E_s)^{1/2}] \tag{5.9}$$

$$t_D = (2m)^{1/2}D/2U_{tot}^{1/2} \tag{5.10}$$

Here $U_{tot} = (U_0 + qs_0E_s + qdE_d)$, d is the length of the acceleration region, E_d is the field strength in the acceleration region, and the '+' sign in the expression for t_s holds when ions are initially moving away from the detector. The '-' sign is valid when ions are initially moving towards the detector. All other parameters are as defined above.

Wiley and McLaren defined the parameter, k_0, as

$$k_0 = (s_0E_s + dE_d)/s_0E_s. \tag{5.11}$$

By equating $\partial t/\partial s = 0$, they obtained the first-order spatial focus condition

$$D = 2U_{tot}^{3/2}/qE_s\,(E_s/E_d\,U_{tot}^{-1/2} + (1-E_s/E_d)(U_0 + qs_0E_s)^{-1/2}). \tag{5.12}$$

When $U_0 = 0$, this equation is simplified; in terms of k_0 it is

$$D = 2s_0 k_0^{3/2}(1 - (d/s_0)/(k_0 + k_0^{1/2})). \quad (5.13)$$

This equation defines the position that the detector should be placed for first-order focusing of the ions to be achieved. The value of D is independent of mass and depends only on the parameters of the ion source. If the position of ionisation changes, it is easy to re-focus the spectrometer by simply adjusting the ratio of fields in the ionisation region.

These equations do not give the focusing condition for the case of a spread in initial energies. In order to obtain this, it is necessary to equate

$$\partial t_{tot}/\partial U_0 = 0. \quad (5.14)$$

This gives

$$D = 2U_{tot}^{3/2}\,(U_{tot}^{-1/2}/qE_d + (1/qE_s - 1/qE_d)(U_0 + qs_0E_s)^{1/2} \pm U_0^{-1/2}/qE_s). \quad (5.15)$$

Due to the presence of the final term, this solution cannot be exact. However, when $U_0 = 0$, this equation reduces to that previously obtained for D. This means that the spatial focus for ions with initially zero kinetic energy, and small displacements around s_0 is essentially the same as that for ions formed at s_0 with small kinetic energies. For the systems studied in this work, the ions have small variations in kinetic energy around the average energy of the molecular beam.

This variation is on the order of 1 meV, assuming a fully expanded seeded molecular beam. Cartwright [11] has shown that under these conditions, the value of D calculated with $U_0 = 0$ is a good approximation to the real case.

An important feature of the double-field extraction region is that the spatial resolution of the mass spectrometer is increased with respect to that of the single-field device.

If the ions have initially zero kinetic energy and are formed over a range of initial positions $s_0 \pm \Delta s/2$, the corresponding change in flight times is denoted by $\Delta t_{\Delta s}$, and the maximum resolvable mass M_s, considering spatial broadening only, is given by

$$\Delta t_{\Delta s} \simeq t_{Ms}/2M_s. \tag{5.16}$$

The value of $\Delta t_{\Delta s}$ can be obtained by expanding in a Taylor series in powers of $(\partial t/\partial s_0)$ and Δs, yielding

$$\Delta t_{\Delta s} = (\partial t/\partial s_0)(\Delta s/2) + 1/2!\,(\partial^2 t/\partial s_0^2)(\Delta s/2)^2 + \text{higher terms}. \tag{5.17}$$

The first term in this expansion is zero from the enforced space focusing conditions. Neglecting terms higher than quadratic in $\Delta s/2$, the following equation for M_s is obtained:

$$M_s = 16k_0(s_0/\Delta s)^2. \tag{5.18}$$

Since M_s depends on k_0, the double-field instrument ($k_0 > 1$) offers greater

spatial resolution than the single-field instrument ($k_0 = 1$).

A time spread in the ion packet width is introduced by the initial ion velocity distribution along the flight tube axis of the spectrometer. Unlike the spatial time spread, the first order effect cannot be eliminated, since as shown above, no exact solution for $(\partial t_{tot}/\partial U_0)_{s0}$ exists. The ion turn-around time, introduced earlier, is given by

$$\Delta t_\theta = 2(2mU_0)^{1/2}/qE_s. \tag{5.19}$$

This cannot be compensated for, even in the case of the reflectron TOF mass spectrometer discussed later. In order to calculate the energy resolution of a Wiley-McLaren type TOF mass spectrometer, the following expression should be used.

$$\Delta t_\theta = t_\theta/2M_\theta. \tag{5.20}$$

Substituting for t_θ, Δt_θ and D/s_0 from the space-focusing condition, the maximum resolvable mass, due to the effects of the initial kinetic energy distribution, is given by

$$M_\theta = 0.25(U_{tot}/U_0))^{1/2}\ ((k_0 + 1)/k_0^{1/2} - (k_0^{1/2}-1)/(k_0 + k_0^{1/2})d/s_0) \tag{5.21}$$

Sanzone [12] demonstrated that the Wiley-McLaren two-field ion source provides the theoretical limit for the energy resolution of a large class of linear TOF spectrometers and provides the practical limit for conventional TOF instruments

which employ time-independent electric fields.

5.3.1 Practical Design Considerations for a Linear TOF Mass Spectrometer.

In practice, ions are formed from a range of initial positions, with a range of initial velocities, and over a range of times determined by the pulse width of the ionisation laser. In order to calculate the mass resolution of the TOF mass spectrometer, it is necessary to estimate the overall ion packet width at the detector. The simplest way to evaluate the contribution of each of the three broadening mechanisms to the overall ion packet width is to calculate the width due to each effect. If the variables s_0 and v_0 are normally distributed about their mean values, with FWHM's Δs_0 and Δv_0 respectively, the following expressions can be applied to calculate the spatial and energy contributions to the peak width:

$$\sigma_{t_s} = (\partial t/\partial s_0)(\Delta s_0) \tag{5.22}$$

$$\sigma_{t_\Theta} = (\partial t/\partial v_0)(\Delta v_0), \tag{5.23}$$

assuming that the instrument is spatially focused. The laser temporal profile can also be approximated by a Gaussian function, with FWHM equal to $\sigma_{t_{laser}}$. If these three variables are independent, the total peak width is given by [13]

$$\sigma_{tot} = [(\sigma_{t_s})^2 + (\sigma_{t_\Theta})^2 + (\sigma_{t_{laser}})^2]^{1/2} \tag{5.24}$$

In the present work, the ionisation laser beam was apertured, and consequently,

the initial spatial distribution of ions was at most 1 mm (i.e. Δs_0 = 1 mm). The translational temperature of the molecular beam gives an indication of the magnitude of α_{t_θ}. Rotational temperatures as low as 8 K have been measured for supersonic expansions of aniline in this spectrometer [14]. Under the experimental conditions employed in the present work, it was not possible to measure the rotational temperature of desorbed and entrained neutrals, but it is thought likely that this would be ~ 20 K. Translational temperatures are more efficiently cooled than rotational temperatures in a supersonic expansion, so a translational temperature of 10 K was assumed, corresponding to initial ion energies of 1 meV. Finally, it was assumed that the laser pulse width was 10 ns FWHM.

In designing a double-field linear TOF device, the system parameters must be chosen to give an optimum combination of mass resolution and ion transmission. The relative importance of these two factors depends on the specific application.

Cartwright [15] has shown that the resolving power of an idealised linear TOF mass spectrometer can be increased indefinitely by decreasing E_s, increasing U_{tot} and choosing an appropriate value of k_0 so that the peak width is minimised for given values of E_s and U_{tot}. Physically, this results in an instrument with a long drift tube and therefore long ion flight times.

If, however, the ion transmission is considered, it can be readily shown that such a TOF device would have low numbers of ions reaching the detector, and therefore low sensitivity. Consider an ion with initial off-axis energy U_o, which acquires total kinetic energy U_{tot} in the axial direction. The ion flight time is

approximated by

$$t_f = D(m/2U_{tot})^{1/2}, \tag{5.25}$$

and the distance moved off-axis is given by

$$d_x = D(U_o/U_{tot})^{1/2}. \tag{5.26}$$

Substituting in the first order space-focus condition gives

$$d_x = 2qE_s(U_o U_{tot})^{1/2}(k_0^{1/2} + E_s/E_d(1-k_0^{1/2})). \tag{5.27}$$

From this expression, it is clear that all the factors which improve resolution, namely high U_{tot} and k_0, result in smaller ion transmissions.

A number of compromises must therefore be reached in the design of the linear TOF mass spectrometer. These are listed below.

1. M_s is shown to increase with $s_0/\Delta s$. It is easy to reduce Δs by focusing or aperturing down the ionisation laser beam. In practice, however, s_0 is limited by the physical size of the ion source.
2. At a first glance, it would appear sensible to operate with the additional constraint of $(\partial^2 t/\partial s_0^2) = 0$. However, this yields $D = 2d(k_0/(k_0 - 3))$, which requires a short drift tube. Hence any improvement in spatial resolution is negated by the unacceptably short flight times. Practical mass spectrometers operate with $(\partial^2 t/\partial s_0^2)$ = a maximum, a condition which requires the use of

a long drift tube.

3. Acceleration to overall high kinetic energies (i.e. high U_{tot}) improves the energy resolution, since the initial kinetic energy is then only a small fraction of the total energy. However, there must be a balance between high overall ion energies and flight times sufficiently long enough to allow good resolution. The latter can be increased by increasing D, but this has the undesirable side-effect of reduced ion transmission.

4. A final consideration arises due to the relative orientations of the flight tube and the molecular beam. Ions extracted into the flight tube retain the component of velocity parallel to the molecular beam direction. If these ions were left to complete their initial trajectories, the majority would miss the detector. By applying a deflection field, these ions can be sent on a trajectory parallel to the axis of the spectrometer. As shown in figure 4.5, a pair of biased parallel plates is mounted above the two-stage ion extractor. Application of a field E_{def} allows compensation for the velocity component of the molecular beam (v_b in figure 5.1(b)), where

$$E_{def} = (2mU_{tot})^{1/2}\, v_b/qL_{def}. \qquad (5.28)$$

Here L_{def} is the axial length of the deflection plate. Since all masses are assumed to be accelerated to approximately the same beam velocity [16], v_b, the transmission of this device is clearly mass-dependent [17]. This sets up a "mass window", outside of which the ion transmission is suppressed. However, by judicious choice of deflection voltages, an appreciable transmission can be achieved over a reasonable mass range.

5.4 An Experimental Linear TOF Mass Spectrometer.

It was decided to construct two TOF instruments using a common ion source region. One of these was a reflecting-geometry TOF mass spectrometer or "reflectron" (see later), which was designed to have its initial flight tube collinear with the molecular beam axis. The second, linear TOF mass spectrometer was constructed as a "stop-gap" instrument. The flight tube of this device was mounted at right angles to the molecular beam axis in order to accomodate the flight tube of the higher resolution reflectron mass spectrometer. This linear TOF mass spectrometer was designed bearing in mind the points outlined above. However, a number of other practical constraints also had to be considered.

Previous studies had shown that a linear flight tube length of 1.2-1.5 m gave a good compromise between resolution and transmission [11]. Also, due to the fact that deflection plates had to be mounted above the extraction optics, the overall length of (s_0 + d) was limited to 5 cm. The potentials applied to the extraction plates were limited to a maximum of 5 kV by the available power supplies. Table 5.1 gives the operating parameters chosen for the spatially- focused linear TOF device.

Figure 5.2 shows a plot of the ion flight time and mass resolution versus ion mass for the linear TOF mass spectrometer with the parameters given in table 5.1. These were calculated using a simple FORTRAN program incorporating the equations of motion given earlier, and a number of adjustable parameters such as ion mass, initial kinetic energy distribution and laser temporal and spatial widths. From this figure it is obvious that a maximum in mass resolution occurs near m/e

Table 5.1 Experimental Parameters for Linear TOF Mass Spectrometer

Repeller - Draw-out distance, s = 35 mm

Draw-out- Centre of laser spot distance, s_0 = 17.5 mm

Draw-out - Flight distance, d = 10 mm

Length of deflection plates, L_{defl} = 30 mm

Drift region length, D = 1.25 m

$V_{Repeller}$ = 2310 V

$V_{Draw\text{-}out}$ = 1930 V

V_{Flight} = 0 V

$V_{Deflector}$ = 0-180 V

Average energy of extracted ions, U_{tot} = 2120 eV

Field strength in draw-out region, E_s = 10857 Vm^{-1}

Field strength in acceleration region, E_d = 193000 Vm^{-1}

k_0 = 11.15

Figure 5.2. Ion flight times and mass resolution as a function of ion mass in the experimental linear TOF mass spectrometer.

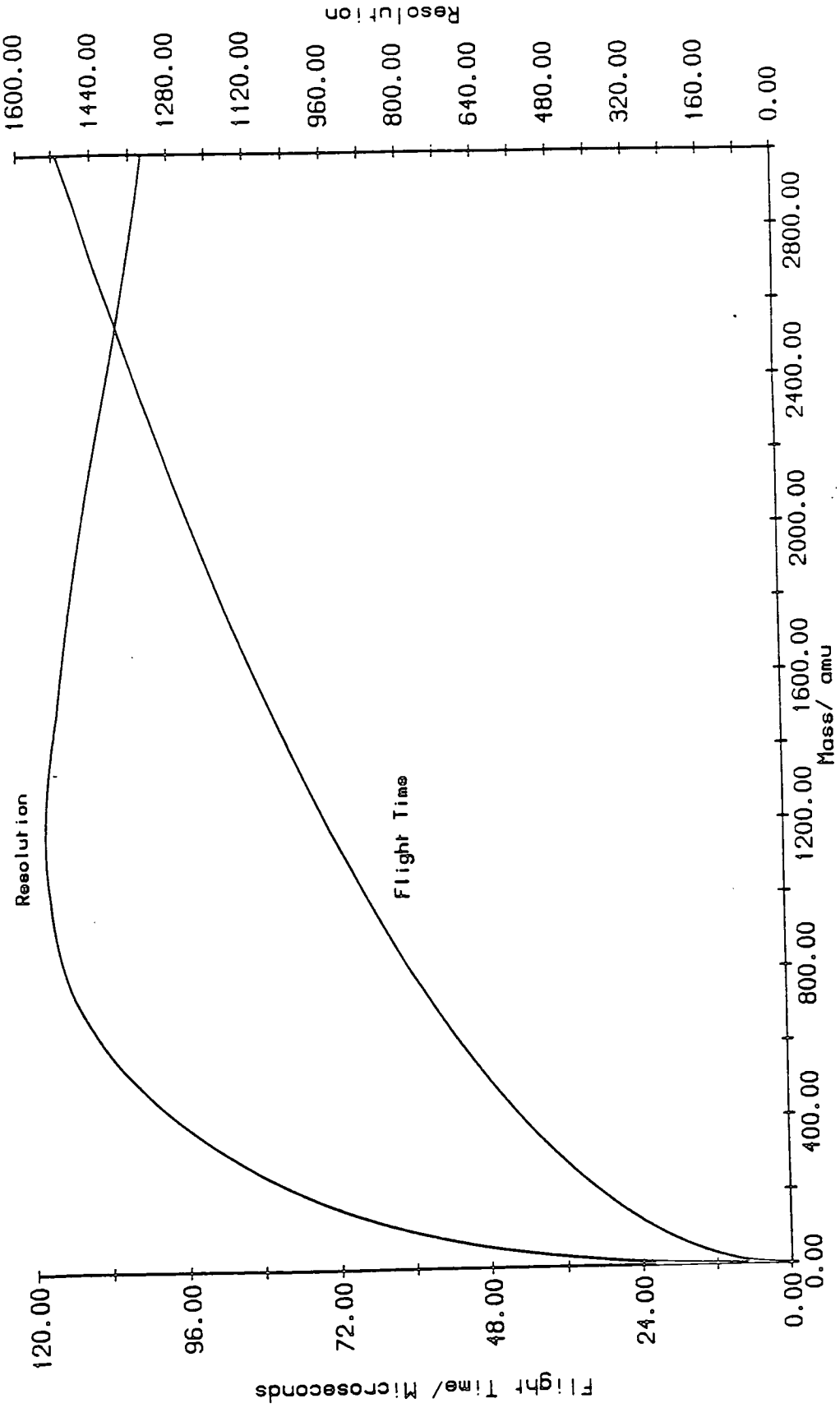

= 1200, with the maximum resolvable mass (i.e. the largest mass at which $\Delta t <$ difference in flight time between ions of mass m and m + 1) being approximately 1500 Da.

The calculated mass resolution of this device at mass 93 (aniline) is ~800, with an ion peak width of 12 ns. Figures 5.3 and 5.4 show the dependence of the flight time for ions of m/e = 93 on v_0 ($=(2U_0/m)^{1/2}$) and s_0, respectively. The flight times in figure 5.3 were calculated with a fixed s_0 (= 17.5 mm) and a distribution of v_0. No account was taken of the temporal width of the laser pulse. At a translational temperature of 10 K, the FWHM of the velocity distribution in the molecular beam is ~ 70 ms^{-1}. This was calculated assuming a one-dimensional Maxwellian velocity distribution, with mean velocity 1766 ms^{-1} (see Appendix A) and standard deviation given by $(kT/m)^{1/2}$, where k is Boltzmann's constant. This range of velocities leads to a flight time distribution of width 6.2 ns, i.e. σ_{t_Θ} = 6.2 ns. As can be seen from Figure 5.4, the dependence of the ion flight time on s_0 in an idealised spatially-focused TOF mass spectrometer is small. Over a (generous) laser spot of 1 mm diameter, centred at s_0 = 17.5 mm, the variation in flight time, for a given v_0, is only 0.13 ns for m/e = 93, i.e. σ_{t_s} = 0.13 ns. Again, it was assumed that the ions were created instantaneously, i.e. $\sigma_{t_{laser}} = 0$. Therefore, in such an idealised TOF mass spectrometer, the main contributions to peak broadening should be from the kinetic energy (velocity) distribution of the neutral precursor molecules and the temporal width of the ionising laser pulse.

Figure 5.5 shows the mass spectrum of aniline obtained under hard ionisation

Figure 5.3. Dependence of flight time on initial velocity v_0.
Calculated for aniline in the linear TOF mass spectrometer.

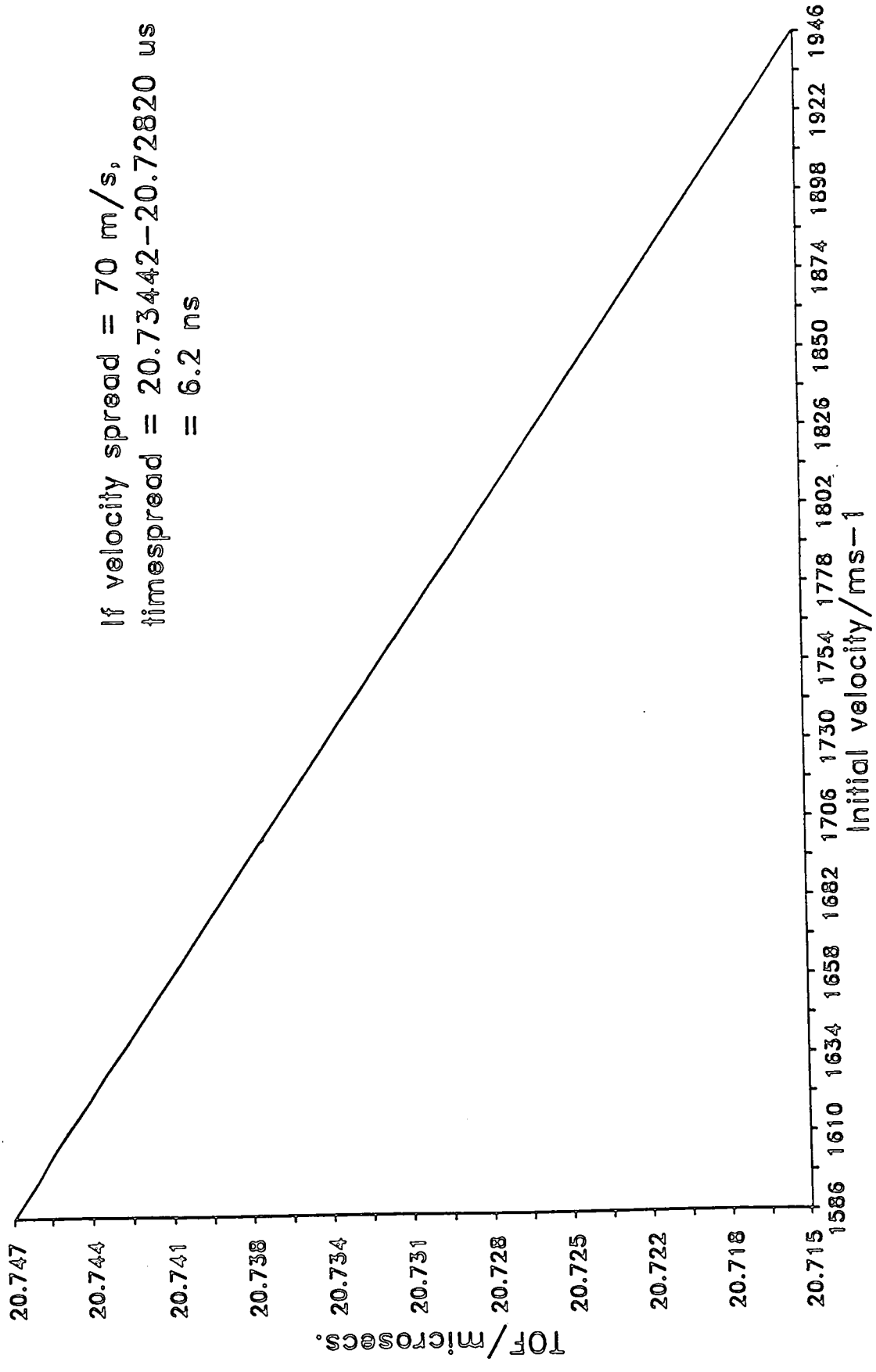

Figure 5.4. Dependence of flight time on position of ionisation s_0.
Calculated for aniline in the linear TOF mass spectrometer.

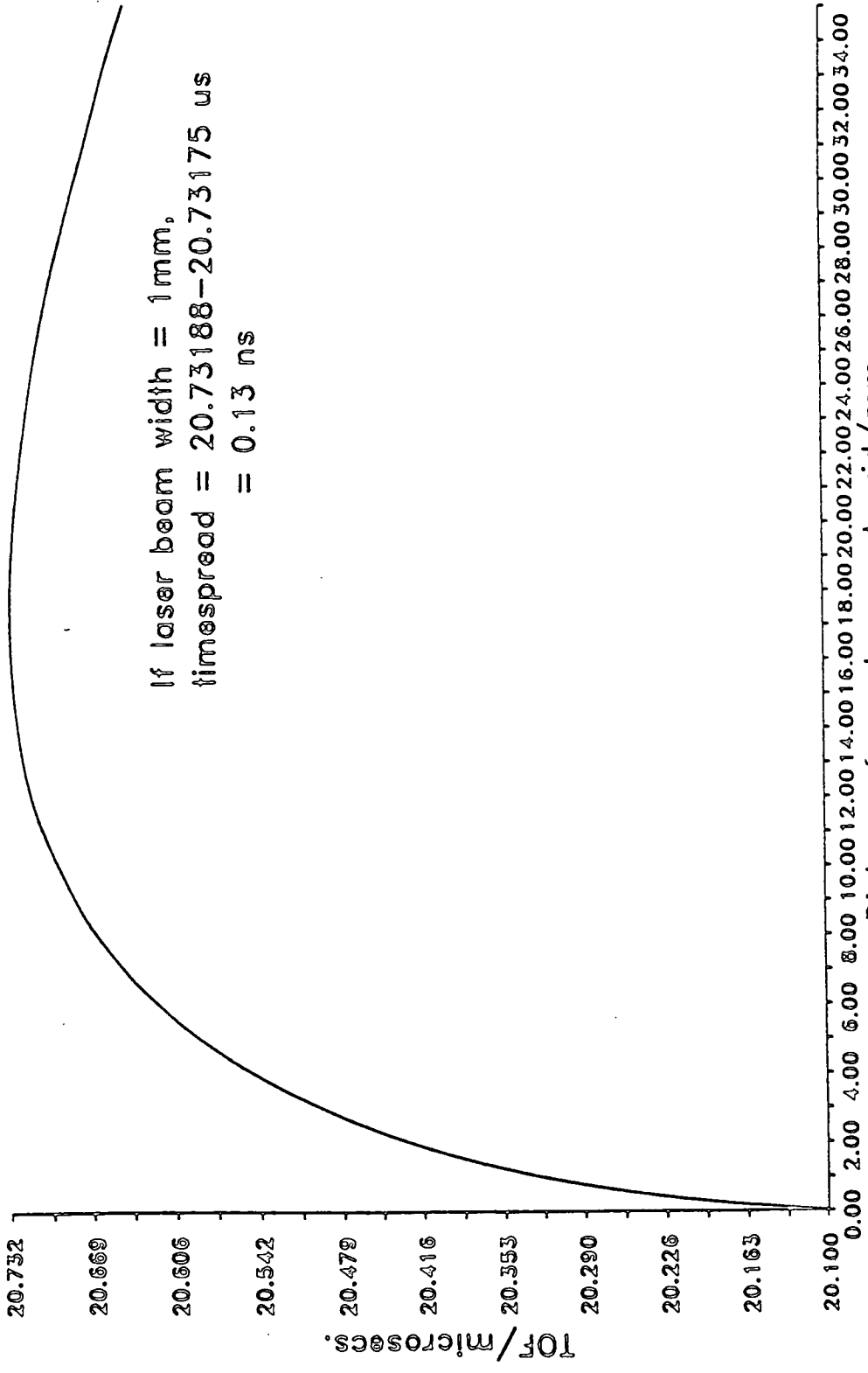

conditions, recorded using the linear TOF mass spectrometer, at λ = 293.75 nm. The photoion peaks are significantly broader ($\sim$ 40-60 ns) than predicted by the above model. This discrepancy can be partially explained by a degradation in mass resolution due to the limited signal sampling rate of the transient digitiser (100 MHz in this case). However, the narrowest aniline peaks that could be obtained were 30 ns FWHM under soft ionisation conditions.

A further broadening effect which cannot be neglected in this particular case is that of coulombic repulsion between ions created in the laser focal volume.

Approximately 5 x 10^9 aniline ions cm^{-3} would be created under hard ionisation conditions with a laser power density of $\sim$ 700 $MWcm^{-2}$. Both absorption and ionisation steps in the R2PI scheme would be saturated under these conditions. Using the expression

$$q^2/4\pi\varepsilon_0 r = 1/2\ mv_c^2, \tag{5.29}$$

the coulombic velocity component v_c can be calculated. Here ε_0 is the permittivity of free space and r is the centre-centre separation of the positively charged ions created within the laser focal spot. With r = 5.85 x 10^{-4} m, the coulombic velocity component is $\sim$22.5 ms^{-1}, yielding an overall coulombic velocity spread of 45 ms^{-1} for aniline. When added to the initial velocity distribution, this yields an overall velocity spread of 115 ms^{-1}. From figure 5.3, this gives a value of σ_{t_θ} = 10.3 ns, and an overall peak width of 15 ns. This peak width is still considerably less than the experimentally observed peak widths. In order to fully account for these observed peak widths, therefore, some aspects of

Figure 5.5. Hard ionisation mass spectrum of aniline recorded in the linear TOF mass spectrometer. λ = 293.76 nm, I = 700 $MWcm^{-1}$.

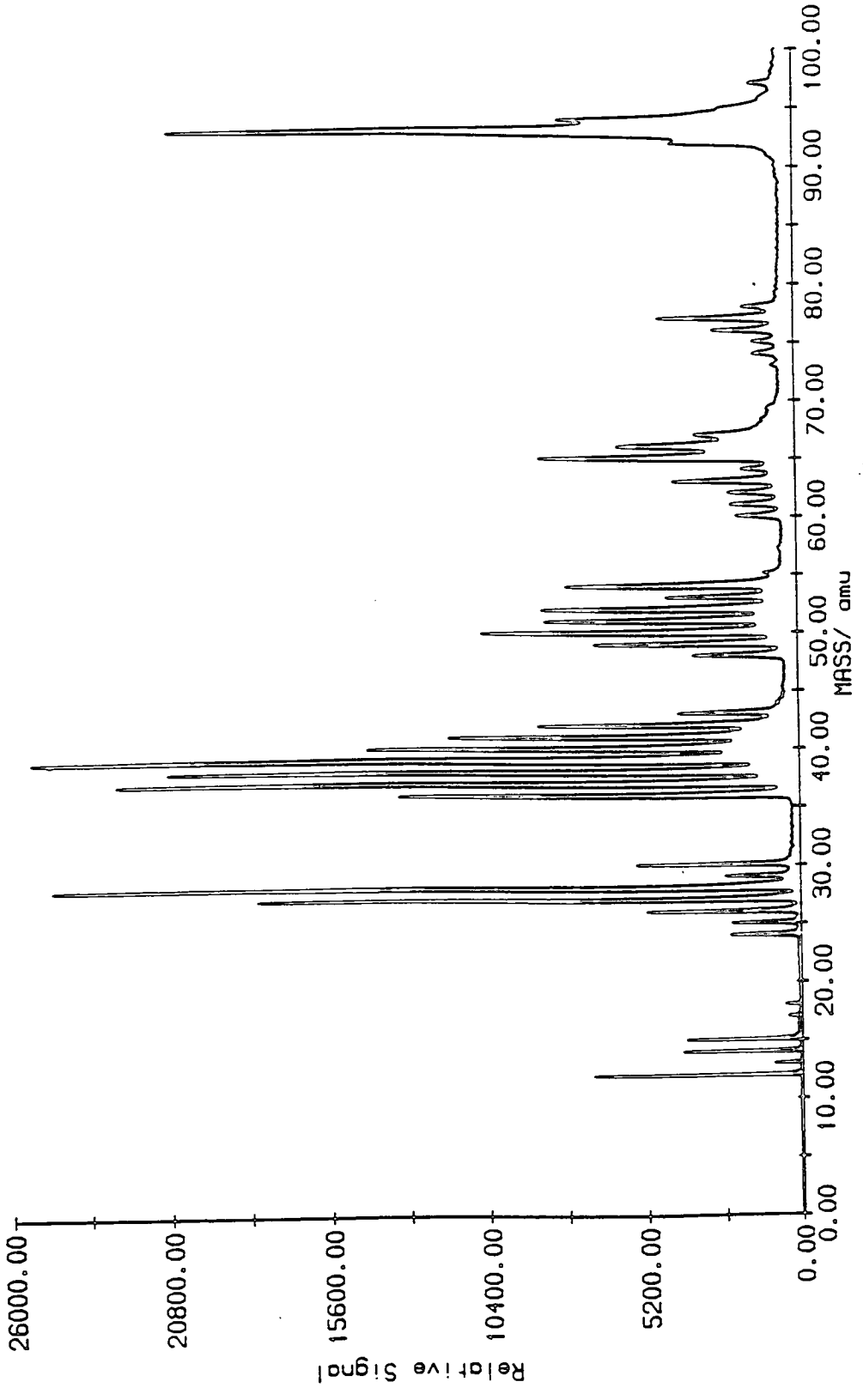

non-ideality in the experimental TOF mass spectrometer must be considered.

The most obvious departure from ideality in the experimental linear TOF mass spectrometer is the fact that the entire "field-free" region is not truly field-free. In fact there is a considerable amount of field penetration at either end of the flight tube, from both the field between the detector and flight tube ground plate and the deflection field. The major peak broadening influence exerted by this latter field arises due to the fact that ions are created over a finite distance along the molecular beam axis. Those ions created furthest downstream pass closer to the positively biased electrode and therefore undergo a greater retardation than those formed further upstream. Further non-ideality is introduced by field inhomogeneities in the ion source and acceleration regions. Figure 5.6 shows a contour plot of the potentials in the extraction optics of the linear TOF device, generated by a numerical solution of Laplace's equation in two dimensions (see Appendix B). There is obviously a certain amount of field penetration at the plate edges. If this leakage is sufficiently high, the fields in the draw-out and acceleration regions will differ from the values set to satisfy the space-focusing condition. Indeed, it may no longer be possible to achieve true space-focusing, since in solving the original equations of motion it was assumed that the field strengths in each region are constant. This can only be achieved by employing infinitely large plates. Cartwright [11] has simulated the ion trajectories in a similar TOF mass spectrometer, obtaining overall peak widths of ~ 30 ns for mass 98 ions, which is in better agreement with the experimental findings. He showed that the broadening effect of both detector and deflection fields was negligible compared to peak broadening due to field inhomogeneities in the ion

Figure 5.6. Potential map for the extraction optics employed in the linear TOF mass spectrometer.

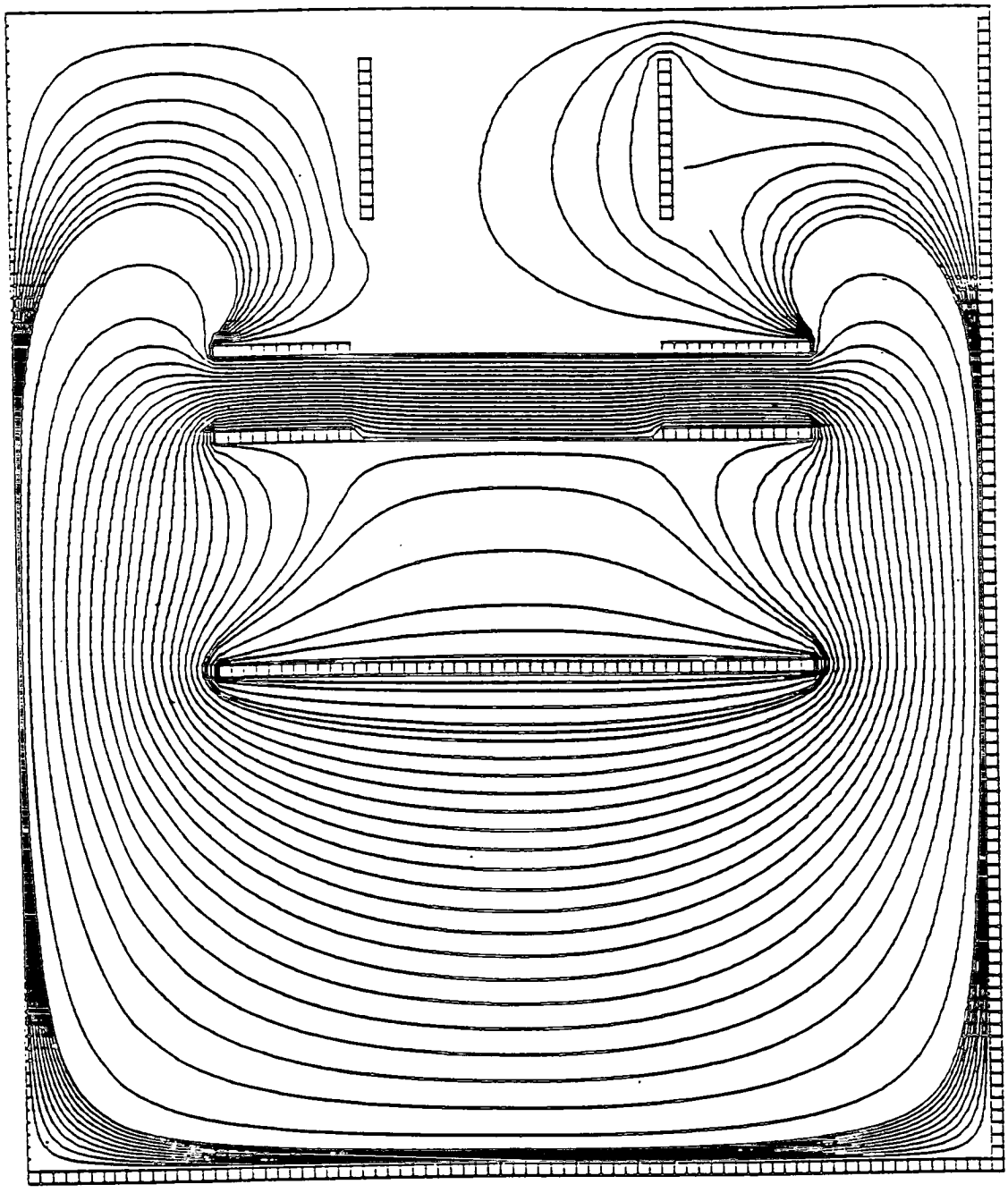

source region.

The effect of field penetration could be reduced by introduction of guard rings between the repeller and draw-out plates in order to improve the uniformity of the fields in each region (figure 5.7). This, however, is not convenient with the currently-used configuration involving perpendicular extraction of ions from a molecular beam, since it is more difficult to introduce both the molecular and laser beams into such a source without excessive scattering of either beam.

The Wiley-McLaren space-focusing instrument proved to be a landmark in the development of a TOF mass spectrometer with improved resolution. However, the maximum resolution from this type of device was still only a few hundred, which was poor compared to sector instruments that could routinely resolve masses of several thousand Da. A number of designs have been proposed to improve the resolution of the TOF mass spectrometer [18]- [20]. Of these, the most widely-used is the reflecting-geometry TOF mass spectrometer or "reflectron" introduced by Mamyrin and coworkers [21], [22].

5.5 Reflectron TOF Mass Spectrometer.

Figure 5.8 shows a schematic of a reflectron TOF mass spectrometer. The reflectron mass spectrometer differs from the linear device discussed above in that, instead of placing an ion detector after the field-free drift region, a two-stage ion mirror is used to "reflect" the ions through a second drift region to the detector. Two geometries are shown in figure 5.8, namely that described by Mamyrin and coworkers in their original papers, and a modified version of this

Figure 5.7. Potential map for the linear TOF mass spectrometer extraction optics, including guard rings.

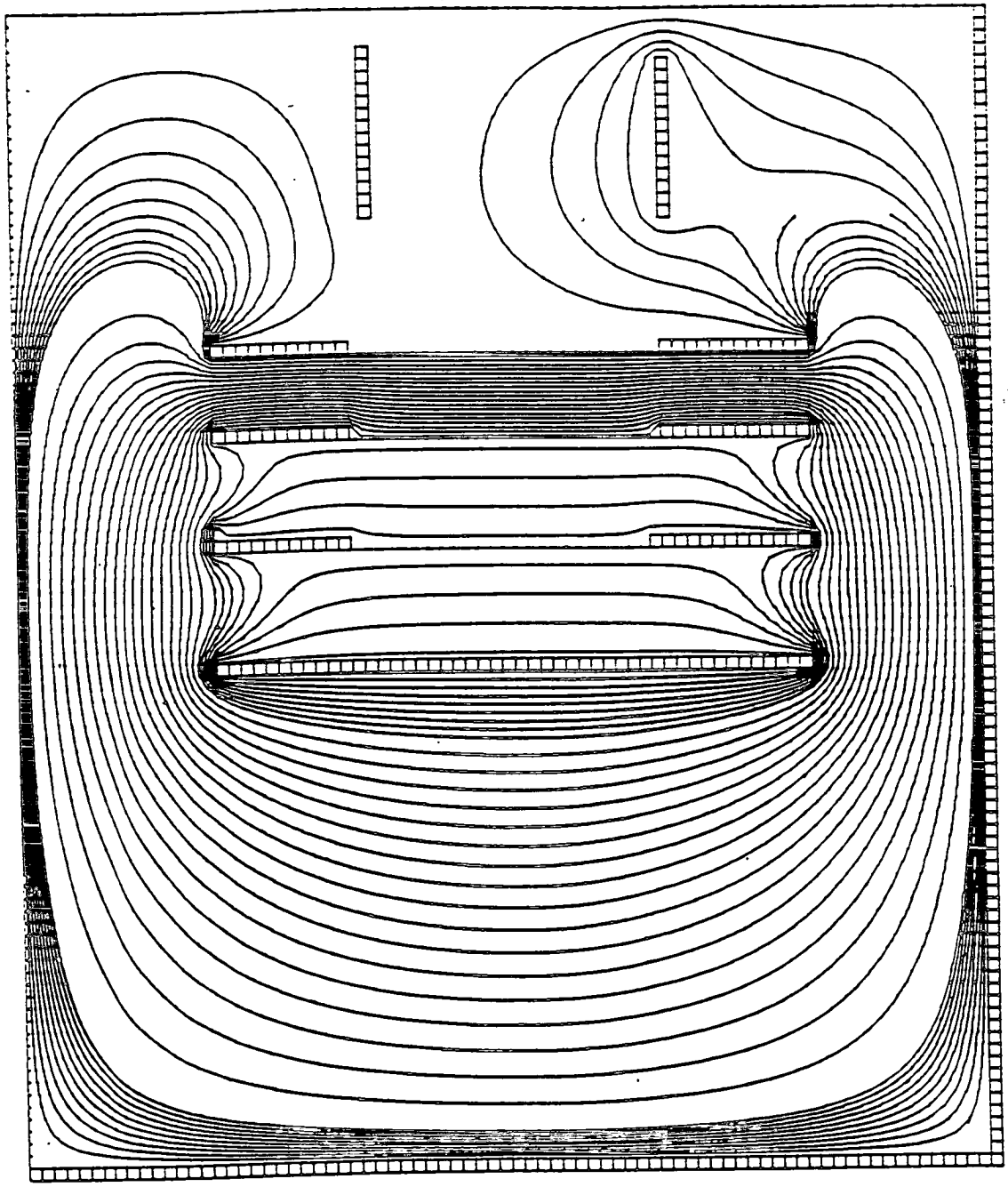

design, used by Schlag and coworkers [4], [7]. These two geometries differ in only one respect, namely the means of orienting the ion packets relative to the reflecting field (mirror) so that they arrive at the detector. In the original design, the ion source was oriented in such a manner that the plane of the ion packets as they were formed was perpendicular to the spectrometer axis. The ions were sent on their desired trajectories by means of a deflection field placed after the extraction optics. The design of Boesl et al. [7] differs in that deflection plates were not employed. Instead, the ion extraction optics and detector were tilted at an angle θ off-axis. The discussion below is based on the original work of Mamyrin et al., but is applicable to the instrument designed at the University of Edinburgh, which followed the design of Boesl et al.

5.5.1 The Mamyrin Reflectron TOF Mass Spectrometer.

The reflectron TOF mass spectrometer has a focusing action which compensates for the range of kinetic energies possessed by ions formed over a finite range of positions in the ion source. In order to achieve this effect, the reflectron mass spectrometer must satisfy three focusing conditions. The first of these is the space-focusing condition of Wiley and McLaren. In the reflectron, ions are initially focused at some distance, l_0, near the flight grid. This is denoted as PS in figure 5.8. Ions of a particular mass-to-charge ratio are in a spatially small packet at this point. Mamyrin [22] pointed out that the "thickness", Δl, of the ion packet at this "pseudo-source" is determined almost entirely by the initial energy spread of the ions ($q\Delta U_0$). Thus

$$\Delta l = l_0(\Delta U_0/U_0)^{1/2}, \tag{5.30}$$

Figure 5.8. Schematic diagram of a reflectron TOF mass spectrometer, showing both Mamyrin and Schlag designs.

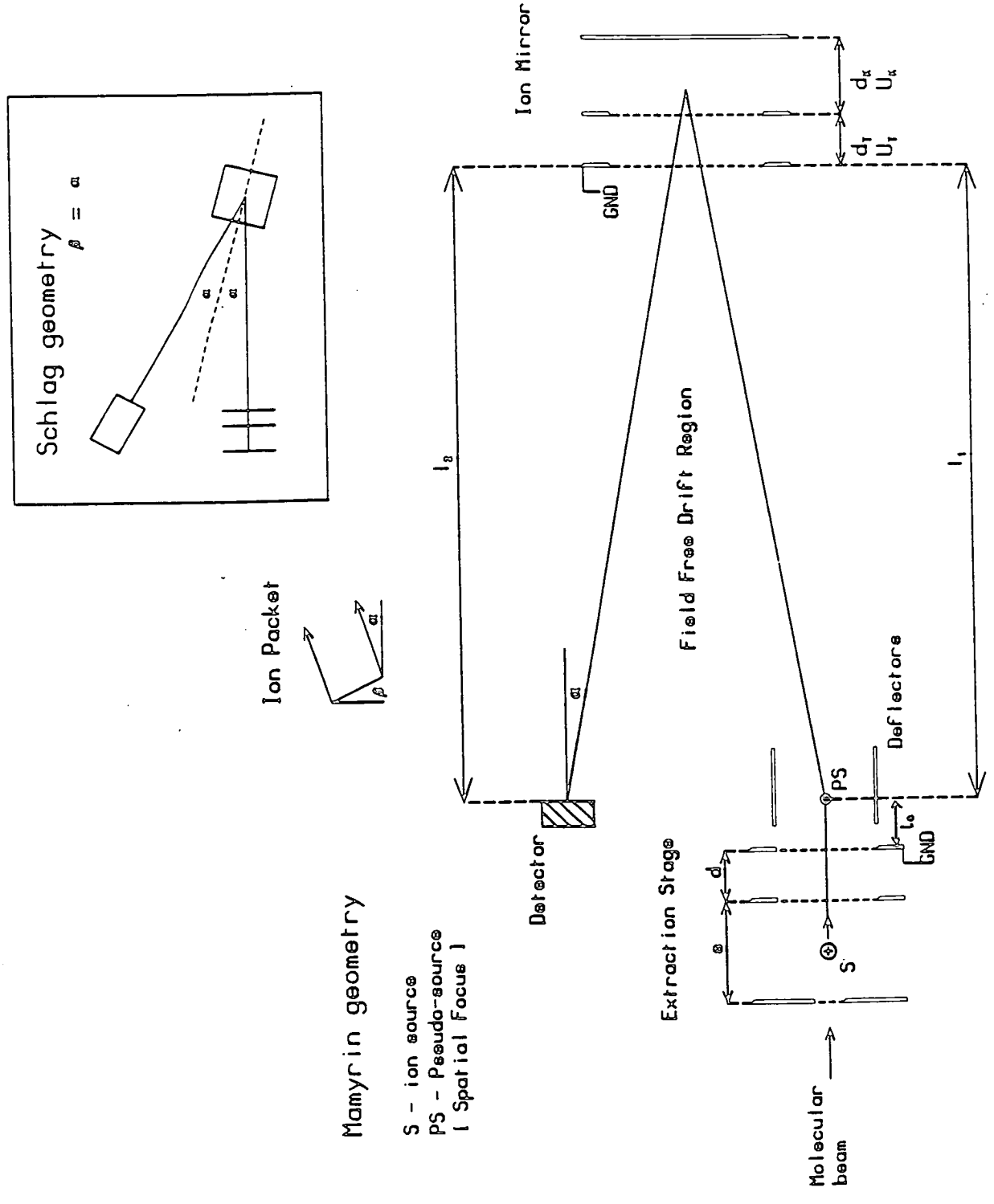

where qU_0 is the ion energy in the drift region and l_0 is the focal length of the ion source. Since the packet thickness in the plane of the space-time focus is proportional to l_0, the value of Δl in a reflectron is much smaller than in an ordinary linear TOF mass spectrometer.

If the ions drift further than this point before encountering the detector, ion packets with different mass-to-charge ratios become increasingly separated in time. However, as the ions packets drift towards the ion mirror, they disperse due to the spread in their initial kinetic energies. This energy spread is, as mentioned previously, determined by the spatial volume in which the ions were formed and the initial translational energy that the neutral precursor molecules possessed in the ion source. In order to combat this loss of resolution, the dispersed ion packet must be reflected and refocused on to the plane of the detector by the action of the ion mirror. For a particular ion packet, the faster moving ions, which arrive at the reflector first, penetrate the field more deeply before being decelerated to rest than their slower-moving counterparts. If the two-stage retardation/reflection field is set up correctly, the extra time spent by the fast ions in the reflector exactly compensates for the reduced time they spend in both legs of the two-stage drift tube. The original narrow packet width at the Wiley-McLaren focal plane is therefore preserved after a long drift time. Thus peak widths are narrow, whilst the time interval between adjacent masses is significantly increased in comparison to a conventional linear TOF mass spectrometer. Thus the mass resolution is also significantly increased with respect to a linear TOF mass spectrometer.

As shown in figure 5.8, the drift region in a reflectron comprises two legs of

length $(l_0 + l_1)$ and l_2 respectively. These lengths are measured orthogonal to the ion mirror, from the centre of the flight grid in the ion source and from the detector grid, respectively. The magnitude of the electric fields in each region of the reflectron mass spectrometer are given by

$$E_s = (V_{rep} - V_{do})/s, \tag{5.31}$$

$$E_d = V_{do}/d, \tag{5.32}$$

$$E_T = -U_T/d_T, \tag{5.33}$$

$$E_K = -U_K/d_K, \tag{5.34}$$

$$E_{det} = V_{MCP}/d_{det}, \tag{5.35}$$

where V_{rep} is the voltage applied to the repeller plate, V_{do} is the voltage applied to the draw-out plate, U_T is the voltage applied to the retarding electrode of the mirror, $(U_T + U_K)$ is the voltage applied to the mirror backplate, V_{MCP} is the voltage applied to the detector, and d_{det} is the distance of detector grid from active surface of MCP.

Ion accelerations are given by

$$a_i = qE_i/m, \tag{5.36}$$

where q and m are the charge and mass of the ion respectively.

The velocities of an ion as it exits the draw-out and flight regions are

$$v_1 = [2a_s s_0 + v_0^2]^{1/2} \tag{5.37}$$

$$v_2 = [2a_d d + v_1^2]^{1/2}, \tag{5.38}$$

where s_0 is defined as above and v_0 is the initial ion velocity directed along the spectrometer axis. The ion velocity component orthogonal to the earthed grid of the mirror is , where θ is the angle between the planes of the ion source and of the mirror,

$$v_3 = [2a_T d_T + (v_2 \cos\theta)^2]^{1/2}, \tag{5.39}$$

whilst the velocity of the ion as it strikes the surface of the detector is

$$v_{MCP} = [2a_{det} d_{det} + v_2^2]^{1/2}. \tag{5.40}$$

The ion flight time is the sum of the times spent in each region of the spectrometer,

$$t_{tot} = t_s + t_d + t_{drift} + t_T + t_K + t_{det}, \tag{5.41}$$

where

$$t_s = (v_1 - v_0)/a_s, \tag{5.42}$$

$$t_d = (v_2 - v_1)/a_d, \tag{5.43}$$

$$t_T = 2(v_3 - v_2\cos\theta)/a_T, \tag{5.44}$$

$$t_K = -2v_3/a_K, \tag{5.45}$$

$$t_{det} = (v_{MCP} - v_2)/a_{det}, \text{ and} \tag{5.46}$$

$$t_{drift} = (l_0 + l_1 + l_2)/v_2\cos\theta. \tag{5.47}$$

The above derivation neglects initial velocity components parallel to the grids of the ion reflector. With $\theta > 0$, initial off-axial components directed to or from the ion detector contribute to the ion flight time. In the above derivation, $(l_0 + l_1 + l_2)$ was assumed to be constant. However, off-axial velocity components alter this, since the point at which the ion strikes the detector changes, hence altering l_2.

In order to derive the focusing conditions, it is necessary to solve the following equations.

$$\partial t/\partial v_2 = \partial t'/\partial U_0 = 0, \text{ and} \tag{5.48}$$

$$\partial^2 t'/\partial v_2^2 = \partial^2 t'/\partial U_0^2 = 0, \tag{5.49}$$

where t' is the time of flight of an ion from the pseudo-source to the detector,

$$t' = t_T + t_K + t_{det} + [l_1 + l_2]/v_2\cos\theta, \tag{5.50}$$

and qU_0 is the average kinetic energy of ions at the pseudo-source.

The kinetic energy of each ion is given by kqU_0, where k is a numerical constant approximately equal to unity. Re-casting the above flight time equations in terms of kqU_0, the following expressions are obtained

$$t_L = L(2qU_0/m)^{-1/2}/k^{1/2}, \tag{5.51}$$

$$t_T = 4d_T(2qU_0/m)^{-1/2}(U_0/U_T)(k^{1/2} - (k-U_T/U_0)^{1/2}), \tag{5.52}$$

$$t_K = 4d_K(2qU_0/m)^{-1/2}(U_0/U_K)(k - U_T/U_0)^{1/2}, \tag{5.53}$$

$$L = l_1 + l_2. \tag{5.54}$$

Expressing t' in terms of k, the following expression is obtained:

$$t' = CF(k), \tag{5.55}$$

where

$$F(k) = A_1 k^{-1/2} + nA_1(k^{1/2} - (k-p)^{1/2}) + (k-p)^{1/2}, \tag{5.56}$$

$$A_1 = LU_K/4d_K U_0, \tag{5.57}$$

$$n = 4d_T U_0/LU_T, \tag{5.58}$$

$$p = U_T/U_0, \tag{5.59}$$

and

$$c = 4d_k(2qU_0/m)^{-1/2}\ U_0/U_K. \tag{5.60}$$

The second-order TOF focusing conditions with respect to energy then become

$$(\partial F/\partial k)_{k=1} = 0, \tag{5.61}$$

and

$$(\partial^2 F/\partial k^2)_{k=1} = 0. \tag{5.62}$$

Since in practice $n << 1$, the following solution is obtained which satisfies the above conditions:

$$A_1 \approx (3.0)^{1/2}, \tag{5.63}$$

$$p \approx 2/3, \tag{5.64}$$

$$F_0 = F_{(k=1)} \approx (16/3)^{1/2}. \tag{5.65}$$

A number of possible combinations of voltages and plate spacings in the mirror fit the above equations. The solutions employed by Mamyrin et al. [22] were

$$U_T \simeq 0.7U_0, \tag{5.66}$$

$$U_K \simeq 0.45U_0, \tag{5.67}$$

$$d_T \simeq 0.008L, \text{ and} \tag{5.68}$$

$$d_K \simeq 0.06L. \tag{5.69}$$

5.6 An Experimental Reflectron TOF Mass Spectrometer.

The reflectron TOF mass spectrometer employed in this work followed the design of Boesl et al. [7], with the ion mirror angled with respect to the extraction optics and the detector. This geometry was chosen for ease of construction, since the three vacuum chambers could be simply mated together along a common axis.

The extraction optics and ion mirror have been described in the previous chapter. The ion extraction optics and first drift region were aligned collinear with the molecular beam axis. The core of the molecular beam was admitted to the ion source through a hole in the repeller plate (see figure 4.6). The second drift region was oriented at 8^o to the first, with the axis of the reflector bisecting this angle. The deflection field was therefore provided by the components of the mirror retarding and reflecting fields, which act perpendicular to the molecular beam axis ($E \sin 4^o$), thereby negating the need for deflectors near the ion source. However, accurate alignment of the mirror is required to optimise both ion

transmission and mass resolution. Since there were no translators attached to the mirror external to the vacuum system, a set of XY deflectors were included in the first drift region to increase the flexibility in ion beam steering.

In order to produce a space focal plane close to the ion source, the value of k_0, and therefore the ratio dE_d/s_0E_s, must be reduced relative to the case for the linear TOF mass spectrometer. A total extraction energy of ~ 1 keV is required for reasonable separation of ion packets of different mass-to-charge ratio, so reducing dE_d is not desirable. The most efficient manner in which to achieve the desired effect therefore is to increase s_0E_s. The parameters chosen for the experimental reflectron mass spectrometer are listed in table 5.2.

Also listed (in parentheses) in table 5.2 are the "ideal" set of parameters for the ion mirror, as calculated using the expressions derived by Mamyrin. This set were the "aimed-for" values in designing the experimental reflectron. The set of parameters that were used were a compromise, which accounted for the actual dimensions of the ion mirror fabricated, the limited precision with which the mirror power supply could be set, and the restricted choice of resistors available for the voltage divider chain employed in the ion mirror.

5.6.1 Theoretical and Experimental Performance of the Reflectron TOF Mass Spectrometer.

A simple FORTRAN program (listed in Appendix C) was written to allow crude modelling of ion flight times in the reflectron mass spectrometer. Although this program takes no account of broadening mechanisms due to the deviation of the ion packet plane from being perpendicular to the axis of the spectrometer, it

Table 5.2 Experimental Parameters for Reflectron TOF Mass Spectrometer

Repeller- Draw-out distance, s = 30 mm

Draw-out- Centre of laser spot distance, s_0 = 20 mm

Draw-out- Flight distance = 10 mm

Interelectrode distance in the mirror retarding region, d_T = 16.0 (13.4) mm

Interelectrode distance in the mirror reflecting region, d_K = 105.0 (101.0) mm

Flight- Space focal plane distance, l_0 = 77.0 mm

Length of first drift region, $(l_0 + l_1)$ = 980.0 mm

Length of second drift region, l_2 = 700.0 mm

Mirror half-angle, $\theta = 4^o$

$V_{Repeller}$ = 1345 V

$V_{Draw-out}$ = 445 V

V_{Flight} = 0 V

$V_{Deflector}$ = 0-50 V

Average total energy extracted by ions, U_0 = 1045 eV

Mirror retarding potential, U_T = 748.3 (732.6) V

Potential in the mirror reflecting region, U_K = 548.7 (471.0) V

Field strength in draw-out region, E_s = 30000 Vm^{-1}

Field strength in acceleration region, E_d = 44500 Vm^{-1}

Field strength in mirror deceleration region, E_T = 46768.8 (54508.9) Vm^{-1}

Field strength in mirror reflecting region, E_K = 5225.7 (4663.4) Vm^{-1}

k_0 = 1.742

does permit the derivation of empirical relationships which allow an idealised description of the resolving power of the mass spectrometer to be examined.

Figures 5.9 and 5.10 show plots, analogous to figure 5.2, of the flight time and mass resolution as a function of ion mass for the "ideal" and "actual" reflectron mass spectrometers using the parameters listed in table 5.2. The data in these figures were derived using the program listed in Appendix C. Considering the "ideal" case first, it is clear that the mass resolution increases with increasing mass, with the maximum resolvable mass being greater than 10000 amu. Although the widths of the ion packets increase with mass, and hence flight time, this is more than compensated for by the increased value of the flight time itself. In this "ideal" case, the ion packet width at the initial Wiley-McLaren focal plane is 11.1 ns for ions of m/e = 93 created by a laser pulse of 10 ns temporal width, and is 13 ns at the detector plane. No significant broadening of the ion packet is caused by the action of the mirror.

The situation in the case of the "actual" experimental reflectron is somewhat different. Here, the resolution also increases with ion mass, but the maximum resolvable mass is only 1500 amu. The reason for this degraded performance is completely due to broadening of the ion packets by the ion mirror. The fields applied to the mirror differ significantly from the values calculated using the expressions derived by Mamyrin, and consequently the ion packets are re-focused in a plane that is closer to the mirror than is is required, i.e. the "focal length" of the mirror is somewhat shorter than it should be. Therefore, by the time the ion packets reach the detector, they have started to re-disperse and the resulting mass resolution is degraded. Here, an ion packet of m/e = 93, created

Figure 5.9. A plot of ion flight time and mass resolution as a function of mass in the "ideal" reflectron TOF mass spectrometer.

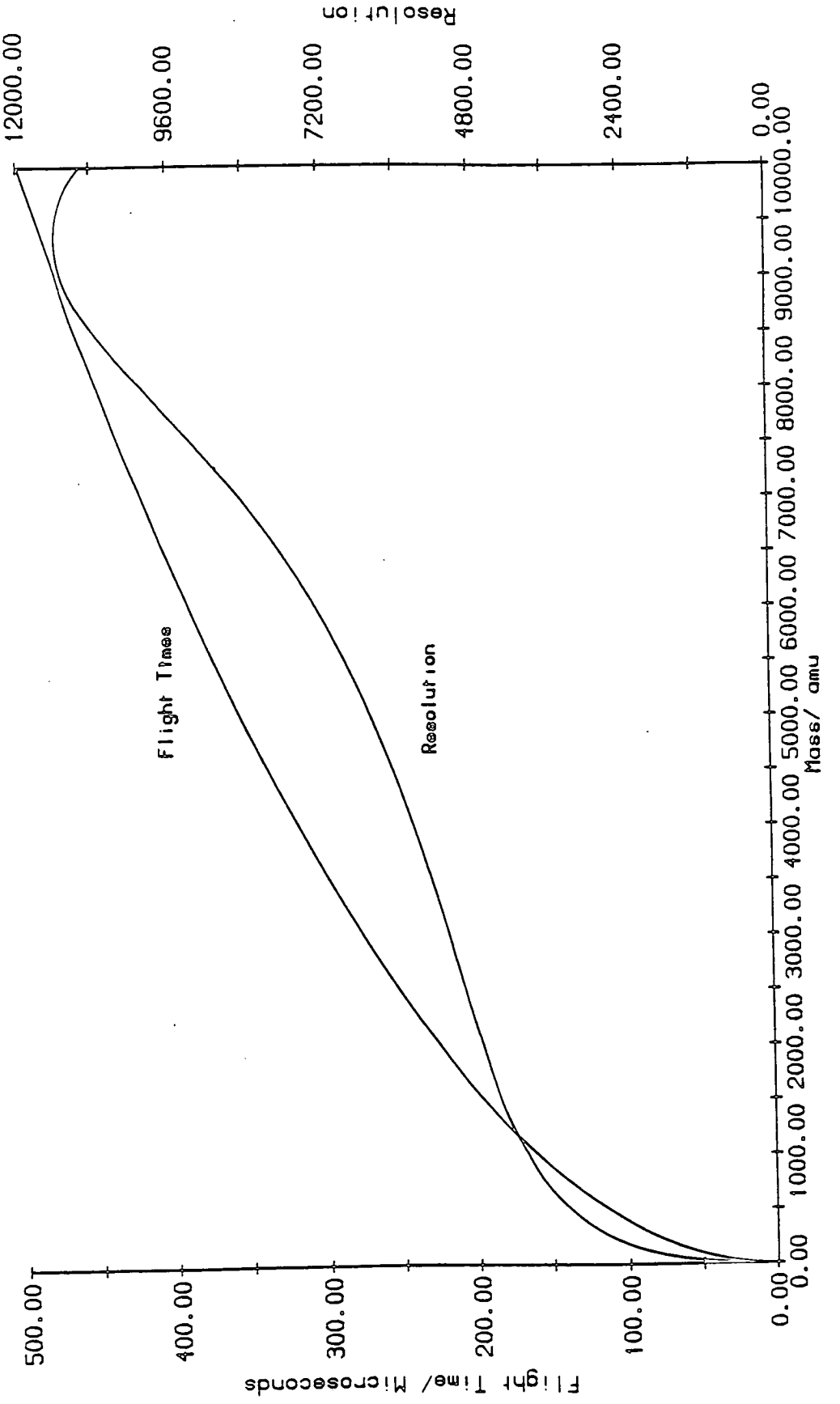

Figure 5.10. A plot of ion flight time and mass resolution as a function of mass in the "actual" reflectron TOF mass spectrometer.

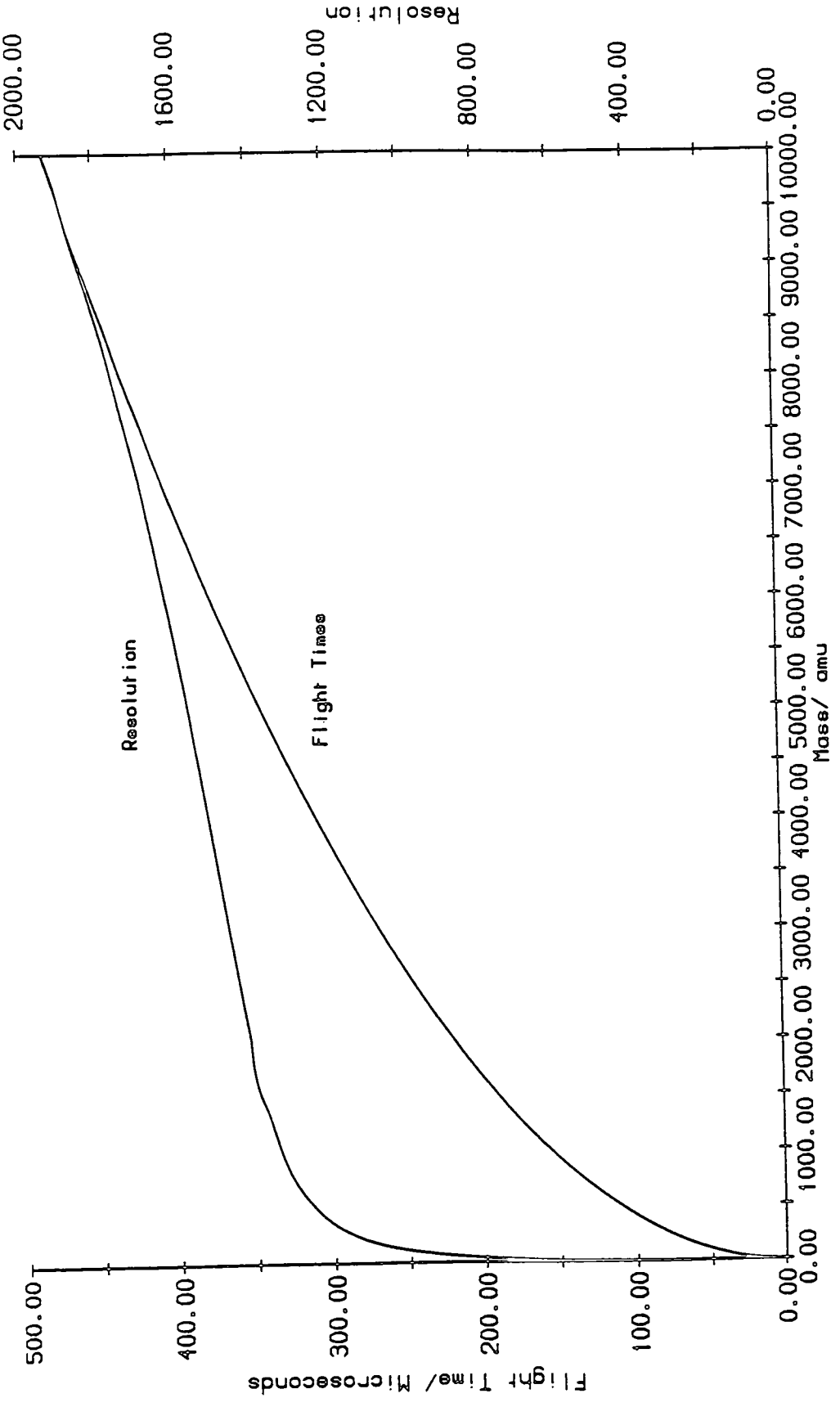

by a laser pulse of 10 ns, is broadened from 11.1 ns at the initial space focal plane to 24.5 ns at the detector. Nevertheless, the theoretical resolution for both "ideal" and "actual" reflectrons is considerably improved on that of the linear TOF mass spectrometer.

As in the case of the linear TOF mass spectrometer, it is not possible to compensate fully for the initial velocity distribution with a reflectron TOF mass spectrometer [7], [23]. Various methods have been employed in order to reduce the effect of the velocity distribution on mass resolution. Schlag and coworkers [4] operated their reflectron by employing a high electric field in the ionisation region and then decelerating the ions in the second stage of the ion lens. This reduced the effect of the initial velocity distribution, but destroyed the space focusing condition. Good mass resolution could therefore only be obtained with a focused laser beam. Poschenrieder [18] described several TOF mass spectrometers that employed electric sectors. He suggested using a single-stage extraction lens, with a spatial focus at $2s_0$, in these devices. Here the ions receive the same nominal drift energy as in the two-step extraction case, but they are accelerated to this energy much more quickly due to the high acceleration field. It has been shown that excellent theoretical mass resolution (22500 at m/e = 78) can be obtained using this device [23]. However, because the ion mirror in a reflectron can compensate only for a finite spread in kinetic energies, a very narrow ionising beam (20 μm spot) must be employed with such a one-step extractor. Instead, in the work described here, the combination of a supersonic molecular beam source and a reasonably high draw-out field has been used to counteract the effect of the initial velocity distribution.

The calculated mass resolution of this device is 1900 ("ideal") and 950 ("actual") for ions of m/e 93. Figures 5.11 and 5.12 show for the case of this "ideal" reflectron TOF mass spectrometer the dependence of the flight time for ions of this mass on v_0 and s_0, respectively. As before, the flight times shown in figure 5.11 were derived assuming a constant value for s_0 (= 2.0 cm) and a variety of values of v_0. At a translational temperature of 10 K, the value of σ_{t_0} is 2.3 ns, compared to 6.2 ns in the case of the linear TOF mass spectrometer. Figure 5.12 illustrates the price that must be paid for achieving a space focus at a very short distance from the extraction optics, namely a reduction in the overall spatial resolution. As mentioned previously, the value of E_s must be increased compared to the value for a linear instrument in order to achieve such a space focus, which means that the spatial resolution of the reflectron is degraded relative to that of a linear TOF mass spectrometer. In the "ideal" reflectron, a 1 mm diameter focal spot for the ionisation laser results in a value of 13.9 ns for σ_{t_s}, which should be compared to a value of 0.13 ns for the linear TOF mass spectrometer. It is therefore clear that a more tightly focused ionisation laser beam must be employed with this ion source. A focal spot of 250 μm diameter results in a more acceptable value for σ_{t_s} of 3.5 ns.

For the reflectron with the "actual" set of parameters used (as given in table 5.2), the dependence of ion flight time on v_0 and s_0 for mass 93 ions is shown in figures 5.13 and 5.14 respectively. Here the value of $\sigma_{t_{t_0}}$ is increased to 2.5 ns. More significantly, figure 5.14 indicates the reduced ability of the ion mirror to compensate for the creation of ions over a finite spatial volume. Here, the value of σ_{t_s} is 60 ns when an ionisation focal spot of 1 mm diameter is used, whilst the

Figure 5.11. Dependence of ion flight time on the initial velocity distribution. Calculated for aniline in the "ideal" reflectron TOF mass spectrometer.

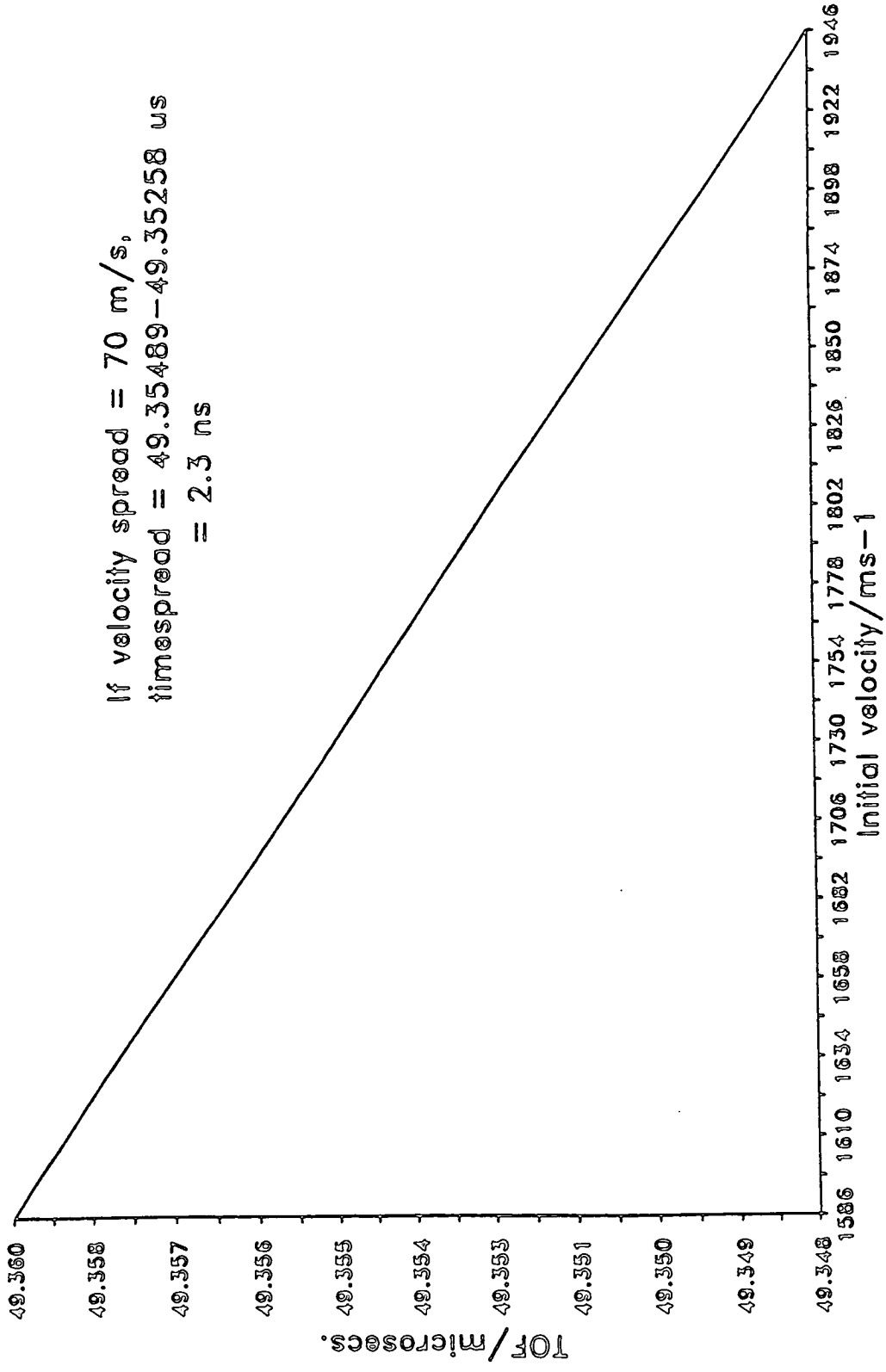

Figure 5.12. Dependence of ion flight time on the initial spatial distribution. Calculated for aniline in the "ideal" reflectron TOF mass spectrometer.

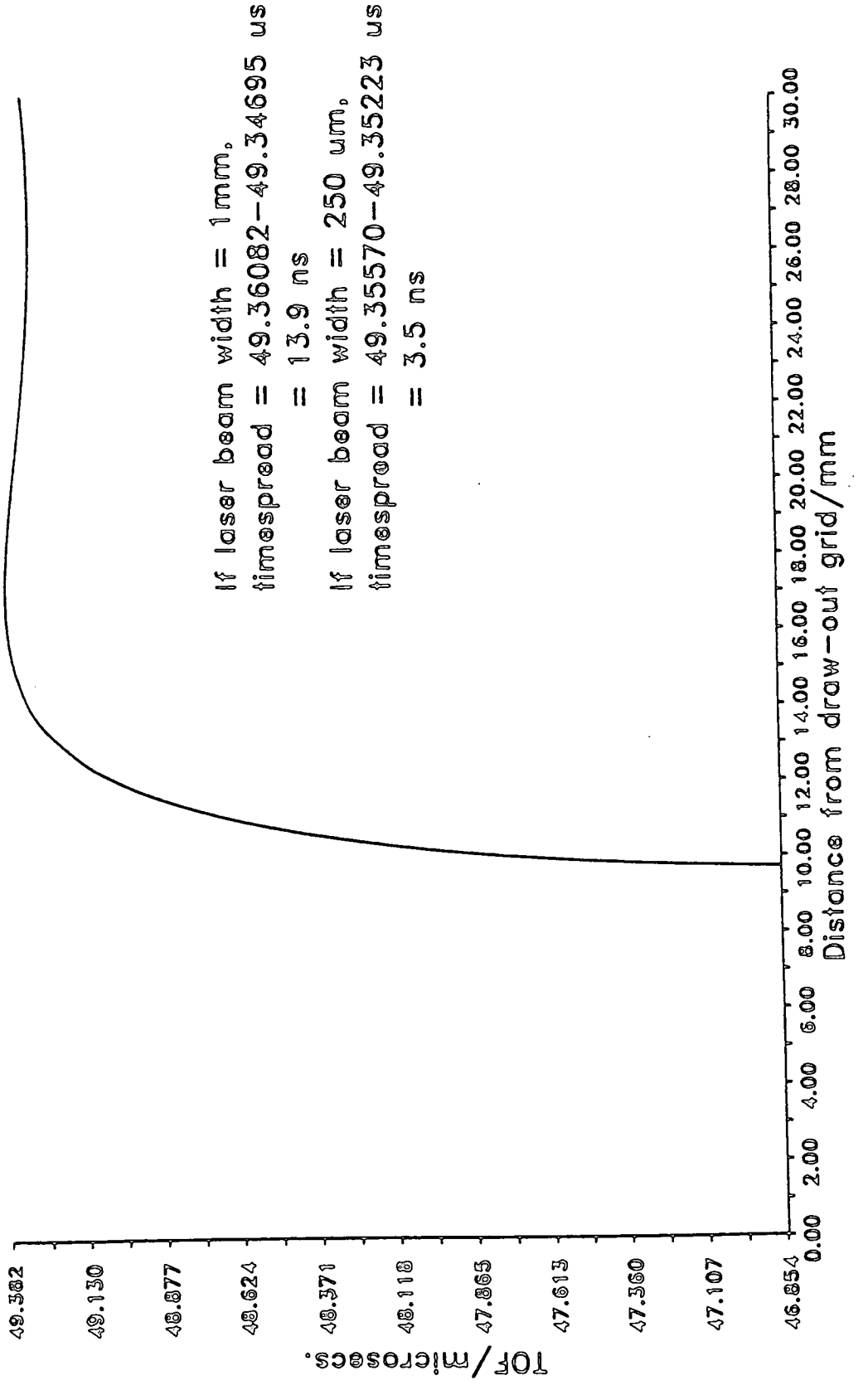

value of this parameter is still 15 ns when a 250 μm diameter spot is employed.

The mass spectra of aniline presented in chapter 3 were obtained with the reflectron TOF mass spectrometer, using the "actual" set of parameters listed in table 5.2. All spectra were obtained with an ionisation laser focal spot size of 250 μm diameter. By comparing figure 3.3(c) with figure 5.5, it is immediately apparent that the mass resolution of the reflectron is considerably better than that of the linear device. Figure 5.15 shows the molecular ion region of aniline recorded under soft ionisation conditions at λ = 293.71 nm. This was obtained using a laser focal spot size of 250 μm diameter and a digitisation rate of 100 MHz. The measured peak widths here are 25 ns FWHM, corresponding to a mass resolution of 850. This should be compared with the calculated values of 24.5 ns and 950, respectively. Figure 5.16 shows the molecular ion region for CO_2 laser desorbed tryptophan (molecular weight 204 amu) ionised at λ = 266 nm under soft ionisation conditions, again with a tightly focused ionisation laser beam. Here the observed peak widths are 40 ns FWHM, corresponding to a mass resolution of 810. The calculated values are a width of 32 ns and a mass resolution of 1110. It is obvious therefore that the calculated mass resolutions are slightly over-optimistic, but are nevertheless a fair approximation to the values observed.

5.6.2 Factors Affecting Experimental Performance of the Reflectron TOF Mass Spectrometer.

A number of effects can influence the observed mass resolution. As in the case of the linear TOF mass spectrometer, these include the limited sampling rate of the transient digitiser, space-charge effects, and the effects of field inhomogeneities in the ion source and mirror regions. Further ion packet broadening can be

Figure 5.13. Dependence of ion flight time on the initial velocity distribution. Calculated for aniline in the "actual" reflectron mass spectrometer.

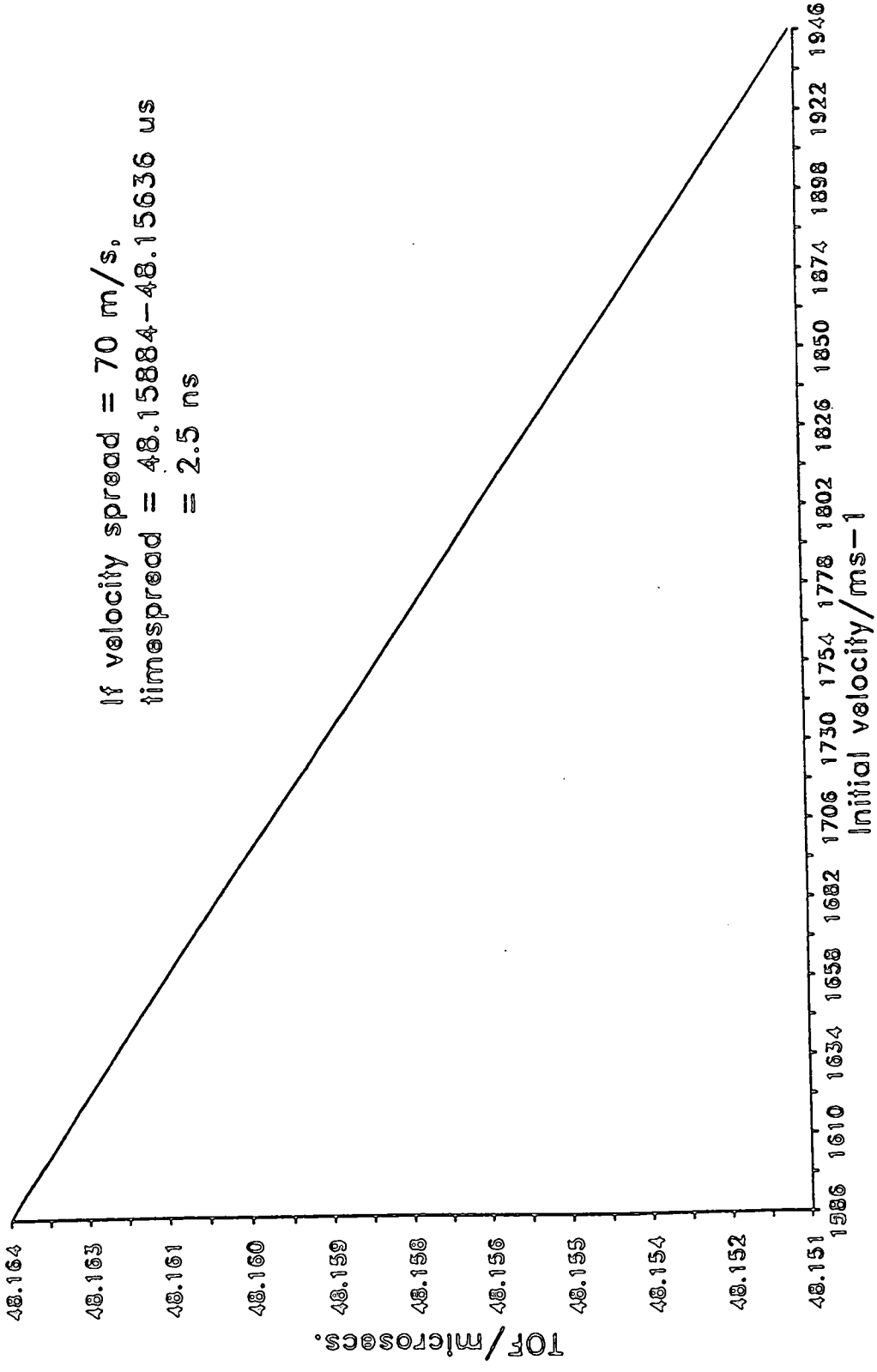

Figure 5.14. Dependence of ion flight time on the initial spatial distribution. Calculated for aniline in the "actual" reflectron TOF mass spectrometer.

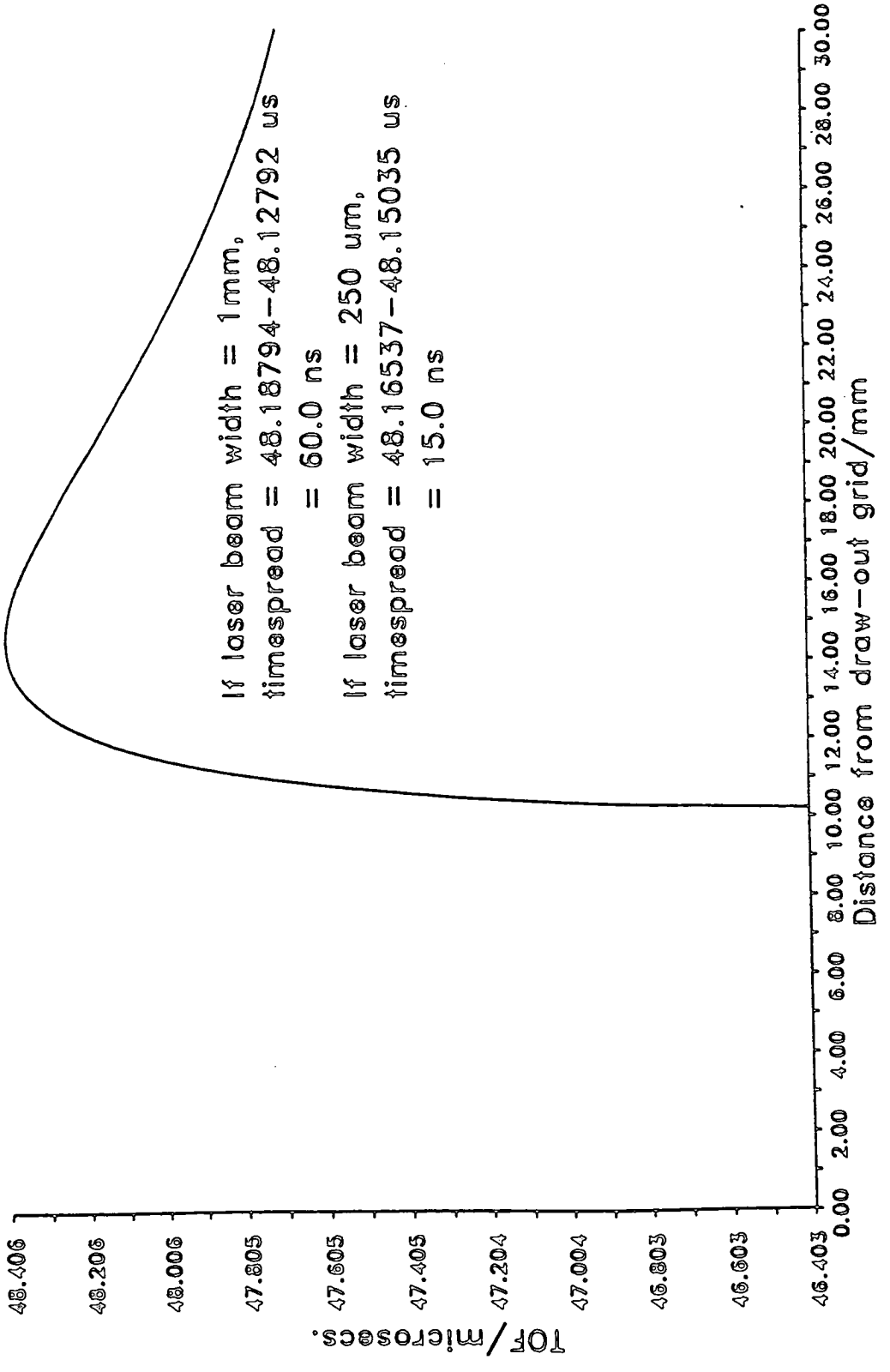

introduced by the fact that the ion packets are not extracted perpendicular to the axis of the mirror [22] and by the effects of field distortions around the meshes on the lens element plates [24]. These effects are discussed below.

Figure 5.17 and 5.18 show potential maps for the reflectron ion extraction optics and the ion mirror, respectively. Surprisingly, perhaps, the presence of an aperture in the repeller plate of the ion source has little effect on the potential at the point of ionisation. Since, as mentioned above, a spatially small ionisation beam is required, there will only be a limited amount of extra broadening of the ion packets due to the presence of the aperture. Attempts to eliminate any field leakage by placing a high-transmission grid over the aperture were not successful, since this was found to cut down transmission of the molecular beam. A more important effect is probably the penetration of the field from both the acceleration and deflection regions into the flight tube. Typically a voltage of 25-50 V was applied to the right-hand deflector in order to compensate for any misalignment of ion trajectories before they entered the mirror. However, due to the lack of a grounded shield around the extraction optics, this field as well as that from the acceleration region could spill out considerably to the nearest earthed surfaces, namely the chamber walls.

Field penetration effects are even more substantial in the case of the ion mirror. In order to calculate the potential map in the mirror, shown in figure 5.18, the mirror axis had to be parallel to the chamber axis, since the simulation program employed could not cater for the angled geometry. The presence of guard rings minimises the penetration of fields from outside the body of the mirror, and their effect on ion trajectories within the mirror itself. The lack of grids on the guard

Figure 5.15. Mass spectrum of aniline recorded in the reflectron TOF mass spectrometer. λ = 293.71 nm, I = 10^5 Wcm^{-2}.

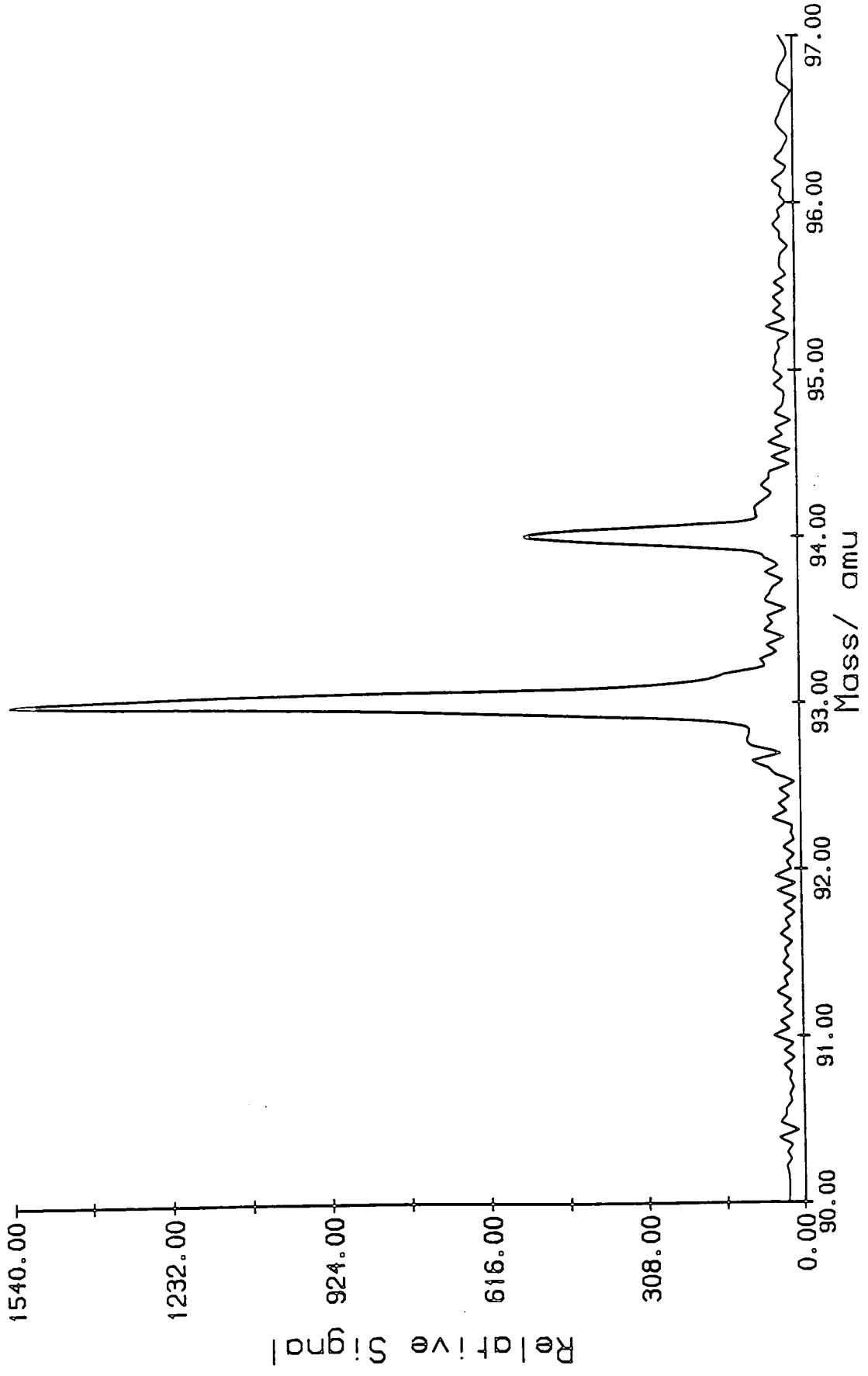

Figure 5.16. Mass spectrum of laser desorbed tryptophan recorded in the reflectron TOF mass spectrometer. λ = 286.96 nm, I = 10^5 Wcm^{-2}.

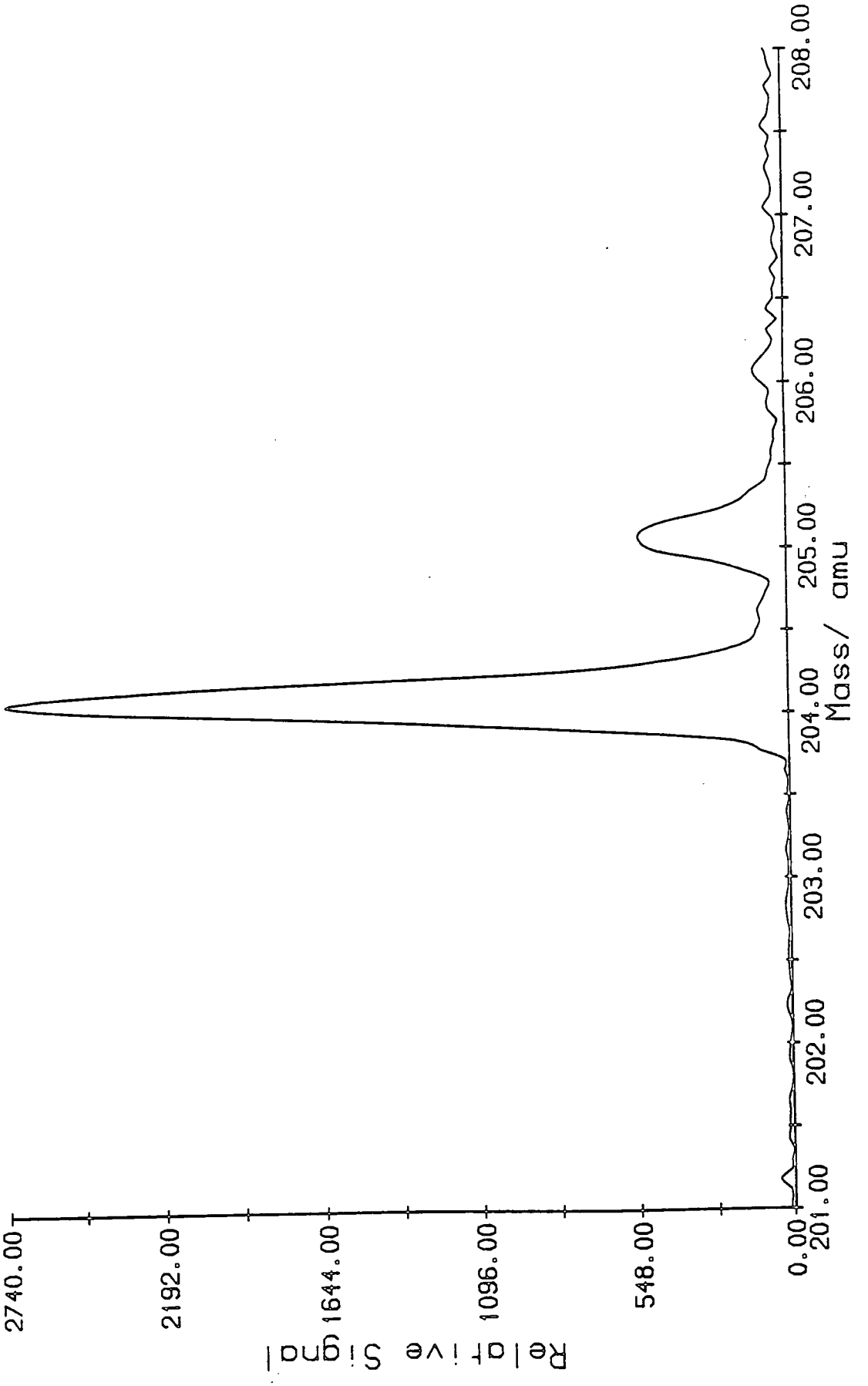

rings, which was necessary in order to maintain a high ion transmission through the mirror, appears to have little effect on the homogeneity of the fields within the mirror. However, extensive field penetration occurs around the earthed entrance grid of the mirror. Voltages of up to 20 V are found on the mirror axis in the drift region directly in front of the mirror entrance, which means that ions have to pass over a "saddle" point before entering and after leaving the mirror. These fringing fields are likely to have detrimental effects on the time focusing behaviour of the mirror.

A design modification which would help to preserve ground potential in the drift region involves mounting the mirror assembly in an earthed collar [25]. This would trap the field within the collar, thereby preventing leakage. An alternative means of achieving the same result would be to increase the diameter of the grounded entrance element of the mirror, which would block field penetration from the back and the sides of the mirror.

The ion packets can also be broadened due to their deviation from the plane perpendicular to the spectrometer axis. In their original paper [22], Mamyrin and coworkers calculated this effect. If the plane of the ion packets leaving the initial space focal plane is at an angle β to the mirror axis, then each point in the initial ion packet, containing ions of all energies from U_{min} to U_{max} moving at an angle α (see figure 5.8), is converted to a packet width Δc at the detector, where

$$\Delta c = 4d_K/U_K \{(U_{max} - U_T)^{1/2} - (U_{min} - U_T)^{1/2}) \tan \alpha. \qquad (5.70)$$

The smallest packet thickness is then given by

Figure 5.17. Potential map of the ionisation region in the reflectron TOF mass spectrometer.

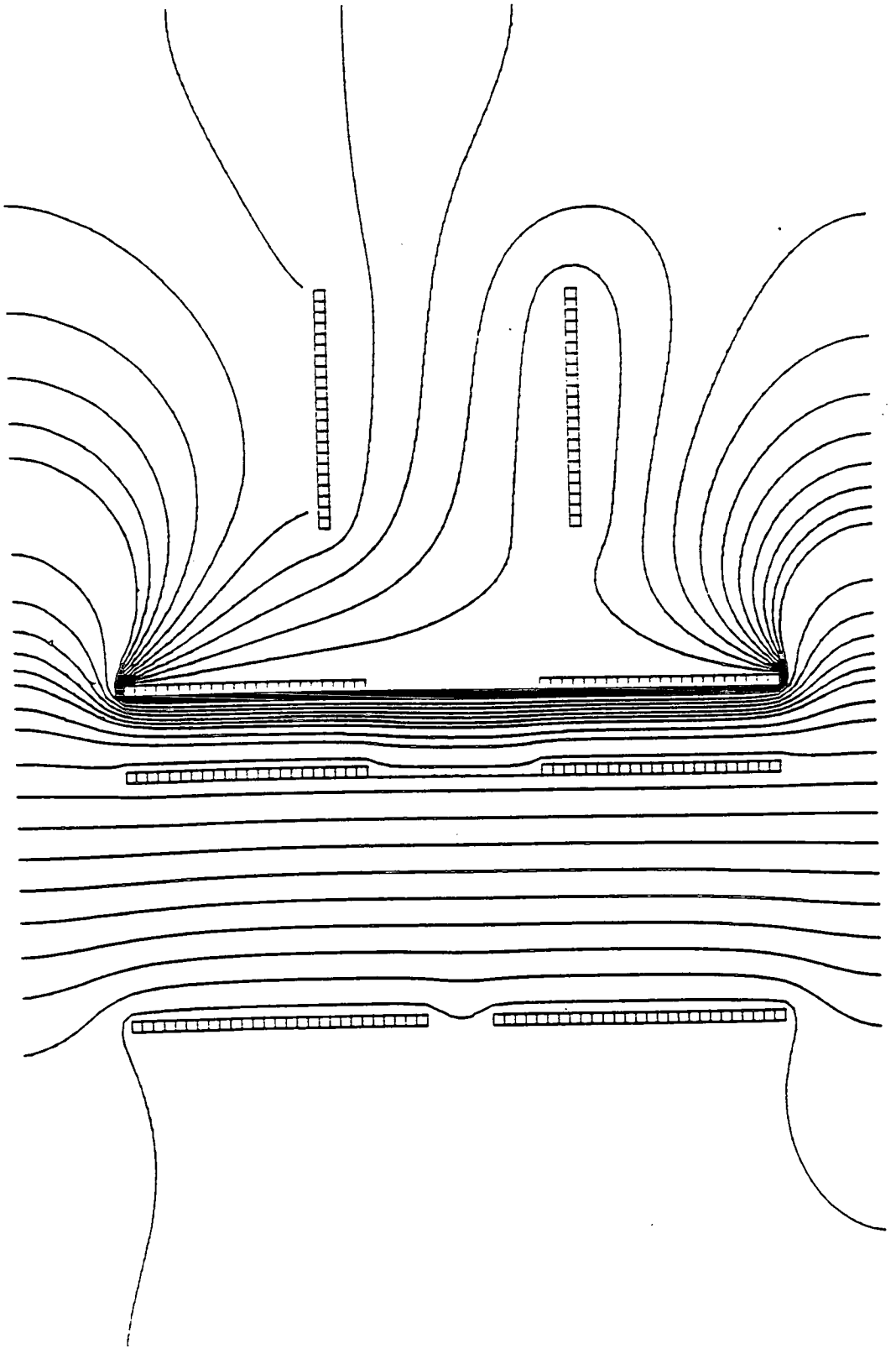

Figure 5.18. Potential map of the ion mirror in the reflectron TOF mass spectrometer. The "actual" parameters, from table 5.2, are used here.

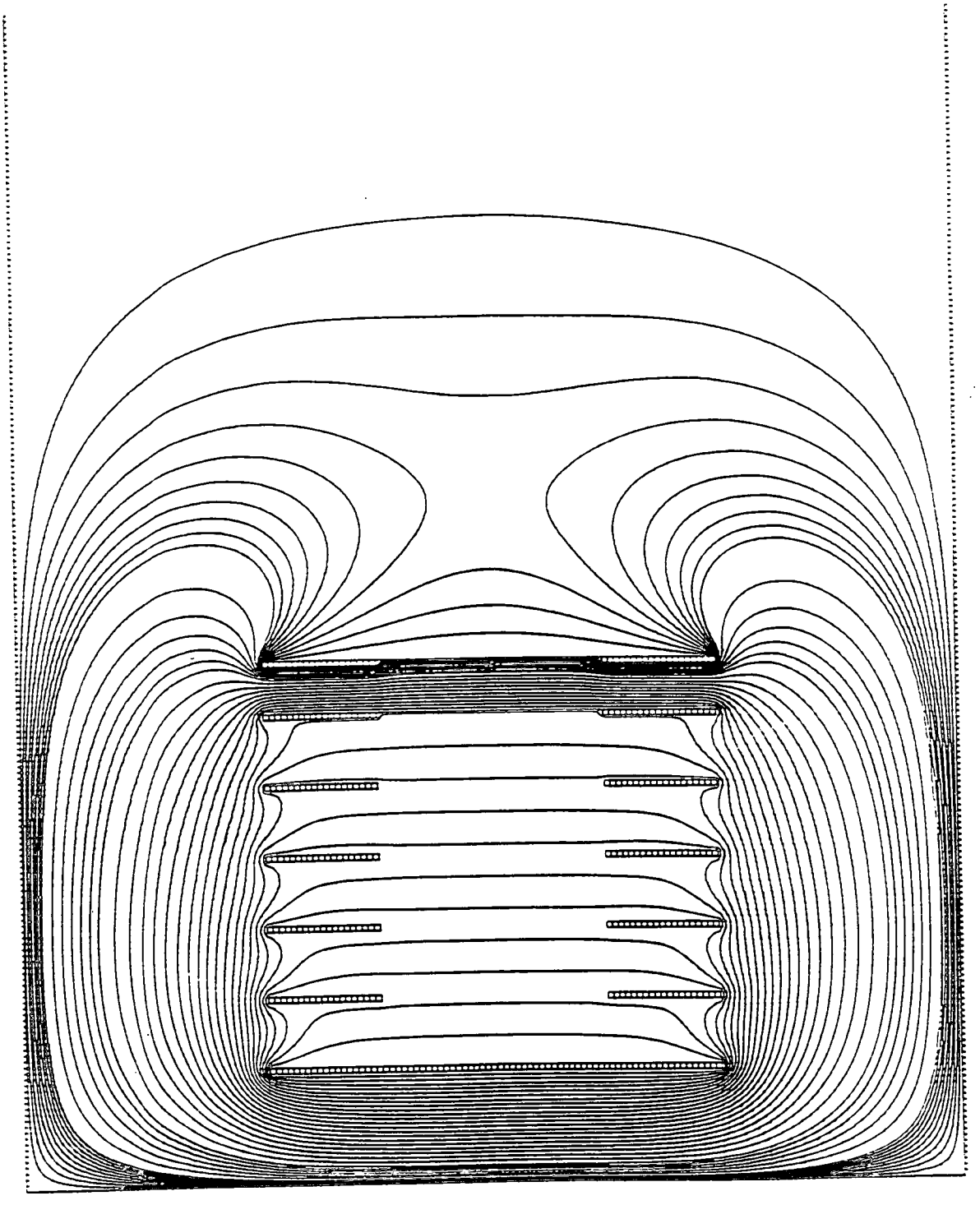

$$\Delta l = \Delta c \sin\beta, \tag{5.71}$$

where Δl has the dimensions of length.

In the present case, $\alpha = \beta = 4^{o}$. Using the parameters listed in table 5.2, a value of $\Delta l = 6.5 \times 10^{-7}$ m is obtained. In order to assess the significance of this number, it must be compared to the thickness of the ion packet at the pseudo-source. Mamyrin derives this value from

$$\Delta L = l_0(\Delta U_0/U_0)^{1/2}, \text{ where } \Delta U_0 = U_{max} - U_{min}. \tag{5.72}$$

Using the parameters listed in table 5.2, a value of $\Delta L = 4.1 \times 10^{-3}$ m is obtained. Thus the effect of packet broadening as a result of $\beta > 0$ is negligible compared to the minimum packet width at the initial space focal plane.

A more important effect that must be considered is that of field distortions in the vicinity of the meshed grids in the reflector. This causes a slight deflection of ions as they pass through the grids, and therefore a slight change in flight times. By increasing the length of the retarding section of the mirror (i.e. d_T), the field in the vicinity of the earthed grid is lowered, so that the deflection of ions passing through it is reduced. Bergmann et al. [24], [25] have shown recently that by greatly increasing the length of this section (by a factor of 18 over that given by Mamyrin as expressed in equation (5.68), but still obeying equations (5.63)-(5.65)), the mass resolution of their reflectron has been increased from less than 8000 to over 35000, with a theoretical limit to the resolution being 150000.

In conclusion, the performance of the reflectron TOF mass spectrometer is limited by a number of factors, of which undoubtedly the most important is the choice of fields used in the ion mirror. From equations (5.66) and (5.67), the correct ratio of U_T to U_K is 14/9, which requires the use of five 1.8 MΩ resistors (rather than five 2.2 MΩ) in the resistor chain, and an external resistor of 14 MΩ instead of 15 MΩ. These were unavailable at the time of construction. Due to the lack of time available, it was deemed more important to investigate the potential uses of laser desorption MPIMS as an analytical method than to fully optimise the resolution of the reflectron TOF mass spectrometer. As can be seen from the spectra presented in chapter 6, the available resolution of the reflectron was sufficiently good for unit mass resolution of nearly all molecules studied. Correction of these fields by changing the value of the elements in the resistor chain will undoubtedly increase the mass resolving power of the instrument. In this case, the upper limit on resolution would be governed by one of the other factors discussed above. Nevertheless, the mass resolution achievable with the experimental reflectron is a factor of ~3 better than that obtained with a simple linear TOF mass spectrometer.

5.7 Ion Transmission.

The second important quantity in mass spectrometry, after mass resolution, is ion transmission. This is defined as the fraction of ions that arrive at the detector relative to the total number created. Ion loss in the linear and reflectron instruments occurs by three distinct mechanisms.

1. Over their flight path, ions may collide with background gas molecules

resulting in deflection of the ions off the flight tube axis. Ions with sufficient off-axial components will either hit the flight tube walls or the non-active part of the detector, and therefore will not be detected. Ion-molecule collisions can be avoided if the pressure is kept sufficiently low, such that the mean free path of the ions is greater than the dimensions of the spectrometer. This factor is negligible in this work, since the chamber pressures were kept below 5×10^{-7} mbar.

2. Apertures in the ion flight path reduce the number of ions transmitted. Although there were no actual apertures (such as slits) stopping down the size of the ion packet, the various regions of the spectrometer were bounded by metal grids. As the ions pass through these grids, which have a finite transmittance, a fraction of them are lost due to collisions with the grids. The fraction of ions transmitted through the spectrometer is given by the grid transmission raised by a power equal to the number of times the ions pass through the grids. For example, the linear TOF mass spectrometer developed in in this laboratory has two grids of 90% transmission in the extraction optics region and an 82% transmitting grid in front of the detector. The overall transmittance is therefore $(0.9)^2(0.82) = 66.4$ %. Ion losses of this type are greater in the reflectron, where the ions pass through 90% transmitting grids in the ion mirror twice each. The overall transmittance is therefore $(0.9)^6(0.82) = 43.6\%$.
3. All the ions extracted into the mass spectrometer drift region have velocity components perpendicular to the direction of extraction due to the velocity distribution of their neutral precursors. If these velocity components are sufficiently large, the ions will miss the detector. In addition, the ions

are not formed at a point source, but over a range of spatial positions. Ions created at these different positions may not be transmitted uniformly to the detector. Also, field inhomogeneities may alter the ion trajectories so that they diverge strongly from the spectrometer axis.

As discussed previously, the ion extraction system in a linear TOF mass spectrometer configured with the flight tube orthogonal to the molecular beam axis has to overcome the large velocity component ($\sim 1766\ ms^{-1}$) acquired in the molecular beam direction. Application of a deflection field should help minimise ion transmission losses, but has the disadvantage that a non-uniform transmission function is introduced. Cartwright [11] has calculated ion trajectories in such a molecular beam linear TOF mass spectrometer, yielding a more realistic overall transmission function of $\sim 8\%$ for this device.

This is not such a problem with the collinear molecular beam/ reflectron geometry that was adopted. The collinear geometry allows both a greater number of ions to be transmitted into the drift tube and (theoretically) a mass independent transmission function. Typically, maximum signal intensities recorded in the reflectron were twice those recorded under similar conditions on the linear TOF mass spectrometer. An experimental measurement of the transmission function of both linear and reflecting geometry mass spectrometers indicated that the transmission profile of the latter was much flatter over a wider mass range (~ 2000 Da) than the linear TOF mass spectrometer [26].

5.8 Mass Calibration of Spectra.

The mass spectra obtained using either the linear or reflecting-geometry TOF mass spectrometers were calibrated by fitting the time of arrival of ions of known mass using Newton's equations of motion in the various parts of the mass spectrometers. If $v_0 = 0$, the total flight time varies as $m^{1/2}$. However, when $v_0 > 0$, this equation becomes more complicated with terms in other powers of m contributing to the flight time. These contributions are small compared to the $m^{1/2}$ term, and allow the time of arrival profile to be fitted to the correct mass by the function

$$t = a + bm^{1/2}, \tag{5.73}$$

where a and b are constants [27].

By fitting the transient digitiser channel number, corresponding to a particular ion time-of-arrival, to its equivalent mass, using a least-means squares program, the coefficients a and b are obtained. Generally a calibrant gas such as aniline was used to give well-characterised ion peaks. An alternative method was to employ hard ionisation conditions and to fit the spectrum using low mass fragment ion peaks corresponding to $C_n H_m^+$, where n = 1 to 4.

5.9 Concluding Remarks.

The two TOF mass spectrometers designed in this work provided satisfactory performances both in terms of mass resolution and ion transmission. The mass

resolving power of the linear TOF mass spectrometer was limited by field inhomogeneities in the ion source, and its overall utility was limited by a fairly sharp transmission function, which set up a mass "window" of ~ 300 amu. The reflectron TOF mass spectrometer provided improved performance in both these respects, with approximately uniform transmission over a range of ~ 2000 amu and an increased mass resolving power. The limiting factor on the performance of the reflectron was undoubtedly the ability of the ion mirror actually constructed to compensate for the initial energy spread of the ions. Nevertheless, the resolution obtained was sufficiently high to allow unit mass resolution for a wide range of molecules. The reflectron TOF mass spectrometer was employed in all the laser desorption MPI experiments carried out as part of this work. The following chapter contains details of the spectra obtained, together with some comments on the sensitivity achieved with the spectrometer design detailed above.

References.

[1] L. Zandee, R. B. Bernstein, J. Chem. Phys., **70**, 1359, (1979)
[2] G. J. Fisanick, T. S. Eichelberger, B. A. Heath, M. B. Robin, J. Chem. Phys., **72**, 5571, (1980)
[3] T. G. Blease, *Ph. D. Thesis*, University of Edinburgh, 1985.
[4] U. Boesl, H. J. Neusser, R. Weinkauf, E. W. Schlag, J. Phys. Chem., **86**, 4857, (1982)
[5] W. C. Wiley, I. H. McLaren, Rev. Sci. Instrum., **26**, 1150, (1955)
[6] L. Q. Huang, R. J. Conzemius, G. A. Junk, R. S. Houk, Anal. Chem., **60**, 1490, (1988)
[7] U. Boesl, J. Grotemeyer, K. Walter, E. W. Schlag, Anal. Instrum., **16**, 151, (1987)
[8] K. Walter, U. Boesl, E. W. Schlag, Int. J. Mass Spectrom. Ion Proc., **71**, 309, (1986)
[9] J. L. Wiza, Nucl. Inst. Methods, **162**, 587, (1979)
[10] D. H. Parker, *Ch. 4 in 'Ultrasensitive Laser Spectroscopy'*, Academic Press (New York), 1983.
[11] P. C. Cartwright, *Ph. D. Thesis*, University of Edinburgh, 1989.
[12] G. Sanzone, Rev. Sci. Instrum., **41**, 741, (1970)
[13] R. B. Opsal, K. G. Owens, J. P. Reilly, Anal. Chem., **57**, 1884, (1985)
[14] A. C. Jones, *private communication*,
[15] P. C. Cartwright, *private communication*,
[16] E. A. Rolfing, D. M. Cox, A. Kaldor, J. Chem. Phys., **81**, 3322, (1984)
[17] E. A. Rolfing, D. M. Cox, A. Kaldor, J. Phys. Chem., **88**, 4499, (1984)
[18] W. P. Poschenrieder, Int. J. Mass Spectrom. Ion Phys., **9**, 357, (1972)
[19] N. L. Marable, G. Sanzone, Int. J. Mass Spectrom. Ion Phys., **13**, 185, (1974)
[20] J. A. Browder, R. L. Miller, W. A. Thomas, G. Sanzone, Int. J. Mass Spectrom. Ion Phys., **37**, 99, (1981)
[21] V. Karataev, B. A. Mamyrin, D. V. Shmikk, Sov. Phys. Tech. Phys., **16**, 1177, (1972)
[22] B. A. Mamyrin, V. I. Karataev, D. V. Shmikk, V. A. Zagulin, Sov. Phys. JETP (Engl. Transl.), **37**, 45, (1973)
[23] R. B. Opsal, *Ph. D. Thesis*, Indiana University, 1985.
[24] T. Bergmann, T. P. Martin, H. Schaber, Rev. Sci. Instrum., **60**, 347, (1989)
[25] T. Bergmann, T. P. Martin, H. Schaber, Rev. Sci. Instrum., **60**, 792, (1989)
[26] A. M. James, *private communication*,
[27] A. M. Butler, *Ph. D. Thesis*, University of Edinburgh, 1989.

Chapter 6
LD-MPI Mass Spectrometry: Some preliminary results.

6.1 Introduction

The previous two chapters contained details of the apparatus which was developed to allow mass spectrometric studies to be carried out on involatile and thermally unstable molecules. In this chapter some of the preliminary results obtained for a variety of such samples using the LD-MPI technique are presented. Some consideration is given to the present degree of sensitivity that can be achieved with the existing reflectron TOF mass spectrometer. Finally, some suggestions are made for improving the performance of the mass spectrometer.

6.2 LD-MPI mass spectra of some polynuclear aromatic hydrocarbons.

The mass spectra of several polynuclear aromatic hydrocarbons (PNAHs) have been obtained using the two-step laser-based technique described earlier. This class of molecules was chosen for the initial LD-MPIMS experiments because they are relatively more stable to heating than many other molecules of interest. It was also of some interest to examine the range of PNAHs which could be studied using this method of sample introduction compared to the heated nozzle approach described in chapter 2.

PNAHs have been widely studied using conventional EI mass spectrometry [1], [2]. General features of the mass spectra obtained are a very intense molecular

ion peak, which is nearly always the base peak, and fragment ions of the type $C_nH_m^+$. The distribution of these fragment ions is usually biased towards n = 1 to 4. The only other significant features are usually $(M-2H)^{+\cdot}$, M^{++} and $(M-2H)^{++}$.

Figures 6.1 to 6.7 show the LD-MPI mass spectra for several PNAHs, namely naphthalene, anthracene, phenanthrene, fluorene, tetracene, perylene and pentacene. Their structures are given in table 6.1. The mass spectra were all recorded using an ionisation laser wavelength of 266 nm, under various regimes of power density. This particular wavelength was employed since it is an easily-produced mid-UV laser photon energy, at which PNAHs have been reported to be efficiently ionised [3], [4]. This high ionisation efficiency is due to two factors. Firstly, PNAHs have dense, almost continuous, absorptions in this wavelength region - for example, the S_1-S_0 origin for tetracene is at 447 nm [5], so that the energy of one 266 nm photon exceeds this by approximately 22000 cm^{-1}. In addition, the ionisation potentials for this class of molecule decrease as the degree of conjugation increases due to resonance stabilisation of the ground ionic state. The vertical ionisation potentials of the PNAHs studied in this work are listed in table 6.2 [6], along with some of their physical constants.

Before considering the mass spectra obtained for these molecules using the technique of LD-MPI mass spectrometry, two important points should be noted. Firstly, the desorption laser power density was held constant at 0.3 $MWcm^{-2}$ during all the experiments described in this chapter. Secondly, the main objective of these experiments was to demonstrate the ability of LD-MPIMS to allow analysis of several classes of molecule. Consequently, whilst samples were

Table 6.1. Structural formulae for the molecules whose LD-MPI mass spectra were obtained in this work.

Naphthalene

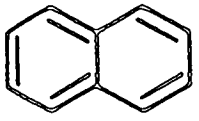

Anthracene

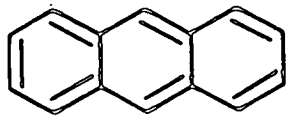

Phenanthrene

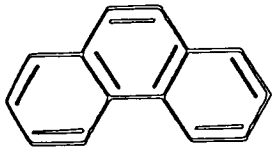

Fluorene

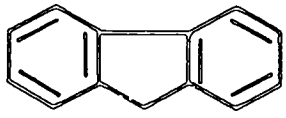

Tetracene

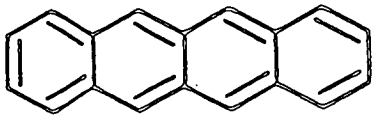

Perylene

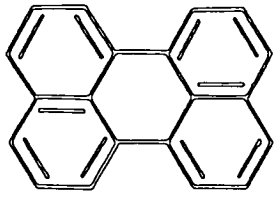

Pentacene

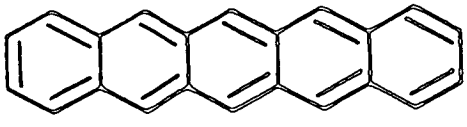

POPOP

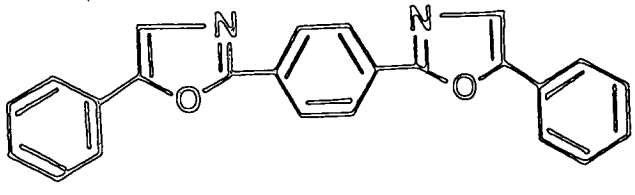

L-tryptophan

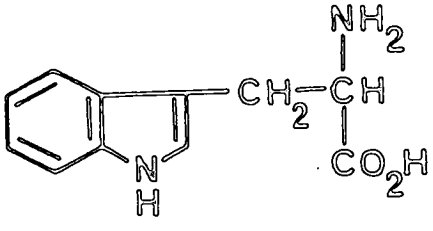

L-tyrosine

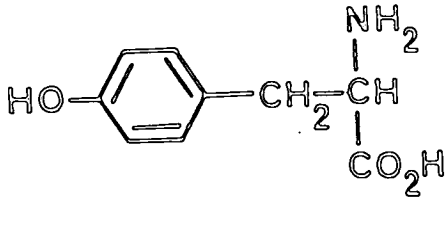

Table 6.1 (cont.). Structural formulae for the molecules whose LD-MPI mass spectra were obtained in this work.

L-phenylalanine

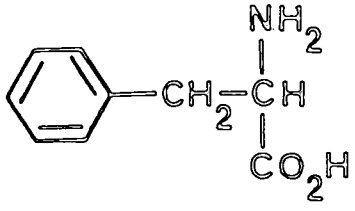

L-histidine

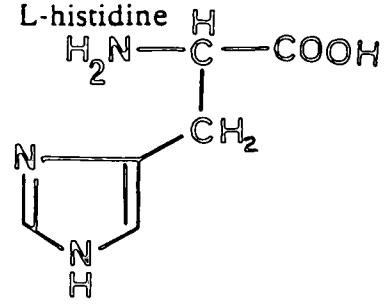

PTH-tryptophan

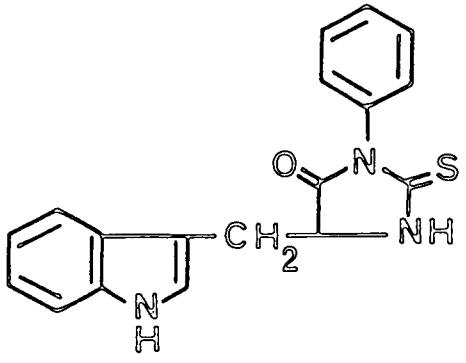

Ni-Etioporphyrin

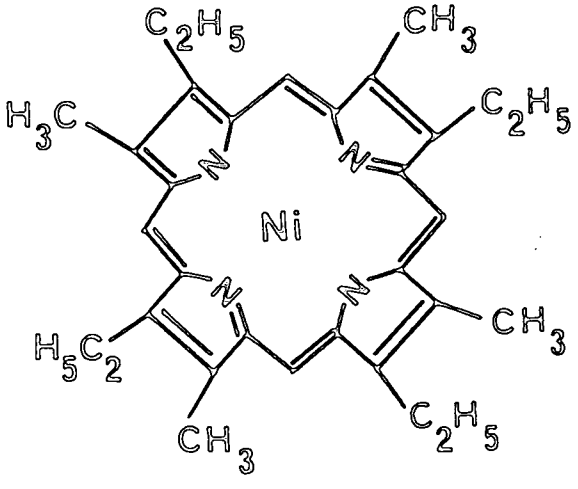

Table 6.2. Some physical properties of the molecules listed in table 6.1.

	Mol.Wt.	M.pt./^{o}C [7]	B.pt./^{o}C [7]	I.P./eV [6]
Naphthalene	128	80.55	218	8.15
Anthracene	178	216.2	340	7.47
Phenanthrene	178	101	340	7.86
Fluorene	166	116	294	7.78
Tetracene	228	357	sub	7.04
Perylene	252	278	sub	7.00
Pentacene	278	270*	sub	6.74
POPOP	364	246		
L-Trp	204	290[d]		
L-Tyr	181	342[d]		
L-Phe	165	283[d]		
L-His	155	287[d]		
PTH-Trp	321			
Ni-etioporphyrin	534			

d = decomposes
* decomposes > 300 ^{o}C
sub = sublimates

generally prepared using 1 mg of the material of interest. the amount of the sample actually deposited on to the sample probe was somewhat arbitrary. In general, a series of spectra for a given molecule were recorded from the same sample. All spectra represent averages over 240 or 250 laser shots. Over the lifetime of the sample, however, the amount of sample desorbed per shot varied greatly (by up to 2 orders of magnitude). Thus, the overall ion signals observed in the mass spectra presented do not always vary in the expected manner with the ionisation laser power density. For example, in figure 6.3(a), the total ion signal, generated by addition of all the peak intensities in the spectrum, is 18966 counts (1 count = 2 mV) at an ionisation laser power density of 1 $MWcm^{-2}$, whereas it is only 16492 counts at 25 $MWcm^{-2}$. The observed trends in fragmentation, however, remain unaffected.

The spectra of the seven PNAHs studied have many common features. For all the molecules, at an ionisation laser power density of 1 $MWcm^{-2}$, "soft" ionisation mass spectra are obtained, with intense molecular ion peaks. Naphthalene, perylene and pentacene exhibit no fragmentation of the molecular ion under these conditions, whilst the apparent fragment ion peak in the anthracene mass spectrum, at mass 167, is an impurity. The spectra for phenanthrene, fluorene and tetracene show the loss of one or two hydrogen atoms at this ionisation power density. Since the appearance potentials for $(M-1)^+$ and $(M-2)^+$ from phenanthrene are between 14 and 19 eV [8], it is clear that the molecular ion, which is produced after the absorption of two UV photons by the ground state molecule, must have absorbed at least one more 266 nm photon. Further fragment ions are observed in the soft ionisation mass

Figure 6.1. LD-MPI mass spectrum of naphthalene at λ = 266 nm.

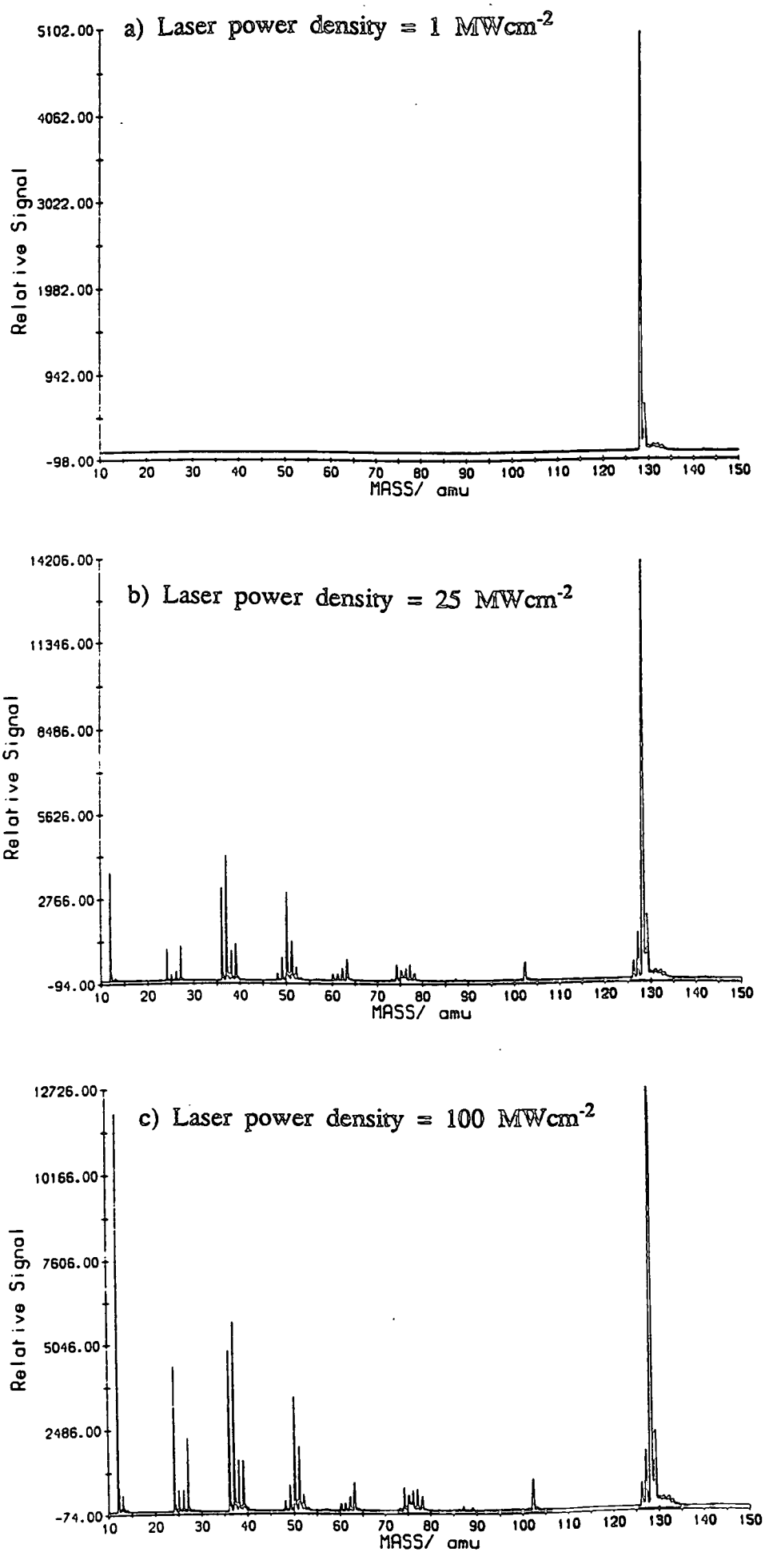

Table 6.3. Mass spectral fragmentation pattern for naphthalene.

1 $MWcm^{-2}$		Calculated*		25 $MWcm^{-2}$		100 $MWcm^{-2}$	
m/e	Signal	m/e	Signal	m/e	Signal	m/e	Signal
128	100	128	100	128	100	128	100
129	11.4	129	11.3	37	29.8	12	94.5
131	1.8	130	0.6	12	25.8	37	44.8
132	1.8	131	0.018	36	22.2	36	38.1
133	1.3	132	3.5×10^{-4}	50	21.1	24	34.6
130	1.2	133	4.9×10^{-6}	129	15.3	50	27.1
134	0.2	134	4.8×10^{-8}	127	11.0	129	18.1
				51	9.5	27	17.7
				39	8.8	51	15.4
				27	8.3	127	13.5
				24	7.5	38	12.3
				38	7.2	39	12.2
				49	5.6	102	7.6
				63	5.2	63	6.9
				102	4.4	49	6.3
				126	4.3	126	5.8
				74	4.1	74	5.8
				77	4.1	77	5.3
				52	3.3	25	5.2
				76	3.2	26	5.2
				62	3.0	76	5.0

* see text

Figure 6.2. LD-MPI mass spectrum of anthracene at λ = 266 nm.

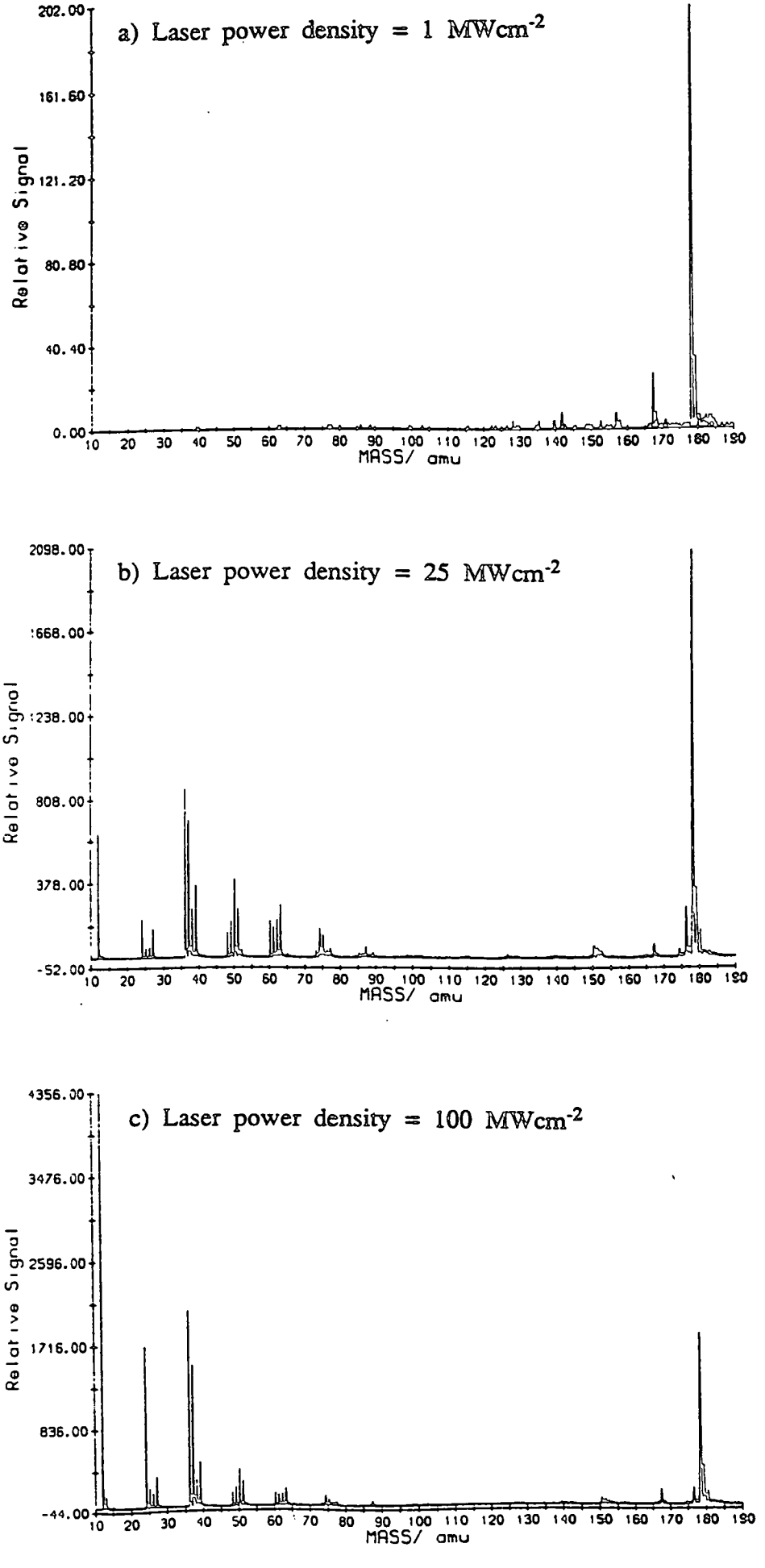

Figure 6.3. LD-MPI mass spectrum of phenanthrene at λ = 266 nm.

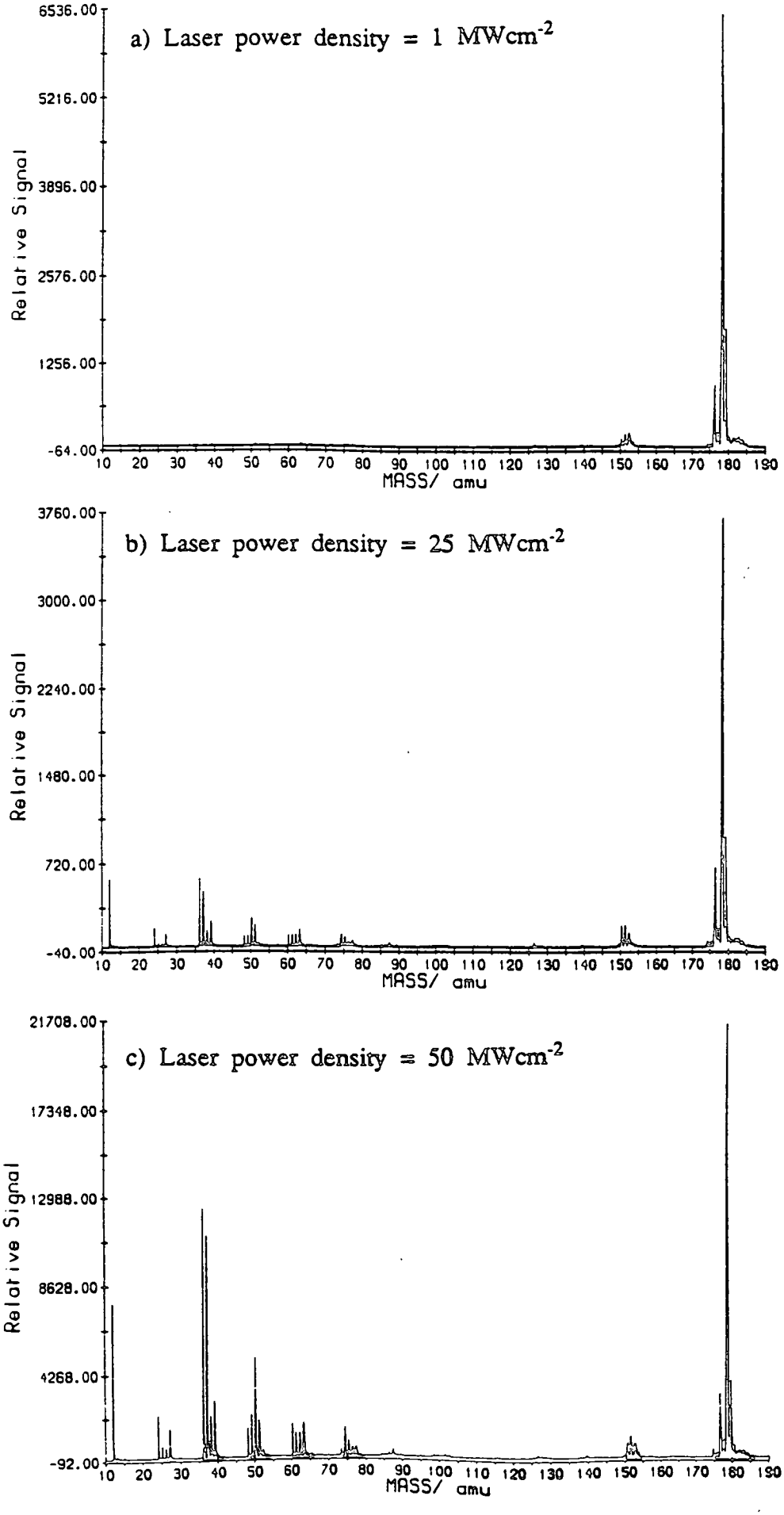

Table 6.4. Mass spectral fragmentation patterns for anthracene and phenanthrene.

Anthracene

1 $MWcm^{-2}$		Calculated		25 $MWcm^{-2}$		100 $MWcm^{-2}$	
m/e	Signal	m/e	Signal	m/e	Signal	m/e	Signal
178	100	178	100	178	100	12	100
179	16.8	179	15.9	36	41.2	36	47.9
167	12.9	180	1.2	37	33.7	178	41.7
168	4.0	181	0.05	12	30.3	24	39.4
142	4.0	182	1.7×10^{-3}	50	19.2	37	34.8
157	4.0	183	3.8×10^{-5}	39	17.5	39	11.1
180	3.0	184	6.6×10^{-7}	179	16.9	179	10.0
182	3.0			63	13.0	50	9.5
183	3.0			176	12.3	27	7.9
181	2.0			38	11.9	38	6.8
184	2.0			51	11.9	51	6.3
				24	9.5	25	5.0
				62	9.2	49	5.0
				60	9.1	63	4.6
				49	8.9	176	4.3
				61	7.5	167	3.9
				27	7.2	180	3.5
				74	7.2	60	3.4
				180	6.8	13	3.0

Phenanthrene

1 $MWcm^{-2}$		Calculated		25 $MWcm^{-2}$		50 $MWcm^{-2}$	
m/e	Signal	m/e	Signal	m/e	Signal	m/e	Signal
178	100	178	100	178	100	178	100
179	27.5	179	15.9	179	25.4	36	57.3
176	14.4	180	1.2	176	18.4	37	51.1
177	3.5	181	0.05	36	15.9	12	35.8
152	3.2	182	1.7×10^{-3}	12	15.6	50	23.3
151	3.0	183	3.8×10^{-5}	37	12.7	179	18.0
180	2.6	184	6.6×10^{-7}	50	6.8	176	15.0
183	2.4			39	6.0	39	13.3
181	2.2			151	5.1	24	10.3
150	1.8			150	5.1	49	10.3
182	1.8			51	5.1	38	10.1
185	1.8			24	4.4	51	8.8
184	1.7			177	4.3	63	8.3
				63	4.0	60	8.0
				38	3.7	74	7.1
				152	3.3	27	7.1
				27	3.0	48	7.0
				74	3.0	62	5.8

spectrum of phenanthrene at mass 150 to mass 152, which is consistent with the loss of C_2H_{2-4} from the molecular ion.

This fragmentation channel appears to be common to all seven PNAHs studied. As the ionisation laser power density is increased to a maximum of 100 $MWcm^{-2}$, all the mass spectra exhibit strong $(M\text{-}C_2H_m)^+$ peaks. The intensity of this cluster of ion peaks remains stronger, relative to the molecular ion, in phenanthrene than in anthracene even under "hard" ionisation conditions, which allows discrimination of the two isomers. As expected, the degree of fragmentation increases with the ionisation laser power density, so that in most cases the mass 12 ion, corresponding to C^+, is observed strongly. This feature of readily controllable fragmentation is unique to MPI as an ionisation technique in mass spectrometry and offers the possibility of simple switching between soft and hard ionisation of any sample. As will be discussed in the following sections, this is of great analytical importance.

The mass spectral data presented in figures 6.1 to 6.7 are summarised in tables 6.3 to 6.8. Here, the ion peak intensities are scaled to the base peak and the strongest peaks listed as a function of the intensity of the UV laser beam. Also included are the calculated molecular ion intensities that might be expected to be observed in a soft ionisation mass spectrum, as evaluated using the natural isotopic abundancies of carbon and hydrogen. It is apparent from these tables that the observed and calculated mass spectra are not in very good agreement. Even taking into account the limited accuracy of the transient digitiser at the 20 MHz digitising rate employed here, the observed intensities of ions corresponding to $(M+2)^+$ and above are in large excess of the vanishingly small

Figure 6.4. LD-MPI mass spectrum of fluorene at $\lambda = 266$ nm.

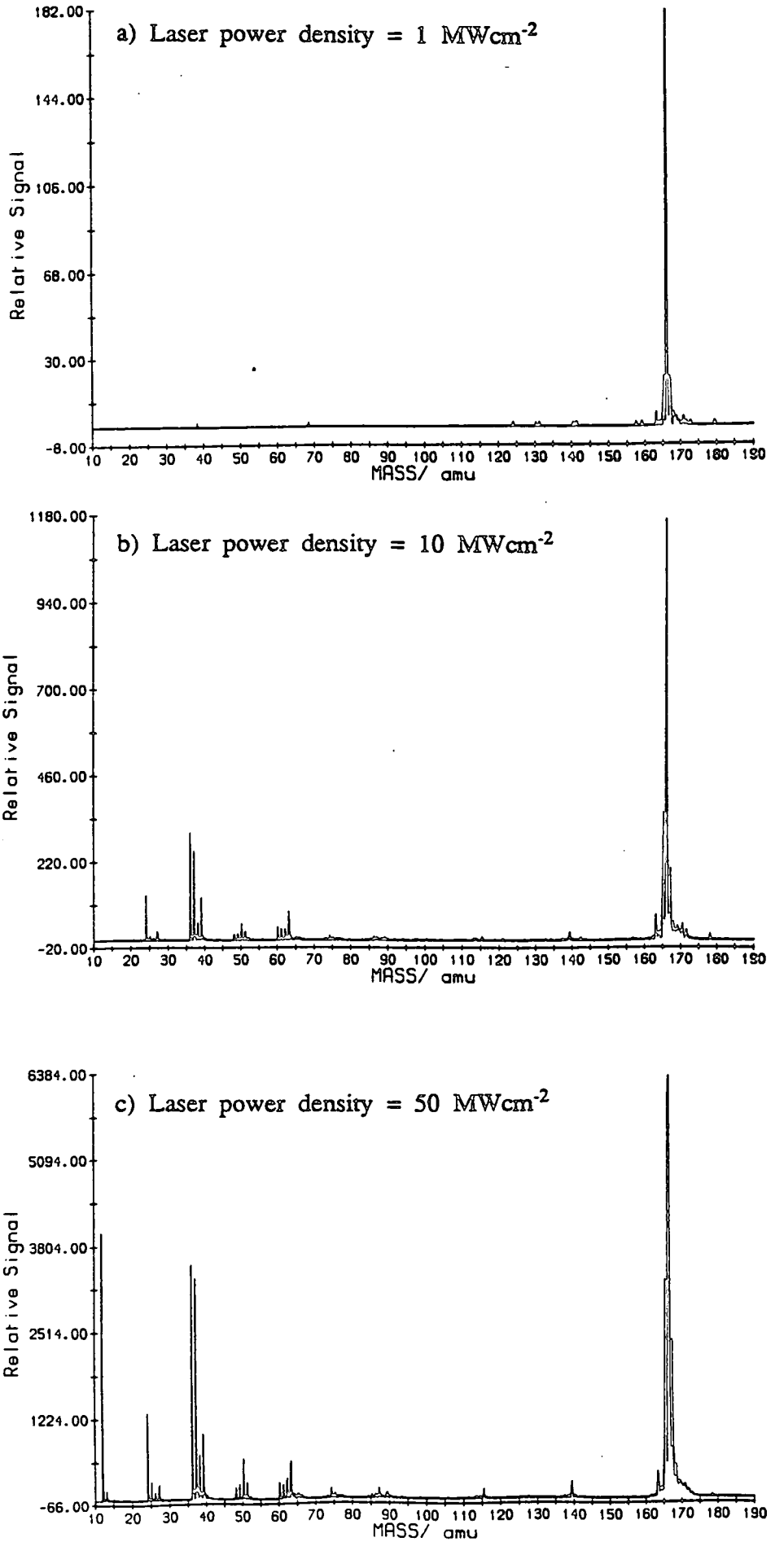

Table 6.5. Mass spectral fragmentation pattern for fluorene.

1 $MWcm^{-2}$		Calculated		10 $MWcm^{-2}$		50 $MWcm^{-2}$	
m/e	Signal	m/e	Signal	m/e	Signal	m/e	Signal
166	100	166	100	166	100	166	100
165	12.1	167	14.7	165	30.3	12	62.8
167	12.1	168	1.0	36	25.6	36	55.3
		169	0.04	37	21.2	37	52.2
				167	17.1	165	51.7
				24	10.8	167	37.5
				39	10.2	24	20.4
				63	6.9	39	15.4
				163	6.1	50	9.6
				168	4.4	63	9.0
				38	4.2	168	8.1
				50	4.1	163	6.5
				170	3.9	38	5.2
				169	3.4	62	4.9
				60	3.2	25	4.4
				61	2.7	139	4.2
				62	2.7	60	4.1
				171	2.4	51	4.1
				164	2.2	169	4.0
				51	2.2	49	3.6
				27	2.2	27	3.6

Figure 6.5. LD-MPI mass spectrum of tetracene at $\lambda = 266$ nm.

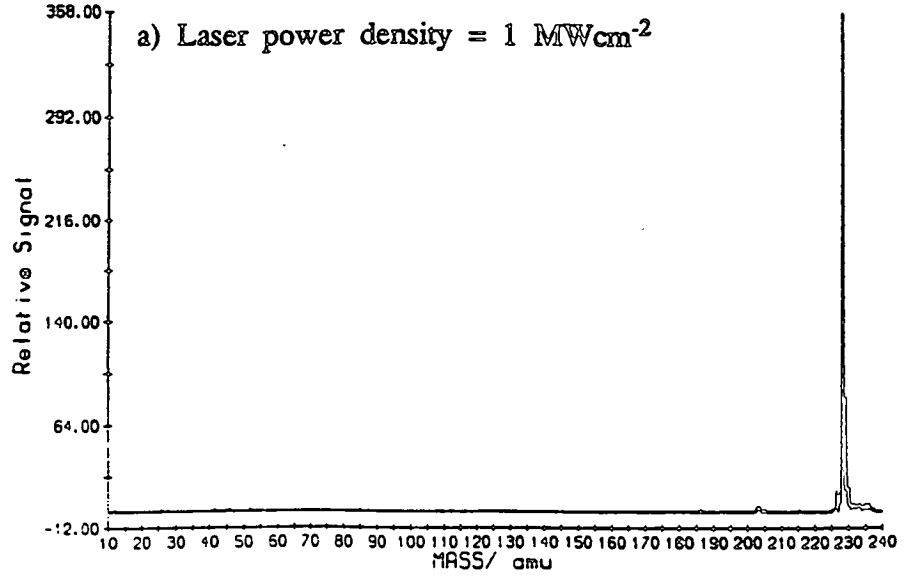

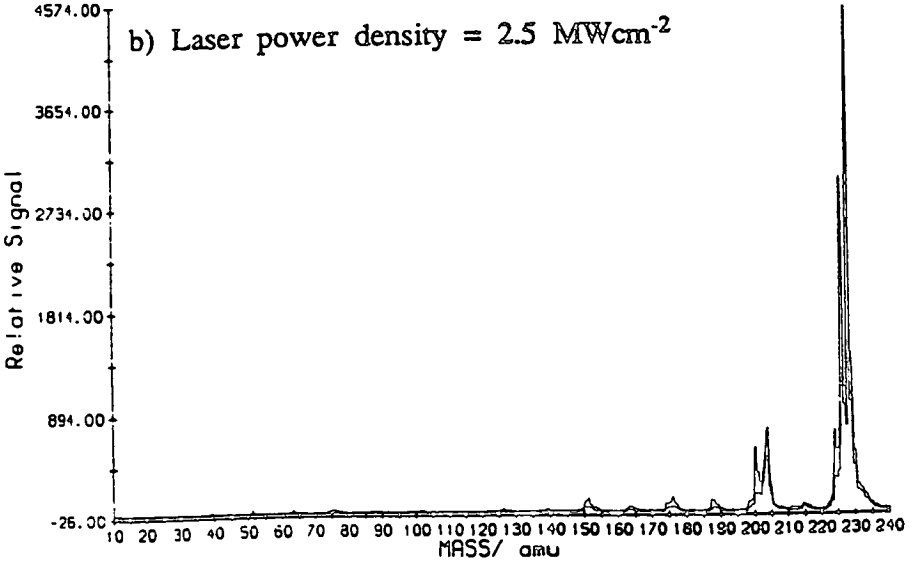

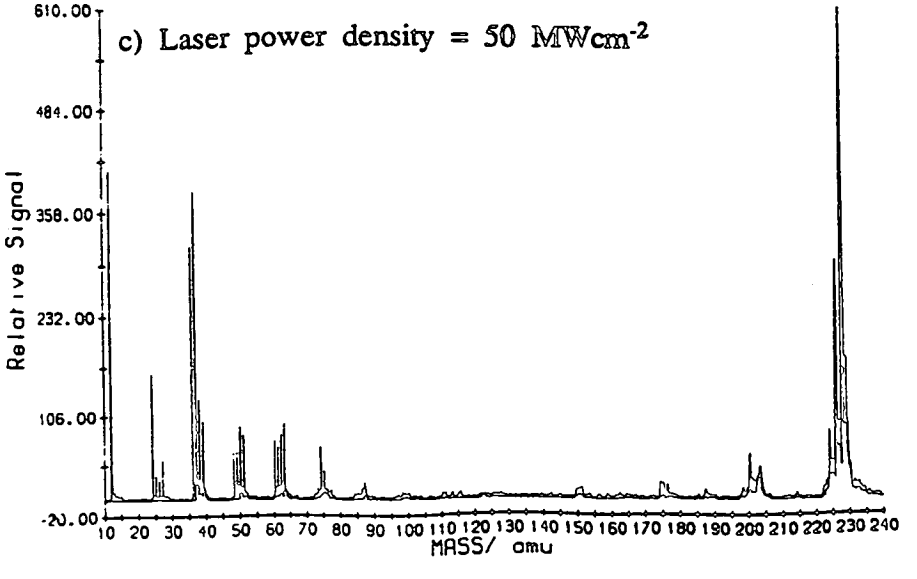

Figure 6.6. LD-MPI mass spectrum of perylene at λ = 266 nm.

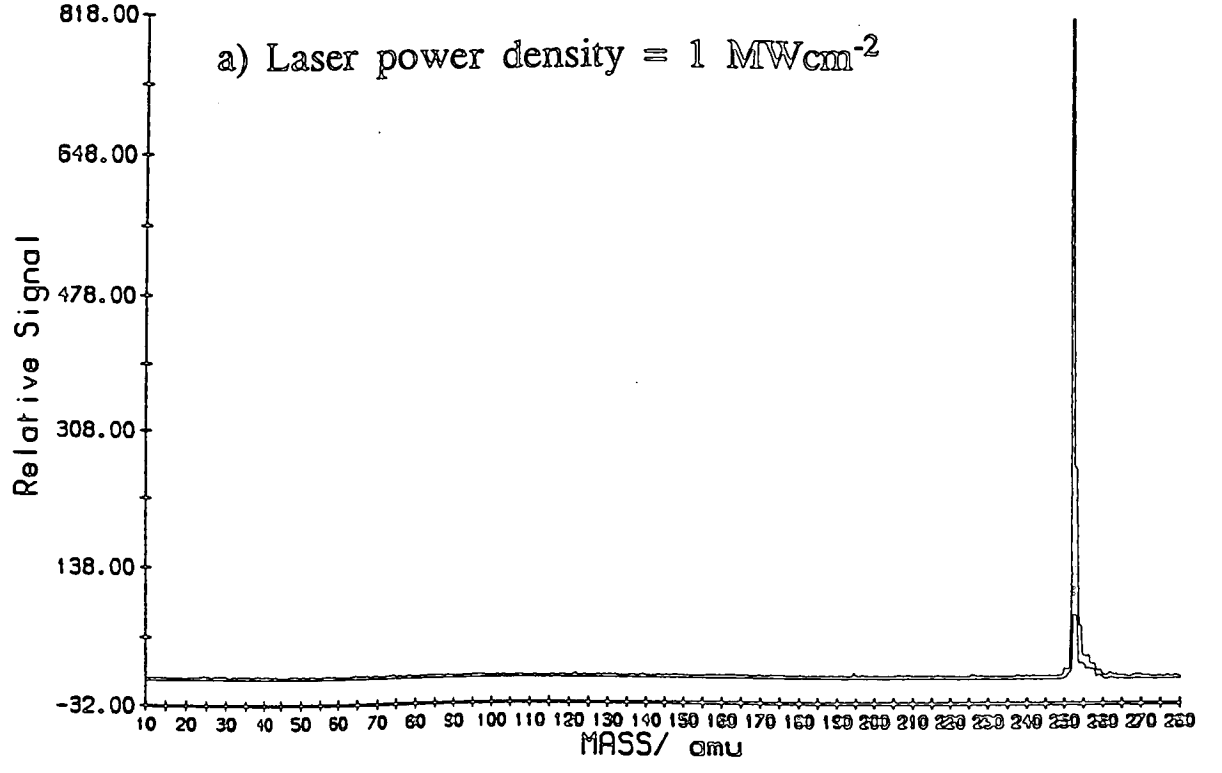

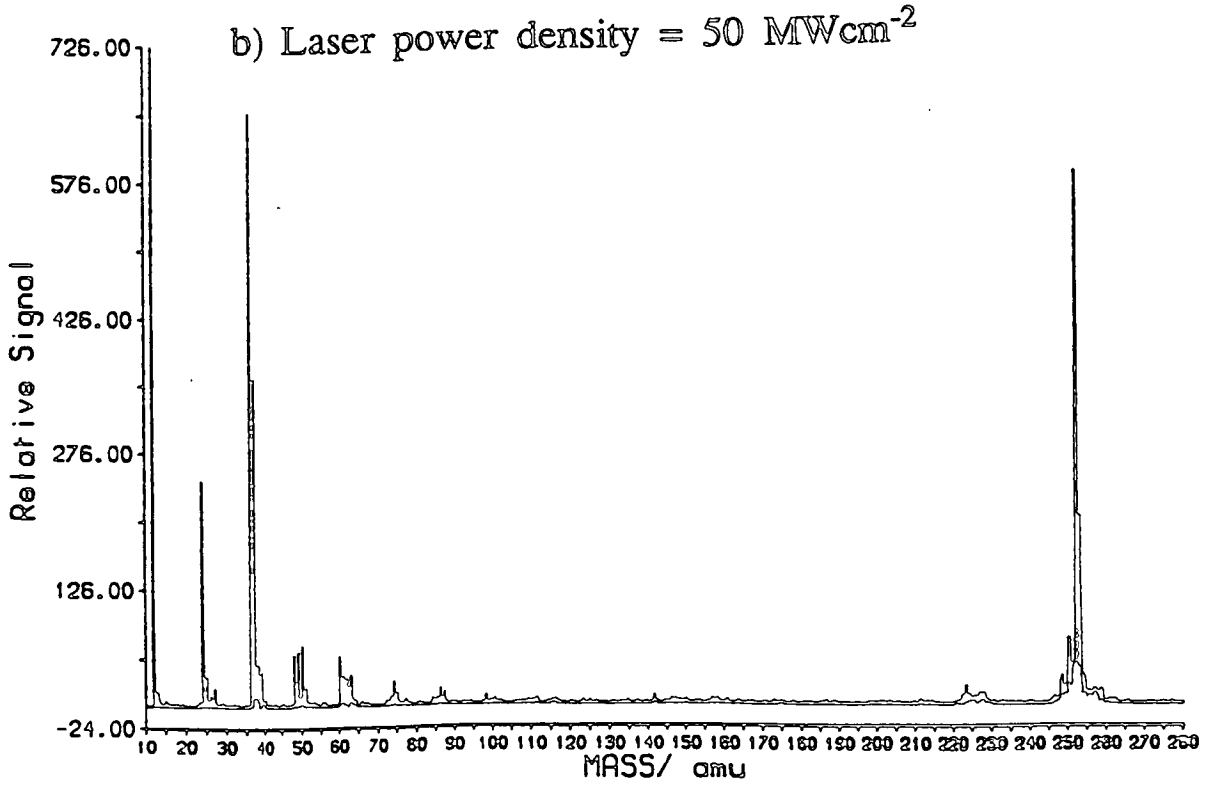

Table 6.6. Mass spectral fragmentation patterns for tetracene and perylene.

Tetracene

1 $MWcm^{-2}$		Calculated		2.5 $MWcm^{-2}$		50 $MWcm^{-2}$	
m/e	Signal	m/e	Signal	m/e	Signal	m/e	Signal
228	100	228	100	228	100	228	100
229	22.8	229	20.4	226	65.9	12	67.2
230	4.9	230	2.0	229	31.2	37	63.0
226	4.3	231	0.11	227	24.3	36	52.1
227	3.8			203	16.6	226	48.9
231	1.6			224	16.1	229	28.9
				200	12.7	24	26.2
				225	12.3	38	20.7
				230	11.9	39	16.1
				204	9.0	63	15.4
				201	7.8	50	14.8
				202	6.2	224	13.8
				231	5.2	62	13.1
				232	4.5	51	13.1
				233	3.3	60	11.8
				176	3.1	74	10.8
				223	2.8	61	10.5
				205	2.8	48	9.5

Perylene

1 $MWcm^{-2}$		Calculated		50 $MWcm^{-2}$	
m/e	Signal	m/e	Signal	m/e	Signal
252	100	252	100	12	100
253	31.8	253	22.6	36	90.1
254	7.8	254	2.4	252	80.7
255	3.4	255	0.165	37	49.6
256	3.4			24	33.9
257	2.2			253	28.1
258	1.5			250	9.9
250	1.5			50	9.1
259	1.2			49	8.3
251	1.2			48	7.7
				60	7.4
				38	6.3
				251	6.1
				39	5.2
				63	4.7
				25	4.4
				61	4.4
				254	4.1
				248	4.1

calculated values. In the absence of any proton transfer reactions, this discrepancy can only be explained by selectively enhanced ionisation of these molecular ions.

6.2.1 LD-MPI mass spectrum of POPOP.

Figure 6.8 shows the mass spectrum obtained for the scintillator molecule POPOP as a function of the ionisation laser power density. The structure of POPOP, (1,4-bis(5-phenyloxazol-2-yl)benzene), is given in table 6.1 and the mass spectral data are summarised in table 6.9. The soft ionisation mass spectrum of POPOP was recorded at 1 $MWcm^{-2}$, and exhibits a strong molecular ion peak at mass 364, with minimal fragmentation, as shown in figure 6.8(a). Increasing the laser power density to 5 $MWcm^{-2}$ results in the appearance of several fragment ions, see figure 6.8(b). The strongest fragment peaks are at mass 77 and 89, corresponding to the mass of one of the benzene groups and the mass of this group plus a carbon atom. Other fragment ions are detected at mass 105, 141, 156 and 164. The structure of these ions is not obvious from simple bond rupture arguments. Increasing the laser power density further still, to 100 $MWcm^{-2}$, does not produce fragment ions more indicative of the structure of the molecule, with only an increase in low mass aromatic-type fragments being observed, see figure 6.8(c).

6.3 LD-MPI mass spectra of amino acids and derivatives.

As will be discussed in section 7.3, a number of different desorption / ionisation techniques have been developed in recent years, primarily in order to obtain

Figure 6.7. LD-MPI mass spectrum of pentacene at $\lambda = 266$ nm.

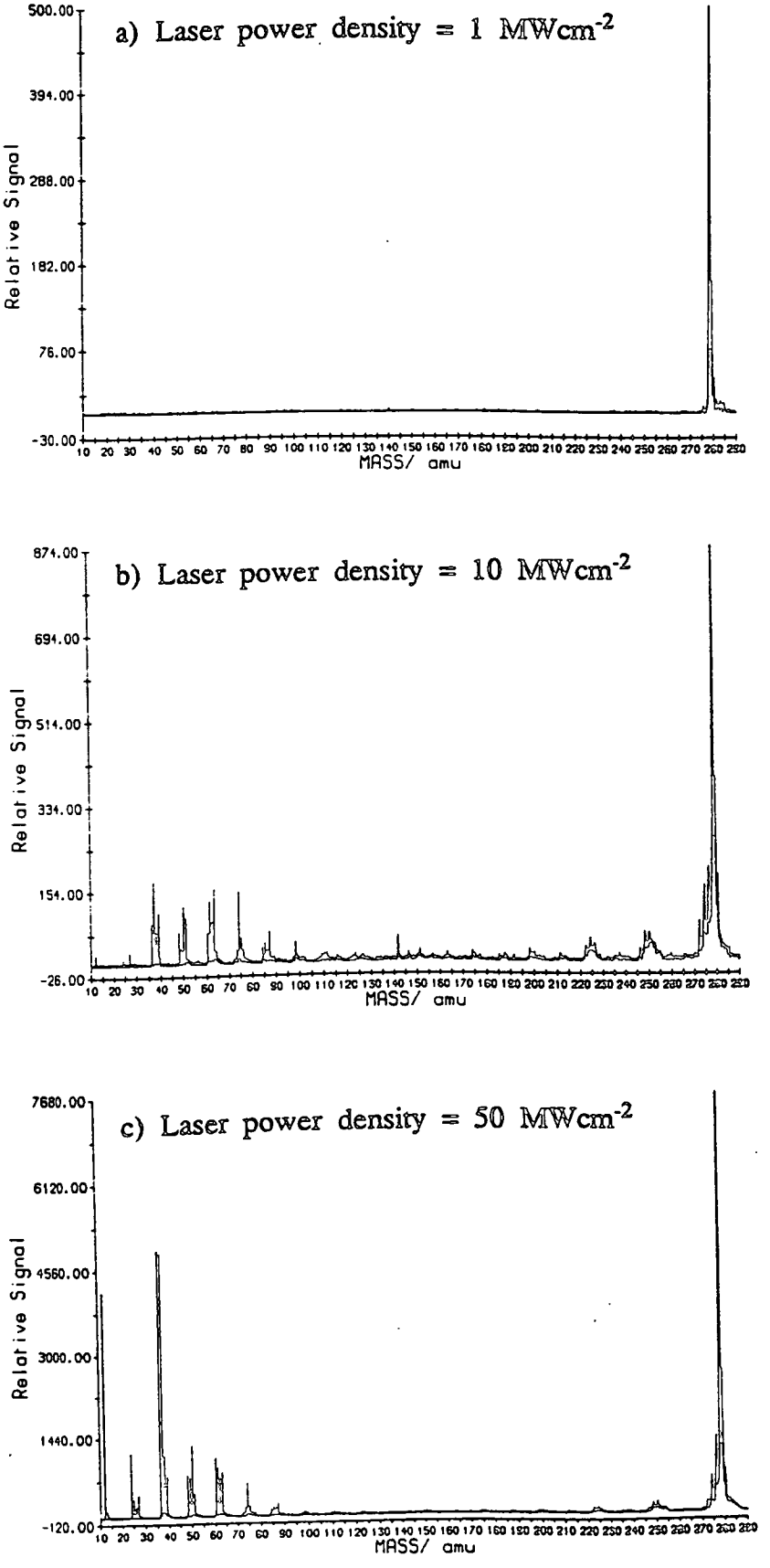

Table 6.7. Mass spectral fragmentation pattern for pentacene.

1 $MWcm^{-2}$		Calculated		10 $MWcm^{-2}$		50 $MWcm^{-2}$	
m/e	Signal	m/e	Signal	m/e	Signal	m/e	Signal
278	100	278	100	278	100	278	100
279	32	279	24.9	279	44.4	36	64.1
280	8.4	280	3.0	276	22.9	37	63.4
281	3.2	281	0.223	280	21.1	12	54.3
283	2.8	282	0.012	37	20.1	279	33.8
284	2.4	283	4.94×10^{-4}	274	18.5	276	17.7
282	2.0	284	1.59×10^{-5}	63	18.1	50	17.2
				74	17.4	24	15.3
				277	15.1	38	14.7
				61	15.1	60	14.1
				50	14.0	61	11.7
				39	12.6	63	10.6
				51	11.2	48	10.0
				62	10.3	280	10.0
				36	10.1	39	9.5
				272	9.8	49	9.3
				48	7.8	62	9.1
				60	7.8	274	8.4
				87	7.8	74	7.9
				248	7.3	277	7.5
				250	7.1	51	5.7

Figure 6.8. LD-MPI mass spectrum of POPOP at λ = 266 nm.

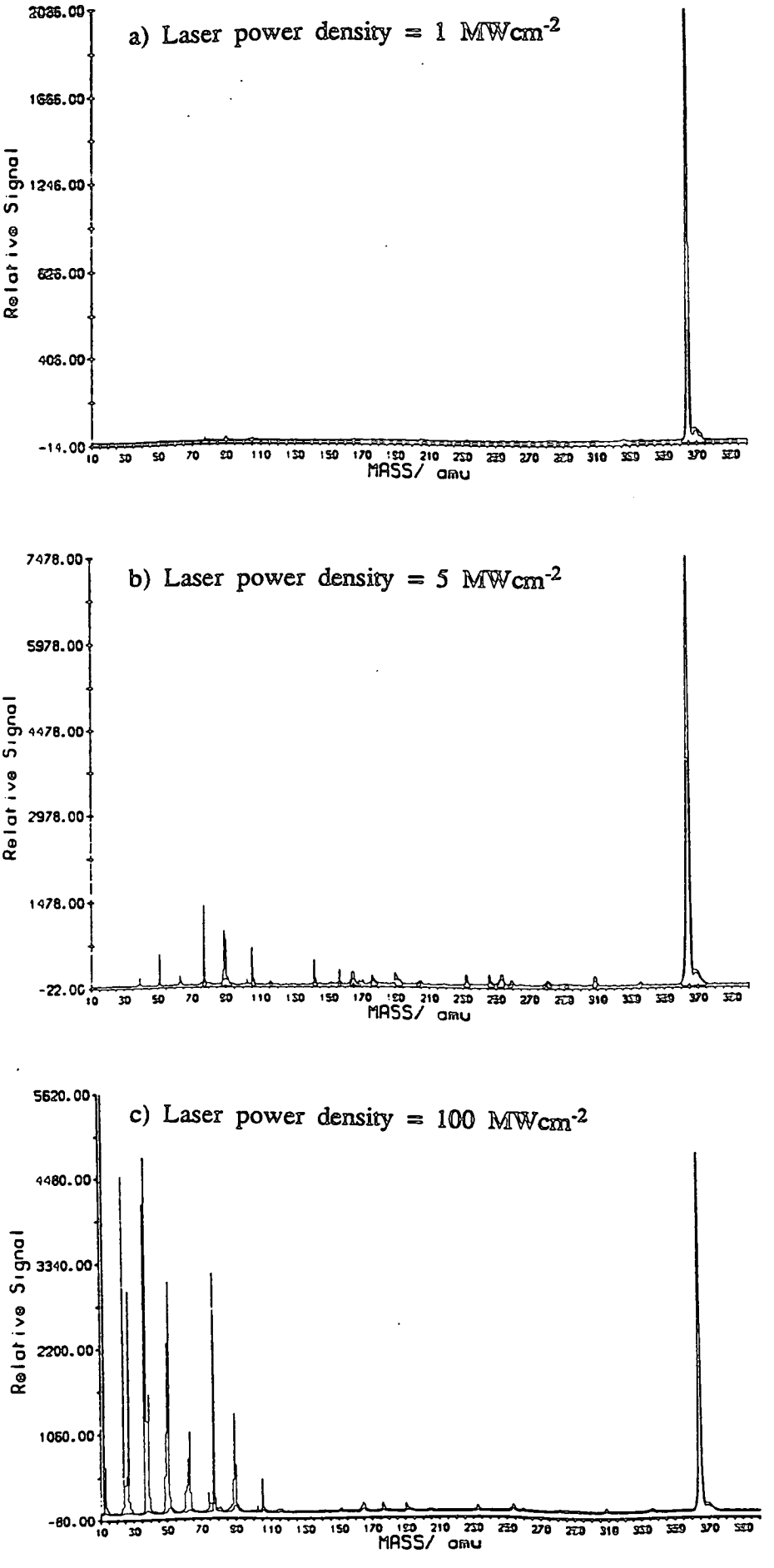

Table 6.8. Mass spectral fragmentation pattern for POPOP.

1 $MWcm^{-2}$		Calculated		5 $MWcm^{-2}$		100 $MWcm^{-2}$	
m/e	Signal	m/e	Signal	m/e	Signal	m/e	Signal
364	100	364	100	364	100	12	100
365	45.2	365	28.0	365	43.8	364	85.1
366	10.2	366	4.2	363	35.7	37	84.7
368	2.9	367	0.44	77	18.7	24	80.2
369	2.8	368	0.036	89	13.1	36	73.4
370	2.4	369	2.4×10^{-3}	366	12.3	77	56.0
371	2.2	370	1.3×10^{-4}	90	10.7	51	54.2
372	1.6			105	9.0	27	52.1
367	1.5			362	8.3	50	39.4
373	1.3			51	7.6	39	27.4
77	1.2			141	6.2	365	23.4
89	1.1			156	3.7	89	22.6
				368	3.6	38	20.7
				88	3.5	63	18.4
				369	3.4	49	17.9
				164	3.3	62	12.0
				190	3.0	90	10.4
				165	3.0	13	10.2
				370	3.0	26	8.0
				246	2.8	48	8.0
				253	2.8	88	7.8

mass spectral information from involatile and thermally labile materials such as biological molecules. One group of this latter class of molecules which is of considerable importance is the amino acids. The EI mass spectra of free amino acids were measured as long ago as 1962 [9], [10]. In most cases, in the EI mass spectra the molecular ion peak is either very weak or not observed, and the fragmentation channels involved depend to a large extent on the type of amino acid studied [11]. These molecules have vanishingly small vapour pressures at room temperature and decompose readily upon heating. They are therefore an ideal set of molecules to study to allow evaluation of the application of LD-MPI MS to biological molecules. Four amino acids were studied in this work, namely L-tryptophan, L-tyrosine, L-phenylalanine and L-histidine.

The structural formulae of these four amino acids are shown in table 6.1. Along with all other amino acids, these molecules have as a common structural feature a free carboxyl group and a free unsubstituted amino group on the α carbon atom. In addition, each amino acid has a characteristic R group. Generally, the amino acids are classified according to the polarity of this R group. Tryptophan (denoted Trp) and phenylalanine (denoted Phe) contain non-polar R-groups, whilst tyrosine (denoted Tyr), which contains a hydroxyl group, has an uncharged but polar R group. Histidine (denoted His), on the other hand, contains an R group which has a slight net positive charge at pH 7.0. This is due to the weakly basic imidazolium function. At pH 6.0 more than 50% of histidine molecules possess a protonated or positively charged R-group, but this has reduced to less than 10% at pH 7.0.

These compounds absorb the 266 nm wavelength radiation through the π^*-π

transition of the aromatic moiety. It is likely that, since there is only partial cooling in the molecular beam, there will be some degree of resonant enhancement in this excitation step, and the subsequent ionisation of these molecules by absorption of a second photon corresponds to R2PI. The liquid-phase UV absorption spectra of the three aromatic amino acids are shown in figure 6.9. These spectra were obtained from 1 mM solutions of the amino acids. The solvents used were methanol for Phe and Trp and 0.1 M HCl for Tyr. It is clear from this spectrum that all three aromatic amino acids absorb UV light significantly, with the relative absorbances at 266 nm being Trp > Tyr > Phe. The UV absorption spectrum of histidine was not measured, but was it was thought likely that since it contains some degree of conjugation, histidine may have a non-zero absorption at 266 nm.

Tables 6.9 - 6.11 summarise the mass spectral data obtained for the three aromatic amino acids under a range of ionisation laser power densities at λ = 266 nm. As before, the measured isotopic peak patterns of the molecular ions are compared with the patterns calculated from the natural isotopic ratios.

6.3.1 L-tryptophan.

As shown in figure 6.10(a), the molecular ion of L-Trp, at mass 204, is the base peak in the soft ionisation LD-MPI mass spectrum at λ = 266 nm. The ionisation laser power density in this case was 4 x 10^5 Wcm^{-2}. However, a fragment peak at mass 130 is also detected strongly under these conditions. This ion, which is the base peak in EI mass spectra of L-Trp, is generated by the loss of the amino acid function from $M^{+\cdot}$, leading to the formation of a fully

Figure 6.9. The liquid-phase absorption spectra of 1 mM solutions of L-Trp, L-Tyr and L-Phe.

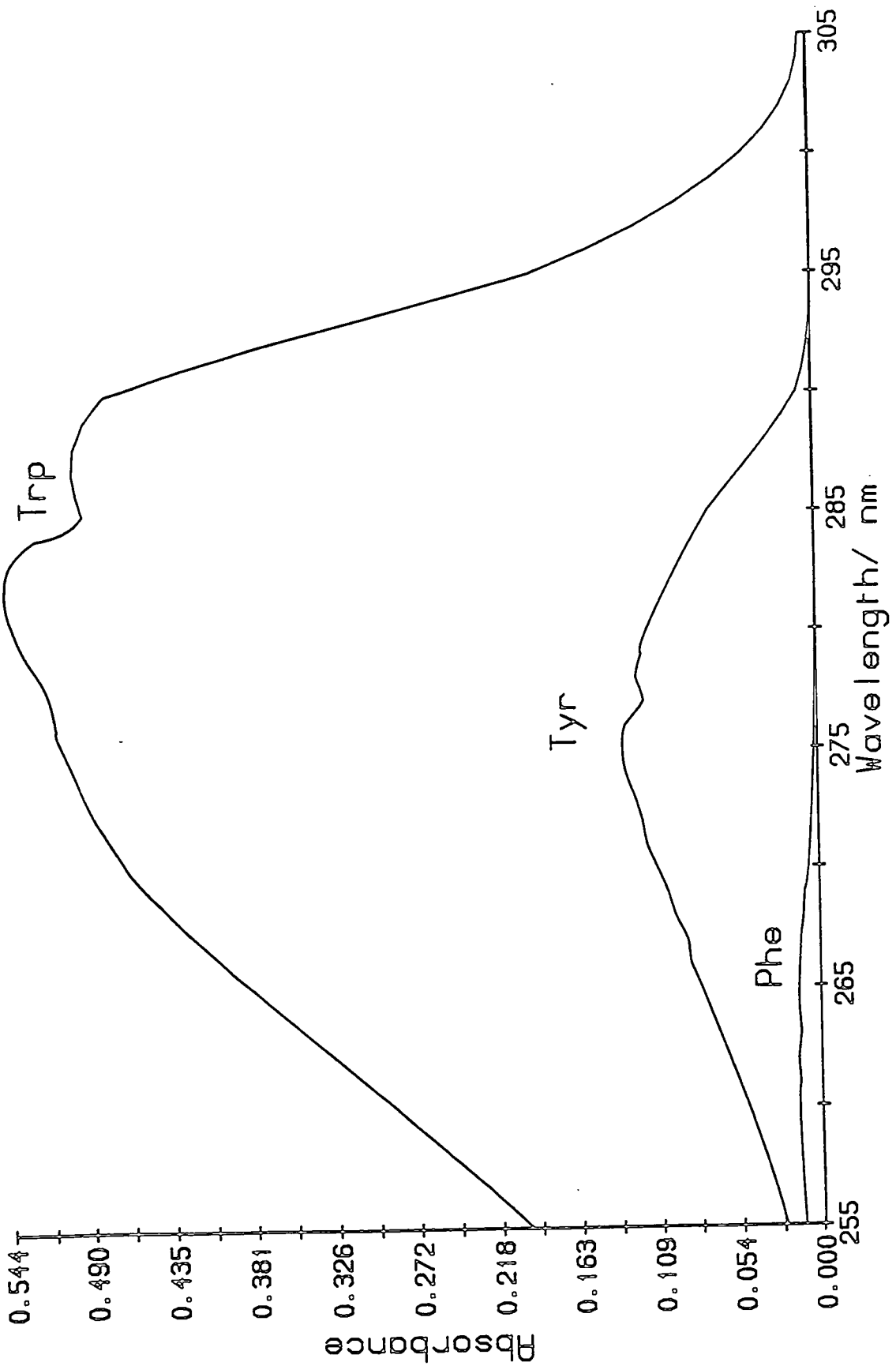

conjugated dehydroindole ion as indicated below. This ion is formed by a radical bond cleavage β to the amino function, a fragmentation channel well-known from EI studies of the aromatic amino acids and their derivatives [2].

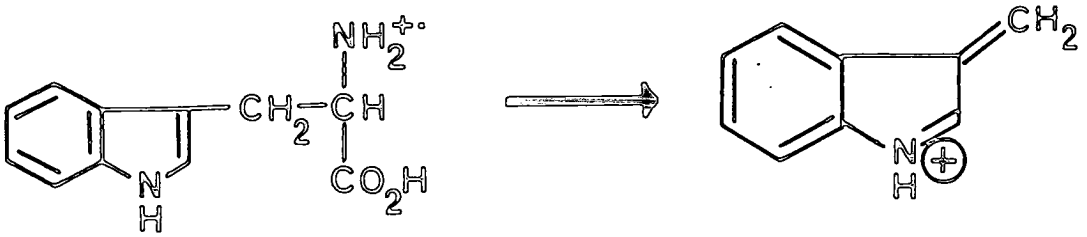

Also shown in figure 6.10(a) is a small cluster of ill-resolved, broad peaks centred at mass 151. The position of this clump of peaks relative to the two main peaks in the spectrum appeared to be dependent on the fields set in the ion reflector, with an apparent shift of ±5 amu possible with a small adjustment of this voltage. It is thought likely that this broad group of peaks is indicative of metastable fragmentation of the molecular ion outwith the extraction region of the ion source.

It is well known from conventional TOF mass spectrometry that ions produced by metastable decay within the acceleration region of the ion extraction optics have longer flight times than "stable" ions of the same mass created at the point of ionisation. This is because the velocity of the parent ions before dissociation is smaller than the velocity that the stable daughter ions would have obtained at the same point in space. As a result, mass peaks due to metastable dissociation in the acceleration region of the extraction optics are shifted to the larger mass of the

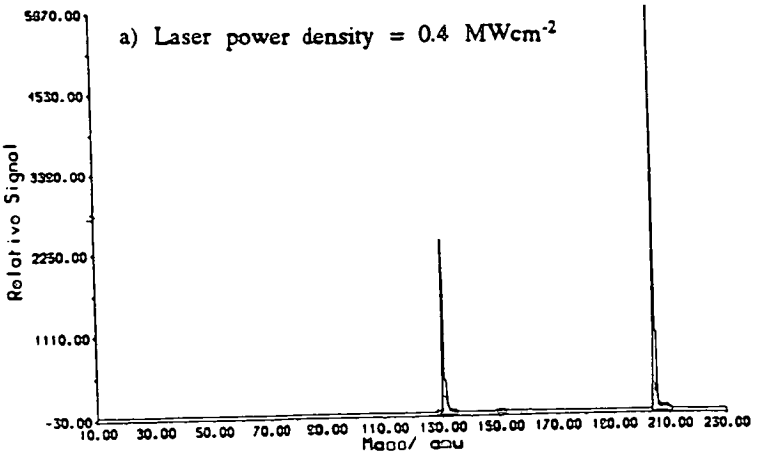

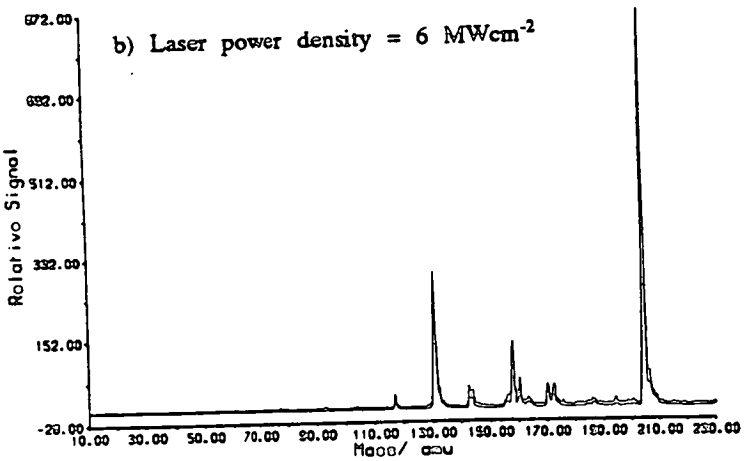

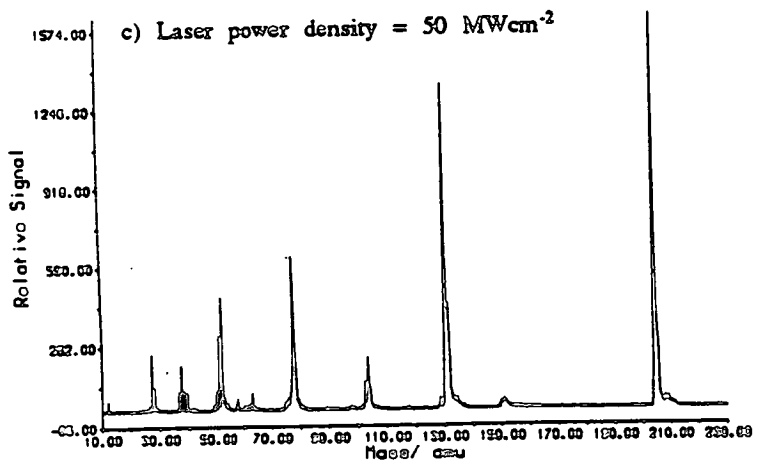

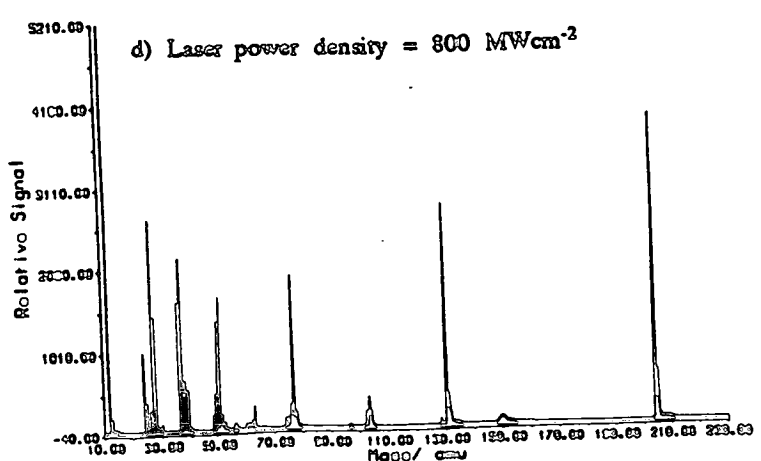

Figure 6.10. LD-MPI mass spectr
of L-tryptophan at λ = 266 nm.

Table 6.9. Mass spectral fragmentation pattern for tryptophan at 266 nm.

0.4 $MWcm^{-2}$		Calculated		6 $MWcm^{-2}$		50 $MWcm^{-2}$		800 $MWcm^{-2}$	
m/e	Signal	m/e	Signal	m/e	Signal	m/e	Signal	m/e	Signal
204	100	204	100	204	100	204	100	12	100
130	42.6	205	13.3	130	34.2	130	82.3	204	75.5
205	19.0	206	1.2	205	23.4	77	38.8	130	54.3
131	8.1	207	0.085	131	16.2	51	28.6	27	52.1
206	1.7	208	0.004	158	16.2	131	26.7	37	42.5
209	1.3			160	7.1	50	18.8	77	37.4
208	1.3			206	6.4	205	18.7	51	32.7
207	1.1			170	5.7	27	14.2	36	31.6
				142	5.5	103	13.2	28	28.3
				172	5.5	37	11.6	50	26.9
				207	5.0	78	7.2	24	19.8
				132	5.0	102	7.0	205	12.7
				203	4.8	28	6.0	38	12.7
				144	4.4	76	5.1	39	10.4
				159	4.4	38	5.0	49	9.2
				117	3.4	49	4.9	131	8.1
				208	3.4	36	4.9	103	7.8
				157	3.2	104	4.8	25	7.4
				156	3.0	132	4.8	76	5.8
				143	2.7	39	4.5	63	5.7
				209	2.5	63	4.3	26	5.4

parent ions. If, however, dissociation occurs in the drift region of a conventional linear TOF mass spectrometer, where all the ions have reached their final velocities, the velocity of the daughter ions corresponds to that of the parent ions. Consequently, it is not possible to distinguish the daughter ions from their parent ions.

Boesl et al. [12], [13] have shown that, if the energy shift produced in a metastable decay is within the energy range that can be corrected for by the ion mirror in a reflectron TOF mass spectrometer, dissociation in the drift tube results in sharp fragment ion peaks at the correct mass. The energy shift of the daughter ions produced in such a metastable decay is given by

$$\Delta E = eV_0(1 - m_l/m_0),$$

where m_0 is the parent ion mass, m_l is the daughter ion mass, and V_0 is the extraction energy of the ions produced in the ion source. With an extraction voltage of 1045 V, this equation yields a value of 479 eV for ΔE, if it is assumed that the daughter ions are of mass 130 and the parent ions are the molecular ions. This is clearly outwith the energy range that can be corrected for by the ion mirror, with the result that these ions appear in the spectrum between the masses of the parent and daughter ions. Grotemeyer et al. [14] reported an intense metastable peak in their soft ionisation LD-MPI mass spectrum of L-Trp at 266 nm. They offered this as evidence that the dehydroindole ion is created from the molecular ion of tryptophan in a single-step fragmentation process.

By increasing the laser power density to about 6 $MWcm^{-2}$, the absorption of at

least one photon by the molecular ion results in the appearance of further fragment ion peaks, as shown in figure 6.10(b). The strongest of these new ion peaks are at mass 159, 170, 142 and 117 respectively. The first of these is simply due to loss of the COOH radical from the molecular ion, yielding tryptamine ions,

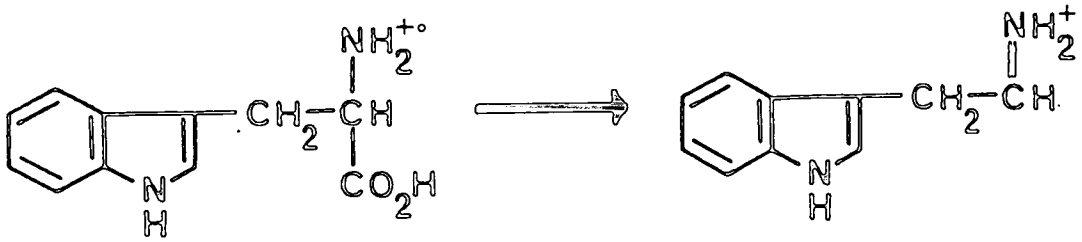

Further loss of NH_3 gives the mass 142 ion. The peak at mass 117, which corresponds to the mass of indole, is probably due to ions formed through loss of C_2H_2 from this latter species, but may also originate from the dehydroindole ion. The structure of the mass 170 ion is not clear.

A further increase of the ionisation laser power density to 5×10^7 Wcm^{-2} results in even greater fragmentation, with low mass fragments such as mass 77, 51, 27 and 37 gaining in intensity relative to the molecular ion, which nevertheless remains the base peak of the spectrum (see figure 6.10(c)). At higher ionisation laser power densities ($I = 8 \times 10^8$ Wcm^{-2}), the molecule is completely dissociated into fragments as small as C^+ ions, as shown in figure 6.10(d). The base peak of this mass spectrum is now at mass 12. However, the molecular ion and dehydroindole ion peaks are still prominent in this spectrum, providing a clear fingerprint for Trp.

The observed fragmentation channel, yielding mass 130 ions even at low laser

power densities, may result from either the desorption or ionisation steps. There are at least three possible mechanisms which may account for the observed spectra:

1. Molecular decomposition may occur during desorption, with subsequent MPI of these species.
2. Photodissociation may preceed ionisation during the MPI scheme.
3. Efficient molecular ion dissociation may occur after ionisation, even at low power densities.

In an attempt to shed light on which of these mechanisms was operative in this case, a second ionisation laser wavelength was chosen. A laser wavelength to the red of 266 nm, close to the S_1-S_0 origin band in tryptophan, was selected.

Levy and coworkers have used a combination of thermospray and thermal desorption techniques to introduce tryptophan into a molecular beam [15]. Using R2PI, they recorded the jet-cooled electronic spectrum of tryptophan in the gas-phase. Whilst some of the spectral features were characteristic of more volatile indole derivatives, they observed a series of strong features, separated by a few tens of wavenumbers, around 290 nm. These features, which are absent from simpler indole containing molecules, were attributed to several conformers of tryptophan, and a prominent peak observed at 34873 cm^{-1} was assigned as the origin band of the S_1-S_0 transition in tryptophan. Under the experimental conditions employed here, it was not possible to observe this type of absorption structure, mainly due to the lack of shot-to-shot stability in the desorption stage. However, if mass spectra were recorded using an ionisation laser wavelength of

286.96 nm at a power density of 3 x 10^5 Wcm^{-2}, it was possible to obtain soft ionisation mass spectra of tryptophan with no fragmentation, as shown in figure 6.11. Similar mass spectra have been obtained by Grotemeyer et al. [14], [16], but at different laser wavelengths.

It is likely that if the mass 130 fragment ion peak observed in figure 6.10(a) was produced via MPI of a neutral fragment formed during desorption, this neutral species, which contains the indole chromophore, would absorb UV radiation sufficiently strongly at 286.96 nm for an ion signal to be obtained. This would be especially true if the degree of molecular beam cooling was not optimised. A more plausible explanation for the observed phenomenon is that at 266 nm, even at low laser power densities, absorption of the two photons required for ionisation excites the tryptophan molecules to an energy in excess of the appearance potential for the dehydroindole ion. At the longer wavelength of 286.96 nm, the energy of two photons is sufficient to ionise the molecule, but insufficient, at low laser power density, to promote any fragmentation. No measurements were made at 286.96 nm for higher power densities. However Grotemeyer et al. [14], [16] reported the appearance of similar fragment ions at wavelengths of 266, 286.0 and 292.0 nm. The relative intensities of the various fragment ion peaks differed at these three wavelengths, under similar power densities, with the most abundant fragmentation observed at the shortest wavelength. It is therefore clear that the observed fragmentation in the LD-MPI mass spectrum of tryptophan is a result of the MPI process, with the softest ionisation possible with a laser wavelength close to the S_1-S_0 origin band.

Figure 6.11. LD-MPI mass spectrum of L-tryptophan at λ = 286.96 nm.

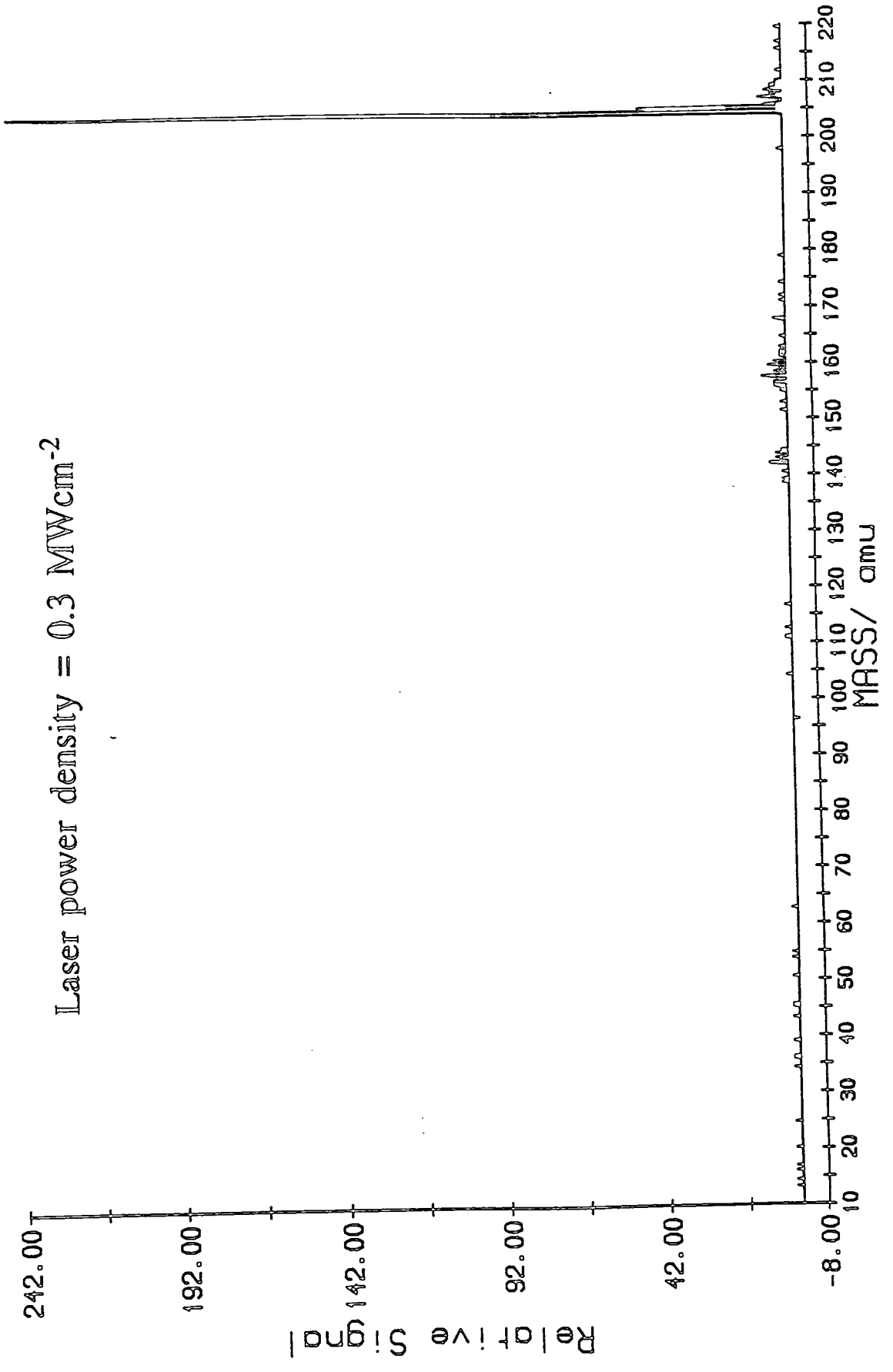

6.3.2 L-tyrosine.

Figure 6.12 shows the LD-MPI mass spectra of tyrosine obtained at λ = 266 nm as a function of the ionisation laser power density. As in the case of Trp, under soft ionisation conditions, the only ions detected are those at mass 181, the molecular ion, and at mass 107, which corresponds to the loss of the complete amino acid function, probably by simple cleavage of the benzylic C_α-C_β bond, forming a stable, even electron fragment ion. It has been proposed that this latter ion takes the form of a hydroxytropylium ion [17],

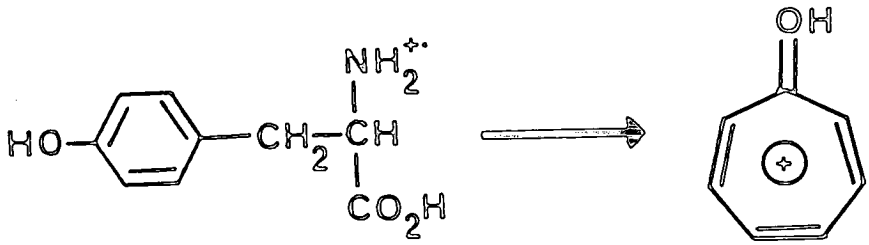

No ion signal was detected at ionisation power densities lower than 1 $MWcm^{-2}$, in contrast to the case of tryptophan. At this power density, the molecular ion is the base peak of the mass spectrum, as shown in figure 6.12(a). Increasing the ionisation laser power density slightly, to around 8 x 10^6 Wcm^{-2}, increases the yield of the mass 107 ion relative to the molecular ion, see figure 6.12(b). Several other fragment peaks start to appear under these conditions, namely those at mass 74, 77 and 136. The former corresponds to the ionised amino acid function NH_2=$CHCOOH^+$, whilst the mass 77 ion almost certainly originates from the bare aromatic ring. As in the case of tryptophan, the mass 136 ion is due to loss of COOH from the molecular ion. Figure 6.12(c) was recorded with an ionisation laser power density of 100 $MWcm^{-2}$. The mass 107 peak is now the base peak of

Figure 6.12. LD-MPI mass spectrum of L-tyrosine at λ = 266 nm.

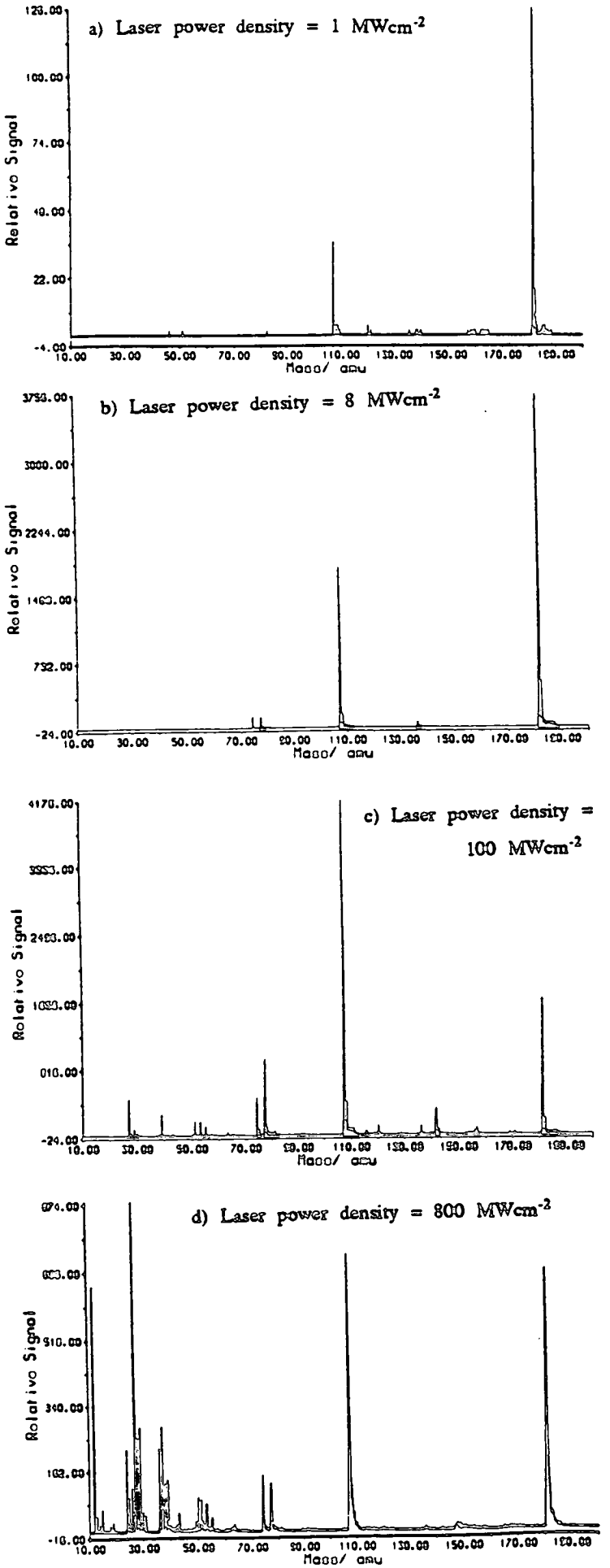

Table 6.10. Mass spectral fragmentation pattern for tyrosine at 266 nm.

1 $MWcm^{-2}$		Calculated		8 $MWcm^{-2}$		100 $MWcm^{-2}$		800 $MWcm^{-2}$	
m/e	Signal	m/e	Signal	m/e	Signal	m/e	Signal	m/e	Signal
181	100	181	100	181	100	107	100	27	100
107	28.6	182	10.7	107	48.3	181	40.6	107	43.5
182	14.3	183	1.1	182	14.1	77	22.9	181	78.7
108	3.2	184	0.081	108	4.4	74	11.4	12	74.9
120	3.2	185	0.005	74	3.6	27	11.0	37	32.4
109	3.2			77	3.5	108	10.2	29	32.3
183	3.2			183	2.0	141	8.0	28	29.0
185	3.2			136	1.9	39	6.6	36	25.8
186	3.2			186	1.7	182	5.0	24	25.3
				184	1.5	51	4.5	74	17.2
				185	1.2	53	4.3	39	16.1
				187	1.2	55	3.1	38	15.1
				109	0.9	120	3.1	77	14.9
				111	0.6	136	2.7	26	13.6
				39	0.5	78	2.6	108	13.6
				53	0.5	29	2.3	182	12.9
				78	0.5	156	2.3	50	10.6
				110	0.5	75	2.2	25	10.4
				137	0.5	110	2.2	51	10.0
				27	0.4	109	1.9	53	8.6
				120	0.4	142	1.9	14	6.8

the spectrum. In addition, several other fragment ion peaks are present at mass 27, 39, 51, 120, 141 and 156. The first three of these are $C_nH_m^+$ ions indicative of the breakdown of the aromatic ring. The mass 120 peak could be formed by loss of either NH_2 or O from the mass 136 ion, but the form of the other two ions is not clear. At 800 $MWcm^{-2}$, the molecule is strongly fragmented, with the base peak being at mass 27, see figure 6.12(d). As in the case of tryptophan, however, the mass 107 and 181 peaks are still prominent, acting as a fingerprint for tyrosine.

The LD-MPI mass spectrum of tyrosine has been reported at a number of ionisation wavelengths [14], [18]- [20]. Grotemeyer et al. [14] reported no fragmentation of the molecular ion under soft ionisation conditions at 272.7 nm, whilst Lubman and coworkers [19] reported similar spectra to those presented here using 280 nm wavelength laser radiation. In their paper, Grotemeyer et al. reported intense metastable peaks at both λ = 266 nm and 272.7 nm, providing evidence that the formation of the hydroxytropylium ion from the molecular ion involves a single-step process.

6.3.3 L-phenylalanine.

The LD-MPI mass spectra of L-phenylalanine as a function of the ionisation laser intensity at λ = 266 nm are presented in figure 6.13. In contrast to both Trp and Tyr, it was relatively difficult to obtain a spectrum for this molecule, and the assignment of several of the spectral features is not so apparent. No signal could be obtained for Phe until the ionisation laser power density was approximately 5×10^6 Wcm^{-2}. Even then, the spectrum obtained, shown in

Figure 6.13. LD-MPI mass spectrum of L-phenylalanine at λ = 266 nm.

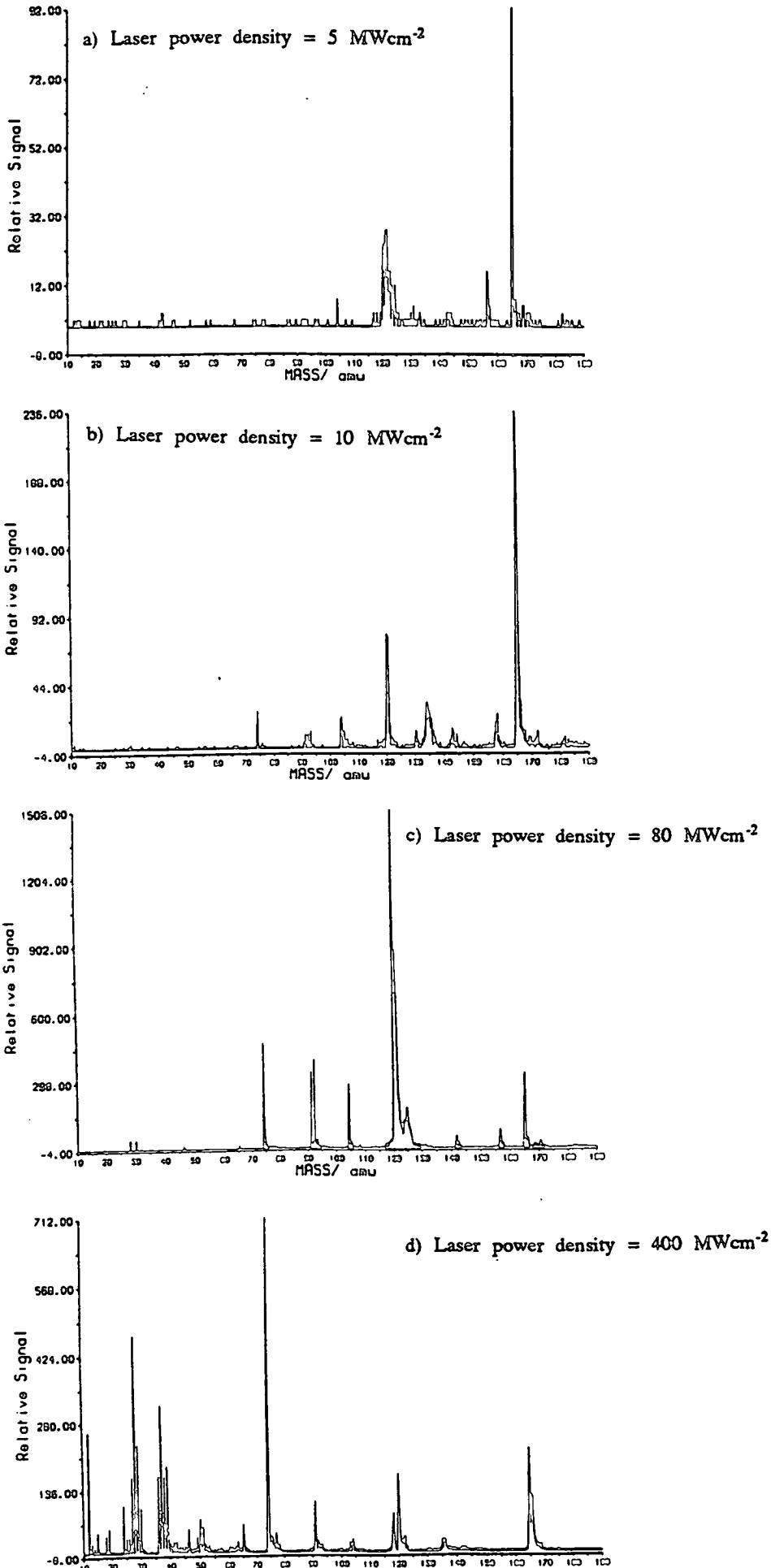

Table 6.11. Mass spectral fragmentation pattern for phenylalanine at 266 nm.

5 $MWcm^{-2}$		Calculated		10 $MWcm^{-2}$		80 $MWcm^{-2}$		400 $MWcm^{-2}$	
m/e	Signal	m/e	Signal	m/e	Signal	m/e	Signal	m/e	Signal
165	100	165	100	165	100	120	100	74	100
120	30.4	166	10.7	120	33.9	121	58.6	28	65.7
121	30.4	167	0.9	164	16.9	74	31.6	37	44.9
122	26.1	168	0.058	166	13.6	92	26.6	12	36.8
156	17.4	169	0.003	134	13.6	91	22.8	29	32.9
123	17.4			74	11.0	165	22.4	165	31.2
124	15.2			158	10.2	104	19.1	39	26.4
166	8.7			104	9.3	122	12.7	120	23.9
104	8.7			135	8.5	125	12.2	36	23.6
167	4.3			157	7.6	124	8.5	38	23.3
				121	6.8	123	7.6	27	23.0
				143	5.9	156	5.7	166	17.4
				167	5.9	126	4.0	91	15.7
				93	5.1	141	3.7	24	14.6
						75	3.7	30	13.8
						166	3.3	118	12.1
						28	3.0	50	10.4
						30	3.0	65	8.7
						93	2.8	51	7.9
						119	2.5	19	7.6
						105	2.1	15	6.5

figure 6.13(a) had a poor signal to noise ratio. Nevertheless, this spectrum exhibits a strong molecular ion peak at mass 165, and shows little fragmentation. Fragment ion peaks are observed at mass 156 and a broad, unresolved peak from mass 120 to 124. As before, the identity of the mass 156 ion is unknown, and may be due to the presence of an impurity in the sample. The mass 120 peak is formed by elimination of COOH from the molecular ion, contrary to the dominant mechanism of complete loss of the amino acid function observed in both tryptophan and tyrosine.

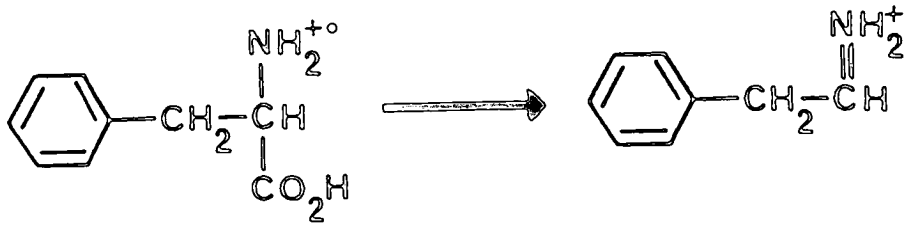

The observed broadness of this peak has no obvious explanation.

Increasing the ionisation laser power density to 10^7 Wcm^{-2} greatly improved the signal to noise ratio of the spectrum, see figure 6.13(b). In this case, a number of fragment ions are observed along with the molecular ion, which is the base peak of the spectrum. The mass 120 peak is the single most intense fragment peak under these conditions, and is considerably sharper than before. A broad metastable-like peak centred at mass 134 is probably indicative that this fragmentation process occurs in one step, by comparison with Trp and Tyr [14]. Other peaks are at mass 74, the ionised amino acid functional group, 156 and 141. Figure 6.13(c) was recorded at an ionisation laser power density of 80 $MWcm^{-2}$. Here, the base peak of the mass spectrum is no longer the molecular

ion, but rather the mass 120 peak. A broad, poorly-resolved peak is centred at mass 125. Due to the poor accuracy with which the ion mirror fields could be set, this peak is thought to be the same metastable feature found at mass 134 in figure 6.13(b). Other strong fragment peaks are at mass 74, 92, 91, 104, 156 and 141. The mass 91 feature is due to bond rupture β to the amino acid function in the molecular ion, leading to the formation of a tropylium ion. As mentioned previously, unlike the other two aromatic amino acids studied, this loss of the amino acid function does not result in the base peak of the partially hard ionisation mass spectrum. The structures of the mass 92, 104 and 141 ionic species are unknown. At 4×10^8 Wcm^{-2}, substantial fragmentation of the molecular ion has occurred, with strong peaks observed corresponding to C_nH_m, where n = 1 to 4, see figure 6.13(d). Under these conditions, the mass 120 peak has undergone a great deal of dissociation, with the result that the mass 74 ion is the most abundant in the spectrum.

Junk and Svec [10] reported a high mass 74 ion current in EI studies of Phe, whilst both Tyr and Trp had low intensity mass 74 peaks. The reason for this is the greater tendency for the more stable (aromatic-CH_2) fragments from Tyr and Trp to accomodate the positive charge than is the case with Phe. Biemann et al. [21] measured the relative intensity of the amine, ester and (aromatic-CH_2) fragments from the amino acid esters of Trp, Tyr and Phe and demonstrated the increasing π-electron density in the aromatic ring on going from Phe to Tyr to Trp. This enhanced electron density increases the ability of the ring to accomodate the charge.

Grotemeyer et al. [14] have obtained mass spectra for Phe at both 266 nm and

272.7 nm. Their results at the shorter wavelength are similar to those presented here. At 272.7 nm, they were again able to obtain the mass spectrum of Phe with no fragmentation of the molecular ion. This is in marked contrast to the results of Lubman and coworkers [19], [20] who were unable to obtain any ion signal from Phe at 222 or 280 nm, and could only obtain a weak signal at 266 nm, at a relatively high laser power density. In addition, Lubman observed increased fragmentation at the ionisation threshold for Phe and Phe-based peptides relative to those containing either Trp or Tyr.

It is clear from the liquid-phase absorption spectrum shown in figure 6.9 that Phe has a smaller absorption cross section at 266 nm than either Tyr or Trp. The addition of a hydroxy group on to the Phe ring, as is the case in Tyr, strongly releases electrons into the aromatic centre, enhancing the π^{*}-π transition probability and lowering the ionisation potential by strong stabilisation of the ionic state. It is therefore also possible that Phe has an ionisation potential too high for R2PI to occur. Irrespective of the cause, the higher laser power needed to ionise Phe at threshold almost certainly causes absorption of additional photons by the molecular ion, resulting in its subsequent fragmentation.

6.3.4 A mixture of L-Trp, L-Tyr and L-Phe.

Measurements on hydrophilic and hydrophobic compounds in a mixture are often difficult to make with most mass spectrometric methods, especially some of the "soft ionisation" techniques. In general, the formation of ions via methods such as FABMS is controlled not only by the proton affinity but also the hydrophilicity of the samples in a given matrix. Since the primary requirement

for a FAB matrix is that it be sufficiently involatile to allow useful spectra to be obtained, hydrogen-bonding, polar matrices such as glycerol are typically used. The strong hydrogen-bonding nature of the matrix gives rise to discriminatory effects, with non-polar, surface active or hydrophobic compounds giving good sensitivity in glycerol, whilst the opposite is true for polar, hydrophilic groups [22].

Very little work has been published on the analysis of mixtures by LD-MPI mass spectrometry [23], [24], [25]. An equimolar mixture of the three aromatic amino acids was therefore prepared in order to investigate the potential application of the technique to the study of simple mixtures. 2.04 mg of tryptophan, 1.81 mg of tyrosine and 1.65 mg of phenylalanine were mixed in an excess of glycerol and colloidal graphite, and about 2 mg of the paste was applied to the sample probe. In this mixture, the tyrosine is likely to be more hydrophilic than the other two amino acids, and might therefore be discriminated against if studied by methods such as FABMS from a glycerol matrix.

Figures 6.14 and 6.15 show the LD-MPI mass spectra obtained from this sample as a function of ionisation laser power density at λ = 266 nm. Figure 6.14(a) was recorded at an ionisation laser power density of 10^6 Wcm^{-2}. Under these conditions, the spectrum is not dissimilar to that obtained from tryptophan itself under soft ionisation conditions. The base peak of the spectrum is at mass 204, and the next strongest peak is at mass 130. Again, the metastable peak at around mass 151 is observed quite strongly. The molecular ion of tyrosine is seen at mass 181 with no apparent fragmentation, but at only 4.5% of the intensity of the base peak. Phenylalanine is not detected at all. Increasing the power density to 5

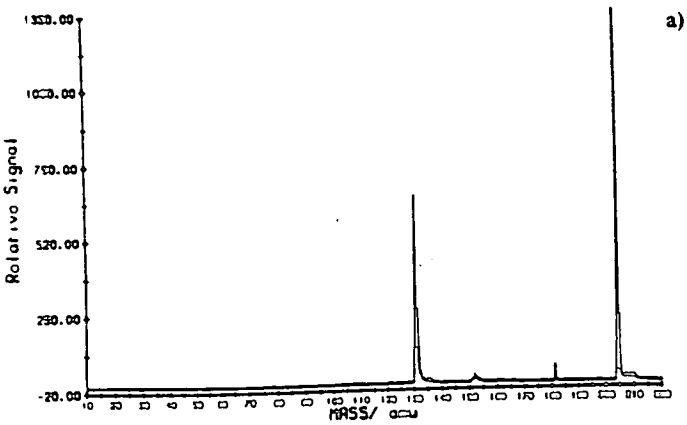

a) Laser power density = 1 $MWcm^{-2}$

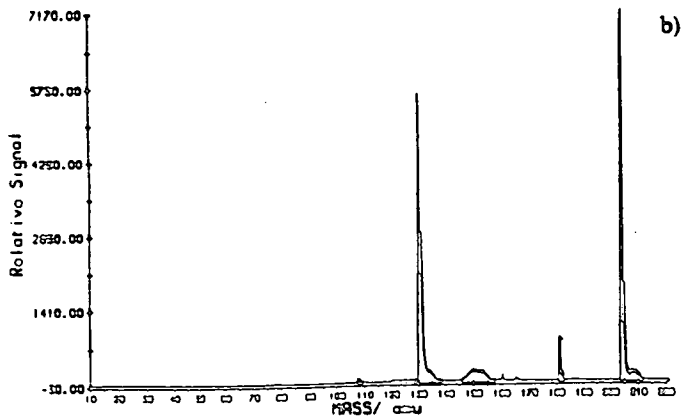

b) Laser power density = 5 $MWcm^{-2}$

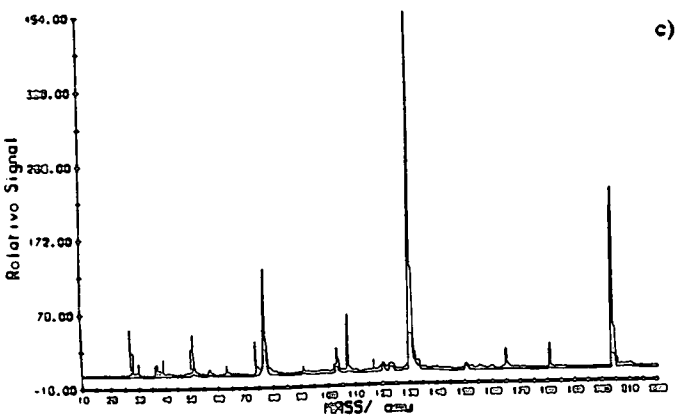

c) Laser power density = 50 $MWcm^{-2}$

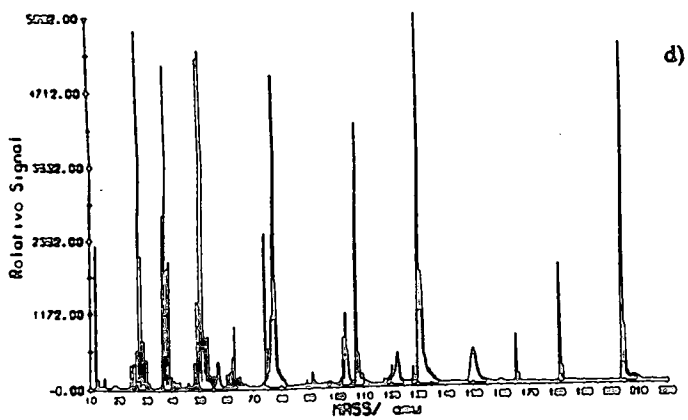

d) Laser power density = 500 $MWcm^{-2}$

Figure 6.14. LD-MPI mass spectrum of an equimolar mix of L-Trp, L-Tyr and L-Phe at λ = 266 nm.

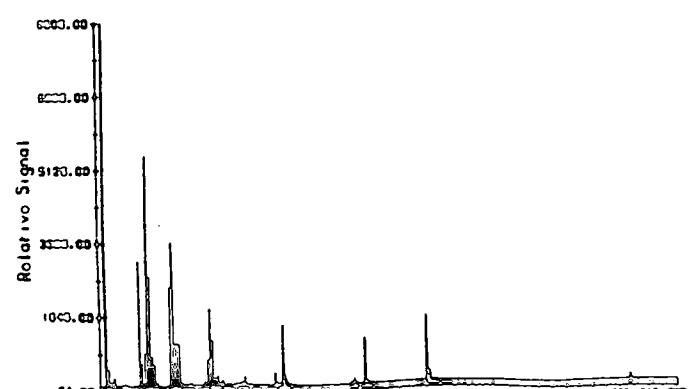

e) Laser power density = 1500 $MWcm^{-2}$

Table 6.12. Mass spectral fragmentation patterns of an equimolar mix of tryptophan, tyrosine and phenylalanine at 266 nm.

1 $MWcm^{-2}$		5 $MWcm^{-2}$		50 $MWcm^{-2}$		500 $MWcm^{-2}$		1500 $MWcm^{-2}$	
m/e	Signal	m/e	Signal	m/e	Signal	m/e	Signal	m/e	Signal
204	100	204	100	130	100	130	100	12	100
130	50.1	130	78.0	204	50.2	27	96.8	27	63.7
131	20.0	131	40.2	77	29.5	204	91.6	37	39.5
205	12.9	205	26.2	131	29.1	51	91.3	24	34.5
181	4.5	181	11.9	107	16.3	50	89.1	28	30.1
132	3.3	132	6.4	27	13.2	37	87.4	36	29.5
152	2.4	149	3.3	50	11.9	77	84.5	50	21.4
207	1.8	133	3.3	51	11.9	107	71.1	130	18.5
209	1.7	134	3.2	205	11.5	36	46.9	77	16.6
133	1.5	151	3.2	74	9.7	74	41.7	107	12.7
153	1.4	150	3.2	181	7.0	12	38.7	51	12.6
206	1.4	153	3.1	103	7.0	28	35.6	38	12.0
210	1.4	207	3.0	28	6.6	39	34.2	39	11.7
		152	3.0	165	5.7	38	32.4	26	9.5
		148	2.9	132	5.3	181	31.7	29	8.2
		182	2.6	39	4.8	131	30.2	49	7.6
		209	2.6	78	4.0	49	23.3	25	6.6
		208	2.3	30	3.5	103	19.0	30	6.2
		135	2.1	37	3.5	76	18.8	13	4.7
		160	2.0	117	3.5	63	16.3	74	3.8
		154	2.0	104	3.5	205	14.8	131	3.2
		107	1.7	63	3.1	78	14.5	78	3.1
		210	1.7	36	3.1	53	13.8	53	2.9
		147	1.4	133	3.1	52	13.5	63	2.8
		155	1.3	134	3.1	165	12.7	52	2.6
		108	1.3	75	2.6	29	12.7	48	2.6
		165	1.1	76	2.6	102	12.6	15	2.4
		146	1.1	120	2.6	26	10.3	103	2.0
		136	1.0	102	2.6	75	10.1	204	1.8
		120	0.9	206	2.6	150	9.2	62	1.7

$MWcm^{-2}$ increases the size of the mass 130 peak relative to the molecular ion peak of tryptophan and introduces a fragment peak at mass 160, see figure 6.14(b). The tyrosine molecular ion peak becomes more pronounced, and is now 11.9% of the base peak. A small peak is clear at mass 107, in keeping with the expected behaviour of tyrosine at this power density. A metastable ion peak is found centred at mass 152, again in keeping with previous observations. Under these conditions, a weak molecular ion for Phe is detected at mass 165, at an intensity of 1.1% of the base peak. This is shown more clearly in figure 6.15(a). Figures 6.14(c) and 6.14(d) were recorded at 50 and 500 $MWcm^{-2}$ respectively, and show the expected behaviour of increasing fragmentation with increasing power density. A number of metastable peaks are obvious in the latter spectrum. Figure 6.15(b) is the molecular ion region of figure 6.14(d) blown up to show the relative intensities of the three molecular ions. Even at a power density of 1500 $MWcm^{-2}$, as shown in figure 6.14(e), where the molecular ions are totally fragmented, the reasonably intense mass 74, 107 and 130 ion peaks act as markers for the presence of the three amino acids. This data is presented, in summarised form, in table 6.12.

Figure 6.16 shows the LD-MPI mass spectrum of the same amino acid mixture recorded at λ = 286.96 nm at a laser power density of 0.3 $MWcm^{-2}$. As might have been expected, this spectrum shows only the tryptophan molecular ion peak with minimal fragmentation. No measurements at higher ionisation laser power densities were made at this wavelength.

These observations are clearly explained by considering the relative absorption cross sections of the three amino acids at both wavelengths. As shown in figure

Figure 6.15. LD-MPI mass spectrum of an equimolar mix of L-Trp, L-Tyr and L-Phe at λ = 266 nm.

a) Laser power density = 5 $MWcm^{-2}$

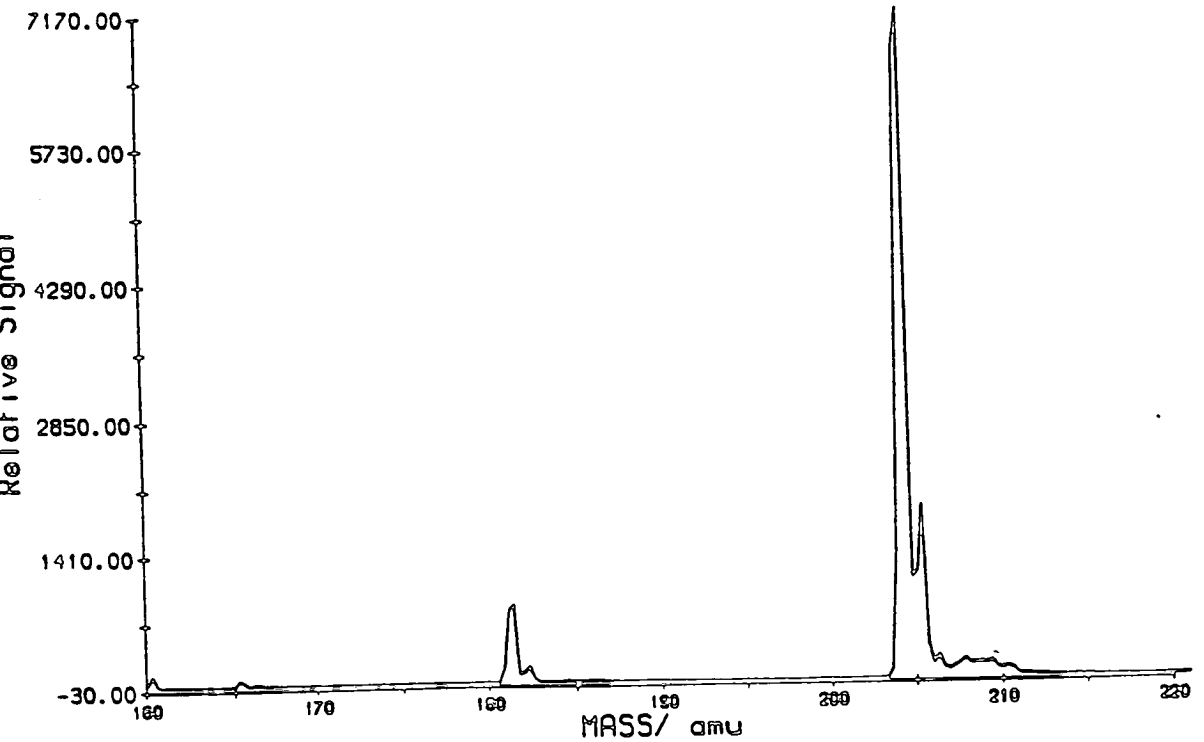

b) Laser power density = 500 $MWcm^{-2}$

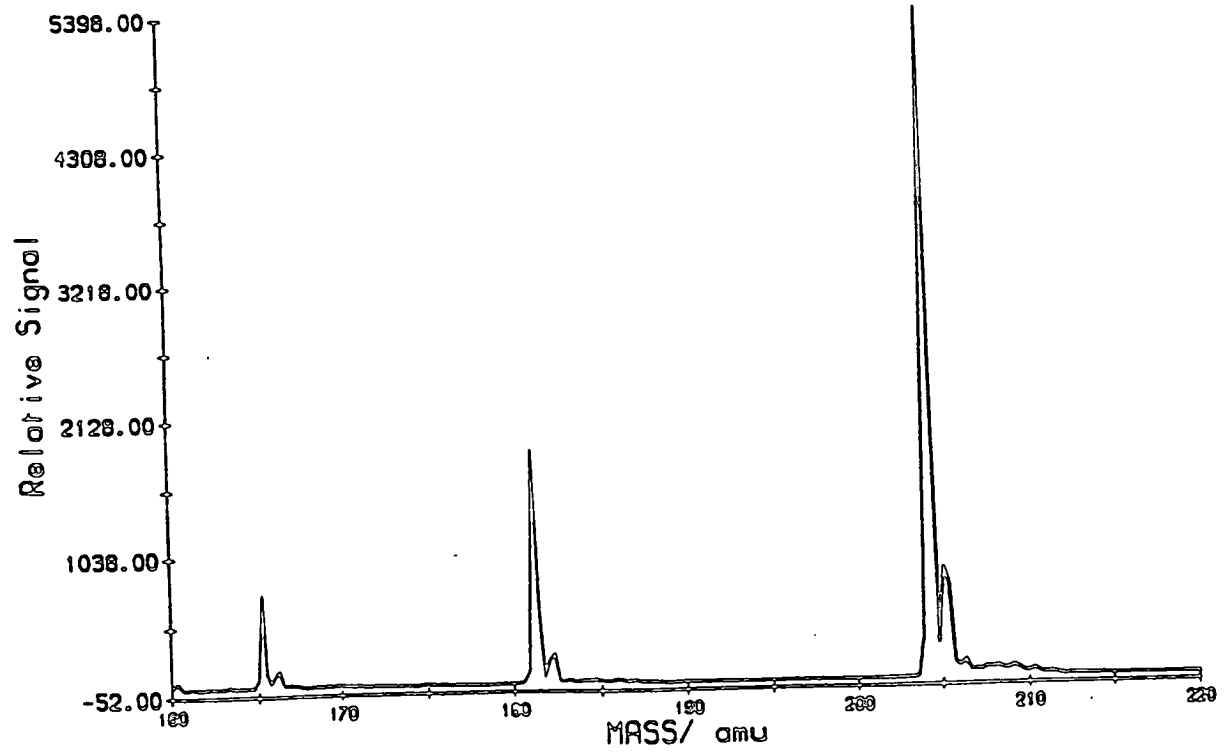

6.9, tryptophan has a strong liquid-phase absorption over the range 255-305 nm, tyrosine has a relatively weaker absorption between 255 and 290 nm, whilst phenylalanine shows a relatively very weak absorption over the range 255-275 nm. These liquid phase spectra, of course, only provide a general indication of the gas-phase absorption contour in the UV for the three molecules. Solvent shifts may be significant, depending on the solvent used. Li and Lubman [26] measured the gas-phase broadband absorption spectra of both Trp and Tyr and compared them with the absorption spectra obtained in a number of solvents. The liquid phase spectra were shifted by 3-5 nm to longer wavelengths. Thus, with a degree of supersonic jet cooling, it is likely that the gas phase spectra of these molecules will show narrower absorption features, but with the same trend in oscillator strength at 266 nm. It is likely that only tryptophan will show a resonant enhancement at 286.96 nm in the cooled gas-phase regime.

There may be small differences between the observed mass spectra and the expected spectra obtained from superposition of the spectra obtained from the individual components under the same ionisation conditions. In order to make this measurement, the spectra in figures 6.10- 6.13 would have to be re-recorded using equimolar sample preparations. More importantly, however, better stability in the amount of material desorbed per shot would be required. Nevertheless, it would appear that, in this case, the observed selectivity in ionisation is due to the gas-phase absorption properties of the molecules, and not to selective desorption of one or another of the components.

Figure 6.16. LD-MPI mass spectrum of an equimolar mix of L-Trp, L-Tyr and L-Phe at λ = 286.96 nm.

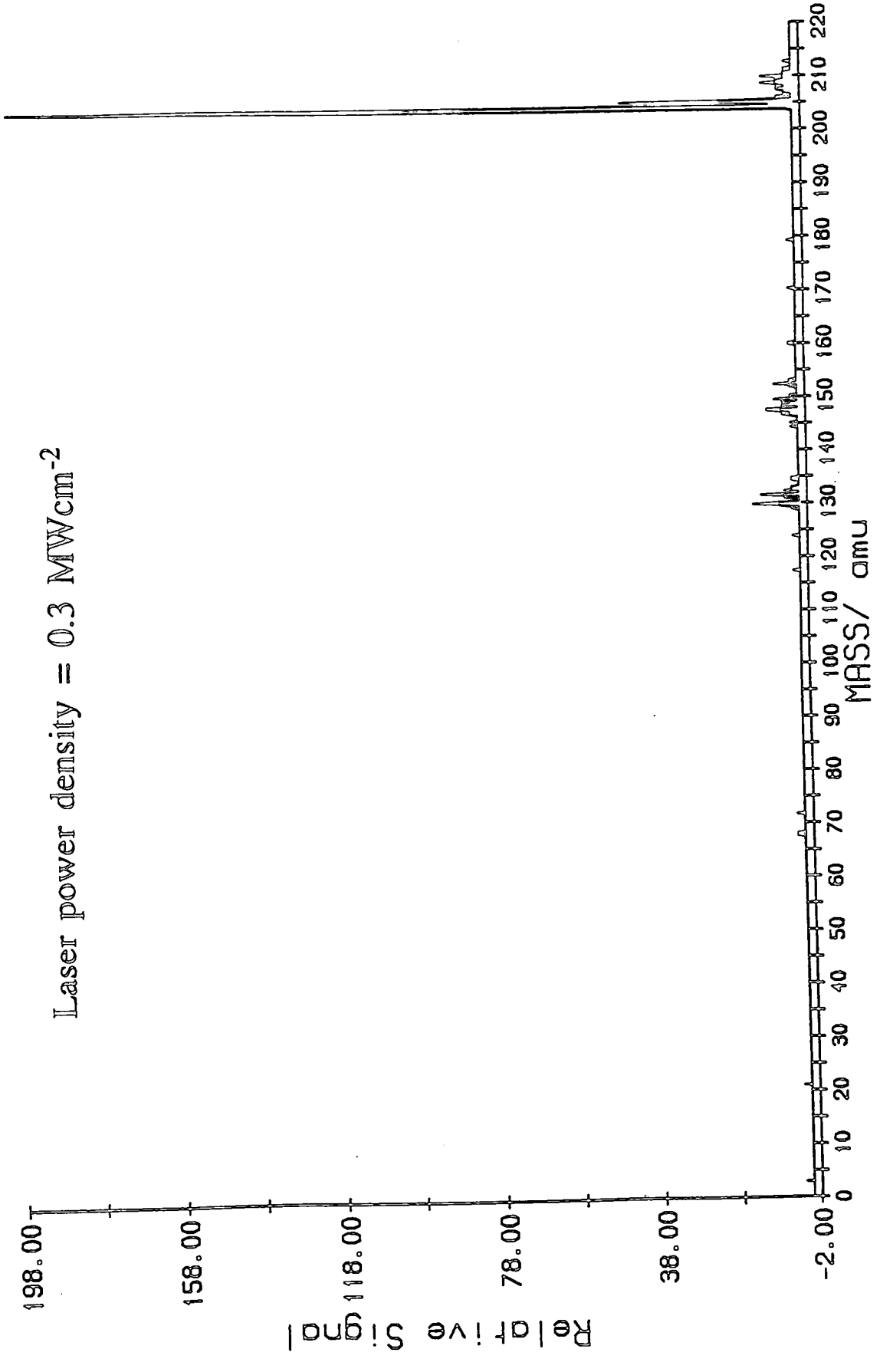

6.3.5 L-histidine.

No ion signal was observed from L-histidine under the experimental conditions employed in this work. This may be due to the ionic nature of this molecule in solution, but is more likely to be due to vanishingly small absorption or ionisation cross sections at λ = 266 nm. Grotemeyer et al. [14], however, reported soft ionisation mass spectra of this molecule at both 266 nm and 250 nm. The base peak of the spectrum obtained at 266 nm was at mass 81, which is produced by the loss of the amino acid function from histidine. Nevertheless, the molecular ion, at mass 155, was observed at about 20 % of the base peak. A similar spectrum was observed at 250 nm, but with an optimised intensity of 77% for the molecular ion. They attempted to explain this unusual trend of increased molecular ion signal at a higher ionisation energy by hypothesising that R2PI occurs at 250 nm, but that the ionisation at 266 nm occurs via a 3-photon non-resonant process.

6.3.6 PTH-tryptophan.

An important reaction of the amino acids is the Edman reaction, in which the free amino acid reacts with phenylisothiocyanate to give the corresponding phenylthiocarbamylamino acid derivative. If this product is treated with acid in nitromethane as a solvent, it cyclises to form the corresponding phenylthiohydantion (PTH) amino acid. This Edman "degradation" is widely used to identify the NH_2-terminal amino acid in polypeptides [27]. The PTH-amino acids are easily separated and identified by HPLC, and their EI mass spectra have also been measured [28]. However, the aromatic amino acid

derivatives give only low-intensity molecular ions under electron bombardment. Recently, the aromatic nature of the PTH-derivatisation has allowed the LD-MPI mass spectra of non-aromatic amino acids to be measured [14], [29].

The mass spectrum of PTH-tryptophan was measured at 266 nm. It is shown in figure 6.17 and summarised in table 6.13. In contrast to the groups of Schlag [14] and Zare [29], who were able to obtain a soft ionisation spectrum for this molecule with no fragmentation of the molecular ion and with a molecular ion intensity of 36% of the spectral base peak, figure 6.17(a) shows a molecular ion intensity of only about 7% at a laser power density of 1 $MWcm^{-2}$. As was observed by Zare's group, the base peak of the mass spectrum under these conditions is the dehydroindole ion peak at mass 130. Other major fragment ion peaks are observed at mass 156, 141, 77, 170, 104 and 192. The mass 192 fragment is due to hydrogen rearrangement and subsequent loss of the side group from the amino acid, whilst the others are formed by rearrangements of either the Trp function or of the PTH ring

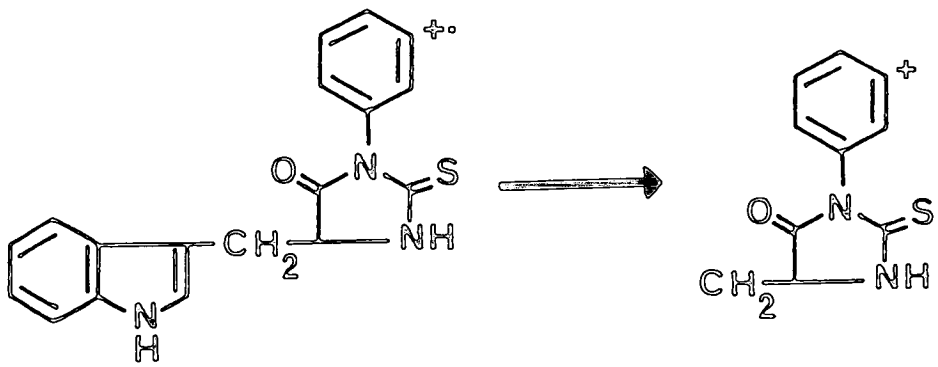

Figure 6.17. LD-MPI mass spectrum of PTH-Trp at λ = 266 nm.

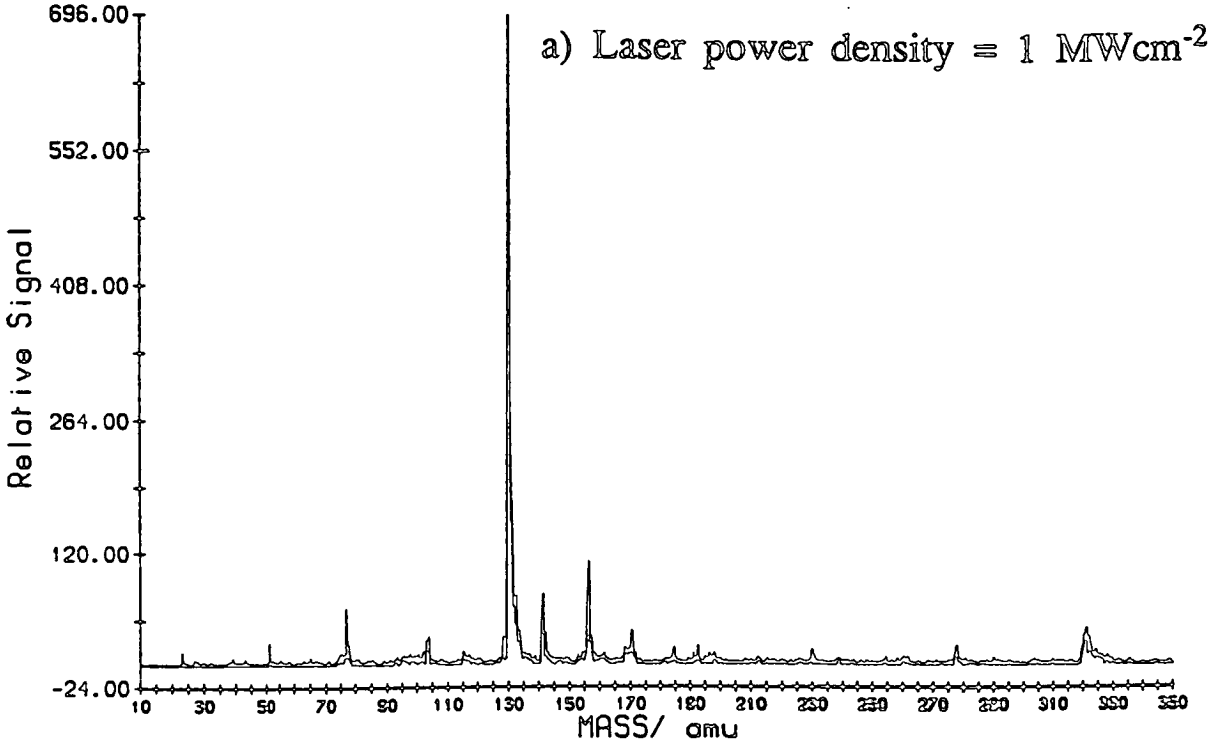

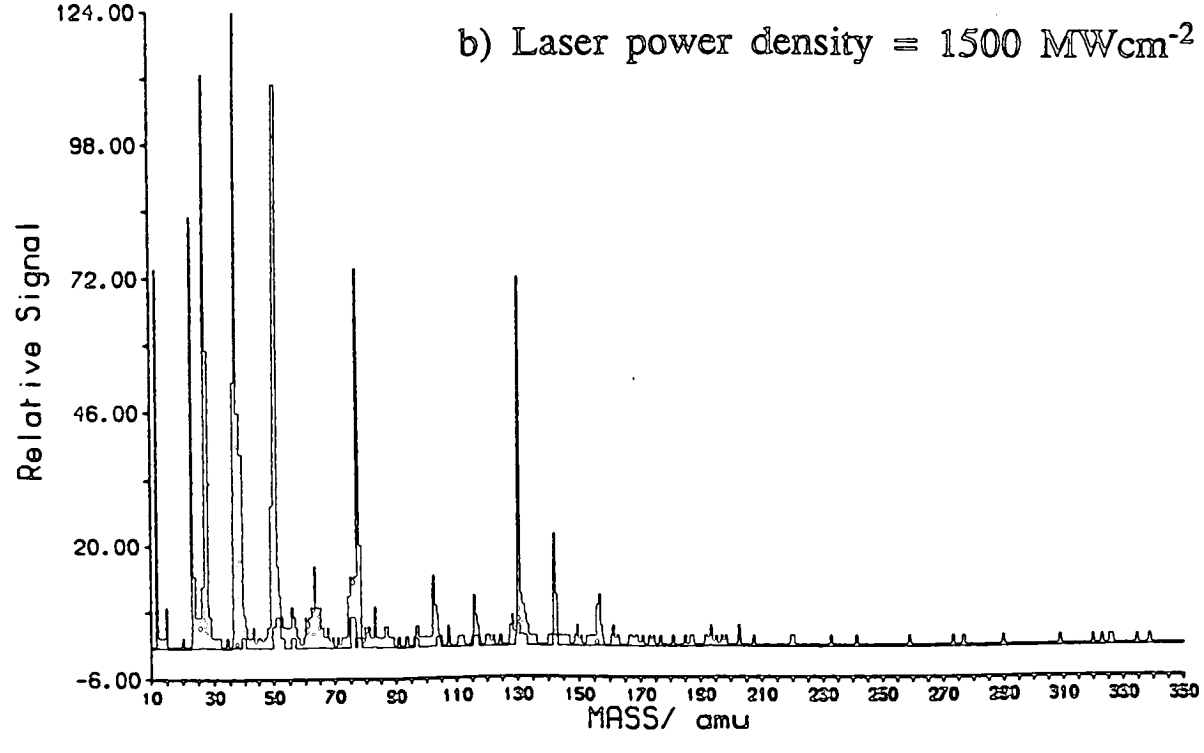

Table 6.13. Mass spectral fragmentation pattern for PTH-tryptophan at 266 nm.

1 $MWcm^{-2}$		1500 MW^{-2}	
m/e	Signal	m/e	Signal
130	100	37	100
131	25.3	27	90.3
156	15.8	50	88.7
141	10.9	51	67.7
132	10.6	23	67.7
76	8.9	12	59.7
321	6.9	77	59.7
170	5.2	130	58.1
133	5.2	28	46.8
142	4.9	38	37.1
320	4.6	36	37.1
322	4.3	49	22.6
157	4.3	141	17.7
104	4.3	78	16.1
128	4.3	63	12.9
103	3.7	24	11.3
51	3.4	75	11.3
77	3.2	76	11.3
192	2.9	102	11.3
168	2.6	26	9.7
184	2.6		

An attempt to reduce the observed degree of fragmentation by lowering the ionisation laser power density to less than 1 $MWcm^{-2}$ resulted in no observable ion signal. For completeness, a hard ionisation mass spectrum was recorded at an ionisation laser power density of 1500 $MWcm^{-1}$. This spectrum, shown in figure 6.17(b), illustrates the almost complete fragmentation of the molecular ion, with the only recognisable "fingerprint" ion peaks being those at mass 130, 141 and 156.

The observed differences between the three independent measurements of the same mass spectrum must reflect differences in the desorption stage of the experiment. Zare's group did not employ jet cooling of the desorbed material, with the consequence that decomposition of the intact neutral molecule may have occurred prior to ionisation. Since the fragmentation of the molecular ion observed in this work was even more marked than in those experiments, despite the use of molecular beam entrainment of the desorbed material, it suggests that quenching/cooling in this beam is not very efficient.

6.4 LD-MPI mass spectra of some porphyrins.

Porphyrins are perhaps the most important and most widespread class of natural pigment. Additionally, in recent years they have been widely used in geochemistry as biomarkers [30]. Biomarkers are organic molecules which are present in fossil fuels, which may have lost sidechains, but whose carbon skeleton has been preserved throughout the geological period since their original deposition in a sedimentary environment. Using these biomarkers, it is possible to establish links between the type of organic material responsible for a particular

oil and its geochemical history. However, in general, apart from those porphyrins obtained from either blood or plants, the quantities of porphyrin that can be isolated in a pure state are often very small. Mass spectrometry is therefore particularly useful in structural studies because of its high sensitivity.

Two porphyrins have been studied as part of this work, namely etioporphyrin and its nickel complex, Ni-etioporphyrin. The structure of the latter molecule is given in table 6.1; etioporphyrin itself differs from this complex through replacement of the central Ni by two H atoms. Both samples were provided by the BP Research Centre, Sunbury-on-Thames, and were used without further purification.

Figure 6.18(a) shows the soft ionisation MPI mass spectrum of etioporphyrin recorded at λ = 266 nm (I = 0.5 $MWcm^{-2}$). As detailed in table 6.14, this spectrum is dominated by the strong molecular ion peak at mass 478. Under these conditions, the only other peaks of interest are at mass 463 and mass 448, which correspond to the loss of one and two methyl groups respectively from the side chains on the macrocycle. The identity of these peaks can be assigned through comparison with the EI mass spectra of etioporphyrin.

The EI mass spectrum of etioporphyrin has been obtained using a heated direct inlet system as outlined in chapter 3 [31]- [33]. The molecular ion is by far the most intense peak in this spectrum. Fragment ions fall into two distinct groups; a high mass group consisting of singly-charged ions and a lower mass group consisting of doubly-charged species. There are no peaks observed below mass 200. The most abundant fragment ions are those from the loss of $-CH_3$, 2 x $-CH_3$,

Figure 6.18. LD-MPI mass spectra of etioporphyrin and Ni-etioporphyrin at $\lambda = 266$ nm.

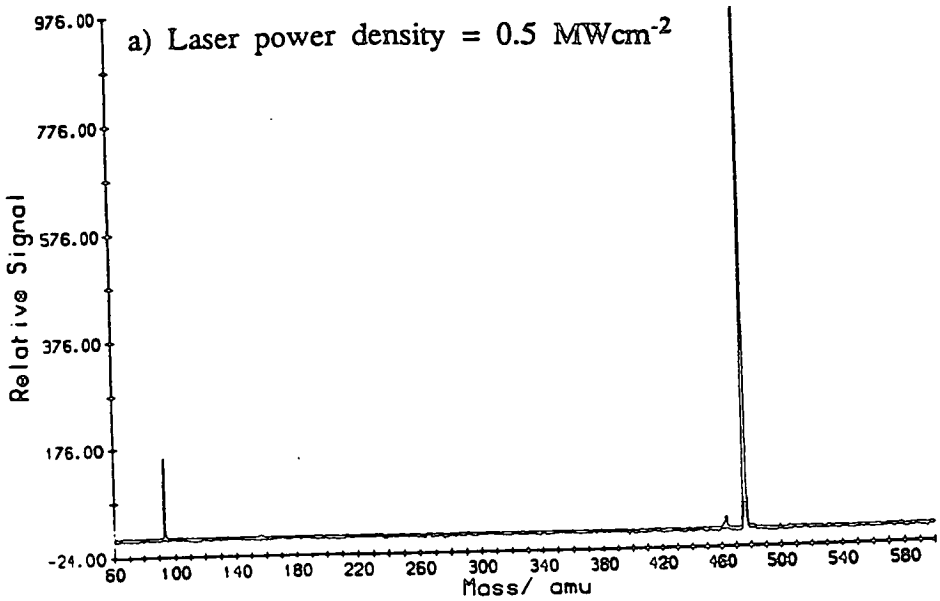

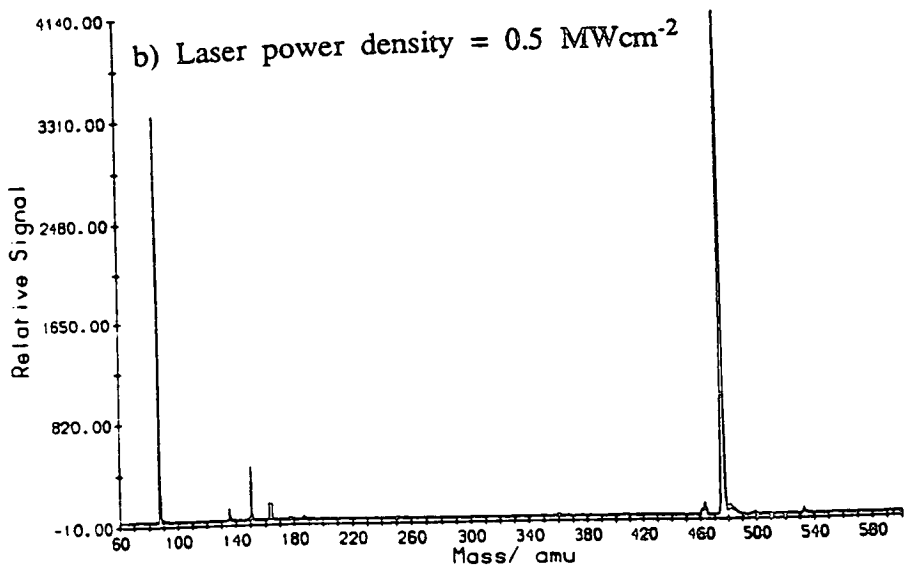

c) Laser power density = 16 MWcm^{-2}

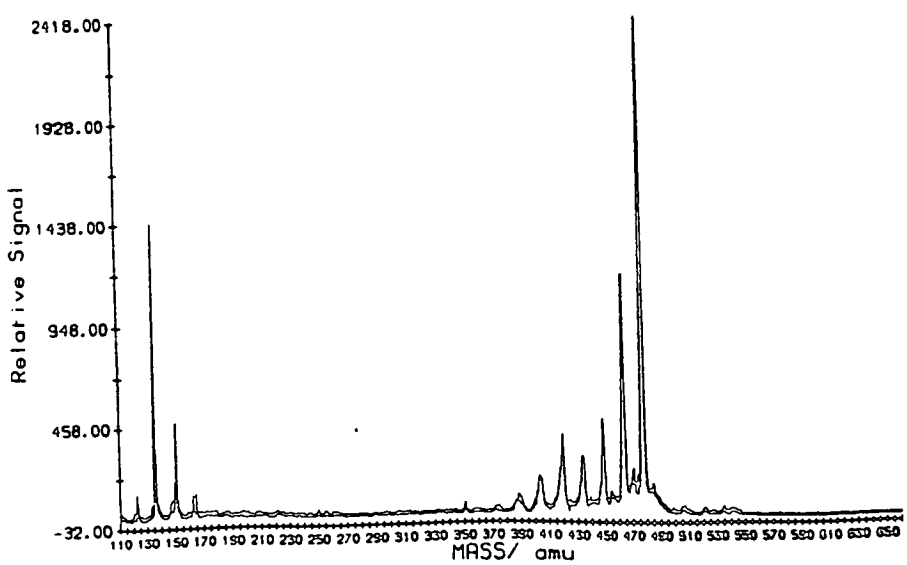

Table 6.14. Mass spectral fragmentation pattern for etioporphyrin and Ni-etioporphyrin at 266 nm.

etioporphyrin 0.5 $MWcm^{-2}$		Ni-etioporphyrin 0.5 $MWcm^{-2}$		Ni-etioporphyrin 16 $MWcm^{-2}$	
m/e	Signal	m/e	Signal	m/e	Signal
478	100	478	100	478	100
479	39.3	479	48.0	135	59.4
480	7.0	480	13.7	463	48.1
463	3.1	150	11.3	150	19.4
481	2.9	162	4.2	448	19.0
464	1.6	164	3.8	418	15.7
484	1.4	463	3.0	136	13.3
482	1.2	481	2.8	433	11.4
483	1.2	484	2.5	434	10.1
448	1.2	534	1.9	470	8.9
		487	1.8	417	8.8
		483	1.7	419	8.8
		460	1.7	149	7.4
		151	1.7	403	7.3
		187	1.5	404	6.6
		464	1.4	432	6.4
		177	1.3	485	5.9
		465	1.3	416	5.9
		482	1.3	431	5.8
		360	1.3	402	5.5
		148	1.2	122	4.9
		163	1.0	164	4.9
		536	0.9	415	4.8
		537	0.8	162	4.6
				454	4.3
				445	4.2
				388	3.8
				373	1.4
				534	1.4

-H and $-C_2H_5$. These side chain fragmentations are "benzylic" in character, with fission occurring at the bond β to the macrocycle

i.e. $[Porphyrin\text{-}CH_2\text{-}R]^{+\cdot} \rightarrow Porphyrin\text{-}CH_2^{+} + R\cdot$

Comparison of spectra of related compounds has allowed the relative stability of the various side chains commonly found in porphyrins to be assessed [34]. The Me group is more stable than the Et group, suggesting that the observed loss of $-CH_3$ is due to benzylic fission in the Et groups.

Obviously, the highly aromatic system in porphyrins is very stable, allowing wide delocalisation of one (or two) positive charges in the species produced by ionisation. The fact that the ions formed by benzylic cleavage in the side chains never exceed the intensity of M^+ in EI spectra (in contrast, say, to alkylbenzenes where mass 91 is the base peak) has been explained by postulating that the ring expansion to give a pyridinium cation (corresponding to the tropylium ion in alkylbenzenes) cannot take place due to the rigidity of the ring system.

The doubly-charged ions observed in EI mass spectra of porphyrins are of comparable intensity to the singly-charged ions, although the doubly-charged molecular ion is not necessarily the most intense of these species. Due to the different ionisation mechanisms operating in EI-MS and MPI-MS, these doubly charged ions were not detected in the experiments carried out here.

Some porphyrin-metal complexes, which are stable and relatively volatile, have also been studied by conventional EI mass spectrometry. Since most porphyrins fragment in such a way as to give even-electron daughter ions, introduction of a

metal suitable to alter this behaviour has been used to obtain alternative fragmentation patterns, thereby providing new structural information.

With porphine itself, and with its derivatives which contain only aromatic substituents, thus forming a common π system, ionisation occurs by removal of one electron from the π system, and fragmentation involves the loss of an odd number of radicals. If, however, a complexed metal is present, the odd number of electrons in the π system of M^+ can be avoided by removal of an electron from the metal. Fragmentation that retains an even number of electrons will then be favoured. If, on the other hand, alkyl or hetero substituents are present, the aromaticity of the macrocycle can be retained if ionisation occurs, either by the removal of a non-bonding electron from a heteroatom, or by concomitant fragmentation (e.g. alkylporphines which yield benzylic $-CH_2^+$). In these cases, the fragmentation behaviour of a metal complex will be similar to that of its uncomplexed precursor. Thus, the EI mass spectrum of Ni-etioporphyrin [35], [36] shows a strong molecular ion at mass 535, with small fragment ion peaks corresponding to the loss of up to six methyl groups.

Figure 6.18(b) shows the LD-MPI mass spectrum of Ni-etioporphyrin at λ = 266 nm under soft ionisation conditions (I = 0.5 $MWcm^{-2}$). In contrast to the reported EI mass spectrum, the base peak of this spectrum is at mass 478, the molecular weight of the uncomplexed porphyrin. The molecular ion of the complex, at mass 534, is observed but only at an intensity of 2% of the base peak. This distribution may reflect the overall small degree of complexation in the sample; however, further work on a series of different porphyrin-metal complexes has shown a similar trend [37]. For example, the mass spectrum of

Cu-tetraphenylporphyrin shows a similar degree of de-metallation as was observed here, when an ionisation wavelength of 266 nm was employed in soft ionisation mode. Upon ionisation at λ = 193 nm, however, the molecular ion was observed as the base peak of the mass spectrum under soft ionisation conditions. This can be explained by considering the ionisation potential of the porphyrins studied [38]. At 266 nm, ionisation requires the absorption of two photons, whereas at 193 nm, one photon ionisation occurs. It seems likely that the excess energy above the molecular IP supplied at 266 nm is sufficient to cause the observed facile de-metallation fragmentation.

Figure 6.18(c) shows the partially-hard ionisation spectrum of Ni-etioporphyrin at 266 nm (I= 16 $MWcm^{-2}$). The poor mass resolution in this spectrum reflects the larger ionisation beam waist employed here (2 mm). This was required due to the extremely small amount of sample (< 1 µg) that remained after previous survey scans, and poor shot-to-shot reproducibility in the desorption signal. Nevertheless, this spectrum shows the expected behaviour in fragmentation. The base peak is at mass 478, with a small molecular ion signal at mass 534. Fragment ion peaks are observed at mass 463, 448, 433, 418, 403, 388, 373 and 353 as detailed in table 6.14. These correspond to the loss of one to eight methyl groups from the macrocycle side-chains. Other fragment peaks are observed at mass 470, which corresponds to the loss of eight hydrogen atoms from the methyl and ethyl side-groups, and at mass 122, 135, 150 and 164. The structures of these fragment ions are not clear, but they are likely to originate from fragmentation of the macrocycle.

6.5 Sensitivity Measurements.

In these preliminary experiments, quantitation was a problem. The ion signal obtained depends on both the power of the desorption laser and the power and wavelength of the ionisation laser. In particular, as mentioned previously, there was a large shot-to-shot fluctuation in the number of neutrals desorbed at a given desorption laser power. A typical sample mixture was made up from 1.4 mg Trp, 11.3 mg glycerol and 1.5 mg of graphite suspension with 3.2 mg of the mixture being applied to the sample probe tip. This was then placed into the vacuum chamber and a total of 2.4 mg was removed after 2430 laser shots. Assuming that the components of the mixture are equally likely to be removed, this is equivalent to an average of 311.7 ng of Trp being removed per laser shot. Thus, 1.53 nanomoles or 9.2×10^{14} molecules of tryptophan were desorbed per laser shot.

The LD-MPI mass spectrum of tryptophan shown in figure 6.19 was recorded over an average of 240 laser shots using the above sample preparation. The total ion signal in this spectrum, generated by summation of the ion signal at each mass, was 4446 counts. Since 1 count is equivalent to 2 mV, the average total ion signal per laser shot is $(4446 \times 2/240)$ mV = 37.05 $mVshot^{-1}$. The signal cable was terminated through 50 Ω, so assuming a detector amplification of 10^6, the current produced per shot was $37.05 \times 10^{-9}/50 = 7.41 \times 10^{-10}$ A. Assuming ion peak widths of 50 ns FWHM, the total charge at the detector is $(7.41 \times 10^{-10} * 50 \times 10^{-9}) = 3.705 \times 10^{-17}$ Coulombs per shot. This is equivalent to 232 ions reaching the MCP per laser shot. Thus, only 25 ions are detected for every 10^{14}

Figure 6.19. LD-MPI mass spectrum of tryptophan, recorded under conditions as detailed in section 6.5 of the text.

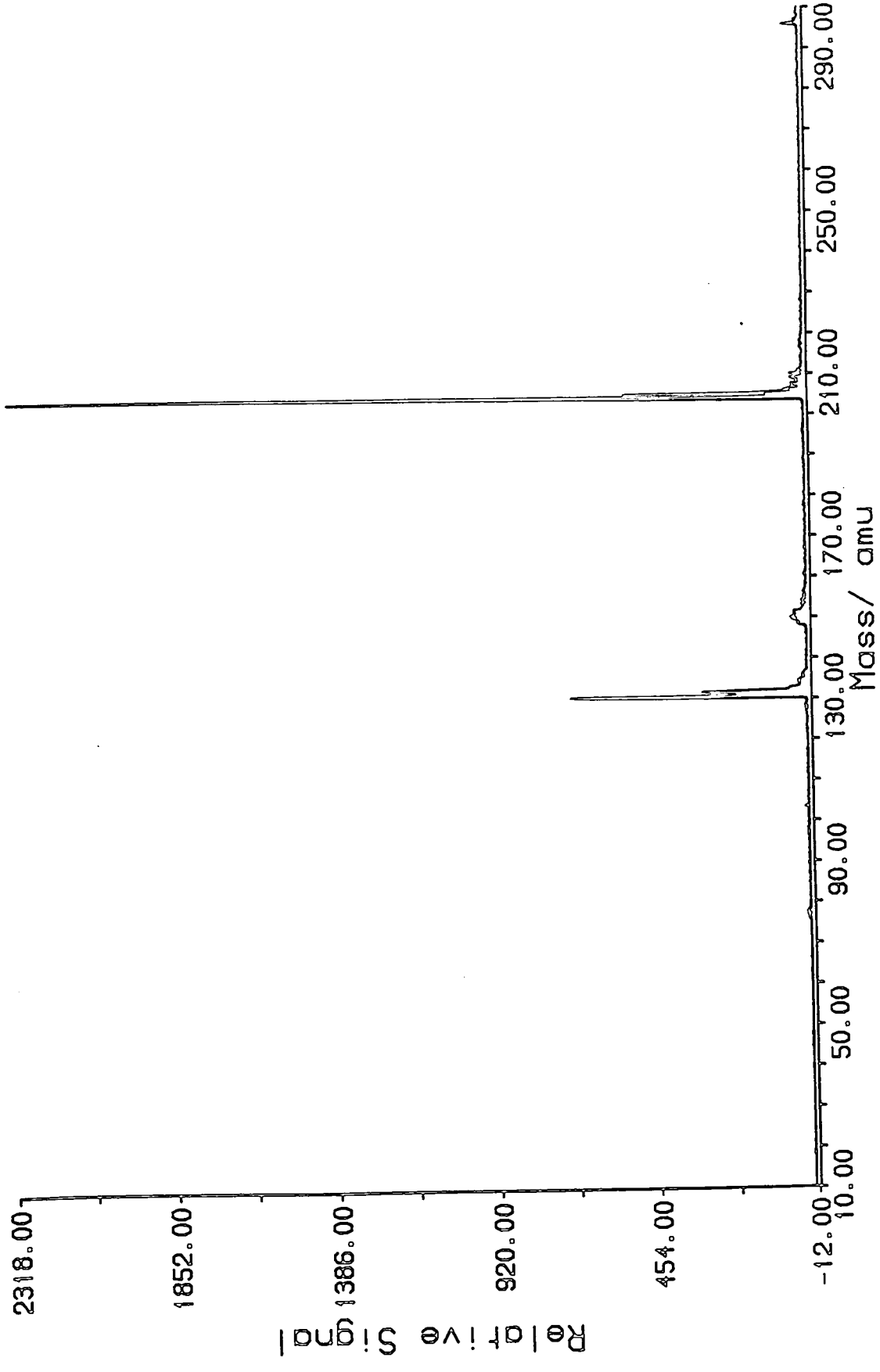

neutral molecules desorbed, which means that the overall efficiency of the process is extremely poor. This, however, is of a similar order of magnitude to the efficiency reported by Tembreull and Lubman [3], who used a similar desorption set-up in a linear TOF mass spectrometer. The single-shot mass spectrum obtained from this sample mixture had a signal to noise ratio of ~5. Thus, it appears that the ultimate detection limit for the experimental set-up employed here is ~ 400 picomoles of tryptophan.

The observed ion signal can, of course, be increased by raising the power density of the ionisation laser, but the main problem in the present experimental set-up is the poor entrainment efficiency of the desorbed material into the expanding molecular beam. The laser beam diameter, typically 200 μm, defines the length of the laser beam- molecular beam region. If the supersonic molecular beam is assumed to be travelling at 1.7×10^5 cms^{-1}, a pulsed molecular beam with a duration time of 900 μs exists over 1.53 m in space. However, as shown in a typical timescan, see figure 4.11, the desorbed material is emitted from the probe over a period of ~ 100 μs, so that the effective "length" of the seeded molecular beam is 17 cm. Since the ionisation laser pulse is 10 ns long, the molecules in the beam hardly move during the pulse. Thus, the laser beam samples about 0.1% of the molecules which cross the laser beam-molecular beam interaction region [4]. If an ionisation efficiency of 1% and an ion transmission of 10% are assumed, and it is further assumed that 1% of the molecular beam is transmitted by the skimmer, then 2.32×10^8 neutrals are entrained in the beam per pulse, which is only ~ 10^{-5} of the number of molecules desorbed per pulse. This low entrainment efficiency has two obvious consequences. Firstly, it places a

limitation on the overall sensitivity of the LD-MPI process, with the unfortunate result that larger quantities of sample are required to obtain a mass spectrum. Secondly, this poor entrainment efficiency negates the advantage that may have been accrued, in terms of improved sensitivity, by probing the desorbed neutral population rather than the nascent ions. Methods which will help to reduce this limiting factor are discussed in the following section.

6.6 Future improvements to existing apparatus.

The LD-MPI reflecting-geometry TOF mass spectrometer designed as part of this work has been used to obtain mass spectra for several classes of important molecules. The mass spectra give strong molecular ion peaks at low UV laser power densities, with controllable fragmentation yielding structurally important information. However, the main drawback with the performance of this apparatus during these preliminary experiments was that relatively large samples ($\sim$ 1 mg) had to be used to allow the recording of mass spectra. Similarly, the large shot-to-shot variation observed in the amount of material desorbed made it impossible to record jet-cooled R2PI spectra of these molecules, which had been one of the original goals of the project. Clearly, a much more reliable way of desorbing the molecules of interest and entraining them into a molecular beam is required. The following section discusses several suggested improvements to the existing apparatus, many of which have been made during the time that has elapsed since these initial experiments were performed, and an assessment is made of the performance of the machine in light of these developments.

The key to a well-behaved desorption source is clearly a stable, well-behaved

desorption laser. Although the PSI LP-30 CO_2 laser provided reasonable shot-to-shot power output, the fact that the infrared laser beam could only be focused to a 2 mm diameter spot meant that, even when running at maximum power, the power density available was insufficient to raise the surface temperature of the sample probe to the point at which strong desorption occurred (see Appendix D). Addition of a matrix element, such as graphite, which is a strong infrared absorber, obviously increased the surface temperature to allow efficient desorption to occur. However, it was clear that the sample was becoming very hot during these experiments- cascades of glowing particles could be seen to be emitted by the surface, some with such force that they were clearly not entrained into the molecular beam, leaving debris in the vacuum chamber. This is therefore not the most efficient way to perform these experiments.

A much more sensible manner in which to approach the problem would be to increase spatial focusing of the infrared laser beam, thereby increasing the available power density. Thus, higher surface temperatures could be obtained without the use of added graphite to the sample. Unfortunately, in order to allow the PSI LP-30 laser beam to be focused down to much smaller focal spot sizes, unstable resonator optics had to be fitted. This obviously took some time (and money) to achieve, and was therefore outwith the scope of this work. However, the PSI LP-30 fitted with these optics gives a much less divergent beam, allowing focal spots of ~ 200 μm in diameter to be achieved. It has been possible, therefore, to dispense with the colloidal graphite from the sample mixtures [37].

The next step towards improved desorption efficiency is to improve the method of sample deposition itself. In these early experiments, a glycerol matrix was

used, in the manner of FABMS [39], since it allowed multiple laser shots to be fired at the same spot on the sample. Presumably, the mechanism here involves the flow of sample in the glycerol into the heated region of the surface, thereby replenishing the supply of sample at that point. If, however, a stable stream of molecules from the desorption probe is required, as it is for spectroscopic purposes, a better way to proceed is to use a movable sample probe. This was always intended to be the case in these experiments, with a motorised screw drive sample stage being included in the original spectrometer design (see figure 4.1).

In this method, the sample, as deposited from an aqueous or methanolic solution, is applied along the length of the sample probe. A thin, reasonably uniform film is formed by this method. The probe is then placed on a rotating, translating screw mechanism so that every desorption laser shot interrogates a fresh part of the sample. It was not possible to translate the rod sufficiently quickly to allow a new portion of the sample to be probed by the relatively large focal spot from the PSI CO_2 laser in its original form. Again, however, this approach has been subsequently incorporated into an improved desorption source now in current use [37].

A further important point which requires consideration is the sample probe itself. In these initial experiments, a stainless steel rod was employed, primarily because it was mechanically stronger than ceramic or glass rods, thereby being less prone to breakage in the sample probe coupling under vacuum. It is likely, however, that materials such as silica would provide better alternatives to steel due to their lower thermal diffusivities. This means that a higher surface temperature would be achieved, at a given laser power density, with a quartz rod

than with one fabricated from stainless steel. Recent experiments [40], however, have shown that although higher nascent ion yields are obtained from a ceramic rod than from a steel one, the amounts of desorbed neutral species are similar from both rods.

One of the major limitations on highly sensitive detection in the early experiments detailed above was poor entrainment efficiency of the desorbed material into the already expanded supersonic molecular beam. A potential solution to this problem has been widely used in the field of metal clusters for a number of years, and has been employed recently in LD-MPIMS by Levy and his coworkers [42]. The basic principle is to encase the sample probe in a metal faceplate which has channels cut in it to allow the entrance and exit of both the desorption laser beam and the molecular beam [41]. The cross sectional dimension of the molecular beam channel is chosen so that the beam undergoes multiple collisions within the faceplate, emerging from the end of the channel as an expanding seeded supersonic molecular beam. Since the available space into which the desorbed material can expand is limited, a higher proportion of the material is likely to be entrained into the beam, the only alternative direction being loss down through the laser channel. Levy and coworkers [42] employ a modified desorption source, which incorporates flat sample discs mounted on a two-way screw mechanism, housed in a faceplate. This "disc" source results in the formation of a cooled molecular beam of desorbed materials, thereby allowing spectroscopic measurements to be made (see section 7.2.4 later).

A final limitation placed on the ultimate sensitivity by the desorption part of the experiment is the fact that desorption occurs over an extended period of time

(~100 μs) whilst the entrained molecules are only ionised during a 10 ns sampling interval. As shown in Appendix D, the temperature at the surface of the probe tip remains elevated, even after the end of the laser pulse, so that, if desorption is a thermal phenomenon, it is not surprising that this long desorption period is observed. The use of a 10 ns rather than a 10 μs pulsed laser might help to alleviate this problem, due to the longer relaxation period available between laser shots.

As was mentioned previously, 266 nm appears to be a good "all-purpose" mid UV ionisation laser wavelength, since most molecules containing an aromatic chromophore show some absorption there in liquid-phase spectra. Under the conditions employed in this work, where the rotational temperature of the desorbed entrained molecules is likely to be quite high, most of these mainly "class A" molecules will undergo some resonance-enhancement at the first absorption step, and therefore undergo R2PI if the molecular ionisation potential is sufficiently low.

If, however, the degree of cooling available in the supersonic expansion is increased, as can be achieved in a faceplate-type desorption source, the R2PI spectra will be considerably simplified, therefore reducing the probability of resonant absorption at 266 nm. On the other hand, by selecting a wavelength where a strong absorption feature occurs, soft ionisation signals will be obtained at lower power densities, and the degree of selectivity available in ionisation will be greatly enhanced.

Of course, this selection of an optimum wavelength requires some *a priori*

knowledge of the type of sample under investigation. If the gas-phase spectroscopy of the "target" molecule or one of its structural precursors is well characterised, a suitable wavelength for ionisation can be readily found. Considerable experimental work is required in this area. However, by building up a database of gas phase R2PI spectra of biological molecules, a very powerful, selective means of ionisation would be available.

One of the major drawbacks associated with an optically discriminatory ionisation source is that much useful information about the sample is lost. This is especially true if "real" analytical samples are to be studied. A reasonably straightforward modification to the current set-up would allow semi-quantitative measurements to be made on samples, by generation of coherent VUV radiation by frequency tripling in a Xe cell [43]. This would generate 118.2 nm wavelength radiation from the third harmonic of a pulsed Nd^{3+}:YAG laser. At this photon energy, most gas phase molecules are ionised by absorption of a single photon. This is a soft ionisation method due to the small probability of absorption of a second photon from the weak light field. Additionally, since single photon ionisation cross sections for molecules which contain greater than ten atoms are much more uniform than the higher-order cross sections involved in MPI [44], semi-quantitative analysis can be performed [45].

Further modifications which would improve the performance of the apparatus are optimisation of the resolution of the reflectron TOF mass spectrometer and faster digitisation rates. At present, only two or three sampling points are taken over an ion peak at the maximum digitisation rate, 100 MHz, of the transient digitiser. Sampling the waveform every 5 ns rather than every 10 ns would

increase the accuracy of the mass spectra obtained.

By largely re-shaping the desorption end of the apparatus in line with the above suggestions, the overall performance has been improved considerably since these early experiments were carried out. Mass spectra have been obtained from samples as small as 10 femtomoles by carefully selecting the ionisation wavelength used. Jet-cooled R2PI spectra of perylene, tryptophan and tyrosine have been obtained, which are in good agreement with those published in the literature. Mass spectra have been obtained from a wide variety of samples, including crude oil, polymers and organic samples deposited on organic substrates. The largest molecule studied so far on the apparatus has been the cyclic decapeptide Gramicidin S, mass 1140, although carbon clusters of up to mass 32000 have been detected [37], [40].

References.

[1] Mass Spectrometry Data Centre, *Eight Peak Index of Mass Spectra*, MSDC, Reading, 1974.

[2] J. H. Beynon, R. A. Saunders, A. E. Williams, *Mass Spectra of Organic Molecules*, Elsevier Publishing, 1968.

[3] R. Tembreull, D. M. Lubman, Anal. Chem., **58**, 1299, (1986)

[4] D. M. Lubman, M. N. Kronick, Anal. Chem., **54**, 660, (1982)

[5] A. Amirav, U. Even, J. Jortner, J. Chem. Phys., **75**, 3770, (1981)

[6] R. Boschi, E. Clar, W. Schmidt, J. Chem. Phys., **60**, 4406, (1974)

[7] R. C. Weast (Ed.), *Handbook of Chemistry and Physics, 70th Edition*, CRC Press, Boca Raton FLA, 1989.

[8] P. Natalis, J. L. Franklin, J. Phys. Chem., **69**, 2935,

[9] K. Biemann, J. A. McCloskey, J. Am. Chem. Soc., **84**, 3192, (1962)

[10] G. Junk, H. Svec, J. Am. Chem. Soc., **85**, 839, (1963)

[11] K. Heyns, H. F. Grützmacher, Ann. Chem., **667**, 194, (1963)

[12] U. Boesl, H. J. Neusser, R. Weinkauf, E. W. Schlag, J. Phys. Chem., **86**, 4857, (1982)

[13] H. J. Neusser, H. Kühlewind, U. Boesl, E. W. Schlag, Ber. Bunsenges. Phys. Chem., **89**, 276, (1985)

[14] J. Grotemeyer, K. Walter, U. Boesl, E. W. Schlag, Int. J. Mass Spectrom. Ion Proc., **78**, 69, (1987)

[15] T. R. Rizzo, Y. D. Park, L. A. Peteanu, D. H. Levy, J. Chem. Phys., **84**, 2534, (1986)

[16] R. C. Beavis, J. Lindner, J. Grotemeyer, E. W. Schlag, Ber. Bunsenges. Phys. Chem., **93**, 365, (1985)

[17] C. J. Cassady, B. S. Freiser, D. H. Russell, Org. Mass Spectrom., **18**, 378, (1983)

[18] R. Tembreull, D. M. Lubman, Anal. Chem., **59**, 1082, (1987)

[19] R. Tembreull, D. M. Lubman, Appl. Spectrosc., **41**, 431, (1987)

[20] L. Li, D. M. Lubman, Appl. Spectrosc., **43**, 543, (1989)

[21] K. Biemann, J. Seibl, F. Gapp, J. Am. Chem. Soc., **83**, (1961)

[22] W. V. Ligon, S. B. Dorn, Int. J. Mass Spectrom. Ion Proc., **61**, 3113, (1984)

[23] J. Grotemeyer, E. W. Schlag, Org. Mass Spectrom., **23**, 388, (1988)

[24] R. N. Zare, J. H. Hahn, R. Zenobi, Bull. Chem. Soc. Jpn., **61**, 87, (1988)

[25] J. H. Hahn, R. Zenobi, J. L. Bada, R. N. Zare, Science, **239**, 1523, (1988)

[26] L. Li, D. M. Lubman, Anal. Chem., **59**, 2538, (1987)

[27] P. Edman, G. Begg, Eur. J. Biochem., **1**, 80, (1967)

[28] H. Hagenmaier, W. Ebbinghausen, G. Nicholsen, W. Vötsch, Z. Naturforsch. B, **25**, 681, (1970)

[29] F. Engelke, J. H. Hahn, W. Henke, R. N. Zare, Anal. Chem., **59**, 909, (1987)

[30] R. P. Philp, J.-N. Oung, Anal. Chem., **60**, 887A, (1988)

[31] A. H. Jackson, G. W. Kenner, K. M. Smith, R. T. Aplin, H. Budzikiewicz, C. Djerassi, Tetrahedron, **21**, 2913, (1965)

[32] J. E. Morandi, H. B. Jensen, J. Chem. Eng. Data, **11**, 81, (1966)

[33] D. B. Boylan, Org. Mass Spectrom., **3**, 339, (1970)

[34] H. Budzikiewicz, *in 'The Porphyrins (Volume 3)', ed. by D. Dolphin*,

Academic Press, New York, 1978.
[35] A. Hood, *in 'Mass Spectra of Organic Ions' (ed. F. W. McLafferty)*. Academic Press, New York, 1963.
[36] M. Meot-Ner, J. H. Green, A. D. Adler, Ann. N. Y. Acad. Sci., **206**, 641, (1973)
[37] A. C. Jones, G. A. Keenan, *unpublished results*.
[38] S. Khandelwal, J. L. Roebber, Chem. Phys. Letters, **34**, 355, (1975)
[39] M. Barber, R. S. Bordoli, G. J. Elliott, R. D. Sedgwick, A. N. Tyler, Anal. Chem., **54**, 645A, (1982)
[40] M. J. Dale, G. A. Keenan, *unpublished results*,
[41] P. C. Cartwright, *Ph. D. Thesis*, University of Edinburgh, 1989.
[42] M. J. Tubergen, J. R. Cable, D. H. Levy, J. Am. Chem. Soc., **110**, 7349, (1988)
[43] J. H. Arps, C. H. Chen, M. P. McCann, I. Datskou, Appl. Spectrosc., **43**, 1211, (1989)
[44] J. Berkowitz, *Photoabsorption, Photoionization and Photoelectron Spectroscopy*, Academic Press, New York, 1979.
[45] J. B. Pallix, U. Schühle, C. H. Becker, D. L. Huestis, Anal. Chem., **61**, 805, (1989)

Chapter 7
LD-MPI Mass Spectrometry as an analytical tool.

7.1 Introduction

Chapter 6 detailed some of the preliminary work carried out at the University of Edinburgh using LD-MPI mass spectrometry to obtain spectra for several classes of molecule. Given the rather exploratory nature of these initial experiments, however, it is unreasonable to judge the analytical capabilities of the technique solely on the results presented in that chapter. In this chapter, therefore, a survey of the LD-MPIMS work also carried out elsewhere is presented, allowing an overview to be taken of the scope and limitations of the method. In concluding, LD-MPIMS is compared to rather more established mass spectroscopic techniques, and its potential as an analytical tool assessed.

7.2 A survey of LD-MPI mass spectrometry work carried out to date.

The development of LD-MPIMS as both a spectroscopic and analytical method has been due primarily to the work of four research groups. In 1986, Grotemeyer and his coworkers published the first of many studies of biomolecules in the gas phase [1]. Employing a combination of pulsed infrared desorption, supersonic molecular beam cooling and ionisation using a tunable frequency-doubled dye laser, they recorded the mass spectrum of native chlorophylls in a reflectron TOF mass spectrometer. The chlorophylls were extracted from the cyano-bacterium *Spirulina geitlerie*, and used without further purification. Under

soft ionisation conditions, at λ = 275 nm, a spectrum was obtained which clearly showed the molecular ions of three different chlorophylls with little fragmentation and no cationisation or protonation. This ground-breaking paper was quickly followed by another, which was to be the prototype for many of the publications that were to follow [2]. Here, the MPI mass spectrum of an unprotected decapeptide, Angiotensin I, was presented. By pumping a π^*-π transition via an absorption of a Tyr residue, at λ = 271.3 nm, a soft ionisation mass spectrum was obtained showing exclusively the molecular ion of Angiotensin I. By increasing the ionisation laser power density, a number of fragmentation products were obtained, which had the extremely useful bonus of allowing a deduction of the full peptide sequence in the gas phase. Four well known fragmentation processes were observed, with fragmentation occurring from both the C-terminal and N-terminal ends of the peptide. (These latter fragment ions can only be deduced from the observation of metastable ions in EI mass spectrometry [3]). It has long been a goal of mass spectroscopists to be able to make such gas-phase measurements, thereby augmenting and, in some cases, by-passing the effective, but rather time-consuming Edman degradation reaction [4]. Consequently, a large percentage of the papers published in the field of LD-MPIMS have been involved in the sequencing of gas-phase peptides [5]- [14]. Around this time, Lubman and coworkers published the LD-MPI mass spectra of several PNAHs using pulsed CO_2 laser desorption followed by ionisation at 266 nm, in a linear TOF mass spectrometer [15]. This paper also reported the jet-cooled mass spectra of several small biological molecules. This latter class of molecules has been the other source of a rich crop of published work in LD-MPIMS [16]- [21].

7.2.1 Peptide analysis by LD-MPIMS.

The field of peptide analysis will be considered first. Tembreull and Lubman reported the study of several Trp-, Tyr- and Phe-based di- and tri-peptides, using desorption into a supersonic beam of CO_2 and subsequent ionisation by R2PI at either 266 or 280 nm [6]. In most cases, mass spectra were obtained with a strong molecular ion signal or characteristic fragment ions such as $(M\text{-}OH)^+$ or $(M\text{-}COOH)^+$. However, in some cases, particularly those peptides containing Phe-, no molecular ion signal was seen at all. This prompted Walter et al. [7] to reinvestigate some of these samples. Using a tunable, rather than a fixed ionisation laser, they were able to record mass spectra with strong molecular ion intensities, with no or minimal loss of the hydroxyl radical or water. The optimum wavelength for Phe-containing species was found to be near the S_1-S_0 origin band transition for toluene, at 272.7 nm [16]. The exact value depended upon the substituent group, with electron withdrawing groups shifting the optimal wavelength to the blue, and electron releasing groups having the opposite effect [8], [22]. As expected, the optimum wavelengths for Tyr- and Trp-containing peptides were red shifted relative to 270 nm. It was demonstrated that "reverse" dipeptides, such as Phe-Leu and Leu-Phe have different features in their LD-MPI mass spectra, characteristic of the structure of the molecules.

Li and Lubman [10] used n-carbobenzoxy(CBZ)-derivatisation to provide an absorption centre at 266 nm for a number of small peptides. Under medium hard ionisation conditions, they were able to utilise small, but significant differences in the laser-induced fragmentation patterns to distinguish between isomeric peptides containing leucine and isoleucine residues. Grotemeyer and Schlag [11]

meanwhile, showed that by separating the desorption process from the ionisation process, it was possible to make mass spectrometric measurements on mixtures containing hydrophilic and hydrophobic peptides with equal probabilities for detection of the two molecules. This demonstrated, as shown in section 6.3.4, that there was no discrimination in the desorption process. A number of medium-large peptides, of molecular weight over 1000 Da, have been studied by LD-MPI mass spectrometry [12]. For example, the complete sequence of substance P (molecular weight = 1346 Da) has been unambiguously deduced from the medium-hard MPI mass spectrum. The largest molecule to have been successfully studied by this method is bovine insulin (molecular weight = 5729 Da). By tuning the ionisation laser wavelength to the π^*-π transition of the Phe or Tyr residues at 272.7 nm, a soft ionisation mass spectrum has been recorded at a laser power density of 10 $MWcm^{-2}$ [13]. Two additional intense signals were identified as the A chain at 2334 Da and the B chain at 3895 Da, which are formed due to the breakage of the two disulphide bridges in the insulin molecular ion.

7.2.2 Small biological molecules.

As mentioned previously, the amino acids are a biologically important class of molecule. Mass spectra of the aromatic amino acids have been presented above, and the mass spectra of derivatised non-aromatic amino acids reported in the literature [10], [16], [17]. However, the LD-MPI mass spectra of only two non-aromatic amino acids have been recorded, namely for histidine and arginine. Grotemeyer et al. [16] measured the LD-MPI mass spectrum for arginine via a non-resonant ionisation scheme at λ = 250 nm. This amino acid is both

extremely polar, being one of the strongest organic acids, and very labile. In fact, until this measurement was made, the only method which had given a pseudomolecular ion signal for arginine was field desorption mass spectrometry. However, the soft LD-MPI mass spectrum exhibited a strong molecular ion at mass 174, with the only other peaks being due to loss of NH_3 from the molecular ion at mass 157 (the base peak of the spectrum), and at mass 116.

Tembreull and Lubman [18] have recorded the mass spectra for several classes of important biological molecules. These include catecholamines and their metabolites, which are neurotransmitters in the human body. These molecules are a typical class of fragile biological molecules, being extremely labile. Nevertheless, soft ionisation mass spectra were recorded at either 266 or 280 nm. The LD-MPI mass spectra of indoleamines, tricyclic phenothiazine based neuroleptic drugs and purine bases were also recorded with minimal fragmentation. Similarly, mass spectra were obtained from a number of vitamins. Of particular interest is the case of thiamine, which is a chloride salt. It is thought that it is desorbed as a neutral salt, which then dissociates to the ionic form and subsequently undergoes fragmentation upon absorption of UV photons, giving a mass spectrum with a weak molecular ion, and fragment peaks corresponding to bond scission at its methylene bridging group.

7.2.3 Matrix effects.

In general, no peaks attributable to the sample matrix are observed in LD-MPI mass spectra, since no resonance enhancement occurs at the UV laser wavelengths employed. However, as shown in figure 6.19, complexes may form

between the matrix material (in this case, glycerol) and the sample under investigation (in this case, Trp) leading to an ion peak at mass 296. With careful control of the ionisation laser power density and sample mixtures, however, this effect can be minimised- no other spectrum presented in chapter 6 shows any evidence for such complexation.

The appearance of an LD-MPI mass spectrum can, however, be radically altered by the use of an appropriate matrix material. For example, Grotemeyer et al. [23], [24] obtained the mass spectra of tris-(2,2' - bipyridyl)-Ru(II) salts using two different matrices. The Ru salts can be desorbed as neutral molecules, either intact or, more probably, after electron attachment to the cation on the surface. If the salts were desorbed from a matrix containing CeO, the formation of $C_{30}H_{24}N_6Ru^+$ was observed, as the base peak of the spectrum, at mass 570. If, however, the salts were mixed with a polyethylene/ gold powder mix, the most intense peak was at Ru^+, with a weak spectral feature at mass 570.

Beavis et al. [9] reported the use of several matrices when studying dipeptides. As mentioned previously, under soft ionisation conditions, M^+ is usually the base peak even for very labile materials. However, a fragment ion due to the loss of water is often observed, with varying degrees of intensity depending on the composition of the peptide and on the intensity of the desorption laser. This loss of water does not occur during the MPI process, and has been shown to to be due to pyrolysis of the sample during the desorption process.

Beavis et al. [9] showed that it is possible to modify the rates and types of chemical reactions occurring at the sample surface during irradiation by addition

of the appropriate matrix material. For example, the mass spectrum of Leu-Trp at λ = 286.5 nm gave a ratio of M^+:$[M-18]^+$ of ~2:1. Addition of 1 mg of Na_3PO_4 per 1 mg of peptide , which is known to promote dehydration in carboxylic acids, to the sample mixture altered this ratio to 1:1.2. On the other hand, addition of 1 mg of glucose per mg of peptide almost completely suppressed the $(M-18)^+$ ion.

The presence of the sugar in the sample keeps the surface temperature low, both during and after irradiation by the infrared laser beam. Sugar pyrolysis, which is endothermic, occurs at lower temperatures than the corresponding process in the dipeptides. It also leads to an excess of water in the environs of the peptide molecules, which helps to drive the peptide dehydration reaction in the other direction.

The use of this type of matrix is by no means unique. Beavis et al. [25] studied the effect of a number of organic and inorganic matrices on the LD-MPI yield. Inorganic matrices which are infrared absorbers, such as Na_3PO_4 and sodium acetate, generally reduced the ion yield from dipeptides, and in many cases suppressed it completely. This was explained by the increased temperature reached by the sample mixture during irradiation by the pulsed infrared desorption laser beam. It was calculated that the temperature would reach at least 1300 K, under which conditions the peptides would pyrolyse. Infrared transparent inorganic matrices, such as NaCl or KBr, helped to increase the yield of intact molecules desorbed, although dipeptides with polar sidechains did not show an improvement in molecular ion yield.

A range of mono- and di-saccharides, none of which were completely transparent at 10.6 μm, were used as matrix materials. In general, the more transparent the matrix, the better the yield of neutral molecules. For a sugar, such as ribose, with a resonant vibrational band at 943.4 cm^{-1}, the yield of neutral molecules vanished completely.

These observations were explained by invoking a non-totally thermal desorption mechanism for the intact molecules. While shock-wave induced "unloading" [26], which has been suggested for both pulsed UV and high energy particle beam desorption, is not thought to occur, transient high pressures can be produced by warming a semi-transparent material by a laser beam on a timescale short with respect to the time needed for the resulting expansion of the sample to relax with the non-irradiated surroundings. A localised stress field is produced, which can relax by producing strain fields. This can result in surface unloading over a long period of time, much longer than the original laser pulse width, and has been proposed as an alternative desorption model to the purely thermal mechanism discussed in chapter 3.

7.2.4 Jet-cooled R2PI spectra of biological molecules.

One of the main goals of the various workers in this particular field of research has been the development of a truly two-dimensional analytical method. As is clear from the preceeding discussion, LD-MPIMS is a potentially powerful analytical method on its own. The combination of mass spectrometry with jet-cooled vibronic spectroscopy, as introduced in chapter 3, is, however, an even more selective technique.

As mentioned previously, Levy and coworkers [27] pioneered the recording of the vibronic spectra of labile organic molecules, when they obtained the R2PI spectrum of tryptophan, by monitoring the M^+ ion signal as a function of wavelength. Initially, they used a combination of thermal desorption and pulsed thermospray techniques, but then they reverted to LD as a means of introducing neutral molecules of interest into a molecular beam. In contrast to the groups of Schlag, Lubman and Zare, the Q-switched output from the second harmonic of a Nd^{3+}:YAG laser was employed for desorption. A disc source/entrainment faceplate system, discussed in section 6.6, was used to obtain efficient cooling in the supersonic molecular beam.

R2PI spectra of a number of small Trp-containing peptides have been reported [22], [28], [29]. In common with the spectrum of Trp itself, a number of sharp features were observed, corresponding to the various conformers of the peptides. Although peptides with Trp at the N-terminal are chemically quite similar to the "reverse" peptides with Trp- at the C-terminal, the jet-cooled vibronic spectra of these molecules showed marked differences. The lowest energy transition in each spectrum of the different Trp- N-terminal peptides (Trp-Gly, Trp-Gly-Gly and Tr-Phe) always occurred within 17 cm^{-1} of 34536 cm^{-1} (cf. 34873 cm^{-1} for Trp [27]). In contrast, the lowest energy transitions in Gly-Trp, Gly-Gly-Trp and Phe-Trp always occurred $\sim$200 cm^{-1} higher in energy, around 34728 cm^{-1}. Thus, electronic spectroscopy is capable of probing subtle differences in the peptide structures.

Lubman and his coworkers have developed their LD-MPI TOF mass spectrometer to make analytical measurements on a number of systems by

combining the jet-cooled R2PI spectroscopy technique developed by Levy with the mass spectrometric methods discussed earlier. Tembreull and Lubman [30] recorded the vibronic spectrum of tyramine using both CO_2 laser desorption and the heated nozzle approach. The desorbed material was entrained into a beam of CO_2 4 mm downstream of the nozzle orifice. Therefore, despite the fact that CO_2 has a longer expansion distance to the free flow region than monatomic gases, it is hardly surprising that the observed cooling was incomplete. Thus, the desorption R2PI spectrum was somewhat broader than that observed from the heated nozzle source.

By optimising source conditions, however, Li and Lubman recorded jet cooled spectra of a number of tyrosine derivatives [31]. These spectra were better resolved, with sharper features than those obtained using the heated nozzle.

In the gas phase, the broad-band gas-phase absorption spectra of tyrosine and tyramine were obtained in a UV-visible spectrophotometer [32]; they were barely distinguishable. The jet-cooled R2PI spectra, however, displayed distinct features and allowed unambiguous spectroscopic identification. Again, the spectra obtained were quite broad, with several sharp bands in the region of the origin band being attributed to the presence of a number of conformers. The recorded spectrum of Gly-Tyr was quite broad, ~ 2 nm FWHM, but again several reasonably sharp peaks were observed along the extended band contour. The mass spectrum of Gly-Tyr recorded at this absorption feature, thought likely to be the S_1-S_0 origin band, showed little fragmentation, with no M-17 or M-18 fragment ion peaks under soft ionisation conditions.

The jet-cooled R2PI spectra of several Tyr-containing dipeptides were also obtained [31]. Although no sharp features were observed, with spectral contours being ~1.5 nm FWHM, the shapes of the contours were distinctive, allowing discrimination of "reverse" peptides- as in the case of Trp-containing peptides, those dipeptides with Tyr- on the C- terminal end and those with Tyr- on the N-terminal end gave different spectra. For example, Ala-Tyr exhibits a peak at 280.5 nm, whilst Tyr-Ala has a contour peaking at ~281.5 nm. At these peak wavelengths, LD-R2PI mass spectra, recorded under soft ionisation conditions, showed $M^{+\cdot}$ exclusively, but at power densities about twenty times less than those required in the case of non-optimised cooling.

In order to evaluate the potential of this combination of jet-cooled R2PI spectroscopy and mass spectrometry, Li and Lubman measured the spectra of mixtures of several indole and catechol derivatives [33]. The mass difference between tryptamine (mass 160) and tryptophol (mass 161) was easily resolvable in these experiments. The ultimate selectivity available by fine-tuning the ionisation wavelength depended on the degree of cooling, which allowed minimisation of the degree of interference from resonant ionisation of hot background molecules. Although there was a further limitation due to the presence of the ^{13}C peak of tryptamine at mass 161, an optical discrimination of 1:100 of tryptamine in tryptophol was obtained by tuning the ionisation laser wavelength to λ = 286.3 nm, the strongest resonance in the tryptamine spectrum. If the target molecule for detection had an origin band at lower wavelength than the origin bands of the other components in a mixture, enhanced discrimination was possible. A discrimination factor of $1:10^5$ was obtained for tryptamine in

tyramine at λ = 286.3 nm, the strongest band obtained for the former, since the latter molecule only ionises at that energy via non-resonant MPI. If, however, the origin band of the molecule of interest was at shorter wavelength than the other origin bands for the components in a mixture, the optical discrimination factor was generally lower, and depended on the spectroscopy of the molecules involved. For example, Li and Lubman were able to discriminate 1 part tryptamine in 1000 parts methoxy-3-acetic acid, but only 1 part indole-3-acetic acid in 70 parts melatonin. The limitation in these cases was obviously due to background absorptions from interfering molecules at frequencies higher than their S_1-S_0 origin bands.

7.2.5 Sensitivity measurements.

The technique of LD-MPIMS has risen to prominence through its ability to allow identification of complex molecules rather than through its ability to measure absolute or relative molecular concentrations. Similarly, no emphasis is placed on the ultimate sensitivity of the technique, with relatively large samples being used to allow mass spectra to be recorded. Zare's group have reported the highest detection sensitivity of any of the groups using LD-MPIMS [17], [19], [34], [35]. They employ the output from a pulsed CO_2 laser to remove the sample, deposited on the inner surface of a rotating glass cup. Each laser shot interrogates a new part of the sample surface. No molecular beam entrainment is used, with the molecules entering the ionisation region of a linear TOF mass analyser, located at a distance of 1 cm from the glass surface. Hahn et al. [19] have demonstrated that the ion signal obtained using this set-up was linear with surface coverage over 5 or more orders of magnitude for several molecules, from

nanomoles to sub-femtomoles. For example, a detection limit, at S/N = 2, of 4 x 10^{-17} moles of protoporphyrin IX dimethyl ester was obtained. The desorption amount was calculated on the basis of the amount of sample deposited on to the substrate, the new area exposed per laser shot, and the assumption that all irradiated molecules are desorbed. The linearity of response appears to be quite reproducible over a wide dynamic range of quantitation.

Similar experiments carried out at Edinburgh, making use of the improvements outlined in section 6.6, have allowed a detection limit of 10 femtomoles to be obtained for perylene, at an ionisation laser wavelength of 193 nm [36]. However, the linearity of the ion signal versus concentration plot was limited to the lowest few sample concentrations used, with the signal plateauing out at higher concentrations (around 1 nmole). This is easily explained by the incomplete desorption of these more concentrated samples; when the sample rod was rastered through the infrared desorption laser beam, appreciable ion signals were obtained at the second and even third passes. This was not the case at the lowest concentrations used, indicating complete sample desorption during the first desorption pulse.

Li and Lubman [33] have reported detection limits for a number of indole derivatives, using soft ionisation at the observed maxima in the jet-cooled R2PI spectra of these molecules. For example, a detection limit of 10 pg was obtained for indole-3-acetic acid. No indication was given as to the linearity of signal response with concentration. The same authors required a minimum of 500 ng of tryptamine to allow a wavelength scan over 1.5 nm to be obtained with reasonable signal-to-noise. Obviously, the same amount of sample could be used

to give a less extensive wavelength scan at better signal-to-noise.

7.3 LD-MPI mass spectrometry as an analytical tool.

LD-MPI mass spectrometry differs from all the other desorption methods in mass spectrometry such as FABMS [37], SIMS [38], [39], ^{252}Cf-PDMS [40] and matrix-assisted LDMS [41] in that the desorption step is separated from the ionisation step in space and time. A comparison of its capabilities with those of these other techniques allows the position of LD-MPI mass spectrometry as an analytical tool to be assessed.

The advantages of LD-MPIMS should be clear from chapter 6 and the previous sections of this chapter. Soft ionisation of a wide range of important samples is possible, yielding the molecular ion $M^{+\cdot}$ with high intensity. No adduct ions are usually formed. Increasing the ionisation laser power density allows controllable fragmentation to be induced in the molecular cation, yielding structurally-significant fragment ions in high yields. In the other desorption methods, the molecular ion is generally not detected, but instead several adduct ions are found which are due to the addition of protons and/ or metal cations to the molecule. Often, especially in FABMS, there is also ionisation of the matrix material. This leads to a considerable amount of non-sample-specific ions, thereby complicating interpretation of the mass spectra. Several of these methods, such as ^{252}Cf-PDMS and field desorption, give very low degrees of fragmentation. Methods such as collision-activated decomposition (CAD) must therefore be employed in order to gain structural information, which generally requires two stages of mass spectrometry and is therefore quite expensive to

perform. In PDMS, the low flux of primary ions generally leaves most of the sample intact, even after prolonged exposure. It is therefore possible to perform chemical, or in the case of peptides, enzymatic, reactions on the remaining sample to yield the information required.

The major disadvantage associated with LD-MPIMS is the requirement for a UV-absorbing chromophore to be present in the molecule for efficient ionisation to occur. This means that the technique can never realistically compete with FABMS as an all-purpose analytical technique allowing analysis of a wide range of samples. As mentioned in section 6.6, the optical selectivity that is possible in ionisation means that it is difficult to make quantitative measurements on the sample. The use of VUV radiation has overcome this problem to a certain extent [42], but is an added experimental complication. Similarly, it is not as easy to control the energy of the desorption laser as it is to control the primary ion beam current in SIMS, for example. Therefore, whilst the latter technique allows surface-sensitive (to a depth of 1-2 nm) analysis (so-called "static" SIMS), or controlled depth profiling (so-called "dynamic" SIMS) of samples, LD-MPIMS is much more a bulk technique. The generation of ions by LD-MPI is still more expensive than their production by most of the other desorption techniques, since at least two lasers, with one preferably being tunable, are required as opposed to an ion gun or fast ion source.

The biggest question mark hanging over the applicability of LD-MPIMS is the upper mass range of molecules that can be successfully desorbed, entrained and ionised. As mentioned previously, the largest molecule studied by this technique is of mass 5729, which should be compared to upper mass ranges of 45000 for

PDMS [43] and 200000 for matrix-assisted LDMS [44]. This latter technique perhaps points the way ahead for LD-MPIMS. Here, the sample of interest is dissolved in a matrix material, such as nicotinic acid [45], [46] or sinapinic acid [47], which strongly absorbs the desorption laser wavelength (in these cases, 266 nm or 355 nm); the wavelength is not absorbed by the species of interest. In this technique, the nascent ion distribution is probed directly, but there is no reason why the desorbed neutrals could not be post-ionised by a UV laser.

Perhaps the strongest advantage that LD-MPIMS has as an analytical technique is its selectivity in ionisation. Thus, small amounts of UV-absorbing materials can be detected from non-absorbing mixtures, or from non-absorbing substrates. As an example of the latter, figure 7.1 shows the SIMS [48] and LD-MPI mass spectra of an unknown UV-absorbing molecule on a cotton substrate [36]. The SIMS spectrum, in the upper part of the figure, clearly shows a large ion signal between mass 12 and mass 150 which is conspicuous by its absence in the lower spectrum, recorded on the linear TOF mass spectrometer at an ionisation wavelength of 193 nm. The three strong peaks in the lower mass spectrum correspond to the molecular ion (at mass 310) of the unknown and two structurally significant fragment ions. By analysis of a cotton sample with no organic deposited on the surface, most of the peaks between 12 and 150 Da in the upper spectrum were assigned to the substrate. The important point here is

Figure 7.1. A comparison of SIMS and LD-MPIMS. The sample comprises an unknown aromatic molecule on cotton.

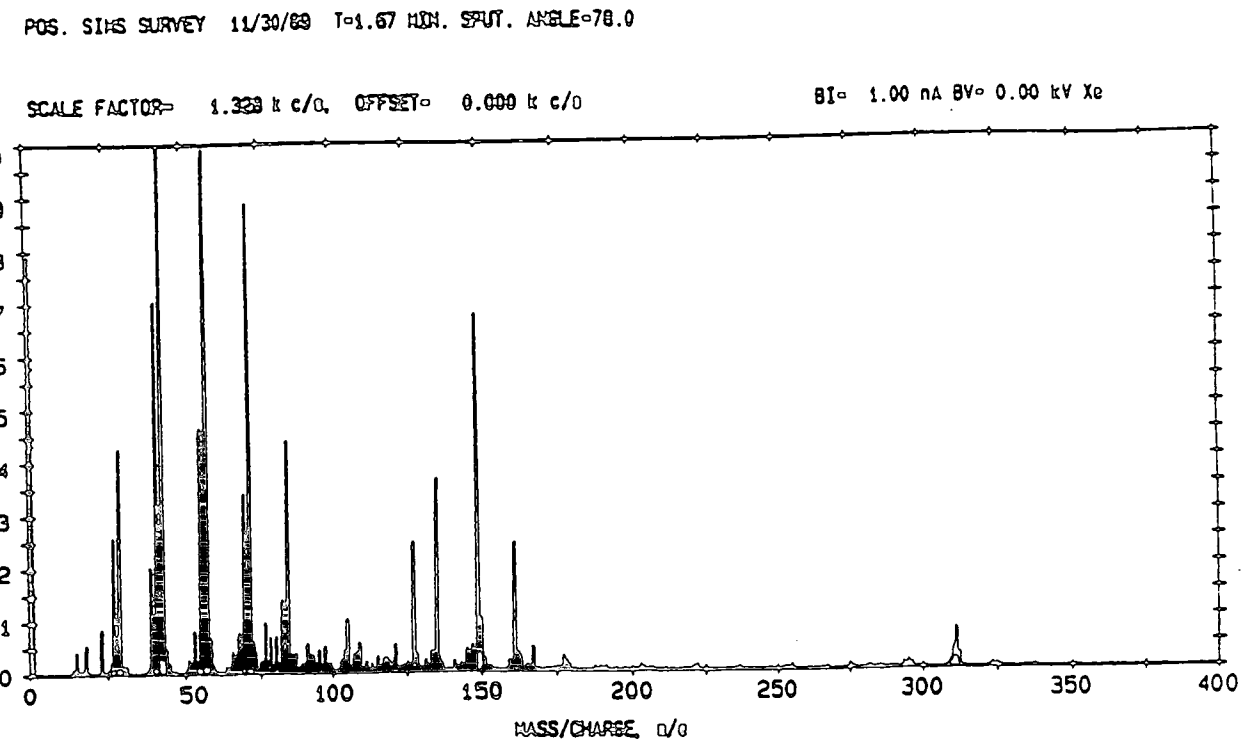

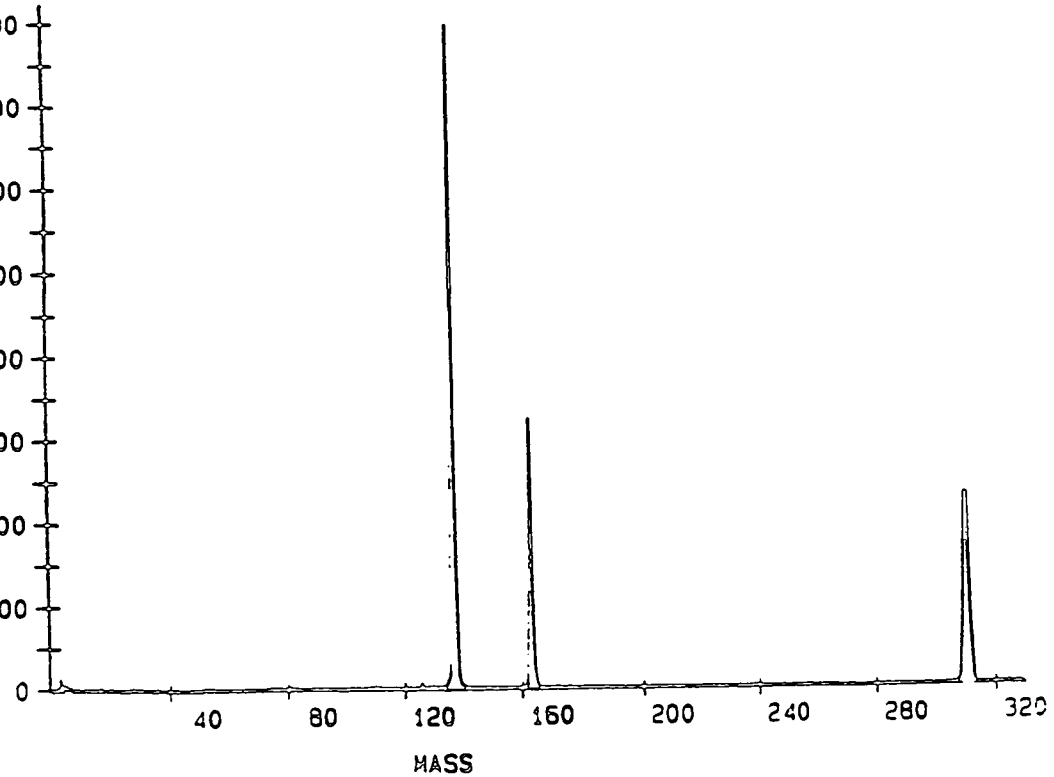

that although similar information can be obtained by both techniques, the LD-MPI mass spectrum is much cleaner. In this specific case, this is not of great significance, since the molecular ion of the molecule of interest is obvious in both spectra. However, if the molecular ion had been at mass 149 it would have been obscured by peaks due to the cotton substrate. Similarly, even if the overall sensitivities of the two techniques were comparable as regards the molecule of interest, at lower sample concentrations, the required information would become lost due to chemical interference in the SIMS spectrum, but not in the LD-MPI mass spectrum.

In conclusion, LD-MPI mass spectrometry is an important new technique, which has, in the five years since its inception, proved to be of great usefulness in the study of involatile and labile species. While it is perhaps not as widely-applicable as the well-established technique of FABMS, it should find its place in the research laboratory as a complementary and supplementary technique to more conventional analytical methods.

References.

[1] J. Grotemeyer, U. Boesl, K. Walter, E. W. Schlag, J. Am. Chem. Soc., **108**, 4233, (1986)

[2] J. Grotemeyer, K. Walter, U. Boesl, E. W. Schlag, Org. Mass Spectrom., **21**, 595, (1986)

[3] H. W. Ronge, H. F. Grützmacher, Rec. Dev. Mass Spectrom. Biochem. Med. Environ. Res., **7**, 255, (1981)

[4] P. Edman, G. Begg, Eur. J. Biochem., **1**, 80, (1967)

[5] J. Grotemeyer, U. Boesl, K. Walter, E. W. Schlag, Org. Mass Spectrom., **21**, 645, (1986)

[6] R. Tembreull, D. M. Lubman, Anal. Chem., **59**, 1003, (1987)

[7] K. Walter, J. Lindner, J. Grotemeyer, E. W. Schlag, Chem. Phys., **125**, 155, (1988)

[8] L. Li, D. M. Lubman, Appl. Spectrosc., **42**, 411, (1988)

[9] R. C. Beavis, J. Lindner, J. Grotemeyer, E. W. Schlag, Chem. Phys. Lett., **146**, 310, (1988)

[10] L. Li, D. M. Lubman, Anal. Chem., **60**, 1409, (1988)

[11] J. Grotemeyer, E. W. Schlag, Org. Mass Spectrom., **23**, 388, (1988)

[12] J. Grotemeyer, E. W. Schlag, Angew. Chem. Int. Ed. Engl., **27**, 447, (1988)

[13] J. Grotemeyer, E. W. Schlag, Org. Mass Spectrom., **22**, 758, (1987)

[14] J. Grotemeyer, E. W. Schlag, Acc. Chem. Res., **22**, 399, (1989)

[15] R. Tembreull, D. M. Lubman, Anal. Chem., **58**, 1299, (1986)

[16] J. Grotemeyer, K. Walter, U. Boesl, E. W. Schlag, Int. J. Mass Spectrom. Ion Proc., **78**, 69, (1987)

[17] F. Engelke, J. H. Hahn, W. Henke, R. N. Zare, Anal. Chem., **59**, 909, (1987)

[18] R. Tembreull, D. M. Lubman, Anal. Chem., **59**, 1082, (1987)

[19] J. H. Hahn, R. Zenobi, R. N. Zare, J. Am. Chem. Soc., **109**, 2842, (1987)

[20] L. Li, D. M. Lubman, Anal. Chem., **61**, 1911, (1989)

[21] L. Li, D. M. Lubman, Int. J. Mass Spectrom. Ion Proc., **88**, 197, (1989)

[22] J. R. Cable, M. J. Tubergen, D. H. Levy, J. Am. Chem. Soc., **109**, 6198, (1987)

[23] R. Beavis, J. Lindner, J. Grotemeyer, I. M. Atkinson, F. R. Keene, A. E. W. Knight, J. Am. Chem. Soc., **110**, 7534, (1988)

[24] J. Grotemeyer, J. Lindner, C. Köster, E. W. Schlag, J. Mol. Struct., **217**, 51, (1990)

[25] R. C. Beavis, J. Lindner, J. Grotemeyer, E. W. Schlag, Z. Naturforsch., **43A**, 1083, (1988)

[26] I. S. Bitensky, E. S. Parilis, Nucl. Instrum. Methods, **B21**, 26, (1987)

[27] T. R. Rizzo, Y. D. Park, L. A. Peteanu, D. H. Levy, J. Chem. Phys., **84**, 2534, (1986)

[28] M. J. Tubergen, J. R. Cable, D. H. Levy, J. Am. Chem. Soc., **110**, 7349, (1988)

[29] J. H. Cable, M. J. Tubergen, D. H. Levy, Faraday Discuss. Chem. Soc., **86**, 143, (1988)

[30] R. Tembreull, D. M. Lubman, Appl. Spectrosc., **41**, 431, (1987)

[31] L. Li, D. M. Lubman, Appl. Spectrosc., **42**, 411, (1988)

[32] L. Li, D. M. Lubman, Anal. Chem., **59**, 2538, (1987)
[33] L. Li, D. M. Lubman, Anal. Chem., **60**, 2591, (1988)
[34] R. N. Zare, J. H. Hahn, R. Zenobi, Bull. Chem. Soc. Jpn., **61**, 87, (1988)
[35] J. H. Hahn, R. Zenobi, J. L. Bada, R. N. Zare, Science, **239**, 1523, (1988)
[36] K. Costello, A. C. Jones, G. A. Keenan, *unpublished results*,
[37] M. Barber, R. S. Bordoli, G. J. Elliott, R. D. Sedgwick, A. N. Tyler, Anal. Chem., **54**, 645A, (1982)
[38] A. Benninghoven, W. K. Sichtermann, Anal. Chem., **50**, 1180, (1978)
[39] F. Adams, F. Michiels, M. Moens, P. Van Espen, Anal. Chim. Acta, **216**, 25, (1989)
[40] P. Roepstorff, Acc. Chem. Res., **22**, 421, (1989)
[41] B. Spengler, M. Karas, U. Bahr, F. Hillenkamp, J. Phys. Chem., **91**, 6502, (1987)
[42] J. B. Pallix, U. Schühle, C. H. Becker, D. L. Huestis, Anal. Chem., **61**, 805, (1989)
[43] G. Jonsson, A. Hedin, P. Hakansson, B. U. R. Sundqvist, H. Bennick, P. Roepstorff, Rapid Comm. Mass Spectrom., **3**, 190, (1989)
[44] F. Hillenkamp, Adv. Mass Spectrom., **11**, 354, (1989)
[45] R. C. Beavis, B. T. Chait, Rapid Comm. Mass Spectrom., **3**, 432, (1989)
[46] R. C. Beavis, B. T. Chait, Rapid Comm. Mass Spectrom., **3**, 436, (1989)
[47] R. C. Beavis, B. T. Chait, Anal. Chem., **62**, 1836, (1990)
[48] Perkin Elmer Physical Electronics Lab., Eden Prairie, Minnesota, *private communication*,

Appendix A
Supersonic Molecular Beams.

The flow of gas from a high pressure reservoir through a small hole into a vacuum chamber creates a molecular beam. This flow is characterised by two parameters, namely the mean free path of the source gas (λ_0) and the dimension of the source orifice which limits the flow (D). The relative size of these parameters determines the behaviour of the molecular beam emerging from the source orifice into the vacuum chamber.

In an effusive molecular beam, λ_0 is on the order of or is larger than D. Gas molecules leave the source largely unperturbed by collisions with one another, so that the beam produced has the same bulk properties as the source gas.

In contrast, if λ_0 is small compared to D, then the density of the source gas is high close to the aperture, and the molecules undergo many collisions with one another as they flow through the orifice. It is possible to treat the gas as a continuous fluid, according to the laws of hydrodynamic flow. The fluid acquires a net velocity in response to a pressure gradient across the nozzle. This type of flow occurs in supersonic nozzle sources. If there is a collimating aperture downstream of the source, such as a skimmer, the resulting expansion is known as a supersonic molecular beam. If this aperture is absent, the resulting flow of gas is known as a supersonic free jet.

As a direct consequence of the two dissimilar mechanisms, effusive and molecular beams differ in several important aspects. Firstly, since the divergence of a supersonic molecular beam is less than that of an effusive beam, the relative

flux through a given area perpendicular to the direction of flow is higher for a supersonic source.

Secondly, in the absence of heat flow to the gas, the directed mass velocity in a supersonic molecular beam can only be achieved at the expense of its random thermal motion. One measure of this thermal motion is the width of the Maxwellian distribution of molecular velocities. As faster molecules collide with their slower-moving counterparts, velocities along the axis of flow tend to become equal. Therefore, the flow of gas through a supersonic nozzle reduces the width of its velocity distribution, and hence its translational temperature. Toennies and Winkelmann [1] made a theoretical study of this process, in which they considered two Maxwellian distributions, one for velocities parallel to and the other for velocities perpendicular to the beam flow axis. These two distributions can have different widths, so that the gas at any point along the expansion can be described by two different temperatures. They showed that two-body collisions reduce the temperature corresponding to the parallel velocity distribution (see later), but that these same collisions tend to increase the perpendicular temperature by transferring random thermal energy into this component of flow. The perpendicular temperature is, however, reduced as a result of a geometrical effect. Molecules with large perpendicular velocities move away from the centreline of the beam, so that if the beam is interrogated sufficiently far downstream, only molecules with small perpendicular velocities are left. The corresponding velocity distribution therefore narrows as the flow proceeds. On the other hand, as mentioned above, the bulk properties of an effusive beam, including velocity distributions in both directions, are similar to those of the

source gas. Therefore, the beam temperature does not change with the distance downstream.

The mechanism of cooling in supersonic expansions is completely general, with the extent of the cooling achieved depending only on the expansion conditions and the nature of the gas. Monatomic gases, which have no internal (rotational, vibrational) degrees of freedom, reach the lowest translational temperatures (0.03 K for He, 2 K for Ar [2]). The main reason for the wide use of supersonic molecular beams in spectroscopy, however, is due to the fact that the rotational and vibrational degrees of freedom can reach equilibrium with the cold translational bath. The rotational and vibrational degrees of freedom of polyatomic molecules are relaxed by collisions as the translational temperature decreases, but the rate of cooling lags behind that of a monatomic gas under similar conditions. Maximum cooling of polyatomic molecules is achieved by seeding a small amount of the polyatomic into an expansion of a monatomic gas such as He or Ar. The properties of the expansion are those of a weighted mixture of the two species, so that the conditions achieved in the expansion can be understood in terms of the behaviour of the pure carrier gas.

Rotational relaxation by collisions is a fairly efficient process, so that the rotational temperature of molecules in a supersonic expansion follows the translational temperature reasonably closely. In general, collisional vibrational relaxation is a less efficient process, and the vibrational temperature lags somewhat behind both T_{TRANS} and T_{ROT}. If the normal modes of the molecule have very different frequencies, they may relax at different rates, so that each vibration may have a different characteristic temperature.

As indicated above, the early stages of a supersonic expansion may be treated by conventional fluid dynamics, assuming hydrodynamic flow conditions where molecules undergo repeated collisions [3]. However, Anderson and Fenn [4] have shown that, at some point in the expansion, this model collapses. This is due to the fact that the gas is not a continuous fluid, but is composed of discrete atoms and molecules. Eventually, the beam density drops to the point at which the two-body collision rate cannot sustain the redistribution of velocity required by the hydrodynamic equations of flow. At this point, there is no longer equilibrium between the translational and internal degrees of freedom, and the vibrational and then the rotational temperatures become "frozen". Ultimately, the collision frequency becomes negligible and the beam enters the free molecular flow regime. Beyond this point, the beam constitutes the ideal spectroscopic medium: isolated molecules, rotationally and vibrationally cold, free of any matrix or collisional perturbations. Furthermore, the beam is protected from interactions with hot background molecules by a shock wave that forms around the expansion. The leading edge of the shock wave is called the Mach disc; for the expansion to be fully protected, the position of the Mach disc should be significantly further away from the nozzle than is the point of beam interrogation (by, in this case, the ionisation laser beam). The following treatment applies only to the region of isentropic flow i.e. the region of high collisional frequency.

For any steady state hydrodynamic flow of a fluid, the conservation of mass requires that the following equation holds:

$$\iint_A \rho U \bar{n}\, dA = \text{constant}, \tag{1}$$

where A is the cross sectional area of the flow, ρ is the density of the fluid, U is the hydrodynamic velocity of the fluid and $\bar{n}$ is a unit vector perpendicular to A. If U is constant throughout A, then

$$\rho UA = \text{constant, and}$$

$$d\rho/\rho + dU/U + dA/A = 0. \tag{2}$$

If the flow is adiabatic, then conservation of energy requires that

$$\int_{H_0}^{H} dH = -\int_{0}^{U} d(mU^2/2), \tag{3}$$

where H is the enthalpy and m is the (molar) mass of the fluid. Then

$$H + mU^2/2 = H_0, \tag{4}$$

where the subscript '0' refers to the state of the fluid at rest.

This equation shows that the net mass flow of the fluid is achieved at the expense of its internal energy.

If the fluid is a perfect gas

$$\Delta H = C_p(T_0 - T),$$

$$C_p - C_v = R,$$

so that $C_p = C_p/C_v(C_p/C_v - 1)^{-1}R$

$$= \gamma R/(\gamma-1), \tag{5}$$

where γ is the heat capacity ratio C_p/C_v. Then

$$\Delta H = (\gamma/(\gamma-1))\ R\ (T_0-T),$$

and

$$mU^2/2 = (\gamma/(\gamma-1))R(T_0-T) \tag{6}$$

or

$$U = ((2\gamma/(\gamma-1))(R/m)(T_0-T))^{1/2}. \tag{7}$$

This shows that there is a maximum velocity which the gas can reach by converting all of its internal energy into directed mass flow. This maximum

velocity is given by

$$U = ((2\gamma/(\gamma-1))kT_0/m)^{1/2}, \quad (8)$$

where k is Boltzmann's constant and m is molecular mass of the gas. If T_0, the stagnation temperature, is taken as the temperature of the gas in the source (which is a reasonable assumption, since the fluid can be considered stationary within the source), then for a beam of He at a source temperature of 300 K, the maximum velocity achieved is 1766 ms^{-1}. This is only a factor of $(2\gamma/3(\gamma-1))^{1/2}$ = 1.29 times larger than the most probable speed of molecules in an effusive beam of He.

Rearranging equation (7), and substituting k for R as above, gives

$$T_0/T = 1 + ((\gamma-1)/2)mU^2/\gamma kT$$

$$= 1 + ((\gamma-1)/2)M^2, \quad (9)$$

where M = U/a is the Mach number, and $a = (\gamma kT/m)^{1/2}$ is the local speed of sound.

This equation shows that the temperature reached by a gas in a supersonic expansion depends only on the Mach number achieved and γ, a property of the gas. Equation (9) is valid for any adiabatic process in a real gas. If the process is reversible as well, which requires no shock waves, no shear forces, no heat sources or sinks and no heat conductivity, the flow is isentropic and two other

relationships can be derived, namely

$$P_0/P = (\rho_0/\rho)^{\gamma} \tag{10}$$

and

$$P_0/P = (T_0/T)^{\gamma/(\gamma-1)}. \tag{11}$$

Substitution from equation (9) gives

$$P_0/P = [1 + (\gamma-1)/2\ M^2]^{\gamma/(\gamma-1)} \tag{12}$$

and

$$\rho/\rho_0 = [1 + (\gamma-1)/2\ M^2]^{1/(\gamma-1)}. \tag{13}$$

The critical pressure ratio that is required to obtain sonic flow ($M=1$) is easily obtained from equation (12) and is

$$P_0/P = [1 + (\gamma-1)/2]^{\gamma/(\gamma-1)}. \tag{14}$$

For $\gamma = 5/3$ (monatomic gases), this pressure ratio is 2.05, a condition that is easily obtained in both sets of vacuum apparatus employed during this work.

A number of other useful expressions have been derived by researchers in this field [1], [2], [4]. The Mach number varies as a function of distance downstream of the nozzle according to

$$M = A(X/D)^{\gamma-1}, \tag{15}$$

where A is a constant (= 3.26 for monatomic gases), X is the distance downstream of the nozzle, and D is the nozzle orifice diameter.

As shown above, the flow velocity cannot exceed a maximum value, so the increasing Mach number is due to the reduced beam temperature and hence local speed of sound. The Mach number, however, cannot keep increasing indefinitely due to the ever-decreasing gas density as a function of distance from the nozzle. The maximum obtainable Mach number is known as the terminal Mach number and is given by

$$M_T = 2.05\varepsilon^{-(1-\gamma)/\gamma}(\lambda_0/D)^{(1-\gamma)/\gamma} \tag{16}$$

$$= 133\,(P_0 D)^{0.4} \text{ for Ar} \tag{17}$$

$$= 148\,(P_0 D)^{0.4} \text{ for Ne} \tag{18}$$

$$= 140\,(P_0 D)^{0.4} \text{ for He}, \tag{19}$$

where ε is a measure of "collisional effectiveness", which relates the change in

mean random velocity per collision to the present mean random velocity. P_0 is the source reservoir pressure in atmospheres, and D is the nozzle orifice diameter in cm.

Equation (15) shows that as the nozzle orifice diameter is increased, the molecules must travel further to achieve a given Mach number. If the flow velocity is constant, this means that they must travel longer in time to achieve a given value of M. Since the probability per unit time that a molecule will make a two-body collision is proportional to the pressure, the quantity P_0D is proportional to the number of binary collisions a molecule has to make before attaining a certain Mach number. Thus, the fact that M_T is a function of P_0D simply means that it is a function of the total number of two-body collisions an average molecule undergoes.

An important property to be able to quantify is the density of gas at a distance downstream of the nozzle orifice. For seeded molecular beams, the source density of the seeded molecule is given by

$$\rho_0 = cP_0/kT_0, \tag{20}$$

where $c = n_Z/n_G$, n_Z is the number of molecules of species Z, and n_G is the number of molecules of the inert carrier gas. The density of the beam as a function of distance downstream, X, and angular displacement from the axial centreline of the expansion, θ, is given by

$$\rho = 0.16\,\rho_0\,(D^2\cos^2\theta)/X^2. \qquad (21)$$

Complex formation sets a limit upon the possible degree of cooling that can be achieved in a supersonic expansion. Such condensation is slow, but at some point atoms and molecules in the beam start to form complexes. The interatomic binding energy is released and may appear as translational kinetic energy, which then re-heats the beam. It is therefore important to minimise the degree of complex formation if the maximum degree of cooling is to be obtained.

The condensation of the carrier gas atoms is minimised in the case of He, which has very weak intermolecular forces. Since there is no bound He_2 species [5], the formation of a pure helium cluster requires at least four-body collisions for initiation. This is therefore a slow process. Complexation between He and the seeded molecule is more likely to occur before the formation of He_x species. This process can be minimised by keeping the concentration of the seed molecule low. One draw-back of using seeded beams of He, however, is the so-called "velocity slip" effect [6] which limits the ultimate degree of cooling possible. In a seeded beam, the initial higher thermal velocity of the He carrier gas causes the heavy seeded molecule to accelerate. This is an essential step before the molecule is efficiently cooled by collisions in the expansion. This acceleration is incomplete at low beam pressures, and a marked difference in velocity is found between the heavy seed molecule and He. Under these circumstances, the translational temperature of the seeded molecule has been found to be considerably higher than that of the He. As the rotational relaxation is expected to be efficient throughout the expansion, T_{ROT} is determined by the

translational temperature of the heavy molecule rather than that of He [7]. This effect can be reduced by increasing either P_0 or D, or by using a heavier carrier gas such as Ar.

In general, the formation of complexes requires at least ternary collisions. The ratio of three-body to two-body collisions is a function of the number density of atoms, so for a given terminal Mach number, the degree of complexation can be minimised by decreasing P_0 and increasing D, keeping P_0D constant. Unfortunately, this increases the mass throughput of the nozzle, and therefore the chamber pressure, for a given pumping speed. Therefore, some degree of compromise is required between Mach number and low complex formation to obtain the lowest practical beam temperatures.

References.

[1] J. P. Toennies, K. Winkelmann, J. Chem. Phys., **66**, 3965, (1977)
[2] R. E. Smalley, L. Wharton, D. H. Levy, Acc. Chem. Res., **10**, 139, (1977)
[3] B. S. Massey, *Mechanics of Fluids*, Van Nostrand Reinhold, London, 1979.
[4] J. B. Anderson, J. B. Fenn, Phys. Fluids, **8**, 780, (1965)
[5] A. P. J. van Deursen, J. Reuss, J. Chem. Phys., **63**, 4559, (1975)
[6] A. Amirav, U. Even, J. Jortner, Chem. Phys., **51**, 31, (1980)
[7] A. Amirav, U. Even, J. Jortner, F. W. Birss, D. A. Ramsay, Can. J. Phys., 278, (1983)

Appendix B
Generation of Potential Maps.

As detailed in Chapter 5, one of the factors which affects the performance of a TOF mass spectrometer is the presence of field inhomogeneities in the ion source region. In a reflectron TOF mass spectrometer, of course, these inhomogeneities may also exist in the ion mirror. In order to ascertain the extent of field penetration from one region of the ion source (or mirror) into another, maps of the electrical potential in these ion optics have been generated.

The equilibrium electrical potential V at a point (x,y) in two dimensional Cartesian space is given by the solution of the Laplace equation

$$\partial^2 V/\partial x^2 + \partial^2 V/\partial y^2 = 0.$$

The solution for this equation is readily obtained using a relaxation method with fixed boundary conditions [1]. The basis of this method is outlined below.

The region of interest is subdivided into a number of square cells. The separation of the parallel lines used to generate these cells is taken as the unit length of the problem. Each vertex of the cells, the "mesh points", is assigned an initial potential. Some of the mesh points, namely those which correspond to the earthed walls of the vacuum chamber (or the copper box surrounding the extraction optics for the linear TOFMS) and the lens plates themselves, are held at a fixed potential. The remaining mesh points are not held at constant potential and are relaxed.

For each relaxable point in turn, the potential at that point is compared to that calculated from the average of its four nearest neighbours,

i.e. $U_{x,y}$ is compared to $1/4(U_{x,y+1} + U_{x,y-1} + U_{x-1,y} + U_{x+1,y}) = V_{x,y}$

If these potentials differ, the potential $U_{x,y}$ is not fully relaxed, and is replaced by $V_{x,y}$. The relaxation is repeated with every mesh point until the potential converges to such a degree that the difference between the potential at each mesh point $U_{x,y}$ and its calculated average value $V_{x,y}$ is negligible. The number of iterations required to achieve full relaxation depends on the accuracy required and the number of mesh point considered. The potential maps shown in chapter 5 were taken to be fully relaxed when the difference between $U_{x,y}$ and $V_{x,y}$ was less than 50 mV for all points.

In simulations of the linear TOF mass spectrometer ion extraction optics, the boundary conditions were imposed by the earthed copper cryoshield which enclosed the optics. This was assumed to be complete, which is obviously an approximation to the true experimental conditions since the copper box was bottomless and had four holes cut in it to allow access of molecular and laser beams.

When the reflectron extraction optics were fitted in the ionisation vacuum chamber, all but three sides of the copper box were removed. In this case, the simulation allowed the relaxing potentials to extend out to the walls of the vacuum chamber, which were assumed to be earthed. The potentials in and around the ion mirror were also simulated using the walls of the vacuum

chamber as an earthed boundary. Again, however, the potential generated is an approximation to the actual potential, because the simulation program could not function with angled plates.

Two programs were employed to obtain the simulations. The first was written in FORTRAN and implemented on the Edinburgh mainframe computer system (EMAS), whilst the second was a commercially-available PC-based program "SIMION". Although both programs gave essentially the same results, the potential maps shown in chapter 5 are those obtained from "SIMION", which executed more quickly and had better associated graphics routines than the home-written program.

"SIMION" allowed a number of arbitrarily chosen potential contours to be plotted. The contours plotted in figures 5.6, 5.7, 5.17 and 5.18 are detailed below.

Figure 5.6: 0-100 V in 10 V steps, 100-2000 V in 100 V steps, 2000-2300 V in 50 V steps.

Figure 5.7: 0-100 V in 10 V steps, 100-1900 V in 100 V steps, 1900-2300 V in 50 V steps.

Figure 5.17: 0-50 V in 10 V steps, 100-1000 V in 100 V steps, 1000-3000 V in 500 V steps, 3000-3350 V in 50 V steps.

Figure 5.18: 0-50 V in 5 V steps, 100-200 V in 20 V steps, 200-1250 V in 50 V steps.

References.

[1] O. Klemperer, *Electron Optics*, Cambridge University Press, 1953.

Appendix C
Reflectron Simulation Program.

```
C     PROGRAM REFLECTRON
C     THE MASTER MENU WRITES TOF PARAMETERS TO THE SCREEN,
C     GIVING THE OPTION TO CHANGE DATA BEFORE
C     EXECUTING THE PROGRAM.
      PARAMETER(NPAR=15)
      IMPLICIT DOUBLE PRECISION(A-H,L-Z)
      DIMENSION TOFPAR(NPAR)
      CHARACTER*1 NUM
      CHARACTER*50 HEAD(NPAR)
      COMMON/BLOCK2/TOFPAR
      COMMON/BLOCK3/T,UAMU,CHARGE,SMAX,SMIN,L23,PI,THETA,
     !DELT,TRESP
      COMMON/BLOCK1/MRM,TIMMRM,PAKWID
      T=BEAMTEMP(T)
      CHARGE=1.6021892D-19
      PI=3.141592654
      THETA=4*(PI/180)
      UAMU=1.6605655D-27
      OPEN(UNIT=10,FILE='REFILE_HEADX')
      OPEN(UNIT=12,FILE='REFILE_TOFPARX6')
      DO 50 I=1,NPAR
      READ(10,100)HEAD(I)
      READ(12,*)TOFPAR(I)
      WRITE(6,120)HEAD(I),TOFPAR(I)
 50   CONTINUE
      CLOSE(10)
      CLOSE(12)
      CALL EMAS3PROMPT('Do you want to change any of this data(Y or N)?'
     !)
 60   READ(5,'(A1)')NUM
      IF(NUM.EQ.'Y'.OR. NUM.EQ.'y')THEN
      CALL EMAS3PROMPT('Which number?')
      READ*,I
      WRITE(6,101)
      WRITE(6,102)HEAD(I)
      WRITE(6,103)TOFPAR(I)
      CALL EMAS3PROMPT('Enter value:')
      READ*, TOFPAR(I)
      CALL EMAS3PROMPT('Do you want to change any more(Y or N)?' )
      WRITE(6,1)
      GOTO60
      ENDIF
      WRITE(6,1)
 39   WRITE(6,2)
      WRITE(6,3)
      WRITE(6,4)
```

```
      WRITE(6,5)
      CALL EMAS3PROMPT('Type appropriate response no.:')
      DELT=TOFPAR(14)*4D-9
      TRESP=TOFPAR(15)*1D-9
      SMIN=TOFPAR(1)-(TOFPAR(12)+(TOFPAR(13)/2))
      SMAX=SMIN+TOFPAR(13)
      READ*,MUN
      IF(MUN.EQ.1)THEN
      CALL WILEY(SMAX,SMIN,L23)
      ELSEIF(MUN.EQ.2)THEN
      CALL EMAS3PROMPT('Type in length of 1st F.F. region(in metres):')
      READ*,L23
      ELSE
      PRINT*,'Type either 1 or 2'
      GOTO39
      ENDIF
      PRINT*,'Length of 1st field-free region/m:'
      WRITE(6,104)L23
 70   WRITE(6,1)
C     A CHOICE OF ROUTINES IS WRITTEN TO THE SCREEN
      WRITE(6,6)
      WRITE(6,7)
      WRITE(6,8)
      WRITE(6,9)
      WRITE(6,1000)
      WRITE(6,1001)
      WRITE(6,1002)
      CALL EMAS3PROMPT('Type appropriate response no.:')
      READ*,INUM3
      WRITE(6,1)
      IF(INUM3.EQ.1)THEN
      CALL TRACK
      GOTO 70
      ELSEIF(INUM3.EQ.2)THEN
      CALL MAXRM
      GOTO 70
      ELSEIF(INUM3.EQ.3)THEN
      CALL EMAS3PROMPT('Change any of the original parameters(Y or N)?
     !')
      GOTO60
      ELSEIF(INUM3.EQ.4.OR.INUM3.EQ.5)THEN
      CALL DISTFN(INUM3)
      GOTO 70
      ELSEIF(INUM3.EQ.6)THEN
      WRITE(6,11)
      ELSE
      WRITE(6,12)
      GOTO70
      ENDIF
```

```
      STOP
1     FORMAT(1X ,'                    ')
2     FORMAT(1x,'Do you want:')
3     FORMAT(1x,'(1)Wiley-McLaren spatial focusing on G£3')
4     FORMAT(1x,'OR')
5     FORMAT(1x,'(2)Free selection of 1st field-free length ?')
6     FORMAT(1x,'Do you want to:')
7     FORMAT(1x,'(1)Follow ion packets through reflectron.')
8     FORMAT(1x,'(2)Calculate maximum resolvable mass.')
9     FORMAT(1x,'(3)Change data.')
1000  format(1x,'(4)Determine TOF as fn. of distance from rep.')
1001  format(1x,'(5)Determine TOF as a fn. of
     &initial velocity of neutrals.')
1002  format(1x,'(6)Stop.')
11    FORMAT(1X,'Program terminated')
12    FORMAT(1X,'Are you blind?!Please type 1,2,3,4,5 or 6.')
100   FORMAT(A50)
101   FORMAT(1x ,'This parameter is')
102   FORMAT(A50)
103   FORMAT(1x ,'Its current value is',T22,G10.3)
104   FORMAT(1X ,F10.3)
120   FORMAT(A50,T55,E11.3)
      END


C     MAXRM WORKS OUT MAX. RES. MASS FOR SYSTEM
C     PARAMETERS INPUT IN MAIN PROGRAM.
C     WORKS, BUT IS TEDIOUSLY SLOW.
      SUBROUTINE MAXRM
      PARAMETER(NPAR=20)
      IMPLICIT DOUBLE PRECISION(A-H,L-Z)
      DIMENSION DELTAT(0:1),TAVGE(0:1),TIME(NPAR)
     *,TVLATE(0:1),TEARLY(0:1),TLATE(0:1)
      COMMON/BLOCK2/LI,DVAR,DT,DK,L3DET,DDET,UI,UD,UT,UK,
     *UDET,DSL,HLB,SDEV,RESPON
      COMMON/BLOCK1/MRM,TIMMRM,PAKWID
      COMMON/BLOCK3/T,UAMU,CHARGE,SMAX,SMIN,L23,PI,THETA,
     *DELT,TRESP
C     STEPPING THROUGH MASSES UNTIL PACKET WIDTH EXCEEDS
C     SEPARATION OF ADJACENT MASSES.
      IM=0
 1    IM=IM+1
      DO 10 I=0,1
      IM=IM+I
      TMAX=0
      TMIN=1D6
      MASS=IM*UAMU
      DO 50 J=1,NPAR
      VO=VELO(J,MASS,T)
```

```
      STEP=(SMAX-SMIN)/(NPAR-1)
      SVAL=SMIN+(STEP*(J-1))
      VG1=SQRT((VO**2)+((2.0*UI*CHARGE*SVAL)/(MASS*LI)))
      VG2=SQRT((VG1**2)+(2.0*UD*CHARGE/MASS))
      VG4=SQRT(((VG2*COS(THETA))**2)+(2.0*UT*CHARGE/MASS))
      VDET=SQRT((VG2**2)+(2*UDET*CHARGE/MASS))
      TIG1=(VG1-VO)*MASS*LI/(UI*CHARGE)
      TG1G2=(VG2-VG1)*MASS*DVAR/(UD*CHARGE)
      TG2G3=L23/VG2
      TG3G4=(VG4-(VG2*COS(THETA)))*MASS*DT/(CHARGE*UT)
      TG4R=-1*MASS*DK*VG4/(CHARGE*UK)
      TG3DET1=L3DET/(VG2*COS(THETA))
      TG3DET2=(VDET-(VG2*COS(THETA)))*MASS
     £*DDET/(UDET*CHARGE)
      TG3DET=TG3DET1+TG3DET2
      TIME(J)=TIG1+TG1G2+TG2G3+TG3DET+(2.0*(TG3G4+TG4R))
      IF(TIME(J).LT.TMIN)THEN
      TMIN=TIME(J)
      ENDIF
      IF(TIME(J).GT.TMAX)THEN
      TMAX=TIME(J)
      ENDIF
50    CONTINUE
      TEARLY(I)=TMIN
      TLATE(I)=TMAX
      TVLATE(I)=TLATE(I)+DELT
      TAVGE(I)=(TVLATE(I)+TEARLY(I))*0.50
      DELTAT(I)=TVLATE(I)-TEARLY(I)+TRESP
10    CONTINUE
      TMOD=TVLATE(0)+TRESP
      IF(TMOD.GT.TEARLY(1))GOTO20
      IM=IM-1
      GOTO 1
20    MRM=IM
      TIMMRM=1D6*TAVGE(0)
      PAKWID=1D6*(TVLATE(0)-TEARLY(0))
      WRITE(6,33)MRM
      WRITE(6,34)TIMMRM
      WRITE(6,35)PAKWID
33    FORMAT(1X,'Max.res.mass for system is  ',E10.5)
34    FORMAT(1X,'TOF for this mass is  ',E10.5,'  microsecs.')
35    FORMAT(1X,'Packet width for this mass is  ',E10.5,' microsecs.')
      RETURN
      END


C     TRACK WORKS OUT ION PACKET VELOCITIES & CUMULATIVE
C     TOFS AT DIFFERENT STAGES THROUGH THE REFLECTRON.
C     DATA OUTPUT IN A FILE CALLED "TRACKTIMES".
```

```
      SUBROUTINE TRACK
      PARAMETER(NPAR=20)
      IMPLICIT DOUBLE PRECISION(A-H,L-Z)
      DIMENSION VO(NPAR),VG1(NPAR),VG2(NPAR),VG3(NPAR),
     *VG4(NPAR),TIG1(NPAR),TG1G2(NPAR),TG2G3(NPAR),TG3G4(NPAR),
     *TG4R(NPAR),TG3DET(NPAR),TSUM(NPAR),X(NPAR),SVAL(NPAR),
     *TIG1C(NPAR),TG1G2C(NPAR),TG2G3C(NPAR),TG3G4C(NPAR),
     *TG4RC(NPAR),TG3DEC(NPAR),TMIN(2),TMAX(2),TEARLY(2),
     *TDIFF1(2),TDIF2C(2),ST2(NPAR),VDET(NPAR),TG3DET1(NPAR),
     *TG3DET2(NPAR),TLATE(2),TOFAV(2)
      COMMON/BLOCK2/LI,DVAR,DT,DK,L3DET,DDET,UI,UD,UT,UK,
     *UDET,DSL,HLB,SDEV,RESPON
      COMMON/BLOCK3/T,UAMU,CHARGE,SMAX,SMIN,L23,PI,THETA,
     £DELT,TRESP
      WRITE(6,328)
      WRITE(6,329)
      WRITE(6,332)
      CALL EMAS3PROMPT('What mass(in amu) do you wish to follow? ')
      READ*,IM
      MASS=IM*UAMU
      OPEN(UNIT=15,FILE='TRACKTIMES',FILETYPE='CHARACTER')
      DO 230 KM=1,2
      IMO=IM+(2-KM)
      MASS=IMO*UAMU
      WRITE(15,300)
      WRITE(15,310)LI,DVAR,L23,L3DET,DT,DK
      WRITE(15,320)
      WRITE(15,330)UI,UD,UT,UK
      WRITE(15,340)
      WRITE(15,350)DELT,SMIN,SMAX
      WRITE(15,353)
      WRITE(15,355)TRESP,IMO
      DO 110 I=1,NPAR
      TSUM(I)=0
  110 CONTINUE
      WRITE(15,357)
      STEP=(SMAX-SMIN)/(NPAR-1)
      DO 115  I=1,NPAR
      SVAL(I)=SMIN+(STEP*(I-1))
      VO(I)=VELO(I,MASS,T)
      WRITE(15,358)I,SVAL(I),TSUM(I),VO(I)
  115 CONTINUE
      DO 120 I=1,NPAR
  120 CONTINUE
      WRITE(15,380)
      DO 130 I=1,NPAR
      VG1(I)=SQRT((VO(I)**2)+(2.0*UI*CHARGE*SVAL(I)/(MASS*LI)))
      TIG1(I)=((VG1(I)-VO(I))*MASS*LI/(UI*CHARGE))*1D6
      TSUM(I)=TSUM(I)+TIG1(I)
```

```
      WRITE(15,370)TSUM(I),VG1(I)
  130 CONTINUE
      WRITE(15,390)
      DO 140 I=1,NPAR
      VG2(I)=SQRT((VG1(I)**2)+(2.0*UD*CHARGE/MASS))
      IF (UD.EQ.0.0D0)THEN
      TG1G2(I)=DVAR/VGI(I)
      ELSE
      TG1G2(I)=((VG2(I)-VG1(I))*MASS*DVAR/(UD*CHARGE))*1D6
      ENDIF
      TSUM(I)=TSUM(I)+TG1G2(I)
      WRITE(15,370)TSUM(I),VG2(I)
  140 CONTINUE
      WRITE(15,400)
      DO 150 I=1,NPAR
      TG2G3(I)=(L23/(VG2(I)*COS(THETA)))*1D6
      TSUM(I)=TSUM(I)+TG2G3(I)
      WRITE(15,370)TSUM(I),VG2(I)
  150 CONTINUE
      WRITE(15,410)
      DO 160 I=1,NPAR
      VG4(I)=SQRT(((VG2(I)*COS(THETA))**2)+(2.0*UT*CHARGE/MASS))
      TG3G4(I)=((VG4(I)-(VG2(I)*COS(THETA)))*MASS
     £*DT/(CHARGE*UT))*1D6
      TSUM(I)=TSUM(I)+TG3G4(I)
      WRITE(15,370)TSUM(I),VG4(I)
  160 CONTINUE
      WRITE(15,420)
      DO 170 I=1,NPAR
      TG4R(I)=(MASS*DK*VG4(I)/(-1*CHARGE*UK))*1D6
      TSUM(I)=TSUM(I)+TG4R(I)
      WRITE(15,425)TSUM(I)
      ST2(I)=-(VG4(I)**2)/(2*UK*CHARGE/(DK*MASS))
      WRITE(6,422)
      WRITE(6,421)I,ST2(I)
  170 CONTINUE
      WRITE(15,410)
      DO 180 I=1,NPAR
      TSUM(I)=TSUM(I)+TG4R(I)
      WRITE(15,370)TSUM(I),VG4(I)
  180 CONTINUE
      WRITE(15,400)
      DO 190 I=1,NPAR
      TSUM(I)=TSUM(I)+TG3G4(I)
      WRITE(15,370)TSUM(I),VG2(I)
  190 CONTINUE
      WRITE(15,450)
      DO 200 I=1,NPAR
      VDET(I)=SQRT((VG2(I)**2)+(2*UDET*CHARGE/MASS))
```

```
      TG3DET1(I)=(L3DET/(VG2(I)*COS(THETA)))*1D6
      TG3DET2(I)=(VDET(I)-(VG2(I)*COS(THETA)))*MASS
     %*DDET/(UDET*CHARGE)
      TG3DET(I)=TG3DET1(I)+TG3DET2(I)
      TSUM(I)=TSUM(I)+TG3DET(I)
      WRITE(15,370)TSUM(I),VDET(I)
  200 CONTINUE
      TMIN(KM)=1D6
      DO 191 I=1,NPAR
      IF(TSUM(I).LT.TMIN(KM))THEN
      TMIN(KM)=TSUM(I)
      ENDIF
  191 CONTINUE
      TEARLY(KM)=TMIN(KM)
      TMAX(KM)=0
      DO 193 I=1,NPAR
      IF(TSUM(I).GT.TMAX(KM))THEN
      TMAX(KM)=TSUM(I)
      ENDIF
  193 CONTINUE
      TLATE(KM)=TMAX(KM)
      TDIFF1(KM)=TLATE(KM)-TEARLY(KM)
      DELTC=DELT*1D6
      TDIF2C(KM)=TDIFF1(KM)+DELTC
      TOFAV(KM)=(TLATE(KM)+TEARLY(KM))/2.0
  230 CONTINUE
      RESOL=(TOFAV(1)-TOFAV(2))*IM/TDIF2C(2)
      WRITE(15,460)
      WRITE(15,470)TOFAV(2)
      WRITE(15,473)
      WRITE(15,470)TDIF2C(2)
      WRITE(15,480)
      WRITE(15,490)RESOL
      WRITE(6,333)
      PRINT*,'Packet average TOF/microseconds'
      PRINT*,TOFAV(2)
      PRINT*,'Packet width(temporal effects included)/microsecs.'
      PRINT*,TDIF2C(2)
      PRINT*,'Resolution for this mass'
      PRINT*,RESOL
      CLOSE(15)
      WRITE(6,299)
  299 FORMAT(1X,'Data held in "TRACKTIMES"')
  300 FORMAT('LI/',T10,'DVAR/',T20,'L23/',T30,'L3DET/',
     *T40,'DT/',T50,'DK/',/,'Metres',T10,'Metres',T20,'Metres',
     *T30,'Metres',T40,'Metres',T50,'Metres')
  310 FORMAT(f4.3,T10,f5.4,T17,F10.5,T30,F6.5,T40,f5.4,T50,F5.4)
  320 FORMAT('UI/',T10,'UD/',T20,'UT/',T30,'UK/',/,'Volts',T10,
     *'Volts',T20,'Volts',T30,'Volts')
```

```
328     FORMAT(1X ,'This section works out the cumulative TOFs at diff
     *erent')
329     FORMAT(1X ,'stages in the RETOF & the corresponding velocities at
     * these stages.')
330     FORMAT(F8.3,T7,F10.2,T17,F10.2,T27,F10.2)
332     FORMAT(1X ,'TOFs are calculated for a no. of ions in a given i
     *on packet.')
333  FORMAT(1X ,'  ')
340  FORMAT('Laser temp. width/',T30,
     *'Extremes of spatial profile/'/,'seconds',T30,
     *'Metres',T50,'Metres')
350  FORMAT(E10.4,T30,E10.4,T50,E10.4)
353  FORMAT('Det. response/',T30,'Mass/'/,
     *'Seconds.',T30,'A.M.U.')
355  FORMAT(E10.4,T30,I5)
357  FORMAT('Ion no.',5X,'Dist. from G1/metres',5X,'Time/Microsecs.',
     15X,'Initial Velocity')
358  FORMAT(I4,15X,E10.4,8X,E10.4,11X,E10.4)
370  FORMAT(E10.5,T30,E12.5)
380  FORMAT('Time at G1/microsec',T30,'Velocity at G1')
390  FORMAT('Time at G2/microsec',t30,'Velocity at G2')
400  FORMAT('Time at G3/microsec',T30,'Velocity atG3')
410  FORMAT('Time at G4/microsec',T30,'Velocity at G4')
420  FORMAT('Time at rest/microsec',T30,'Velocity at rest')
421  FORMAT(i4,10x,f10.5)
422  FORMAT(1X ,'Ion Number',5x,'Length in reflectron/m')
425  FORMAT(E10.5,T30,'Zero')
450  FORMAT('Time at detector/microsec',T30,'Velocity at detector')
460  FORMAT('Packet average TOF/microseconds')
470  FORMAT(E10.4)
473  FORMAT('Packet width(temporal effects included)/microsecs.')
480  FORMAT('Resolution for this mass:')
490  FORMAT(F10.4)
     RETURN
     END


     FUNCTION VELO(I,MASS,T)
     DOUBLE PRECISION G05DDF,CONST,T,VX,VY,VZ,VELO,MASS
C    THIS FUNCTION SIMULATES A MAXWELLIAN VELOCITY
C    DISTRIBUTION IN A SUPERSONIC MOLECULAR BEAM. IT
C    USES A RANDOM NUMBER GENERATOR TO DO SO.
     CALL G05CBF(I)
     CONST=DSQRT(1.3D-23*T/MASS)
     VX=G05DDF(1766.0D0,CONST)
     VY=G05DDF(0.0D0,CONST)
     VZ=G05DDF(0.0D0,CONST)
     VELO=DSQRT(VX**2+VY**2+VZ**2)
     RETURN
```

```
      END


      FUNCTION BEAMTEMP(T)
      WRITE(6,1)
      WRITE(6,2)
      WRITE(6,4)
      WRITE(6,3)
      CALL EMAS3PROMPT('What temp. is the mol. beam (in Kelvin units)?
     !')
      READ(5,*)T
      BEAMTEMP=T
      WRITE(6,3)
    1 FORMAT(1x,'This program evaluates TOFs in a reflectron.')
    2 FORMAT(1X ,'It also tries to simulate the initial velocity ')
    4 FORMAT(1x,'distribution present in a supersonic expansion.')
    3 FORMAT(1x,' ')
      RETURN
      END


      SUBROUTINE WILEY(X,Y,Z)
      IMPLICIT DOUBLE PRECISION (A-H,O-Z)
C     THIS SUBROUTINE CALCULATES THE POSITION OF
C     THE WILEY-McLAREN SPACE FOCAL PLANE.
      COMMON/BLOCK2/A,B,C,D,E,F,G,H,O,P,Q,R,S,U,V
      COMMON/BLOCK3/T,UAMU,CHARGE,SMAX,SMIN,L23,PI,THETA,
     £DELT,TRESP
      ES=G/A
      SVAL=(X+Y)/2
      WKO=1+(H/(SVAL*ES))
      Z=2*WKO*((SVAL*SQRT(WKO))-(B/(SQRT(WKO)+1)))
      RETURN
      END

      SUBROUTINE DISTFN(INUM3)
C     THIS SUBROUTINE AND SUBROUTINE RTIME ARE
C     USED TO CALCULATE THE SPATIAL AND VELOCITY
C     DEPENDENCE OF ION TIME OF FLIGHT.
      IMPLICIT DOUBLE PRECISION (A-H, L-Z)
      COMMON/BLOCK2/LI,DVAR,DT,DK,L3DET,DDET,UI,UD,UT,UK
     *UDET,DSL,HLB,SDEV,RESPON
      COMMON/BLOCK3/T,UAMU,CHARGE,SMAX,SMIN,L23,PI,THETA,
     $DELT,TRESP
      CALL EMAS3PROMPT('What mass do you want to follow?')
      READ*,IM
      MASS=IM*UAMU
      IF(INUM3.EQ.5)THEN
      OPEN(UNIT=17,FILE='EXITG',FILETYPE='CHARACTER')
```

```
      DSL=0.0D0
      X=LI/300.0D0
      DO 100 JJ=1,301
      S=LI-DSL
      DSL=DSL+X
      VO=VELO(1,MASS,T)
      TIME=RTIME(MASS,S,VO)
      TIME=TIME*1.0D6
      S=S*1.0D3
      WRITE(17,*)S,TIME
  100 CONTINUE
      PRINT*,'Data pairs held in EXITG'
      CLOSE(17)
      ELSE
      OPEN(UNIT=18,FILE='velfn',FILETYPE='character')
      CALL EMAS3PROMPT('What is mean of the distribution ? ')
      READ*,MEAN
      CALL EMAS3PROMPT('What is the SD of the distribution ? ')
      READ*,SIGMA
      S=(SMAX+SMIN)/2
      PRINT*,S
      ISIGMA=INT(SIGMA)
      NN=ISIGMA*3
      NM=-1*NN
      NN=NN+MEAN
      NM=NM+MEAN
      do 107 i=NM,NN
      VO=I*1.0D0
      TIME=RTIME(MASS,S,VO)
      TIME=TIME*1.0D6
      WRITE(18,*)VO,TIME
  107 CONTINUE
      PRINT*,'Data in VELFN'
      ENDIF
      RETURN
      END

      FUNCTION RTIME(MASS,S,VO)
      IMPLICIT DOUBLE PRECISION(A-H,L-Z)
      COMMON/BLOCK2/LI,DVAR,DT,DK,L3DET,DDET,UI,UD,UT,UK,
     *UDET,DSL,HLB,SDEV,RESPON
      COMMON/BLOCK3/T,UAMU,CHARGE,SMAX,SMIN,L23,PI,THETA,
     *DELT,TRESP
      VG1=SQRT((VO**2)+((2*UI*CHARGE*S)/(MASS*LI)))
      VG2=SQRT((VG1**2)+(2*UD*CHARGE/MASS))
      VG4=SQRT(((VG2*COS(THETA))**2)+(2.0*UT*CHARGE/MASS))
      VDET=SQRT((VG2**2)+(2*UDET*CHARGE/MASS))
      TIG1=(VG1-VO)*MASS*LI/(UI*CHARGE)
      IF(UD.EQ.0.0D0)THEN
```

```
TG1G2=DVAR/VG1
ELSE
TG1G2=(VG2-VG1)*MASS*DVAR/(UD*CHARGE)
ENDIF
TG2G3=L23/(COS(THETA)*VG2)
TG3G4=(VG4-(VG2*COS(THETA)))*MASS*DT/(CHARGE*UT)
TG4R=-1.0*MASS*DK*VG4/(CHARGE*UK)
TG3DET1=L3DET/(VG2*COS(THETA))
TG3DET2=(VDET-(VG2*COS(THETA)))/(UDET*CHARGE)
TG3DET2=TG3DET2*MASS*DDET
TG3DET=TG3DET1+TG3DET2
RTIME=TIG1+TG1G2+TG2G3+TG3DET+(2.0*(TG3G4+TG4R))
RETURN
END
```

Appendix D
Heating of a Surface by Pulsed Laser Irradiation.

An important point to consider in laser desorption studies is the properties of the substrate from which the sample is desorbed. The desorption model proposed by Zare and Levine [1] attributes the rapid heating of the sample to an absorption of the incident desorption laser light by the substrate. It is therefore useful to attempt to model the transient temperature profile generated in the substrate following irradiation by this CO_2 laser pulse.

The temperature profile generated in the substrate depends on the relative sizes of the energy penetration depth or "skin" depth and the thermal diffusion length for the sample under irradiation. The skin depth is given by

$$L = 1/\alpha, \tag{1}$$

where α is the absorption coefficient of the substrate (units = cm^{-1}), whilst the thermal diffusion length, calculated for heat diffusion in a plane during the laser pulse, is given by

$$d = (2 Dt)^{1/2}, \tag{2}$$

where D is the thermal diffusivity of the sample (units = $cm^2 s^{-1}$) and t is the duration of the heating pulse.

If d is small compared to the beam diameter, the heat flow across the surface is negligible and the temperature profile is generated by solution of a one

dimensional heat diffusion equation. The one dimensional heat diffusion equation yields

$$\partial T(x,t)/\partial t = \partial/\partial x\,(D\,\partial T(x,t)/\partial x) + E(x,t)/\rho C_p, \qquad (3)$$

where E (Wcm^{-3}) is the heat term arising from the impinging laser beam, ρ (gcm^{-3}) is the sample density, and C_p is the sample heat capacity.

Ready [2] gave a solution of this equation, for the case of constant thermal parameters and high absorption coefficient (10^5-10^6 cm^{-1}), as

$$T(x,t) = (1-R)(1/K)(D/\pi)^{1/2}\int I(t-\tau)\exp(-x^2/4D\tau)\tau^{1/2}\,d\tau, \qquad (4)$$

where I(t) is the incident laser power density (Wcm^{-2}), R is the reflectivity and K is the thermal conductivity ($Wcm^{-1}K^{-1}$) of the sample. The ratio $K/\rho C_p$ gives D, the thermal diffusivity.

If $L < d$, the heat source can be treated as being localised at the surface of the substrate. Equation (4) has been used to obtain analytical expressions for the surface temperature rise in metals heated by pulsed laser irradiation. These derivations have generally assumed a localised source of heat at the metal surface. This is valid for most metals, which have high absorption coefficients over a wide range of laser wavelengths. In the case of insulating materials such as quartz, this assumption becomes more questionable. Furthermore, quartz has more strongly temperature-dependent thermal parameters (K, C_p, D and d) than metals. In such a situation, modelling of the surface temperature can be

performed numerically, by solving the heat diffusion equation by a finite difference method [3]. The details of this procedure are given below.

If a one dimensional heat diffusion model is considered, the substrate is divided into a series of elements along a line perpendicular to the surface. Each element, except that one at the surface, has length Δx, and is centred at a node. The surface acts as a node, so that the element closest to the surface has length $\Delta x/2$. For each element (except that one at the surface), the energy balance is

$$K[T(m+1,p) + T(m-1,p) - 2T(m,p)]\,\Delta t/\Delta x + I(m,p)[1-\exp(-\alpha x)]\Delta t = \rho C_p \Delta x[T(m,p+1) - T(m,p)], \quad (5)$$

where $T(m,p)$ is the temperature of node m at time p, $T(m,p+1)$ is the temperature at the same position at time interval Δt later, and $I(m,p)$ is the heating power incident on element m at time p. The temperature of each mode is given by

$$T(m,p+1) = D\Delta t(\Delta x)^{-2}[T(m+1,p) + T(m-1,p)] + I(m,p)[1-\exp(-\alpha\Delta x)]\Delta t/[\rho C_p \Delta x] + [1-\{2D\Delta t/(\Delta x)^2\}]T(m,p). \quad (6)$$

As the surface is the mode $m=0$, the surface temperature is

$$T(0,p+1) = 2D\Delta t(\Delta x)^{-2}T(1,p) + (1-R)\,I(0,p)[1-\exp(-\alpha\Delta x/2)]\Delta t/[\tfrac{1}{2}\rho C_p \Delta x]$$

$$+ [1-\{2D\Delta t/(\Delta x)^2\}]T(0,p) \quad (7)$$

The numerical solution is stable if the coefficient of T(m,p) is positive, which requires suitable choice of Δt and Δx. I(m,p) is calculated from

$$I(m,p) = I(m-1,p) \exp(-\alpha\Delta x) \quad (8)$$

and

$$I(1,p) = (1-R)\, I(0,p) \exp(-\alpha\Delta x/2). \quad (9)$$

The accuracy of the calculation depends upon the size of Δx and Δt chosen, and the available computing power.

Two substrate materials were modelled, namely stainless steel and quartz. The optical and thermal properties of these materials are listed in table D.1.

The intensity of laser light as a function of time was calculated from the measured pulse energy and temporal profile (see figure 4.8) of the PSI LP-30 CO_2 laser, and assuming a laser focal spot of 2 mm diameter.

Figure D.1 shows the calculated temperature for a stainless steel substrate as a function of depth. The maximum surface temperature, T_{max}, is only 331 K and is reached after 22 μs, corresponding to a heating rate of 1.4×10^6 Ks^{-1}. This low surface temperature is mainly due to a combination of the high reflectivity and high thermal conductivity of the stainless steel. It is clear that there is significant

Table D.1. Thermal properties of quartz and stainless steel.

	Quartz [3]	Stainless Steel
$K/Wcm^{-1}K^{-1}$	0.014	0.3 [5]
$C_p/Jg^{-1}K^{-1}$	0.670	0.4512 [5]
ρ/gcm^{-3}	2.2	8.86
D/cm^2s^{-1}	0.0095	0.0750
α/cm^{-1}	2.7×10^3	10^8
R at 10.6μm	12%	90% [2]
$\Delta t/\mu s$	1	1
$\Delta x/\mu m$	5	5

Figure D.1. The laser-induced temperature profile of stainless steel, heated by a 0.3 $MWcm^{-2}$ PSI LP-30 CO_2 laser beam.

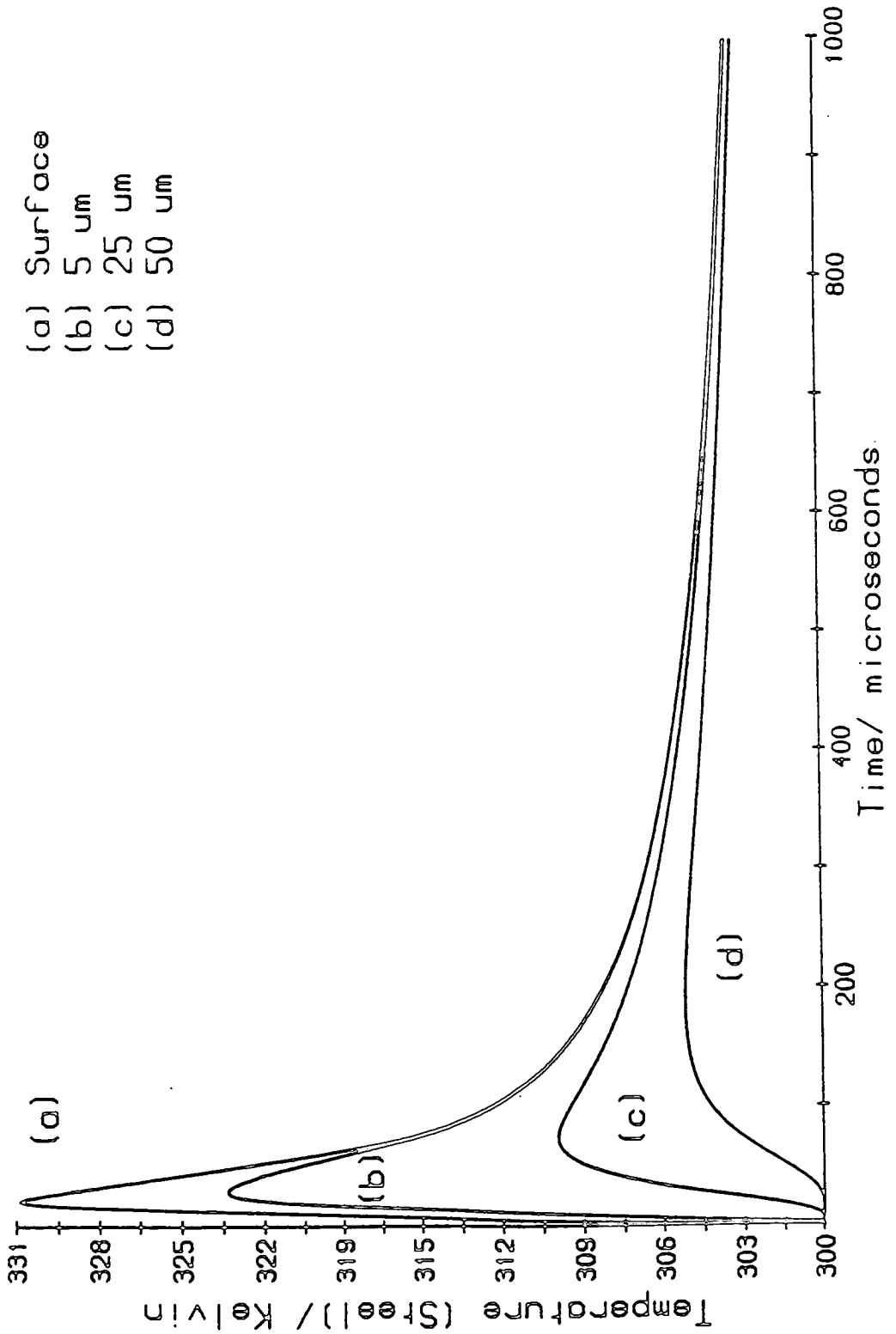

heat penetration into the bulk of the substrate due to its high thermal conductivity. For example, the maximum temperature at a depth of 50 μm is 305 K, which corresponds to a temperature increase that is 16% of the increase at the surface.

Figure D.2 shows the calculated temperature profile for a quartz substrate as a function of depth. The most striking feature of this plot is the significantly higher surface temperature that is attained- here T_{max} is 1587 K at a delay time of 33 μs. This is primarily due to the lower reflectivity of quartz relative to stainless steel at $\lambda = 10.6$ μm, and also to its lower thermal diffusivity. The calculation shows that the bulk of the material reaches quite a high temperature (424 K at 50 μm), which is primarily due to the larger skin depth of quartz relative to steel. However, this is a proportionately lower temperature relative to the surface (9.6%) than is the case with stainless steel. If the behaviour of both materials are modelled with the same values of R and α (12% and 2.7×10^3 cm^{-1} respectively), a similar trend is found i.e. the surface temperature of quartz is higher than that of steel (see figure D.3) and this temperature is more localised at the surface of the material.

Zare and coworkers [4] have measured the surface temperature of a quartz substrate under CO_2 laser irradiation using a calibrated Pt thin film resistance thermometer. They observed a maximum surface temperature of 723 K using a CO_2 laser pulse intensity similar to that employed here. In order to simulate their observed temperature profile, they had to consider the temperature dependence of the thermal parameters. Using the values listed in table D.1, they obtained a similar plot to figure D.2. However, by allowing both K and C_p to

Figure D.2. The laser-induced temperature profile of quartz, heated by a 0.3 $MWcm^{-2}$ PSI LP-30 CO_2 laser beam.

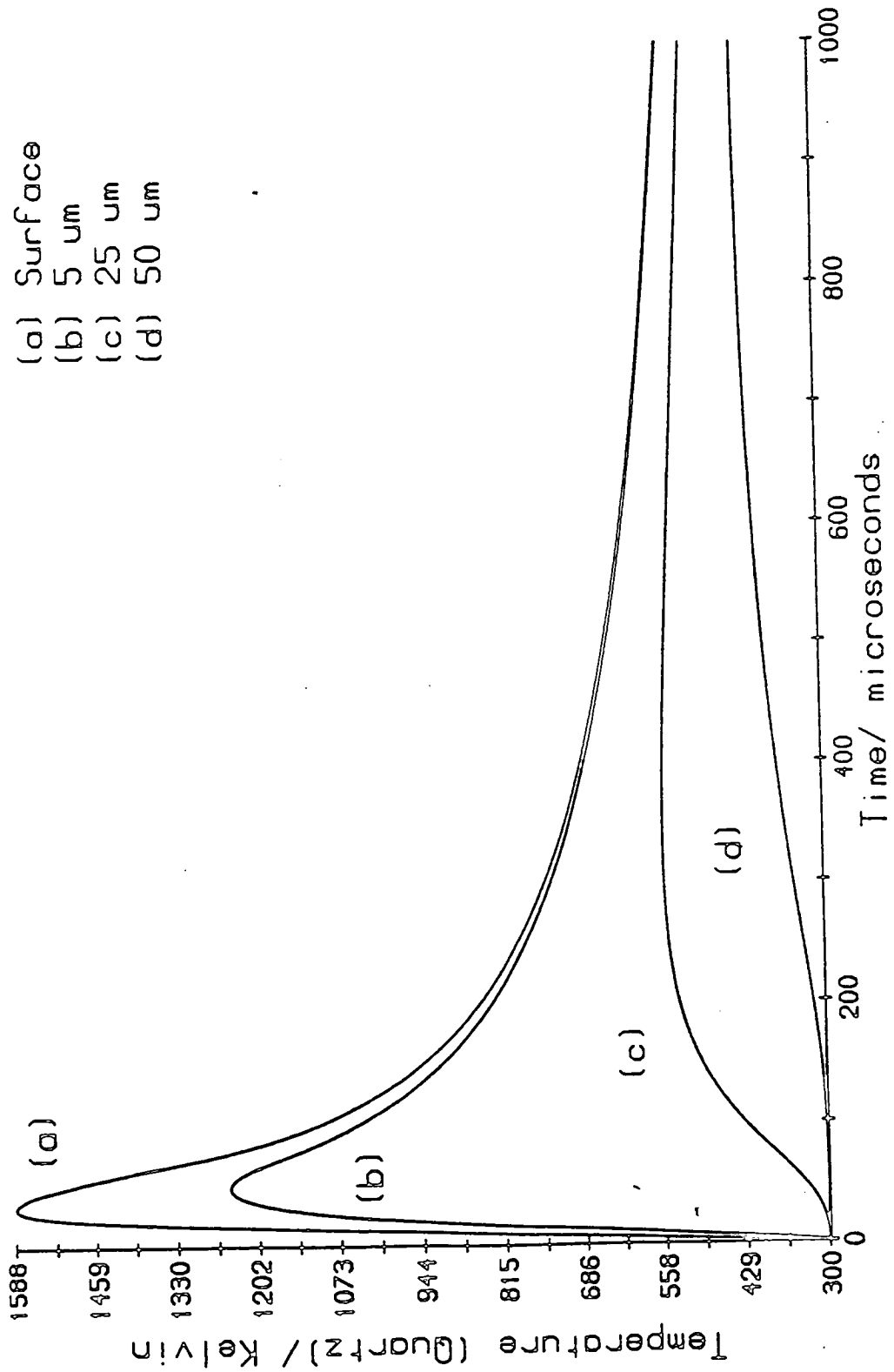

vary with temperature, very good agreement with the measured temperature profile was achieved. This, of course, required an accurate tabulation of K(T) and $C_p(T)$, which was not available at the time the present simulations were carried out.

Two conclusions can be drawn from these simulations:

1. The relatively low degree of surface heating obtained with the PSI LP-30 CO_2 laser (at power densities of 0.3 $MWcm^{-2}$), as shown in figure D.1, probably explains the inability to detect any signals in the LD-MPIMS experiments in the absence of the colloidal graphite mix. A more tightly focused CO_2 laser beam would improve the situation. For example, if a 200 μm diameter focal spot is employed, the value of T_{max} at the surface is increased to 3385 K see figure D.4).
2. The ability to heat a quartz surface up to higher temperatures than a stainless steel rod, under similar laser irradiation conditions, has obvious ramifications when studying materials with low vapour pressures. In the limit of available laser power, it should be possible to obtain larger LD-MPIMS signals using a quartz substrate.

Figure D.3. Comparison of the surface temperature profiles of stainless steel and quartz, assuming identical values for the reflectivity and absorption coefficient of both materials.

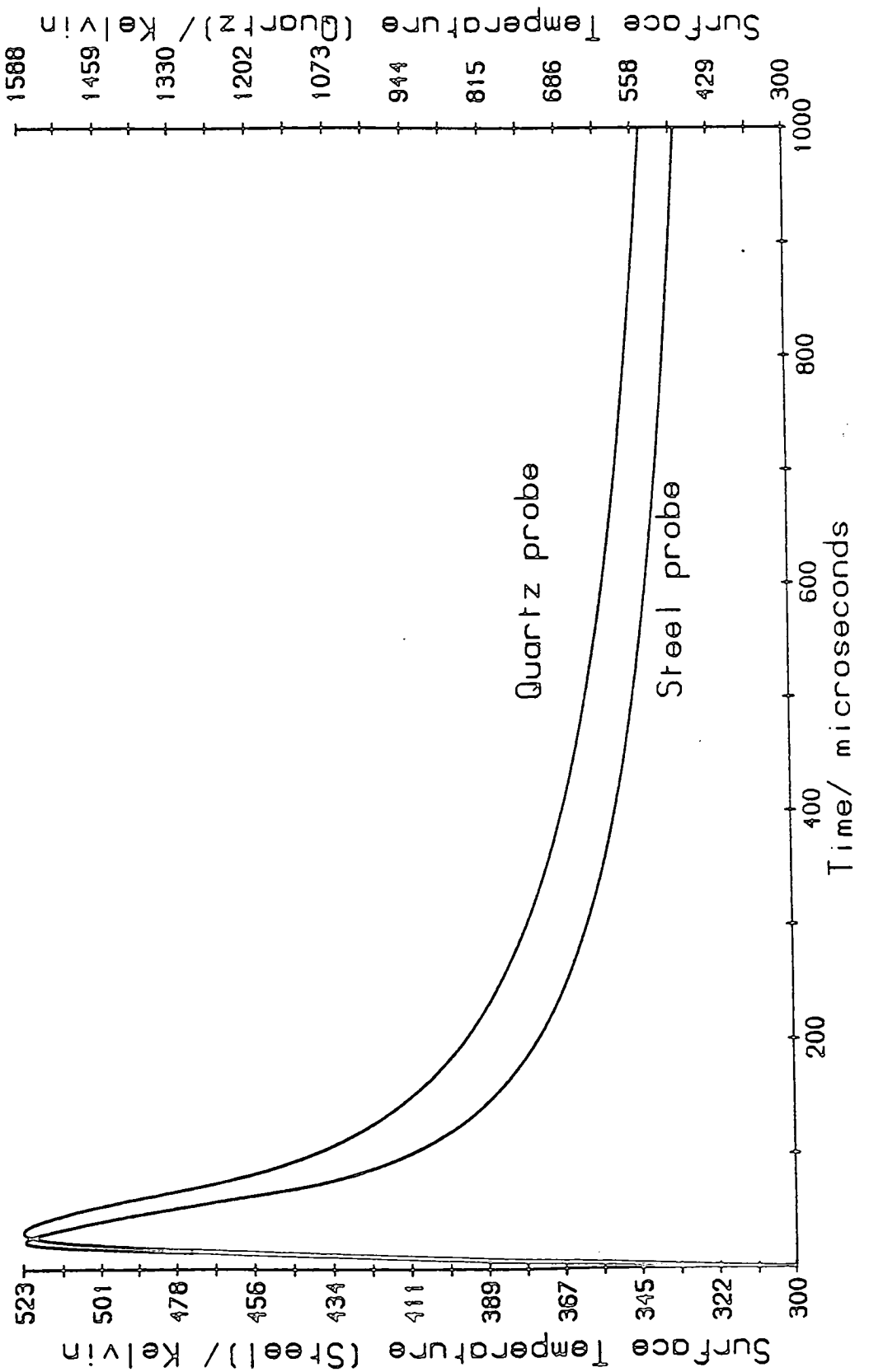

Figure D.4. The laser-induced temperature profile of stainless steel, heated by a 30 $MWcm^{-2}$ PSI LP-30 CO_2 laser beam.

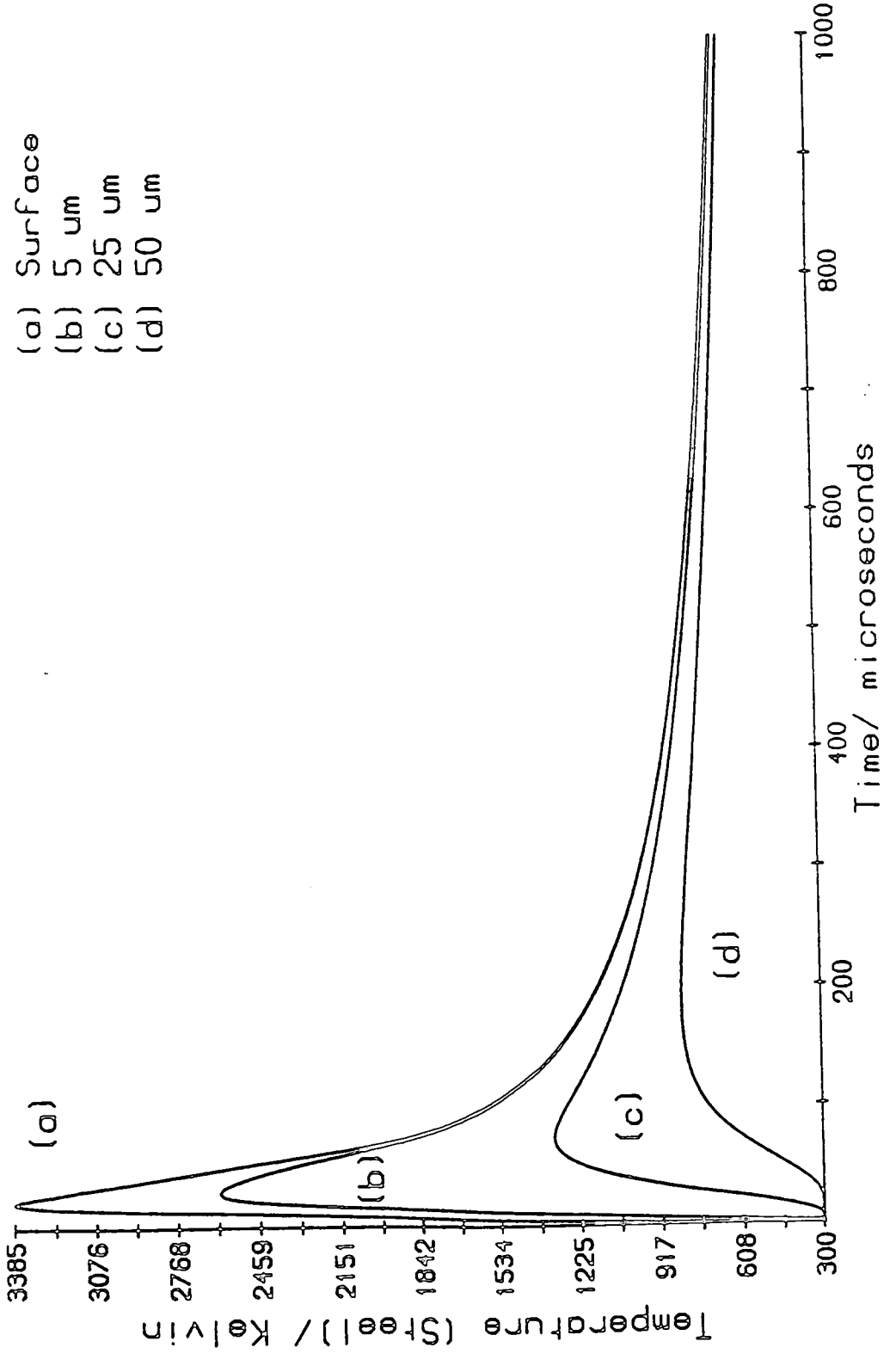

References.

[1] R. N. Zare, R. D. Levine, Chem. Phys. Letters, **136**, 593, (1987)

[2] J. F. Ready, *Effects of High-Power Laser Radiation*, Academic Press, New York, 1971.

[3] J.-M. Phillipoz, R. Zenobi, R. N. Zare, Chem. Phys. Letters, **158**, 12, (1989)

[4] R. Zenobi, J. H. Hahn, R. N. Zare, Chem. Phys. Letters, **150**, 361, (1988)

[5] R. C. Weast (Ed.), *Handbook of Chemistry and Physics, 70th Edition*, CRC Press, Boca Raton FLA, 1989.

Appendix E
Courses and Conferences Attended

In accordance with the regulations of the Department of Chemistry, University of Edinburgh I have attended the following courses during my period of study:

1. Atmospheric Chemistry
2. Laser Physics
3. Mass Spectrometry
4. Quantum Physics 2
5. Reaction Dynamics
6. Recent Developments in Physical Chemistry
7. Scientific German
8. Signal Processing
9. Theoretical Chemistry

In addition I have attended the Laser Chemistry research group meetings, departmental seminars, joint Edinburgh - Heriot-Watt laser chemistry group meetings, and the following conferences:

1. Faraday Division, High Resolution Spectroscopy Group, York, 1985
2. Scottish Quantum Chemistry Group, Strathclyde, 1986
3. NATO ASI on Structure/Reactivity and Thermochemistry of Ions, Les Arcs 1986
4. Royal Institution Symposium on Jet Spectroscopy, London, 1986
5. XIth International Symposium on Molecular Beams, Edinburgh, 1987
6. Faraday Division, High Resolution Spectroscopy Group, Birmingham, 1988